UNIVERSIDAD AUTÓNOMA DE MADRID

FACULTAD DE CIENCIAS

DEPARTAMENTO DE FÍSICA APLICADA

Characterization of the fundamental properties of $Cu_2ZnSn_{1-y}Ge_y(S,Se)_4$ compounds for photovoltaic applications

Memoria que presenta

Eduard García Llamas

Para optar al grado de

Doctor

Directores:

Dr. D. José Manuel Merino Álvarez

Dr. D^{a}. Ana Raquel Caballero Mesa

2016

A Jullieth y Abril,

A mi familia,

"*Sometimes it is the people no one can imagine anything of, who do the things no one can imagine.*"

-The Imitation Game-

Acknowledgements

There are many people to whom I would like to express my gratitude for their help in many ways during the course of this work and I would not like to forget any of them.

Firstly and foremost, I would like to express my sincere gratitude to my supervisors Dr. Raquel Caballero and Dr. José Manuel Merino for the continuous support of my Ph.D. study and related research, for they patience, motivation, and immense knowledge. Their guidance helped me in all the time of research and writing of this thesis. I could not have imagined having a better supervisors and leaders to guide me in this thesis.

Beside my supervisors, I would like to thank to Prof. Dr. Máximo León as a leader of the Photovoltaic Materials Group. Every day, he gave me a teaching lesson how to manage and lead a group fruitfully and successfully.

I would like to thank all members of the Applied Physics Department, past and present, for being an excellent company as well as for their great help, support, and teamwork throughout the past years.

Special thanks also go to all the people at KESTCELLS project, especially the young ESRs. We have shared a lot of great experiences and troubles that make us closer and even friends. I wish you all the best and I hope that you will enjoy your careers and, most important, lives. I would also like to thank all the groups that I have been part of during my stays, exchanges and measurements time at University of Luxembourg, Helmholtz-Zentrum Berlin, Freie Universität Berlin, Institut Laue-Langevin, Catalonia Institute for Energy Research and ABENGOA Solar. Especially the leader groups Prof. Siebentritt, Prof. Schorr, Prof. Pérez-Rodríguez and Dr. Delgado. Moreover, thanks to the people that help me with neutron diffraction measurements, Dr. Puente-Orench from ILL and Dr. Franz from HZB, with the WDX measurements, Dr. Gurieva from HZB, and with the resistivity measurement, Dr. Guc from Academy of Science of Moldova. KESTCELLS project gave me the opportunity to move around the world, especially around Europe, and it has given me unique experiences to learn about new places, people and cultures. Of course, I would like to thanks the financial support of Marie Curie Actions. Whitout their support would not be possible to be part of the KESTCELLS project in the FP7-PEOPLE-2012-ITN program.

My sincere thanks also goes to Dr. Rosalía Serna, Dr. Victor Izquierdo-Roca, and Dr. Edgardo Saucedo, who provided me an opportunity to join them, and who gave access to their laboratories and research facilities. Without their precious support it would not be possible to conduct Ellipsometry, Raman measurements and device fabrication, respectively, in this research.

I thank my fellow labmates for the stimulating discussions, for the sleepless nights we were working together before deadlines, and for all the fun we have had in the last years. In particular, I am very grateful to Dr. Gallach and Arancha Gómez that they became more than friends, they became part of my family. It would be impossible to perform this thesis without their help in all the aspects. Futhermore, it would be much more difficult or even not possible to perform this work without the technicians of applied physics department, the glassmaker specialists of SEGAINVEX, and the technicians of the SIdI, to all of them thank you very much.

Lastly, I would like to thank my family: my parents and my brother for supporting me throughout my life.

And finally there are two very especial people I need to thank to. I am very grateful and lucky to have a very unique woman to my side during this entire journey, how gave support, enthusiasm and energy during all these years. Together, we became stronger and we have been blessed with an extraordinary present, our daughter. This little baby has been changing extraordinarily our lives and gave us much more energy to work for a better future all together

Abstract

$Cu_2ZnSn_{1-y}Ge_y(S,Se)_4$ (CZGTSSe) has been co-related with the successful $CuIn_{1-y}Ga_y(S,Se)_2$ as a promising candidate to be used as absorber material for photovoltaic applications. The main advantages of the CZGTSSe solution are that it does not contain rare or expensive elements and, as a consequence, it has a potential cost reduction for its industrialization.

The aim of this work was to investigate the fundamental properties like structural, optical, vibrational and electrical, of $Cu_2ZnSn_{1-y}Ge_y(S,Se)_4$ in single crystals grown by chemical vapor deposition and in polycrystalline samples synthesized by Bridgman method and solid state reaction. By this way, this thesis contributes to understand and enhance the knowledge of the properties of these compounds that can lead to improve device efficiencies. Another objective was the fabrication of solar cells of the material previously synthesized.

The crystal structure of $Cu_2ZnSn_{1-y}Ge_y(S,Se)_4$ single crystals and polycrystalline quaternary semiconductors compounds with a wide range of Ge contents have been investigated. The chemical composition of the compounds was measured by wavelength dispersive X-ray (WDX) and energy dispersive X-ray (EDX) spectroscopies. The compounds were grinded to powders and measured by X-Ray and Neutron diffraction. On the one hand, the single crystals experimental data from both diffraction techniques were analyzed simultaneously by Rietveld refinements. On the other hand, the polycrystalline compound refinements were performed only using the neutron diffraction experimental data. In both cases, the Rietveld analysis of the diffraction data gave valuable information like the tetragonal lattice constants, anion coordinates, cation-anion distances, site occupancy factors of the cations and the point defects type with the change of the [Ge/(Ge+Sn)] atomic ratio.

The linear optical properties of $Cu_2ZnSn_{1-y}Ge_y(S,Se)_4$ high quality single crystals with a wide range of Ge contents have also been investigated in the visible and near infrared range using spectroscopic ellipsometry measurements. From the analysis of the complex dielectric function spectra, it has been found that the bandgap energy E_0 increases continuously with the Ge content. In the case of the polycrystalline form of these compounds, it appears the same linear behavior of the band gap when the germanium

increases. Furthermore, the evolution of the interband transitions E_{1A} and E_{1B} has been also determined. The understanding of the incorporation of Ge into the $Cu_2ZnSn(S,Se)_4$ lattice is fundamental in order to develop efficient bandgap engineering of these compounds towards the fabrication of kesterite-based thin film solar cells with enhanced performance.

Raman spectroscopy was used to evaluate the zone-center optical phonons of $Cu_2ZnSn_{1-y}Ge_y(S,Se)_4$ single crystals, leading to a complete characterization of their vibrational properties. The analysis has been performed by using Raman scattering spectra excited with three different excitation wavelengths. The Raman spectra show the characteristic peaks for different $Cu_2ZnSn_{1-y}Ge_yS_4$ and $Cu_2ZnSn_{1-y}Ge_ySe_4$ samples. The two mode behavior was found for most of the peaks in both compounds. However, the most intense mode exhibited one mode behavior in selenium containing compounds and two mode behavior in sulfur containing compounds, in the single crystal form. Moreover, it was shown that for the polycrystalline compounds, there were present one and two mode behavior of the main peak for selenium and sulfur compounds, respectively. Finally, the Raman scattering was used to identify clearly the presence of secondary phases in the Cu_2ZnSnS_4 compounds, as well as for the thin films.

The conductivity versus temperature ($\sigma(T)$) measurements were used to identify two different conduction mechanisms for the single crystals. The thermal activated conduction process dominates at higher temperature ranges and the Mott variable range hopping fits better with the experimental results at lower temperatures. At low temperature, it was correlated the defects found with the Rietveld refinements in the structural characterization section with the energy of the width of the band acceptor determined by $\sigma(T)$ measurements.

Finally, photovoltaic devices based on CZTSSe using the synthesized compounds as precursors for absorber thin films solar cells were manufactured and characterized by Intensity versus Voltage and EQE measurements.

Resumen

La solución sólida $Cu_2ZnSn_{1-y}Ge_y(S,Se)_4$ (CZGTSSe) se ha correlacionado con la exitosa $CuIn_{1-y}Ga_y(S,Se)_2$ como un candidato prometedor para ser utilizado como material absorbente para aplicaciones fotovoltaicas. Las principales ventajas de los compuestos CZGTSSe son que no contienen elementos raros o caros y, como consecuencia, implican una posible reducción de costes para su industrialización.

El objetivo de este trabajo consistió en la investigación de las propiedades fundamentales, estructurales, ópticas, vibracionales y eléctricas, de monocristales de $Cu_2ZnSn_{1-y}Ge_y$ $(S,Se)_4$ crecidos mediante deposición química en fase vapor y de muestras policristalinas sintetizadas por Bridgman y reacción en estado sólido. De esta manera, esta tesis contribuye a entender y mejorar el conocimiento de las propiedades de estos compuestos que pueden conducir a mejorar la eficiencia de los dispositivos. Otro objetivo adicional consistió en la fabricación de células solares con el material previamente sintetizado.

Se ha investigado la estructura cristalina de los monocristales de $Cu_2ZnSn_{1-y}Ge_y(S,Se)_4$ así como la de los mismos compuestos semiconductores en forma policristalina con una amplia variación en el contenido de Ge. La composición química de los compuestos se midió por dispersión de longitud de onda de rayos X (WDX) y por energía dispersiva de rayos X (EDX). Los compuestos en forma de polvo fueron medidos mediante difracción de rayos X y de neutrones. Por una parte, se analizaron de manera simultánea los datos experimentales de ambas técnicas de difracción para las muestras monocristalinas mediante refinamiento Rietveld. Por otro lado, los refinamientos de los compuestos policristalinos se realizaron utilizando sólo los datos experimentales de la difracción de neutrones. En ambos casos, tras el análisis de los datos de difracción por Rietveld, se obtuvo información importante, tal como los parámetros de red, las coordenadas fraccionarias de los aniones, las distancias catión-anión, los factores de ocupación de los cationes y los tipos de defectos puntuales, con el cambio de la relación atómica [Ge/(Ge+Sn)].

Las propiedades ópticas lineales de los monocristales $Cu_2ZnSn_{1-y}Ge_y(S,Se)_4$ de alta calidad con una amplia variedad en contenido de Ge también se han investigado en el rango visible e infrarrojo cercano utilizando mediciones de elipsometría espectroscópica.

A partir del análisis de los espectros de la función dieléctrica compleja, se ha encontrado que la energía de la banda prohibida, $E_{0,}$ aumenta de manera continua con el aumento del contenido de Ge. En el caso de los compuestos policristalinos, parece que la energía de la banda prohibida sigue el mismo comportamiento lineal cuando el germanio aumenta. Por otra parte, la evolución de las transiciones interbanda, E_{1A} y $E_{1B,}$ también fue determinada. Entender la incorporación de Ge en la red atómica de los compuestos $Cu_2ZnSn(S,Se)_4$ es fundamental para el desarrollo de la ingeniería de la banda prohibida de estos compuestos para llegar a la fabricación de células solares de lámina delgada de kesterita con un mayor rendimiento.

La espectroscopía de Raman se utilizó para evaluar la zona central óptica de los fonones de los monocristales de $Cu_2ZnSn_{1-y}Ge_y(S,Se)_4$, lo que ha llevado a la caracterización completa de sus propiedades de vibración. El análisis se ha realizado mediante el uso de espectros de Raman obtenidos con tres diferentes longitudes de onda de excitación. Los espectros muestran los picos característicos de las diferentes muestras de $Cu_2ZnSn_{1-y}Ge_yS_4$ y $Cu_2ZnSn_{1-y}Ge_ySe_4$. Se encontró un comportamiento bimodal para la mayoría de los picos en ambos compuestos. Sin embargo, para los monocristales se vio claramente que el modo más intenso exhibe un comportamiento de un solo modo para los compuestos con selenio y un comportamiento bimodal para los compuestos con azufre. Por otra parte, se observó que, para los compuestos policristalinos, el comportamiento de un solo modo y bimodal seguía presente para el pico principal de los compuestos de selenio y azufre respectivamente. Por último, se utilizó la dispersión de Raman para identificar claramente la presencia de fases secundarias en los compuestos Cu_2ZnSnS_4, así como para las películas delgadas.

Las medidas de conductividad frente a la temperatura ($\sigma(T)$) se utilizaron para identificar dos mecanismos de conducción diferentes en los monocristales. El proceso de conducción activado térmicamente domina en rangos de temperaturas más altas y el rango de Mott de “hopping” variable encaja mejor con los resultados experimentales a temperaturas más bajas. En este último rango, se correlacionaron los defectos encontrados mediante los refinamientos Rietveld, en la caracterización estructural, con la energía de la anchura de la banda aceptora determinada mediante las medidas de $\sigma(T)$.

Finalmente, se realizaron dispositivos fotovoltaicos basados en el compuesto CZTSSe. Las láminas delgadas del absorbente se depositaron a partir de los compuestos

sintetizados previamente. Con dicha capa delgada se fabricaron células solares y se caracterizaron mediante medidas de intensidad versus voltaje y EQE.

Index

List of abbreviations

CBM: Conduction-band minimum

CIGS: $Cu(In,Ga)Se_2$

CIGSSe: $Cu(In,Ga)(S,Se)_2$

CISe: $CuInSe_2$

CVT: Chemical vapor transport deposition

CZGS: Cu_2ZnGeS_4

CZGSe: $Cu_2ZnGeSe_4$

CZTGS: $Cu_2ZnSn_{1-y}Ge_yS_4$

CZTGSe: $Cu_2ZnSn_{1-y}Ge_ySe_4$

CZTGSSe: $Cu_2ZnSn_{1-y}Ge_y(S,Se)_4$

CZ(T,G)(S,Se): $Cu_2ZnSn_{1-y}Ge_y(S,Se)_4$

CZTS: Cu_2ZnSnS_4

CZTSe: $Cu_2ZnSnSe_4$

CZTSSe: $Cu_2ZnSn(S,Se)_4$

EDS: Energy-dispersive X-ray spectroscopy

EDX: Energy-dispersive X-ray spectroscopy

EQE: External quantum efficiency

FWHM: Full width at the half maximum

GDOES: Glow discharge optical emission spectroscopy

IR: Infrared

LO: Longitudinal optical splitting

M-VRH: Mott variable range hopping

ND: Neutron diffraction

NIR: Near-infrared

PCE: Power conversion efficiency

PV: Photovoltaic

KS: Kesterite structure

SEM: Scanning electron microscope

ST: Stannite structure

SS: Solid state reaction

TA: Thermal activation

TE: Thermionic emission

TO: Longitudinal optical splitting

UV: Ultra-violet

VBM: Valance band maximum

WDX: Wavelength dispersive X-ray

XRD: X-ray diffraction

XRF: X-ray fluorescence

Chapter 1

Introduction

This chapter introduces the current status of the PV sector and the properties and thin film technology of the quaternary chalcogenide semiconductors. In the last section, it is explained the thesis objectives and motivation.

1.1. Current status

The conversion of light into electrical energy, photovoltaic (PV) effect, is one of the most attractive types of energy conversion. In 1839, Alexandre Edmond Becquerel observed the photovoltaic effect via an electrode in a conductive solution exposed to light [1]. In 1877, Adams and Day observed the PV effect in solidified selenium [2] and in 1904, Hallwachs made a semiconductor-junction solar cell with copper and copper oxide. However, this time was a discovery period but without any real understanding of the science behind the operation of these first PV devices. The key events for the PV understanding were the Bell Labs announcement of the Silicon solar cell [3] in 1954 with the Pearson, Chapin, and Fuller patent [4] in 1957 with an 8% efficient Silicon solar cell [5].

At the present time, the population growth brings new challenges for everyone. One of the biggest issues is to match the growing energy demand of the whole population. As a result of the rising oil prices, the finite fossil fuel supplies, and the drawbacks of fossil energies in the environment as greenhouse effect [6], it becomes necessary that the energy generation sector shifts towards the renewal energies such as the PV technology. Currently, most of the solar cell market is based on silicon devices, but the high cost of silicon wafers production and the high demand levels, makes photovoltaic an expensive technology. Si-wafer based-PV technology accounted for about 93% of the total production in 2015 [7], in part because of the mature silicon industry, as well as the device stability and power conversion efficiencies offered by crystalline silicon (the current record efficiency is 26.0% [8]). Nevertheless, this Si technology is based on an absorber with indirect band gap; consequently it is necessary a thick layer, around 100 μm [9], to absorb enough fraction of the incident solar radiation and convert it into electricity. Moreover, because the grain boundaries work as recombination centers in Si-based technology, it is necessary to produce the perfect single crystal substrates to obtain the highest efficiency solar modules, thus contributing to higher cost. Due to the high cost for the Si-monocrystalline technology, the silicon industry has invested in the Si-polycrystalline technology. This technology has the advantage to lower the production cost but decrease the efficiency to 20% [10].

As a consequence, it becomes worthy to invest in the research of PV low cost alternatives. Nowadays, the alternative of cheap solar cell energy is based on thin films technology with direct band gap. The most common absorber materials for thin films are $Cu(In,Ga)Se_2$ (CIGS), also known as chalcopyrite, and CdTe with efficiencies of 22.6% [11] and 22.1% [12] respectively. Because of the direct band gap and the corresponding high absorption coefficient of 10^{-4}-$10^{-5}cm^{-1}$, the amount of absorber material utilization can be reduced to 1-2 μm layer thickness, which usually is enough to absorb most of the incident solar radiation. Additionally, these thin film technologies have a reduced requirements for film crystalline quality because the grain boundaries are less active as recombination centers [13] and, as a consequence, allow to lower cost routes to be employed in the layer deposition. Also, Silicon industry developed Si thin film solar cells but only achieved efficiencies of 10.5% [10].

Although being promising, these thin film technologies present some drawbacks which could restrict the production of $Cu(In,Ga)Se_2$ and CdTe. These restrictions consist on heavy metal usage like Cd and limitations in supply for In, Se and Te [14,15]. The abundance of indium in the upper continental crust is estimated to be 0.05 ppm compared with an abundance of 25, 71 and 5.5 ppm of copper, zinc and tin respectively [16]. The world-wide indium production amount is of the order of 600 metric tons per year [17,18], although most of this is used for transparent conductive coatings for the growing flat panel display industry. An investigation, based on current production trends, indicates that the world-wide production of indium can support approximately a CIGSSe production capacity of GW/year, well below the desired TW/year production [18]. Taken into account these considerations, there is a clear need to identify an absorber material for thin film solar cells which is composed of abundant and less toxic elements, while still providing adequate device performance, in order to be able to match the development and growth of PV technology.

A potential alternative to those thin film compounds are the I_2-II-IV-VI_4 ones (I=Cu; II=Zn; IV=Ge,Sn; VI=S,Se), a series of quaternary chalcogenide semiconductors with suitable direct band gaps [19], large band-edge absorption (Figure 1.1) [20] and p-type conductivity, as absorbers for thin film solar cells. These quaternary chalcogenides include compounds like Cu_2ZnSnS_4 (CZTS), $Cu_2ZnSnSe_4$ (CZTSe), Cu_2ZnGeS_4 (CZGS), $Cu_2ZnGeSe_4$ (CZGSe), $Cu_2ZnSn_{1-y}Ge_yS_4$ (CZTGS) and $Cu_2ZnSn_{1-y}Ge_ySe_4$ (CZTGSe).

Figure 1.1 shows the absorption coefficient versus the energy of the CZTS and CZTSe kesterite compounds. Also, for comparison there is the absorption coefficient of chalcopyrite CISe. Kesterite and chalcopyrite compounds are expected to have similar characteristics due to isovalency and closeness in crystal structure. However, the last record efficiency reported of 12.6% [21] for kesterite is still very far away from the highest performance of $Cu(In,Ga)Se_2$ (CIGSe) solar cells, 22.6 % [11]. One of the key of the success of CIGSe is the capacity of tuning the absorber band gap [22]. Recently, it has been shown that this band gap tuning can be also applied on CZTSSe by partially replacing tin with germanium [23–30]. The role of the Ge/Sn ratio in $Cu_2ZnSn_{1-y}Ge_y(S,Se)_4$ (CZTGSSe) is analogous to the Ga/In ratio in high efficient CIGSe solar cells. Improved efficiency of kesterite thin film solar cells has been already reported by replacing Sn with Ge, with device efficiencies of 11.0% [31]. However, not a lot is known about their fundamental properties and so, this work will be focused on the $Cu_2ZnSn_{1-y}Ge_yS_4$ (CZTGS) and $Cu_2ZnSn_{1-y}Ge_ySe_4$ (CZTGSe) compounds with different contents of Ge and Sn. Next, a summary of the investigated properties of I_2-II-IV-VI_4 compounds is presented. Finally, a description of thin film solar cells based on these compounds is also shown.

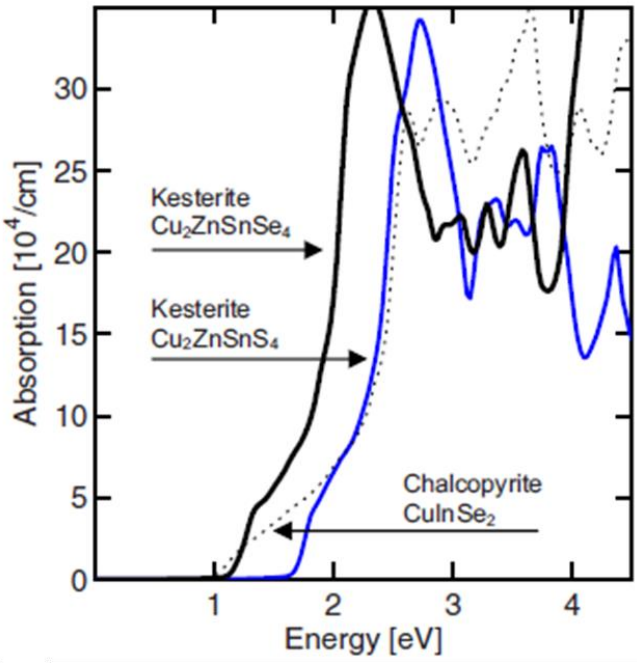

Figure 1.1: Absorption coefficients of kesterite CZTS (blue solid line) and kesterite CZTSe (black solid line). For comparison, the absorption coefficient of chalcopyrite CISe is also presented (dotted line) [20].

1.2. Structural properties

The zinc-blende related structures adopted by these compounds, kesterite and chalcopyrite, depend on the degree and type of metal cation ordering within the face-centered cubic array of chalcogenide anions with both metals and chalcogens adopting a tetrahedral coordination. These I_2-II-IV-VI_4 compounds are formed by replacing the III (In) cations with an equal number of II (Zn) and IV (Sn,Ge) metals in the ternary chalcopyrite structure I-III-VI_2 ($CuIn(S,Se)_2$) with $I\bar{4}2d$ space group (see Figure 1.2(a)). When the ordering of the metals is such that I (Cu) and IV (Sn,Ge) atoms alternate on the z=0 and ½ planes, where z is the fractional coordinate along the long c-axis of the structure, and I (Cu) and II (Zn) atoms alternate on the z=¼ and ¾ planes, this is known as the kesterite structure (KS) with $I\bar{4}$ space group (Figure 1.2(b)). However, when II (Zn) and IV (Sn,Ge) atoms alternate on the z=0 and ½ planes and only I (Cu) resides on the z=¼ and ¾ planes, this is known as the stannite structure (ST) with $I\bar{4}2m$ space group. While the kesterite structure has the same basic I/VI (Cu/S) structure as chalcopyrite, the stannite structure requires some reorganization of the Cu sublattice. Theoretical calculations predict that the lowest energy configuration for CZTSe and CZTS corresponds to the kesterite structure [23,32,33], nonetheless the difference in energy between kesterite and stannite is much smaller for the selenides versus the sulfides, suggesting a stronger tendency of the selenide compounds to incorporate stacking faults involving alternative layering sequences. These structural differences have a direct effect in the band gap energy transition. The band gap energy in the sulfides is higher than the selenide compounds [20,23].

Table 1.1 shows the theoretical calculated and experimental lattice parameters (a(Å) and c(Å)) for the kesterite and stannite structures of the CZTS, CZTSe, CZGS, and CZGSe compounds. The difference between the kesterite and stannite structures for CZTS and CZTSe is small and difficult to discern in the experimental measurements due to the intrinsic possible associated error. On the other hand, the compounds with the presence of germanium show a clearer difference between the kesterite and stannite structure, especially for the CZGS compound.

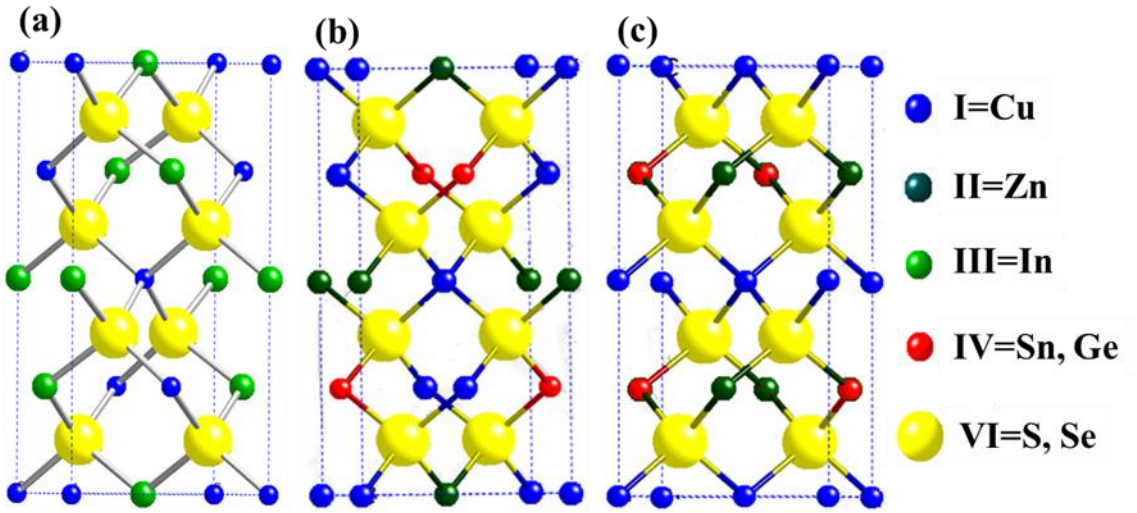

Figure 1.2. Schematic representation of the chalcopyrite $CuIn(S,Se)_2$ (I_2-III-VI_2) (a), kesterite CZTG(S,Se) (I_2-II-IV-VI_4) (b), and stannite CZTG(S,Se) (I_2-II-IV-VI_4) (c) structures. The unit cell boundaries are denoted with dashed lines. Atomic radii are arbitrarily chosen.

Table 1.1. Lattice parameters of CZTS , CZTSe, CZGS and CZGSe. The CZTS and CZTSe values were extracted from [34] and the CZGS and CZGSe values were extracted from [24].

Unit cell parameters	**Cu_2ZnSnS_4 (CZTS)**				**$Cu_2ZnSnSe_4$ (CZTSe)**			
	KS (calc.)	**ST (calc.)**	**KS (exp.)**	**ST (exp.)**	**KS (calc.)**	**ST (calc.)**	**KS (exp.)**	**ST (exp.)**
a (Å)	5.443	5.403	5.432	5.426	5.717	5.696	5.680	5.688
c (Å)	10.786	10.932	10.840	10.810	11.378	11.455	11.360	11.338
Unit cell parameters	**Cu_2ZnGeS_4 (CZGS)**				**$Cu_2ZnGeSe_4$ (CZGSe)**			
	KS (calc.)	**ST (calc.)**	**KS (exp.)**	**ST (exp.)**	**KS (calc.)**	**ST (calc.)**	**KS (exp.)**	**ST (exp.)**
a (Å)	5.264	5.328	5.270	5.342	5.602	5.583	5.606	-
c (Å)	10.843	10.741	10.509	10.540	11.259	11.325	11.040	-

1.3. Phase diagrams

There is little information about the phase diagrams of I_2-II-IV-VI_4 compounds. There are only four experimental phase diagram papers published so far [35–38]. All the publications were done at the Volyn State University in Ukraine and their results are based in differential–thermal analysis. Two of them are related with the sulphide kesterites, one specifically with the Cu_2ZnSnS_4 (CZTS) compound [35] and the other

with Cu_2ZnGeS_4 (CZGS) [36]. The other two reports are about the phase diagrams of selenide kesterites, more specifically the $Cu_2ZnSnSe_4$ (CZTSe) [37] and $Cu_2ZnGeSe_4$ (CZGSe) [38] compounds.

Figure 1.3 shows the isothermal section of the Cu_2S-SnS_2-ZnS (a) [35], Cu_2S-GeS_2-ZnS (b) [36], Cu_2Se-$SnSe_2$-ZnSe (c) [37] and Cu_2Se-$GeSe_2$-ZnSe (d) [38] systems at 670 K, where we can find the I_2-II-IV-VI_4 compound (I = Cu, II = Zn, IV = Sn, Ge and VI= S, Se) in the center of each ishothermal section. In these sections presented here, there is a small range of existence of the kesterite single phase. As an example, for the CZTS compound, such range of existence is predicted within 1-2% maximum deviation in the composition at growth temperatures around 823 K. Whether we compare this existence region with the chalcopyrite one, which have similar structure as it had been mentioned in Section 1.2, the phase diagram of the chalcopyrites allows for Cu poor compounds with a 4% deviation in composition at the growth temperature [39]. Chalcopyrites and kesterites stability regions based on total energy calculations can be compared. Under Cu-rich conditions, the stability region of Cu_2ZnSnS_4 extends over an area in the chemical potential μ_{Sn}–μ_{Zn} diagram which is about 1 eV long and 0.1eV wide [40–42], whereas the stability region of $CuInSe_2$ chalcopyrite is as long as in the kesterite structure (1 eV) but wider with 0.5 eV [43]. These parameters are analogous for the other kesterite compounds and, as a consequence, it is thus predicted that constraints on forming single phase are stricter for kesterite than for chalcopyrite compounds.

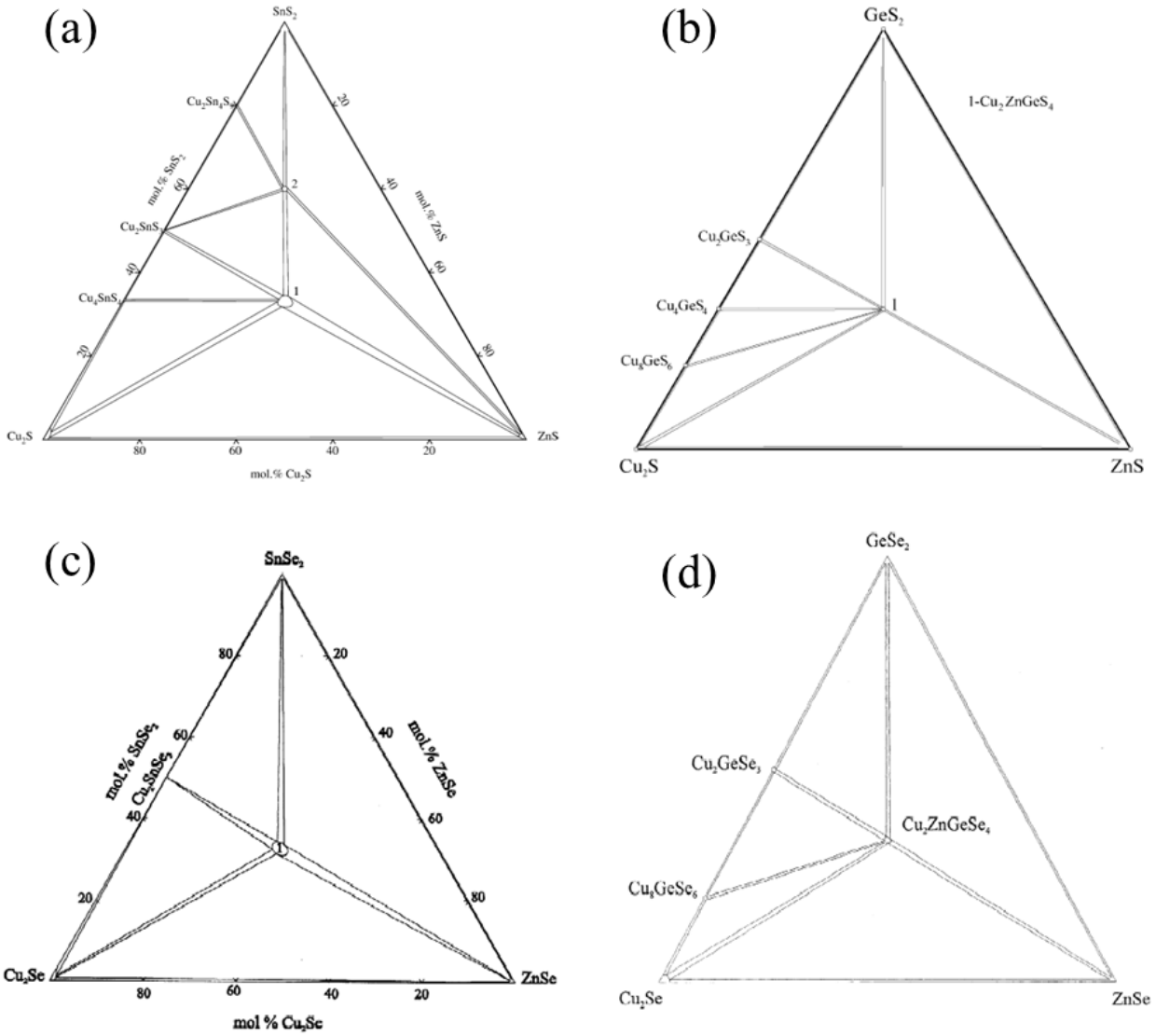

Figure 1.3. Isothermal sections of Cu_2S-SnS_2-ZnS (a) [35], Cu_2S-GeS_2-ZnS (b) [36], Cu_2Se-$SnSe_2$-ZnSe (c) [37] and Cu_2Se-$GeSe_2$-ZnSe (d) [38] systems at 670 K. In the center of each system is located the I_2-II-IV-VI_4 compound (I = Cu, II = Zn, IV = Sn, Ge and VI= S, Se).

1.4. Optical properties and band structure

In spite of this promising result of 11% [31] efficiency for CZTGSSe compounds, mentioned above, there is not much known about their optical properties and the effect of the atomic ratio *x*= [Ge/(Ge+Sn)] (the *x* atomic ratio is the experimental value of the *y* value present in the chemical formula $Cu_2ZnSn_{1-y}Ge_yS_4$ or $Cu_2ZnSn_{1-y}Ge_ySe_4$. In other words, *y* is the nominal or desired value of the *x* atomic ratio). So far, Morihama et al. [44] have reported information on the structural properties of $Cu_2ZnSn_{1-y}Ge_ySe_4$ (CZTGSe) alloys by X-ray diffraction and determined the band gap energies by diffuse-

reflectance spectra. Grossberg et al. [45] have studied the recombination mechanisms of CZTGSe by photoluminescence. In both cases, a linear increase of the bandgap from 0.9 eV to 1.3 eV at room temperature with the Ge content was shown. On another hand, there is even less information about the optical properties of $Cu_2ZnSn_{1-y}Ge_yS_4$ (CZTGS) alloys. A fundamental band gap energy E_0 = 2.2 eV and 2.0 eV for Cu_2ZnGeS_4 single crystal and single-crystalline nanowire arrays respectively have been reported in [46] and [47] respectively. Recently, E_0 = 1.59 eV and 1.90 eV have been determined for $Cu_2ZnSn_{0.9}Ge_{0.1}S_4$ and $Cu_2ZnSn_{0.5}Ge_{0.5}S_4$ single crystals respectively by spectroscopic ellipsometry [29]. The addition of Ge gives the possibility to control the bandgap of the absorber in a wider region from 1 to 2.3 eV, expanding the range of values available by varying the anion compositions in CZTSSe [48]. This is of main interest for the development of new multi-junction devices where photovoltaic conversion is optimized by improving the device efficiency in different spectral regions.

From band structure calculations, the upper valence band in CZTGSSe consists of antibonding Cu 3d and S(Se) 3p(4p) orbitals whereas the bottom of the conduction band consists of antibonding orbitals of Sn 5s and S(Se) 3p(4p). In these calculations, the Zn atom does not affect the valence band maximum or the conduction band minimum [49]. However, some calculations predict that Sn substitution, due to disorder or non-stoichiometry, on the Zn site can create a detrimental deep level due to a +IV→+II transition inside the band gap [50].

In [51], it was calculated the band structures of Cu_2ZnSnS_4 (CZTS) and $Cu_2ZnSnSe_4$ (CZTSe) in kesterite (KS) and stannite (ST) structures in the Brillouin zone. Figure 1.4 shows the calculated band structures through high-symmetry points (T-G-N) of the first Brillouin zone of the tetragonal lattice. It is clearly seen that there is no significant difference between band structures of these KS and ST structures. But in the G symmetry point it can be observed qualitatively that for both compounds the KS structures have higher values than the ST structures for the direct transition. This transition is correlated with the band gap energy which values are shown in Table 1.2. Furthermore, the energy transition from N(A): $2\pi/a(0.5\ 0.5\ 0.5)$ and T(Z): $2\pi/a(0\ 0\ 0.5)$ symmetry points to the first conduction band are known as the energy of the second (E_{1A}) and the third (E_{1B}) threshold, respectively. Moreover, in the band structures (Figure 1.4) it can be appreciated that the most noticeable discrepancy between the band structures of the two materials

comes from the atomic mass difference between the S and Se atoms. This mass difference also leads to a narrower gap energy in the phonon frequencies of CZTSe. Table 1.2 shows the calculated and the experimental band gap energy values for the CZTS, CZTSe, CZGS and CZGSe for kesterite and stannite structures. Furthermore, the calculated direct energy transition of E_{1A} and E_{1B} are also shown for the CZGS and CZGSe compounds. Also, there is the experimentally obtained direct energy transition values of E_{1A} and E_{1B} for the CZGS with kesterite structure [24]. All the experimental and calculated values present the same tendency, where the direct energy transition values of the kesterite structure are higher than those of the stannite structure.

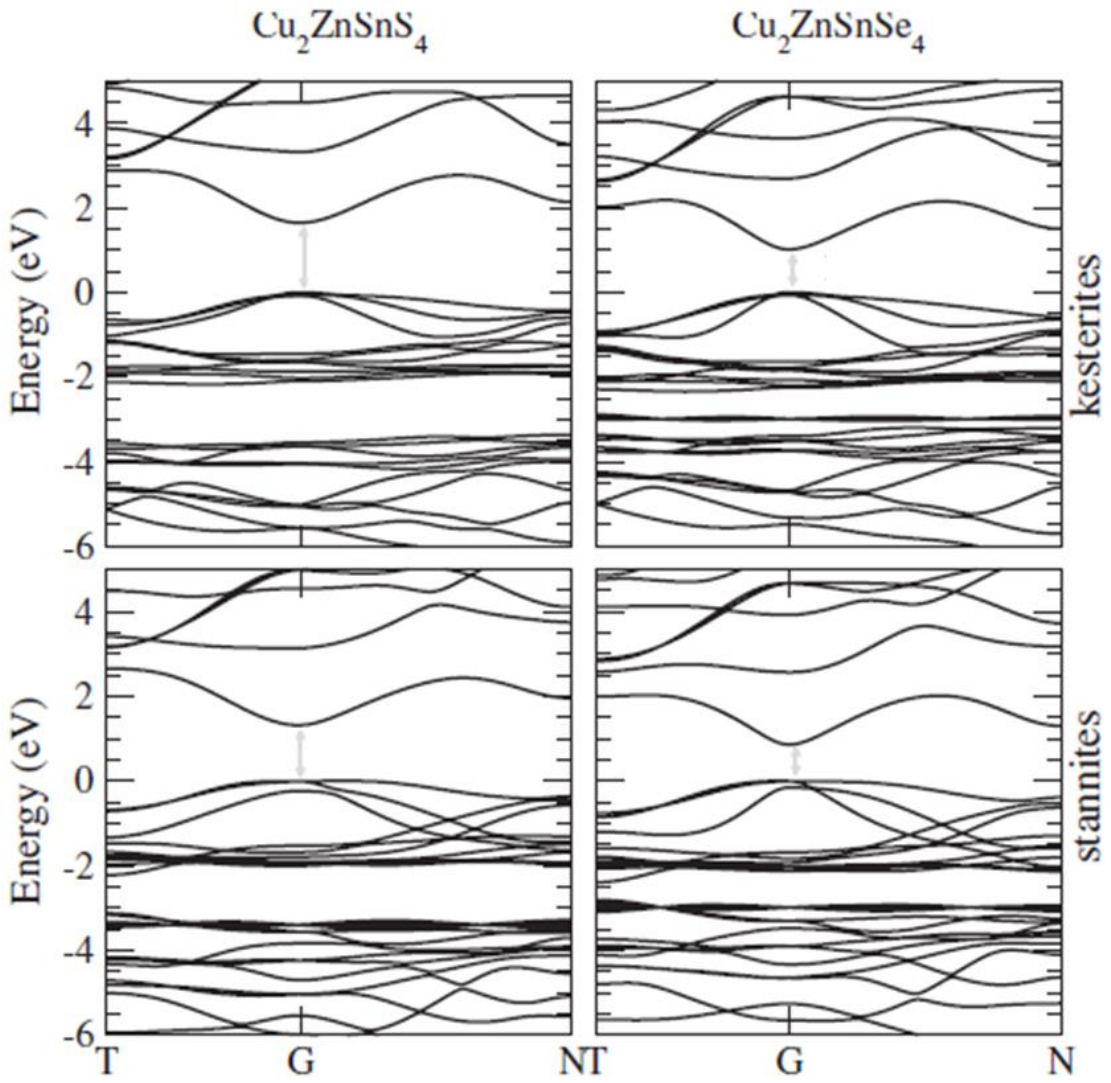

Figure 1.4. Calculated band structures for Cu_2ZnSnS_4 kesterite (upper left corner) and stannite (lower left corner) structures and $Cu_2ZnSnSe_4$ kesterite (upper right corner) and stannite (lower right corner) structure, extracted from [51]. Band gap transition is indicated with grey arrows in G symmetry point.

Table 1.2. Theoretical calculated CZTS and CZTSe energy transition values, extracted from [32], and the experimental energy transition values, extracted from [34]. The calculated and experimental CZGS and CZGSe energy transition values were extracted from [24].

Energy transition (eV)	**Cu_2ZnSnS_4 (CZTS)**				**$Cu_2ZnSnSe_4$ (CZTSe)**			
	KS (calc.)	**ST (calc.)**	**KS (exp.)**	**ST (exp.)**	**KS (calc.)**	**ST (calc.)**	**KS (exp.)**	**ST (exp.)**
E_g	1.50	1.38	1.50	1.45	0.96	0.82	1.00	0.90
Energy transition (eV)	**Cu_2ZnGeS_4 (CZGS)**				**$Cu_2ZnGeSe_4$ (CZGSe)**			
	KS (calc.)	**ST (calc.)**	**KS (exp.)**	**ST (exp.)**	**KS (calc.)**	**ST (calc.)**	**KS (exp.)**	**ST (exp.)**
E_g	2.43	2.14	2.28	-	1.60	1.32	1.63	1.29
E_{1A}	2.99	2.66	2.87	-	2.35	1.84	-	-
E_{1B}	4.10	3.83	4.28	-	3.58	3.17	-	-

1.5. Vibrational properties

In order to determine the vibrational properties, it is necessary to calculate the Brillouin-zone-center phonon frequencies for the kesterite (KS) and stannite (ST) structures of CZTSe and CZTS. Since these structures have eight atoms per primitive cell, there are a total of 24 modes, three of them are acoustic modes and equal to zero at the zone center. The irreducible representation of these Brillouin-zone-center phonon modes in the KS structure can be written as:

$$\Gamma = 3A \oplus 6B \oplus 6E$$

Equation 1-1

In this case, all the modes are Raman active. Besides, B and E modes are also infrared (IR) active and present longitudinal and transversal optical (LO-TO) splitting.

Similarly, the phonon modes in the ST structure can be written as:

$$\Gamma = 2A_1 \oplus 1A_2 \oplus 2B_1 \oplus 4B_2 \oplus 6E$$

Equation 1-2

From these modes, only the A_2 one is not Raman active. The B_2 and E modes are also IR active, and they present LO-TO splitting due to their polar character. The A_1 symmetry mode is expected to be the strongest line in the Raman spectra, in agreement with the behavior observed for the closely related chalcopyrite crystals [52].

Table 1.3. Brillouin-zone-center phonon frequencies (in cm^{-1}). Values are given with their mode symmetries of Raman peaks from Cu_2ZnSnS_4.

Experimental (cm^{-1}) [53]	**Symmetry exp.**	**Calculated (cm^{-1})** [54]	**Symmetry calc.**
66	E/B	79.2 79.2	E(TO/LO)
83	E/B	92.3 93.1	B(TO/LO)
97	E/B	101.4 101.4 / 104.2 104.3	E(TO/LO) / B(TO/LO)
143	E/B	166.1	E(TO/LO)
166	E/B	179.6 179.9	B(TO/LO)
252	E/B	269.1 285.1	B(TO/LO)
272	E/B	278.2 289.8	E(TO/LO)
287	A	302.1 309 309.7 314.1	A A E(TO/LO)
337	A	335.2 332.7 336.1	A B(TO/LO)
347	E/B	341.4	E (TO)
353	E/B	353.2 / 354.8 366.4	E(LO) / B(TO) B(LO)

Usually, Raman spectroscopy is performed with green light with an excitation wavelength around 532 nm. Furthermore, for better identification of Raman modes, Raman measurements with different excitation wavelengths from ultra-violet (UV) to near-infrared (NIR) regions might be performed. NIR excitation conditions are used due to the expected increase in the intensity of the Raman modes because of near-resonant Raman effects. This is expected to take place, in particular, for the polar modes of CZTS–like peaks, which are NIR active and are usually observed as very weak peaks in standard Raman scattering conditions. More specifically, using the 325 nm excitation wavelength there is a strong increase in the relative intensity of the experimental Raman peaks (Table 1.3) at 166, 252, 272 and 347 cm^{-1}; using the 632.8 nm excitation wavelength there is an enhancement in the experimental Raman peaks at 66, 83 and 97 cm^{-1} and the 785 nm excitation wavelength also shows an increase in intensity of the experimental Raman peak at 143 cm^{-1}. These enhancements or increase of the relative intensities are in relation to those from the Raman measurements at the standard green excitation wavelength (532 nm) [55].

1.6. Electrical properties

The electrical properties of the I_2-II-IV-VI_4 compounds are a sensitive subject due to the difference in composition that could imply the presence of several intrinsic defects including vacancies (V_{Cu}, V_{Zn}, V_{Sn}, V_{Se} and V_S), antisite defects (Cu_{Zn}, Zn_{Cu}, Cu_{Sn}, Sn_{Cu}, Zn_{Sn}, and Sn_{Zn}), and interstitial defects (Cu_i, Zn_i, and Sn_i) [32,56]. Usually, the most common defect present in a I_2-II-IV-VI_4 cell is mainly the antisite Cu_{Zn} as will be explain in depth in section 1.7. Reported resistivity of CZTS thin films was significantly different [57–59], and the most suitable value for CZTS and CZTSe thin films should range from $10^{-3}\Omega\cdot$cm to $10^{-1}\Omega\cdot$cm according to published data for CZTS solar cells [60]. For CZTSe [61,62] thin films, the resistivity values are located around 0.1 and 0.8 $\Omega\cdot$cm. In both cases, the carrier density was reported to vary from $10^{16}cm^{-3}$ to $10^{19}cm^{-3}$ [59,63–68], although extremely high and extremely low concentrations were also reported for CZTS [67,69]. Hall effect measurement results showed that carrier mobility of CZTS and CZTSe changed from lower than 0.1 to as high as 30 $cm^2V^{-1}s^{-1}$, while most published values were in the range of 1 to 10 $cm^2V^{-1}s^{-1}$ [59,61,66–72]. The reported Hall mobilities are measurements that might reflect thin film quality. As a consequence, the lower mobility might indicates that the optimized thickness of the absorber layer in CZTS and

CZTSe devices might not be as optimized as that for CIGS [73]. Generally these films are prepared on insulating substrates to prevent parallel conduction in the Hall measurements. Thus, these reported electrical properties may not reflect those of the thin films grown on metal-coated substrates for the PV devices due to different grain growth, structure and incorporated impurities. Electrical characterization, including mobility and carrier density, are still therefore a need in the I_2-II-IV-VI_4 compounds, with special care that the films are single phase and deposited in the same configuration as that used in devices [74].

1.7. Thin film solar cells

The most common metric of performance for a solar cell is the device efficiency, generally expressed as

$$PCE = FF \times Voc \times J_{sc}/P_{in}$$

Equation 1-3

where PCE is the power conversion efficiency, FF is the fill factor, V_{oc} is the open circuit voltage, J_{sc} is the short circuit current and P_{in} is the input power (typically 100 mW cm^{-2}, corresponding to 1 Sun AM1.5G solar spectrum illumination).

In the last thirty years, the efficiency of the thin film technology of the I_2-II-IV-VI_4 compounds has been improved remarkably from one of the first efficiencies of 2.3% [75] for CZTS until the record efficiency of 12.6% [21] for the kesterite compound $Cu_2ZnSn(S,Se)_4$, prepared using a hydrazine-based pure solution approach. On the other hand, hydrazine is explosive, hepatotoxic, and carcinogenic. Hence it is necessary to understand better the nature of these compounds to find out a new way to produce the devices and achieve better efficiencies without using toxic agents. One of the main challenges in the processing of CZT(S,Se) compounds is the presence of secondary phases. As mentioned in section 1.3, the volume of the stable region for CZTS [76] and CZTSe [56] is small, and a deviation from that region will cause the formation of $Cu_y(S,Se)$ ($1< y < 2$), Zn(S,Se), $Sn(S,Se)_y$ ($1< y < 2$), or $Cu_2Sn(S,Se)_3$ secondary phases, which would have a negative effect on their power conversion efficiency (PCE) [77].

Theoretical calculations have indicated that the isolated anti-site defect Cu_{Zn} has the lowest formation energy, which is different from the case of $CuInSe_2$ where the dominant

defect is the Cu vacancy. As the energy difference for other acceptors (V_{Cu} , V_{Zn} , Zn_{Sn} , Cu_{Sn}) relative to the dominant Cu_{Zn} is not very large (less than 1 eV), these defects may also be present in much smaller concentrations. Three computational defect studies [40,41,49] of Cu_2SnZnS_4 agree on a formation energy of the copper vacancy between 0.6 – 0.8 eV, and a value of the copper vacancy close to 0 eV above VBM (shallow acceptor) under copper-poor conditions. The relative concentrations can be tuned by controlling the material growth conditions. The anti-site defect Cu_{Zn} induces a deep acceptor level in the band gap, which can cause a Fermi-level pinning that deteriorates the power conversion efficiency [78]. Actually, for CZTSSe the formation energies of most acceptor defects are lower than those of donor defects, explaining the experimentally observed p-type conductivity and indicating that n-type doping will be difficult in the CZTSSe compounds [40,56]. Most of the reported high efficiency kesterite solar cells exhibit copper-poor and zinc-rich conditions, in which the formation energy of Cu vacancy (V_{Cu}) defects increases accordingly. As mentioned above, the V_{Cu} defect behaves as a shallow acceptor and less likely to promote detrimental Fermi-level pinning. It is also possible that the anti-site defect Cu_{Zn} is formed, although the density should be relatively small. The copper-poor and zinc-rich conditions also suppress the Sn_{Zn} defect, which behaves as a deep-level donor defect acting as a recombination center.

It is important to note that the dominant defect Cu_{Zn} has an acceptor level at 0.12 eV above the valence band, deeper than that of V_{Cu} (0.02 eV above VBM). The shallow level of V_{Cu} is common in Cu-based chalcopyrites like $CuInSe_2$ and $CuGaSe_2$ [79,80]. The deeper level of Cu_{Zn} can be explained by considering that the Cu on Zn site enhances the p–d hybridization between Cu and S/Se. Low temperature photoluminescence measurements of CZTS identified two shallow acceptor states (10 and 30 meV above the VBM) [81], which could be attributed to two symmetry inequivalent Cu vacancy sites. The deep level of the dominant antisite defect is negative for CZTS solar cell efficiency, as it will decrease the open-circuit voltage. Therefore, it should be beneficial to decrease the formation energy and enhance the population of shallow V_{Cu} relative to Cu_{Zn} using Cu-poor and Zn-rich growth conditions. Experimentally this condition has led to high solar cell efficiencies [82].

Figure 1.5 shows the structure of a complete kesterite thin film device. Generally, soda-lime glass is used as substrate material, but also other materials as polyimide or stainless

steel can be used for that. Typically, a Mo back contact is deposited onto the substrate. After that, the p-type semiconductor absorber layer is grown, kesterite in the present case. CdS is the most extensively thin film used as buffer layers, being the n-type semiconductor. Nowadays, Cd-free alternatives are also being studied, as for example Zn(S,O) [83]. Later, a transparent conductive oxide or window layer of intrinsic zinc oxide and doped zinc oxide, normally with Al, or In_2O_3:SnO_2 is grown. The grids of nickel and aluminum are finally deposited as front contact to enhance the current collection.

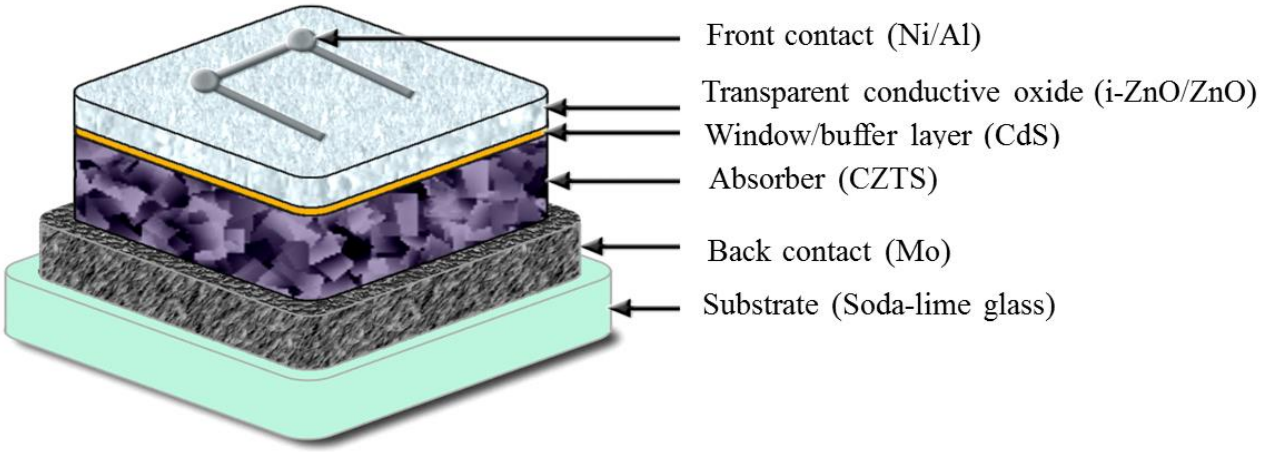

Figure 1.5. Scheme of a kesterite thin film device.

1.8. Thesis motivation and objectives

The first objective of the present work was the synthesis of $Cu_2ZnSn_{1-y}Ge_yS_4$ or $Cu_2ZnSn_{1-y}Ge_ySe_4$ (CZ(T,G)(S,Se)) bulk compounds to study the fundamental properties. Secondly, the goal of this thesis is to study deeply the structural, optical, vibrational and electrical properties of the CZ(T,G)(S,Se) measured by X-Ray and neutron diffraction, ellipsometry, Raman spectroscopy, and conductivity versus temperature measurements (Chapter 3) to enhance and contribute to the knowledge of these materials, leading to higher solar cell performances. As mentioned above, the partial substitution of Sn with Ge allows tuning the band gap energy, being very attractive for tandem solar cells.

Complementarily, photovoltaic devices, based on CZTSSe using the synthesized compounds as precursors for absorber thin films evaporation, were manufactured. Thus, the direct application of the material synthesized and studied in the two main objectives proposed in this thesis was demonstrated.

Besides the "Introduction" and "Conclusions" chapters, this thesis is structured in two parts. Part I is about the analysis of fundamental properties of the bulk compounds (Chapter 3). In Part II, the experimental details and synthesis of the thin films deposition as well as the characterization of the solar cell devices are presented (Chapter 4). Moreover, the chapter 2 describes all techniques used to characterize the samples.

1.9. References

[1] E. Becquerel, Mémoire sur les effets électriques produits sous l'influence des rayons solaires, Comptes Rendus. 9 (1839) 561–567. doi:10.1017/CBO9781107415324.004.

[2] W.G. Adams, D.R. E., The action of light on selenium, Proc. R. Soc. 167 (1877) 313–349.

[3] D.M. Chapin, C.S. Fuller, G.L. Pearson, A New Silicon p-n Junction Photocell for Converting Solar Radiation into Electrical Power, J. Appl. Phys. 25 (1954) 676. doi:10.1063/1.1721711.

[4] D.M. Chapin, B. Ridge, C.S. Fuller, G.L. Pearson, B. Township, S. County, B. Telephone, Solar Energy Converting Apparatus, 1957.

[5] L.M. Fraas, Low-Cost Solar Electric Power, 2014. doi:10.1007/978-3-319-07530-3.

[6] S.H. Schneider, The Greenhouse Effect: Science and Policy, Science. 243 (1989) 771–81.

[7] I. Fraunhofer Institute for Solar Energy Systems, Photovoltaics report, 2015. doi:26.05.2014.

[8] K. Masuko, M. Shigematsu, T. Hashiguchi, D. Fujishima, M. Kai, N. Yoshimura, T. Yamaguchi, Y. Ichihashi, T. Mishima, N. Matsubara, T. Yamanishi, T. Takahama, M. Taguchi, E. Maruyama, S. Okamoto, Achievement of More Than 25% Conversion Efficiency With Crystalline Silicon Heterojunction Solar Cell, IEEE J. Photovoltaics. 4 (2014) 1433–1435. doi:10.1109/JPHOTOV.2014.2352151.

[9] A. Shah, P. Torres, R. Tscharner, N. Wyrsch, H. Keppner, Photovoltaic Technology : The Case for Thin-Film Solar Cells, Science. 285 (1999) 692–698. doi:10.1126/science.285.5428.692.

[10] M.A. Green, K. Emery, Y. Hishikawa, W. Warta, E.D. Dunlop, Solar cell efficiency tables (Version 45), Prog. Photovolt Res. Appl. 23 (2015) 1–9. doi:10.1002/pip.2573.

[11] ZSW achieves record lab CIGS cell efficiency of 22.6%, Pv. (2016). http://www.pv-magazine.com/news/details/beitrag/zsw-sets-new-thin-film-solar-world- record-with-226-efficient-cigs-pv-cell_100024995.

[12] First Solar pushes CdTe cell efficiency to record 22.1%, Pv-Magazine. (2016). http://investor.firstsolar.com/releasedetail.cfm?ReleaseID=864426. http://www.pv-magazine.com/news/details/beitrag/first-solar-sets-new-cadmium-telluride-thin-film-cell-efficiency-record-at-221_100023341#axzz45ztGXNLh.

[13] I. Visoly-Fisher, S.R. Cohen, A. Ruzin, D. Cahen, How polycrystalline devices can outperform single-crystal ones: Thin film CdTe/CdS solar cells, Adv. Mater. 16 (2004) 879–883. doi:10.1002/adma.200306624.

[14] C. Wadia, A.P. Alivisatos, D.M. Kammen, Materials Availability Expands the Opportunity for Large-Scale Photovoltaics Deployment, Environ. Sci. Technol. 43 (2009) 2072–2077. doi:10.1021/es8019534.

[15] B.A. Andersson, Materials availability for large-scale thin-film photovoltaics, Prog. Photovoltaics Res. Appl. 8 (2000) 61–76. doi:10.1002/(SICI)1099-159X(200001/02)8:1<61::AID-PIP301>3.0.CO;2-6.

[16] S.R. Taylor, S.M. McLennan, The continental crust: Its composition and evolution and evolution, 1985. doi:10.1017/CBO9781107415324.004.

[17] G. Phipps, C. Mikolajczak, T. Guckes, Indium and Gallium: long-term supply, Renew. Energy Focus. 9 (2008) 56–59. doi:10.1016/S1471-0846(08)70140-9.

[18] M. Woodhouse, A. Goodrich, R. Margolis, T.L. James, M. Lokanc, R. Eggert, Supply-chain dynamics of tellurium, indium, and gallium within the context of PV

manufacturing costs, IEEE J. Photovoltaics. 3 (2013) 1–6. doi:10.1109/JPHOTOV.2013.2242960.

[19] O.D. Miller, E. Yablonovitch, S.R. Kurtz, Strong internal and external luminescence as solar cells approach the Shockley-Queisser limit, Photovoltaics, IEEE J. 2 (2012) 303–311. doi:10.1109/JPHOTOV.2012.2198434.

[20] C. Persson, Electronic and optical properties of Cu_2ZnSnS_4 and $Cu_2ZnSnSe_4$, J. Appl. Phys. 107 (2010) 53710. doi:10.1063/1.3318468.

[21] W. Wang, M.T. Winkler, O. Gunawan, T. Gokmen, T.K. Todorov, Y. Zhu, D.B. Mitzi, Device characteristics of CZTSSe thin-film solar cells with 12.6% efficiency, Adv. Energy Mater. (2013) 1–5. doi:10.1002/aenm.201301465.

[22] A.M. Gabor, J.R. Tuttle, D.S. Albin, M.A. Contreras, Noufi, Rommei, High-efficiency $CuIn_xGa_{1-x}Se_2$ solar cells made from $(In_x,Ga_{1-x})_2Se_3$ precursor films, Appl. Phys. Lett. 65 (1994) 198–200.

[23] S. Chen, X.G. Gong, A. Walsh, S.H. Wei, Electronic structure and stability of quaternary chalcogenide semiconductors derived from cation cross-substitution of II-VI and I-III-VI_2 compounds, Phys. Rev. B - Condens. Matter Mater. Phys. 79 (2009) 1–10. doi:10.1103/PhysRevB.79.165211.

[24] D. Chen, N.M. Ravindra, Electronic and optical properties of Cu_2ZnGeX_4 (X=S, Se and Te) quaternary semiconductors, J. Alloy Compd. 579 (2013) 468–472. doi:10.1016/j.jallcom.2013.06.048.

[25] G.M. Ford, Q. Guo, R. Agrawal, H.W. Hillhouse, Earth Abundant Element Cu_2 $Zn(Sn_{1-x}Ge_x)S_4$ Nanocrystals for Tunable Band Gap Solar Cells: 6.8% Efficient Device Fabrication, Chem. Mater. 23 (2011) 2626–2629. doi:10.1021/cm2002836.

[26] Q. Guo, G.M. Ford, W.C. Yang, C.J. Hages, H.W. Hillhouse, R. Agrawal, Enhancing the performance of CZTSSe solar cells with Ge alloying, Sol. Energy Mater. Sol. Cells. 105 (2012) 132–136. doi:10.1016/j.solmat.2012.05.039.

[27] S. Bag, O. Gunawan, T. Gokmen, Y. Zhu, D.B. Mitzi, Hydrazine-Processed Ge-Substituted CZTSe Solar Cells, Chem. Mater. 24 (2012) 4588–4593.

doi:10.1021/cm302881g.

[28] C.J. Hages, S. Levcenco, C.K. Miskin, J.H. Alsmeier, D. Abou-Ras, R.G. Wilks, M. Bär, T. Unold, R. Agrawal, Improved preformance of Ge-alloyed CZTGeSSe thin-film solar cells trhough control of elemental losses, Prog. Photovoltaics Res. Appl. 23 (2013) 376–384. doi:10.1002/pip.2442.

[29] R. Caballero, I. Victorov, R. Serna, J.M. Cano-Torres, C. Maffiotte, E. Garcia-Llamas, J.M. Merino, M. Valakh, I. Bodnar, M. León, Band-gap engineering of $Cu_2ZnSn_{1-x}Ge_xS_4$ single crystals and influence of the surface properties, Acta Mater. 79 (2014) 181–187. doi:10.1016/j.actamat.2014.06.040.

[30] R. Caballero, J.M. Cano-Torres, E. Garcia-Llamas, X. Fontané, A. Pérez-Rodríguez, D. Greiner, C. a. Kaufmann, J.M. Merino, I. Victorov, G. Baraldi, M. Valakh, I. Bodnar, V. Izquierdo-Roca, M. León, Towards the growth of $Cu_2ZnSn_{1-x}Ge_xS_4$ thin films by a single-stage process: Effect of substrate temperature and composition, Sol. Energy Mater. Sol. Cells. 139 (2015) 1–9. doi:10.1016/j.solmat.2015.03.004.

[31] A.D. Collord, H.W. Hillhouse, Germanium Alloyed Kesterite Solar Cells with Low Voltage Deficits, Chem. Mater. (2016) 2067–2073. doi:10.1021/acs.chemmater.5b04806.

[32] S. Chen, X.G. Gong, A. Walsh, S.H. Wei, Crystal and electronic band structure of Cu_2ZnSnX_4 (X=S and Se) photovoltaic absorbers: First-principles insights, Appl. Phys. Lett. 94 (2009) 1–3. doi:10.1063/1.3074499.

[33] S. Nakamura, T. Maeda, T. Wada, Phase Stability and Electronic Structure of In-Free Photovoltaic Materials: Cu2ZnSiSe4 , Cu2ZnGeSe4 , and Cu2ZnSnSe4, Jpn. J. Appl. Phys. 49 (2010) 121203/1-6. doi:10.1143/JJAP.49.121203.

[34] A. Khare, B. Himmetoglu, M. Johnson, D.J. Norris, M. Cococcioni, E.S. Aydil, Calculation of the lattice dynamics and Raman spectra of copper zinc tin chalcogenides and comparison to experiments, J. Appl. Phys. 111 (2012) 083707/1-9. doi:10.1063/1.4704191.

[35] I.D. Olekseyuk, I.V. Dudchak, L.V. Piskach, Phase equilibria in the Cu_2S–ZnS–

SnS_2 system, J. Alloys Compd. 368 (2004) 135–143. doi:10.1016/j.jallcom.2003.08.084.

[36] O. V Parasyuk, L. V Piskach, Y.E. Romanyuk, I.D. Olekseyuk, V.I. Zaremba, V.I. Pekhnyo, Phase relations in the quasi-binary Cu_2GeS_3–ZnS and quasi-ternary Cu_2S–Zn(Cd)S–GeS_2 systems and crystal structure of Cu_2ZnGeS_4, J. Alloys Compd. 397 (2005) 85–94. doi:http://dx.doi.org/10.1016/j.jallcom.2004.12.045.

[37] I. V. Dudchak, L. V. Piskach, Phase equilibria in the Cu_2SnSe_3 –$SnSe_2$ –ZnSe system, J. Alloys Compd. 351 (2003) 145–150.

[38] Y.E. Romanyuk, O. V Parasyuk, Phase equilibria in the quasi-ternary Cu_2Se–ZnSe–$GeSe_2$ system, J. Alloys Compd. 348 (2003) 195–202.

[39] T. Gödecke, T. Haalboom, F. Ernst, Phase equilibria of Cu-$InSe_I$: stable states and non-equilibrium states of the InCuSe subsystem, Zeitschrift Für Met. 91 (2000) 622–634. http://cat.inist.fr/?aModele=afficheN&cpsidt=1493433 (accessed July 23, 2016).

[40] S. Chen, X.G. Gong, A. Walsh, S.H. Wei, Defect physics of the kesterite thin-film solar cell absorber Cu_2ZnSnS_4, Appl. Phys. Lett. 96 (2010) 021902/1-3. doi:10.1063/1.3275796.

[41] A. Nagoya, R. Asahi, R. Wahl, G. Kresse, Defect formation and phase stability of Cu_2ZnSnS_4 photovoltaic material, Phys. Rev. B - Condens. Matter Mater. Phys. 81 (2010) 113202/1-4. doi:10.1103/PhysRevB.81.113202.

[42] S. Chen, J.H. Yang, X.G. Gong, A. Walsh, S.H. Wei, Intrinsic point defects and complexes in the quaternary kesterite semiconductor Cu_2ZnSnS_4, Phys. Rev. B. 81 (2010) 245204. doi:10.1103/PhysRevB.81.245204.

[43] C. Persson, Y.J. Zhao, S. Lany, A. Zunger, n-Type doping of $CuInSe_2$ and $CuGaSe_2$, Phys. Rev. B - Condens. Matter Mater. Phys. 72 (2005) 035211/1-14. doi:10.1103/PhysRevB.72.035211.

[44] M. Morihama, F. Gao, T. Maeda, T. Wada, Crystallographic and optical properties of Cu2Zn(Sn1−xGex)Se4 solid solution, Jpn. J. Appl. Phys. 53 (2014) 1–6.

doi:10.7567/JJAP.53.04ER09.

[45] M. Grossberg, K. Timmo, T. Raadik, E. Kärber, V. Mikli, J. Krustok, Study of structural and optoelectronic properties of $Cu_2Zn(Sn_{1-x}Ge_x)Se_4$ (x=0 to 1) alloy compounds, Thin Solid Films. 582 (2014) 176–179. doi:10.1016/j.tsf.2014.10.055.

[46] M. León, S. Levcenko, R. Serna, G. Gurieva, A. Nateprov, J.M. Merino, E.J. Friedrich, U. Fillat, S. Schorr, E. Arushanov, Optical constants of Cu_2ZnGeS_4 bulk crystals, J. Appl. Phys. 108 (2010) 1–5. doi:10.1063/1.3500439.

[47] L. Shi, P. Yin, H. Zhu, Q. Li, Synthesis and Photoelectric Properties of Cu_2ZnGeS_4 and $Cu_2ZnGeSe_4$ Single-Crystalline Nanowire Arrays, Langmuir. 29 (2013) 8713–8717.

[48] J. He, L. Sun, S. Chen, Y. Chen, P. Yang, J. Chu, Composition dependence of structure and optical properties of $Cu_2ZnSn(S,Se)_4$ solid solutions: An experimental study, J. Alloys Compd. 511 (2012) 129–132. doi:10.1016/j.jallcom.2011.08.099.

[49] T. Maeda, S. Nakamura, T. Wada, First principles calculations of defect formation in in-free photovoltaic semiconductors Cu_2ZnSnS_4 and $Cu_2ZnSnSe_4$, Jpn. J. Appl. Phys. 50 (2011) 04DP07/1-6. doi:10.1143/JJAP.50.04DP07.

[50] K. Biswas, S. Lany, A. Zunger, The electronic consequences of multivalent elements in inorganic solar absorbers: Multivalency of Sn in Cu_2ZnSnS_4, Appl. Phys. Lett. 96 (2010) 201902/1-3. doi:10.1063/1.3427433.

[51] S. Botti, D. Kammerlander, M.A.L. Marques, Band structures of Cu_2ZnSnS_4 and $Cu_2ZnSnSe_4$ from many-body methods, Appl. Phys. Lett. 98 (2011) 241915/1-3. doi:10.1063/1.3600060.

[52] W.H. Koschel, F. Sorger, J. Baars, Optical phonons in I-III-VI_2 compounds, Le J. Phys. Colloq. 36 (1975) C3–177/181. doi:10.1051/jphyscol:1975332.

[53] X. Fontané, V. Izquierdo-Roca, E. Saucedo, S. Schorr, V.O. Yukhymchuk, M.Y. Valakh, A. Perez-Rodriguez, J.R. Morante, Vibrational properties of stannite and kesterite type compounds: Raman scattering analysis of $Cu_2(Fe,Zn)SnS_4$, J. Alloys

Compd. 539 (2012) 190–194. doi:10.1016/j.jallcom.2012.06.042.

[54] T. Gürel, C. Sevik, T. ÇağIn, Characterization of vibrational and mechanical properties of quaternary compounds Cu_2ZnSnS_4 and $Cu_2ZnSnSe_4$ in kesterite and stannite structures, Phys. Rev. B. 84 (2011) 1–7. doi:10.1103/PhysRevB.84.205201.

[55] M. Dimitrievska, A. Fairbrother, X. Fontané, T. Jawhari, V. Izquierdo-Roca, E. Saucedo, A. Pérez-Rodríguez, Multiwavelength excitation Raman scattering study of polycrystalline kesterite Cu_2ZnSnS_4 thin films, Appl. Phys. Lett. 104 (2014) 1–5. doi:10.1063/1.4861593.

[56] S. Chen, A. Walsh, X.G. Gong, S.H. Wei, Classification of Lattice Defects in the Kesterite Cu2ZnSnS4 and Cu2ZnSnSe4 Earth-Abundant Solar Cell Absorbers, Adv. Energy Mater. 25 (2013) 1522–1539. doi:10.1002/adma.201203146.

[57] K. Moriya, K. Tanaka, H. Uchiki, Cu_2ZnSnS_4 thin films annealed in H_2S atmosphere for solar cell absorber prepared by pulsed laser deposition, Jpn. J. Appl. Phys. 47 (2008) 602–604. doi:10.1143/JJAP.47.602.

[58] J. Zhang, L. Shao, Cu_2ZnSnS_4 thin films prepared by sulfurizing different multilayer metal precursors, Sci. China, Ser. E Technol. Sci. 52 (2009) 269–272. doi:10.1007/s11431-009-0013-8.

[59] K. Ito, T. Nakazawa, Electrical and Optical Properties of Stannite-Type Quarternary Semiconductor Thin Films, Jpn. J. Appl. Phys. 27 (1988) 2094–2097. doi:10.1143/JJAP.27.2094.

[60] H. Katagiri, K. Saitoh, T. Washio, H. Shinohara, T. Kurumadani, S. Miyajima, Development of thin film solar cell based on Cu_2ZnSnS_4 thin films, Sol. Energy Mater. Sol. Cells. 65 (2001) 141–148. doi:10.1016/S0927-0248(00)00088-X.

[61] R.A. Wibowo, E.S. Lee, B. Munir, K.H. Kim, Pulsed laser deposition of quaternary $Cu_2ZnSnSe_4$ thin films, Phys. Status Solidi Appl. Mater. Sci. 204 (2007) 3373–3379. doi:10.1002/pssa.200723144.

[62] G. Suresh Babu, Y.B. Kishore Kumar, P. Uday Bhaskar, S. Raja Vanjari, Growth

and characterization of co-evaporated $Cu_2ZnSnSe_4$ thin films for photovoltaic applications, J. Phys. D. Appl. Phys. 41 (2008) 205305/1-7. doi:10.1088/0022-3727/41/20/205305.

[63] J.J. Scragg, P.J. Dale, L.M. Peter, G. Zoppi, I. Forbes, New routes to sustainable photovoltaics: Evaluation of Cu_2ZnSnS_4 as an alternative absorber material, Phys. Status Solidi Basic Res. 245 (2008) 1772–1778. doi:10.1002/pssb.200879539.

[64] P.A. Fernandes, P.M.P. Salomé, A.F. Da Cunha, B.A. Schubert, Cu_2ZnSnS_4 solar cells prepared with sulphurized dc-sputtered stacked metallic precursors, Thin Solid Films. 519 (2011) 7382–7385. doi:10.1016/j.tsf.2010.12.035.

[65] F. Liu, K. Zhang, Y. Lai, J. Li, Z. Zhang, Y. Liu, Growth and Characterization of Cu_2ZnSnS_4 Thin Films by DC Reactive Magnetron Sputtering for Photovoltaic Applications, Electrochem. Solid-State Lett. 13 (2010) H379–H381. doi:10.1149/1.3481764.

[66] G. Zoppi, I. Forbes, R.W. Miles, P.J. Dale, J.J. Scragg, L.M. Peter, $Cu_2ZnSnSe_4$ Thin Film Solar Cells Produced by Selenisation of Magnetron Sputtered Precursors, Prog. Photovoltaics Res. Appl. 17 (2009) 315–319. doi:10.1002/pip.886.

[67] T. Tanaka, T. Nagatomo, D. Kawasaki, M. Nishio, Q. Guo, A. Wakahara, A. Yoshida, H. Ogawa, Preparation of Cu_2ZnSnS_4 thin films by hybrid sputtering, J. Phys. Chem. Solids. 66 (2005) 1978–1981. doi:10.1016/j.jpcs.2005.09.037.

[68] Z. Zhou, Y. Wang, D. Xu, Y. Zhang, Fabrication of Cu_2ZnSnS_4 screen printed layers for solar cells, Sol. Energy Mater. Sol. Cells. 94 (2010) 2042–2045. doi:10.1016/j.solmat.2010.06.010.

[69] V.G. Rajeshmon, C.S. Kartha, K.P. Vijayakumar, C. Sanjeeviraja, T. Abe, Y. Kashiwaba, Role of precursor solution in controlling the opto-electronic properties of spray pyrolysed Cu_2ZnSnS_4 thin films, Sol. Energy. 85 (2011) 249–255. doi:10.1016/j.solener.2010.12.005.

[70] F. Liu, Y. Li, K. Zhang, B. Wang, C. Yan, Y. Lai, Z. Zhang, J. Li, Y. Liu, In situ growth of Cu_2ZnSnS_4 thin films by reactive magnetron co-sputtering, Sol. Energy

Mater. Sol. Cells. 94 (2010) 2431–2434. doi:10.1016/j.solmat.2010.08.003.

[71] C.P. Chan, H. Lam, C. Surya, Preparation of Cu_2ZnSnS_4 films by electrodeposition using ionic liquids, Sol. Energy Mater. Sol. Cells. 94 (2010) 207–211. doi:10.1016/j.solmat.2009.09.003.

[72] T. Moges, D.-H. Kuo, Defects and Its Effects on Properties of Cu-Deficient $Cu_2ZnSnSe_4$ Bulks with Different Zn-Sn Ratios, Appl. Phys. Express. 5 (2012) 091201/1-3. doi:10.1143/APEX.5.091201/meta.

[73] M. Jiang, X. Yan, Cu2ZnSnS4 Thin Film Solar Cells: Present Status and Future Prospects, in: Sol. Cells - Res. Appl. Perspect., 2013: pp. 107–143. doi:10.5772/50702.

[74] A. Polizzotti, I.L. Repins, R. Noufi, S.-H. Wei, D.B. Mitzi, The state and future prospects of kesterite photovoltaics, Energy Environ. Sci. 6 (2013) 3171–3182. doi:10.1039/c3ee41781f.

[75] T.M. Friedlmeier, N. Wieser, T. Walter, H. Dittrich, H.W. Schock, Heterojunctions based on Cu_2ZnSnS_4 and $Cu_2ZnSnSe_4$ thin films, in: Proc. 14th Eur. Conf. Photovolt. Sci. Eng. Exhib., 1997: pp. 1242–1245.

[76] A. Walsh, S. Chen, S.H. Wei, X.G. Gong, Kesterite thin-film solar cells: Advances in materials modelling of Cu_2ZnSnS_4, Adv. Energy Mater. 2 (2012) 400–409. doi:10.1002/aenm.201100630.

[77] H. Xie, Y. Sánchez, S. López-Marino, M. Espíndola-Rodríguez, M. Neuschitzer, D. Sylla, A. Fairbrother, V. Izquierdo-Roca, A. Pérez-Rodríguez, E. Saucedo, Impact of Sn(S,Se) secondary phases in $Cu_2ZnSn(S,Se)_4$ solar cells: A chemical route for their selective removal and absorber surface passivation, ACS Appl. Mater. Interfaces. 6 (2014) 12744–12751. doi:10.1021/am502609c.

[78] X. Liu, Y. Feng, H. Cui, F. Liu, X. Hao, G. Conibeer, D.B. Mitzi, M. Green, The current status and future prospects of kesterite solar: a brief review, Prog. Photovoltaics Res. Appl. (2016). doi:10.1002/pip.

[79] S.B. Zhang, S.H. Wei, A. Zunger, Defect physics of the $CuInSe_2$ chalcopyrite

semiconductor, Phys. Rev. B. 57 (1998) 9642–9656.

[80] S. Siebentritt, M. Igalson, C. Persson, S. Lany, The electronic structure of chalcopyrites - Bands, point defects and grain boundaries, Prog. Photovoltaics Res. Appl. 18 (2010) 390–410. doi:10.1002/pip.936.

[81] K. Hones, E. Zscherpel, J. Scragg, S. Siebentritt, Shallow defects in Cu_2ZnSnS_4, Phys. B. 404 (2009) 4949–4952. doi:10.1016/j.physb.2009.08.206.

[82] T.K. Todorov, K.B. Reuter, D.B. Mitzi, High-efficiency solar cell with earth-abundant liquid-processed absorber, Adv. Mater. 22 (2010) E156–E159. doi:10.1002/adma.200904155.

[83] E. Garcia-Llamas, J.M. Merino, R. Gunder, K. Neldner, D. Greiner, Y. Sánchez, V. Izquierdo-Roca, E. Saucedo, A. Steigert, M. León, S. Schorr, R. Caballero, Cu_2ZnSnS_4 thin film solar cells grown by fast thermal evaporation and thermal treatment, Sol. Energy. (2016). Under review.

Chapter 2

Experimental Procedures

This chapter introduces the techniques used for the characterization of the samples that have been studied in this work. It covers the basic concepts and principles of each method. Also it lists the features and parameters used, and shortly discusses important issues of each technique with respect to the analysis of the kesterite material.

2.1. Chemical composition

2.1.1. Energy Dispersive X-ray spectroscopy (EDX) [1]

Energy-dispersive X-ray spectroscopy (EDX or EDS) is a powerful technique that is ideal for revealing what elements are present in a particular sample. Basically, EDX consists of detecting the characteristic X-rays produced by each element after bombarding a sample with high energy electrons in an electron microscope. Using a process known as X-ray mapping, information about the elemental composition of a sample can then be overlaid on top of the magnified image of the sample. What makes EDX particularly useful is that the amount of X-rays emitted by each element present in a sample bears a direct relationship with the concentration of that element (mass or atomic fraction). This is why it is possible to convert the X-ray measurements into a final X-ray spectrum and to assess the concentrations of the various chemicals present in a sample.

An EDX system typically consists of several key units. These include: a semiconductor detector housed with a field-effect transistor (FET) preamplifier, cooled to a sub-ambient temperature; and a main amplifier that provides further amplification and a fast pulse inspection function to reduce pile-up events. All of them can be fully controlled with a computer-assisted system, such as a multichannel analyzer (MCA) or a computer-assisted X-ray analyzer (CXA), allowing for unattended and automated operation.

When the electron beam hits the sample, there is a high probability that characteristic X-rays will be generated. The generation of this X-rays are produced due to the inelastic collision of the electrons from the incident beam and the electrons in the inner-shells of the atoms in the samples; in the moment that an inner shell electron is ejected from its orbit, leaving a vacancy, another shell electron falls down from a higher level into the vacancy and it could give off some amount of energy in the form of X-rays. The energy and intensity of these X-ray lines/peaks can be used to make elemental qualitative and quantitative analysis. The resulting X-ray escapes from the sample and reaches the detector, creating a charge pulse. This short-lived current is then converted into a voltage pulse with an amplitude reflecting the energy of the detected X-ray.

Finally, this voltage pulse is converted into a digital signal and one more count is added to the corresponding energy channel. Once the measurement is completed, the accumulated counts produce a typical X-ray spectrum with the major peaks superimposed on the background. Figure 2.1 shows a characteristic spectrum of the CZTGS compound measured by EDX.

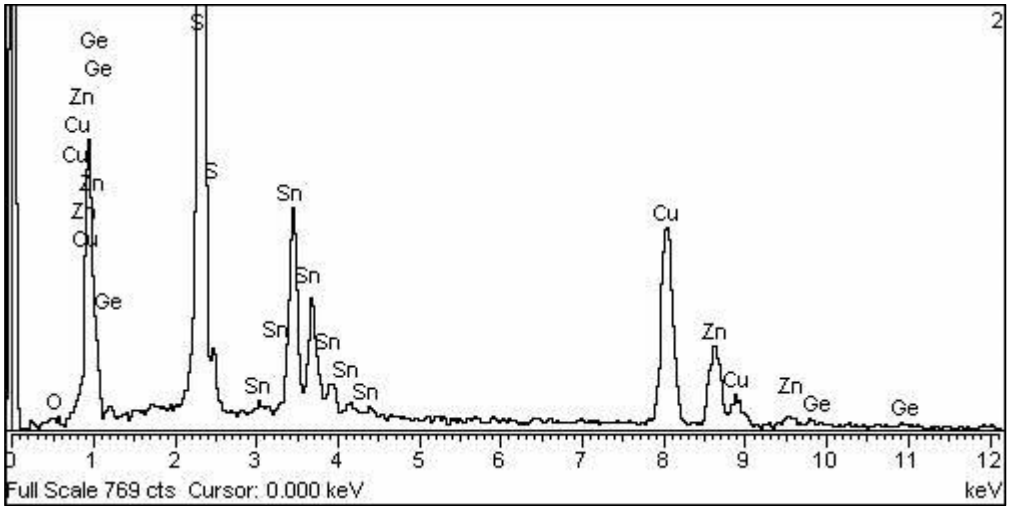

Figure 2.1. A CZTGS energy-dispersive X-ray spectrum showing the main elemental peaks superimposed on the background.

In this work, the measurements were done in the Servicio Interdepartamental de Investigación at UAM in Madrid. The composition of the samples, both bulk and thin films, was measured by energy dispersive X-ray (EDX) (Oxford Instruments, model INCAx-sight) inside a Hitachi S-3000N scanning electron microscope. The measurements were performed at 20 kV (samples without Ge) and 25 kV (samples with Ge) operating voltage and the Cu-, Zn-, Ge-, S-K lines and Sn-L line were used. The relative error of the concentration values is 1% maximum.

2.1.2. Wavelength Dispersive X-ray (WDX)

WDX is a method closely related to EDX and it is based on the same electron-sample interaction. A beam of electrons is accelerated in an evacuated electron column of an Electron microprobe system or scanning electron microscope (SEM) to the sample surface with sufficient energy to generate characteristic X-rays for the elements to be analyzed.

Once X-rays are generated in the sample, they are selected using an analytical crystal with specific lattice spacing. The geometry of the X-rays generated by the sample and the analytical crystal is such that they maintain a constant take-off angle. When the X-rays encounter the analytical crystal at a specific angle (θ), only those X-rays that satisfy the Bragg's Law are reflected and a single wavelength beam is passed on to the detector. The wavelength of the X-rays reflected into the detector may be varied by changing the position of the analyzing crystal relative to the sample. Consequently, X-rays from only one element at a time can be measured on the spectrometer and the position of the analytical crystal must be changed in order to adjust it to a characteristic wavelength of another element. There is commonly more than a single analytical crystal in a WDX spectrometer and, in the case of most instruments, there are typically multiple spectrometers with a suite of analytical crystals. Several different analytical crystals with dissimilar crystal lattice spacings (d-spacings) are normally used for WDX so that the spectrometers can reach all of the elemental wavelengths of interest and it will optimize its performance in different wavelength ranges [2].

The effective resolution of a WDX system may vary from 20 eV to 5 eV or less. The resolution is not detector-dependent, whereas, the resolution of the EDX system is dependent on the resolution of the detector. This can vary from 150 eV or less for a liquid nitrogen cooled Si(Li) detector or 150-220 eV for various solid state detectors.

The Excitation Efficiency or detection sensitivity, usually expressed in ppm per count-per-second (cps), is another important factor for determining the detection limits, repeatability, and reproducibility. The relative excitation efficiency is improved by having more x-rays sources closer to the energy of the element of interest but above the absorption edge. WDX generally uses direct unaltered X-rays excitation, which contains a continuum of energies with most of them not optimal for exciting the element of interest. On the other hand, EDX analyzers may use filters to reduce the continuum energies at the elemental lines, and effectively increasing the percentage of X-rays above the element absorption edge. At the end, the detection sensitivity for WDX is, usually, between 100 to 500 ppm, while for EDX is around 1000 to 5000 ppm.

The sample preparation to extract the chemical composition consists of embedding ascertain amount of the synthesized sample in an epoxy disc. This epoxy disc was mechanically polished to flatness the sample and the surface was cleaned with alcohol to perform accurate measurements. To ensure a good accuracy, it was executed a minimum of 10 measurements in each grain.

The WDX was important to find out the number and composition of the phases. This information was important to perform a more accurate Rietveld analysis from the X-ray and Neutron diffraction data.

In this work, the measurements were done at the Freie Universität Berlin at the Crystallography Department in Berlin. The equipment had an electron microprobe system (JEOL-JXA 8200) assembled with a wavelength dispersive X-ray spectroscopy unit (WDX). In order to calibrate the measurement, elemental standards for Cu, Zn, Sn, Ge, Se and the mineral chalcopyrite as standard for S have been used. The averaging over all the measurements did not exceed the 1% error, originated by the instrumental error.

2.1.3. X-Ray Fluorescence (XRF)

X-ray fluorescence (XRF) spectroscopy is a method closely related to EDX and WDX since it is based in the same phenomena. XRF has become a well-established and developed multi-element technique, capable of supplying accurate quantitative and qualitative information on the elemental composition of a variety of materials in a non-destructive manner. The XRF technique has a wide dynamic range, high precision and minimal requirements for sample preparation.

The main difference between EDX/WDX and XRF is that in EDX/WDX an electron beam is used, while XRF uses a photon beam to hit the samples. An incident photon beam (XRF) experiences a photon absorption interaction with the specimen while an electron beam (EDX and WDX) primarily experiences a Coulomb interaction with the specimen. This difference affects to the penetration depths and as a consequence produces different interaction with the samples. There are three important matrix effects that should be taken into account in the case of quantitative analysis like the effect of the atomic number, the absorption and the enhanced fluorescence.

As mentioned above, the XRF produces a photon-atom interaction like in the case of EDX and WDX techniques [3]. There are three possible photon-atom processes: the first process is the photoelectric effect in which the photons cause the ejection of an electron leaving a hole in the atom which, when the vacancy is filled by another electron, emits a fluorescence photon that has the energy difference between the electron and the hole level; the second process is the Rayleigh scattering in which the photon changes momentum but not energy; and finally, the third process is the Compton scattering in which both momentum and energy are transferred to the electrons comprising the atom. The desired interaction in XRF is the photoelectric effect, provided that the energy of the X-rays detected is a measure of the elements concentration.

In this thesis, the measurements were done at the Institut de Recerca en Energia de Catalunya (IREC) in Barcelona. The X-ray fluorescence spectroscopy was carried out in a Fisherscope XVD equipment, which had been previously calibrated with measurements by inductively coupled plasma optical emission spectroscopy (ICP-OES, Perkin Elmer Optima 3200 RL).

2.1.4. Glow Discharge Optical Emission Spectroscopy (GDOES) [4]

Glow Discharge Optical Emission Spectroscopy (GDOES) provides rapid, direct bulk analysis and depth profiling analysis of solids: metals, glasses and ceramics.

GDOES operation can be described as follows: The sample to measure will be in contact with the analytical Glow Discharge (GD). Inside the sheath (anode) adjacent to the sample (cathode) will generate ionized gas atoms that will accelerate towards the sample (cathode).

The ions will impact on the surface of the sample causing detachment (sputtering) of the surface atoms. These dislodged atoms migrate into the plasma, and they will be excited due to their collisions with electrons and/or metastable gas particles. Upon returning to their fundamental energy state, the atoms will emit characteristic photons, whose characteristic spectrum is measured by a spectrometer which can detect the elements present in the sample.

GD experimental devices consist of (Figure 2.2), mainly, in a small cylindrical vacuum chamber, a sheath (which will act as an anode), the sample (which will act as

a cathode) and a slit through which the emitted light is collected. An inert gas (usually Ar) at low pressure (0.1 to 10 torr), is continuously injected through the anode and pumped outwardly by the vacuum pumps.

Inside the vacuum chamber, a typical analytical GD is achieved by applying a potential difference (100V to several kV) between the anode space and the sample. The anode is usually placed at ground potential and the potential is applied to a contact with the sample. If this applied potential is constant, it is called "direct current Glow discharge" (dc-GD). When the applied potential has a different range of frequencies (kHz-MHz), it is called "Radio Frequency Glow discharge" (rf-GD). In the first case it is only possible to analyze conductive samples while the second can be applied to conductive and insulator samples.

In a glow discharge, cathodic sputtering is used to remove material layer by layer from the sample surface. The atoms, removed from the sample surface, migrate into the plasma where they are excited through collisions with electrons or metastable carrier gas atoms. The characteristic spectrum emitted by this excited atom is measured by the spectrometer and the intensities are recorded as a function of time. Based on a calibration method, established beforehand, these qualitative results can be transformed in a quantitative content depth profile.

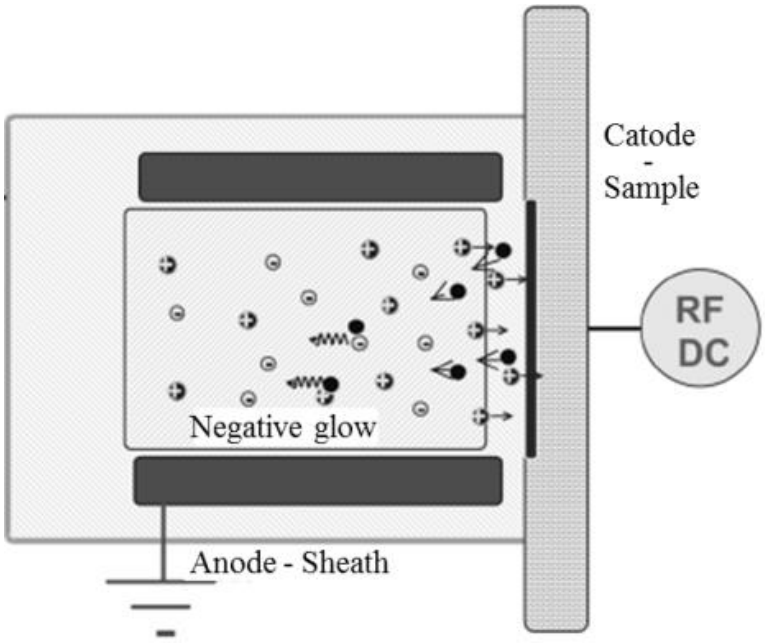

Figure 2.2. Schematic drawing of a GD source, extracted from [5].

2.2. Structural characterization: X-Rays Diffraction (XRD) and Neutron Diffraction (ND)

X-rays and neutron powder diffraction were performed to extract the structural parameters and their changes related with the change in composition of the compounds.

The diffraction phenomenon on a periodic structure has the same wave behavior for X-rays than for neutrons. The periodic structure acts as a three dimensional grating. The waves scattered at different angles interact between them and the result is a diffracted wave whereas the maximum intensities meet the Bragg's law [6]:

$$2d_{hkl}\,sin(\theta) = n\lambda$$

Equation 2-1

where d_{hkl} is the spacing of the lattice planes, Θ is the angle at which the radiation beam hits the array of atoms and λ is the wavelength. Figure 2.3 shows the representation of the condition for a constructive interference following the Bragg's law. The diffracted intensity following the Bragg's law leaves the sample at a 2Θ angle with respect to the incident radiation beam.

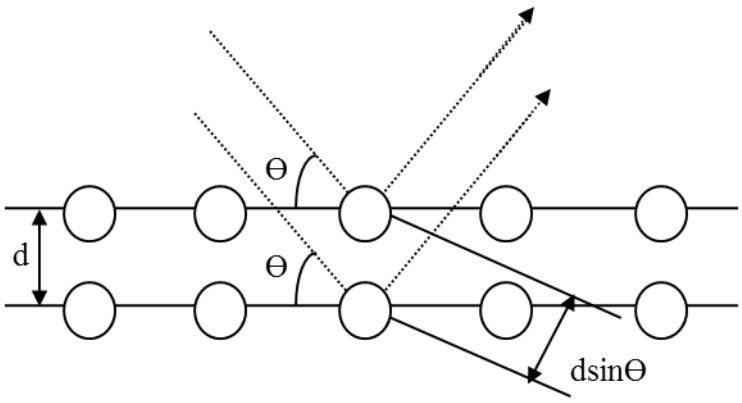

Figure 2.3. Schematic representation of Bragg's law

Geometrically, it is easy to consider groups of atoms which maintain the same distance between them and located in parallel planes with an interplanar distance *d*, and refer to them as a family of planes. To refer to each of these families, the "Miller indexes" (*h k l*) are used, which denote the group of a set of planes perpendicular to

the direction [h k l] for a given structure. For each crystalline structure the values of these interplanar distances can be calculated according to the unit cell parameters (a, b and c) and the angles between the axes (α, β and γ). In the case of a tetragonal structure, where a = b ≠ c and α = β = γ = 90º:

$$\frac{1}{d^2} = \frac{(h^2+k^2)}{a^2} + \frac{l^2}{c^2}$$

Equation 2-2

and the diffracted X-rays are determined by the size and shape of the unit cell following the Bragg's law.

Normally, the intensity I_{hkl} of a Bragg diffraction peak is proportional to the square of the structure factor F_{hkl}, I_{hkl} α $|F_{hkl}|^2$. The structure factor F_{hkl} describes the Fourier transformation of the electron density and the summation of the scattering contribution of each lattice. The structure factor can be expressed as [7]:

$$F_{hkl} = \sum_{n=0}^{N} f_n \, exp\{2\pi i(hx_n + ky_n + lz_n)\}$$

Equation 2-3

where the summation extends over all the N atoms of the unit cell. f_n is the X-ray scattering factor, h, k, l are the Miller indexes and x, y, z are the coordinates of each atom [8]. .

In neutron diffraction, the scattering factor f_n of Equation 2-3 is substituted by the neutron scattering amplitude b_n, which defines the interaction of the neutron with the nucleus of each atom.

In general, X-rays or neutron diffraction are a very useful techniques to get structural information due to its intrinsic properties. However, conventional X-rays present some disadvantages, but also advantages:

1. Interacts with the electron density of the atoms, and do not interact with the nucleus.
2. Atomic scattering power varies smoothly with the variation of Z. It is difficult to distinguish between atoms with low differences in Z.

3. Strongly absorbed by all atoms except those ones with low atomic number (Z). Therefore, elements with low Z can barely be measured.
4. The X-ray scattering amplitude is strongly dependent on $\sin\Theta/\lambda$ (Figure 2.4a), making it very difficult to get good quality X-ray data at high $\sin\Theta/\lambda$.
5. Largely insensitive to magnetic moments, so they do not show up in the measure.
6. Readily available as intense beams, being possible to get enough information with short-time measurements.

The main properties of neutron scattering are summarized next, showing the benefits and/or drawbacks:

1. The neutron is uncharged, so it penetrates easily into a bulk sample; the neutron interacts with the atomic nuclei of the sample.
2. Atomic scattering power varies erratically with atomic number. It is possible to distinguish between isoelectronic cations (see Figure 2.4b).
3. Weakly absorbed by most materials, independent of Z. For most materials, absorption cross sections are proportional to the neutron wavelength, so the absorption lengths are inversely proportional to the wavelength.
4. Neutron scattering amplitude is not dependent on $\sin\Theta/\lambda$ (see Figure 2.4b), it provides good quality neutron data at high $\sin\Theta/\lambda$.
5. Scattered by magnetic moments because neutron possesses a magnetic moment and it makes easy interactions with the unpaired electrons of the sample.
6. Low intensity beams. It is necessary to expose the sample during a long time to get enough information.

It is easy to compare the X-rays and neutron diffraction properties and conclude that despite the X-ray technique is much more accessible and economical, this is not sufficient in certain cases, in particular to distinguish between the cation Cu^{+}, Zn^{2+} and Ge^{4+}, which have the identical number of electrons. Due to these limitations, it was necessary to conduct neutron diffraction experiments.

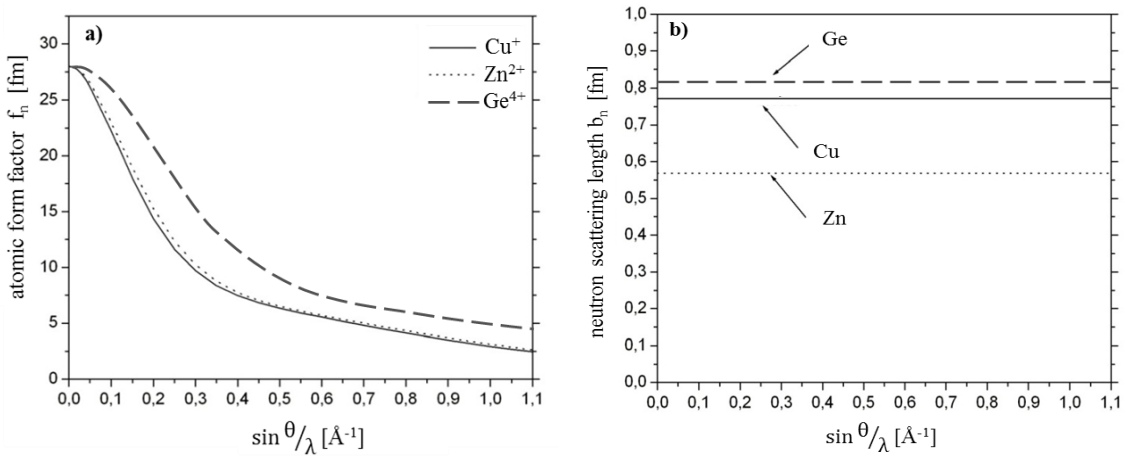

Figure 2.4. Scattering amplitudes of three isoelectronic cations. The atomic form factor f_n of Cu^+, $Zn^{2+}$and Ge^{4+} (a). The coherent neutron scattering length b_n for Cu, Zn and Ge (b). Extracted and modified from [7]

In the case of the kesterite compounds, the atomic scattering factors of Cu^+, Zn^{2+} and Ge^{4+} follow the same tendency and almost overlap, especially for Cu^+ and Zn^{2+}, and diminish substantially with the increasing sinΘ/λ, as it can be seen in Figure 2.4a. The neutron scattering length of copper and zinc are different, b_{Cu}=7.718(4) fm, b_{Zn}=5.680(5) fm, b_{Ge}=8.185(20) fm [9], and it can be seen in Figure 2.4b that b_{Cu} and b_{Zn} keep constant over the whole range of sinΘ/λ. Then, neutron diffraction experiments give stronger reflections at high angles than in the case of X-ray diffraction. Neutron diffraction pattern gives reliable and accurate information of the atomic positions in the structure especially because the peaks are located at are well-defined high Θ angles, and the above mentioned cations can be distinguished in their lattice positions through the structure factor.

The powder XRD diffractograms were performed in an X-Pert PRO θ-2θ device applying the Bragg-Brentano geometry and using copper K-alpha1 (Cu Kα1) radiation. The instrument had a primary monochromator of Germanium, and a X'Celerator detector. The normal operating conditions during measurements were 45 kV and 40 mA.

The neutron diffraction experiments were performed at the D1B instrument at the Institut Laue-Langevin (ILL) (Grenoble, France) working at 1.284 Å, 1.287 Å, and 1.288 Å wavelength at room temperature. The power supplied by the reactor ranged from 43 MW to 57 MW. The samples were placed inside a Ø6 or 3 mm cylindrical vanadium-can. Vanadium was chosen because it has an atomic coherent scattering

cross section negligible when it is compared with the incoherent cross section. Then, the diffraction measurement gets an increase in the background because of the vanadium, but the great benefit is the absence of Bragg peaks in the diffraction patterns [10]. In addition, neutron powder diffraction experiments were performed in the Research Reactor BER II, and more specifically in the instrument E9 at the Helmholtz-Zentrum Berlin für Materialien und Energie (HZB) (Berlin, Germany). The measurements were performed in a neutron fine resolution powder diffractometer with a flux of 10^5 neutrons/cm^{2}s, wavelength of 1.7986 Å, and at room temperature. The sample holder was a cylindrical vanadium receptacle of 6 mm of diameter.

Rietveld Refinement is a method developed by Hugo M. Rietveld to determine the crystal structure. The theoretical fundaments of the Rietveld method have been explained in detail in [11], but in summary, the Rietveld method refines the selected parameters by the user to minimize the difference between an experimental pattern and a model one based on the hypothesized crystal structure and instrumental parameters.

To perform the refinement of the diffraction patterns of the samples, there are two necessary basic requirements. The first one is an accurate set of diffraction data. The second requirement is to have a reasonable starting structural model, that is, some information like spatial group and approximated atomic positions. In this case, the FullProf Suite software package has been used [12].

Below it is shown the strategy followed for the refinements of the diffraction diagrams:

1. Refinement of the background. It was performed by hand, fixing several points in the background line, far enough from any possible reflections, and after that, these points were refined by the program.
2. Refinement of scale factor and zero-shift while all other structural parameters were fixed.
3. Lattice constant refinement (a, b, c) with the cation site occupation factors fixed, consistent with the WDX/EDX analysis values.
4. In the case of the X-ray diffraction data refinement, it was necessary to refine the U, V and W values. These values depend on the instrument features and configuration. For the Neutron diffraction data, this step was not necessary

because the manager of the neutron diffraction instrument provided us with a file with the instrument resolution.

5. Refinement of shape factor.
6. Refinement of the anion positions (X,Y,Z).
7. Refinement of the isotropic temperature factors (B_{iso}). Whether it is not possible to refine B_{iso}, then it was refined the overall temperature factor (B_{ov})
8. Refinement of the cation site occupancy factors (Occ.).

The last three points of the refinement only applied in the neutron diffraction data analysis or in the simultaneous refinements with neutron and X-ray data.

In all cases, it is essential to plot the observed and experimental patterns frequently. The examination of the differences in the pattern is a quick and efficient method to detect problems in the model or in the input file controlling the refinement process. The order of the steps above was not strict in all samples analyzed and in some cases was altered to avoid problems of lack of convergence in the refinements.

As a measure of the improvement and the quality of the refinement between the experimental and calculated patterns, the following agreement factors were used:

$$\text{Bragg Factor:} \quad R_{Bragg} = 100\,\frac{\sum_n |I_{obs} - I_{calc}|}{\sum_n |I_{obs}|}$$

Equation 2-4

where I_{obs} is the observed integrated intensity (experimental) and I_{calc} refers to the calculated integrated intensity.

$$\text{Reduced chi-square:} \quad \chi_v^2 = \left\{\frac{R_{wp}}{R_{exp}}\right\}^2$$

Equation 2-5

where R_{wp} and R_{exp} are the weighted profile and the expected weighted profile factors, respectively:

$$R_{wp} = 100\left\{\frac{\sum_n w_n |y_{obs} - y_{calc}|^2}{\sum_n w_n |y_{obs}|^2}\right\}^{1/2}$$

Equation 2-6

$$R_{exp} = 100\left\{\frac{\sum_n (n-p)}{\sum_n w_n |y_{obs}|^2}\right\}^{1/2}$$

Equation 2-7

where y_{obs} and y_{cal} are the observed and calculated intensity points in the patterns, respectively. w_n is equal to $1/\sigma^2$, where σ^2 is the variance of y_{obs}. n-p is the number of degrees of freedom; n is the total points taken into account where there are Bragg contributions, and p is the number of refined parameters [12].

2.3. Optical characterization: Spectroscopic ellipsometry

The spectroscopic ellipsometry technique analyzes the elliptical polarization of the light after being reflected by a surface. Such ellipticity is caused by the reflection of the linearly polarized light when it hits a surface. Figure 2.5 shows a scheme of an ellipsometer. The light source can be either a laser or a broad-band source such as a xenon gas discharge or a quartz-halogen lamp. In the case of a broad-band source the light is passed through a monochromator to select a narrow band of frequencies. Ellipsometry performed over a wide range of photon frequencies is known as spectroscopic ellipsometry. The light leaving the monochromator is passed through a linear polarizer. After reflection from the sample surface, the light experiences a relative phase shift θ between its *s* and *p* components (vertical and horizontal component, respectively) and becomes elliptically polarized. There are several variations in the method to detect the ellipticity of the reflected light. In Figure 2.5 a compensator introduces another relative phase shift $-\theta$ which exactly cancels the ellipticity induced by the reflection and the light becomes linearly polarized again. This null condition can be easily detected by passing the light through an analyzer, which consists of another linear polarizer oriented to block out the light after the compensator [13].

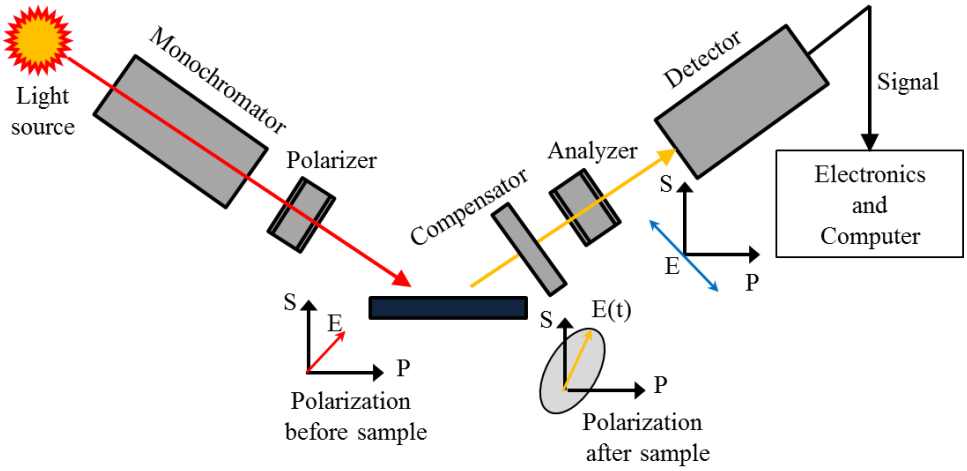

Figure 2.5. Schematic of an ellipsometer. P and S denote polarizations parallel or perpendicular to the plane of incidence, respectively. Based on [13]

As mentioned above, the electric field of the reflected light can be decomposed into two orthogonal components whose relative amplitudes and phases define the ellipticity of the reflected light. These amplitudes and phases might be determined theoretically as the complex ratio (ρ) of the reflection coefficients for perpendicular (r_p) and parallel (r_s) polarizations, which is also called the complex reflectance ratio or complex Fresnel reflection coefficient:

$$\rho = r_p / r_s$$

Equation 2-8

which is expressed in a conventional manner in terms of two angles:

$$\rho = \tan \psi \exp(i\Delta)$$

Equation 2-9

where,

$$\tan \psi = |r_p| / |r_s|$$

Equation 2-10

$$\Delta = \varphi_p - \varphi_s$$

Equation 2-11

Therefore, $tan\psi$ represents the modulus of the reflection coefficients for perpendicular and parallel polarizations, and Δ represents the relative phase shift between the p and s components of the reflected light.

It is possible to obtain the complex refractive index ($\tilde{n}$) combining the Fresnel coefficient (ρ), the Fresnel equations and the Snell's law:

$$\tilde{n} = n_0 sin\varphi_0 \left[1 + \left(\frac{1-\rho}{1+\rho}\right)^2 tan^2\varphi_0\right]^{1/2} = n_0 tan\varphi_0 \left[1 - \frac{4\rho}{(1+\rho)^2} sin^2\varphi_0\right]^{1/2}$$

Equation 2-12

Since the complex refractive index is related to the dielectric function ε(ω) by,

$$\varepsilon(\omega) = \varepsilon_r - i\varepsilon_i = \tilde{n}^2 = (n^2-k^2)-i2nk$$

Equation 2-13

where ε_r is the real part of the dielectric function, ε_i is the imaginary part of the dielectric function, n is the refractive index, and k is the extinction coefficient; as a consequence, by spectroscopic ellipsometry it is possible to measure the real and imaginary parts of the dielectric function.

In this thesis, the spectroscopic ellipsometry measurements were carried out in the Laser Processing Group of Instituto de Óptica Daza de Valdés, CSIC. The measurement of the spectroscopic ellipsometry parameters, ψ and Δ, of the crystals was carried out using a variable angle spectroscopic ellipsometer (Woollam VASE) at room temperature at three incidence angles of 60º, 65º and 70º, to ensure a consistent and accurate determination of the dielectric function in the 0.75-4.5 eV photon energy range, using 0.03 eV steps. In order to obtain reliable data for the optical properties of the bulk crystals, the preparation of a good quality surface is extremely important to minimize the surface roughness and oxide formation effects [14,15]. Recently, we have observed the modification of the values of the effective transitions energies because of the presence of GeO_2 on the surface of these single crystal compounds [16]. Therefore, the crystal samples were thoroughly polished using colloidal silica polishing suspension (Mastermet) in order to remove the oxides that might be formed at the surface, measuring the ellipsometric parameters ψ and Δ immediately after that. The complex effective dielectric function ($\varepsilon(E) = \varepsilon_1(E) + i\varepsilon_2(E)$) was determined by

simulations with the WVASE ellipsometry analysis software assuming a two-phase (substrate-ambient) model [14,15]. The second derivative spectra of the real (ε_1) and imaginary parts (ε_2) of the effective dielectric functions have been used to determine the change of the fundamental band gap E_0 [17] as a function of the compositional changes of the compounds, and the corresponding interband transitions E_{1A} and E_{1B}.

2.4. Vibrational characterization: Raman spectroscopy

As mentioned above, the photons can interact with matter through different physical processes. Among them, there is the light scattering, which is characterized by modifying the momentum of the incident photon. Moreover, the light scattering may be elastic, which does not involve modification of the photon energy, or inelastic (Raman) where there is an exchange of energy between matter and the incident photon. The physical process of light scattering is illustrated in Figure 2.6: a monochromatic light of known energy interacts with the material, and most of the light is elastically back-scattered (Rayleigh scattering); a small number of photons (typically 1 in 10^6) interacts with the crystal lattice and undergoes an inelastic (Raman) scattering by generating (Stokes) or absorbing (anti-Stokes) a phonon, and thus has a slightly lower or higher energy than the incident light. By measuring the energy of the scattered light from a sample, Raman spectra can be generated, which are strongly dependent on material composition, structure, defects, and other factors.

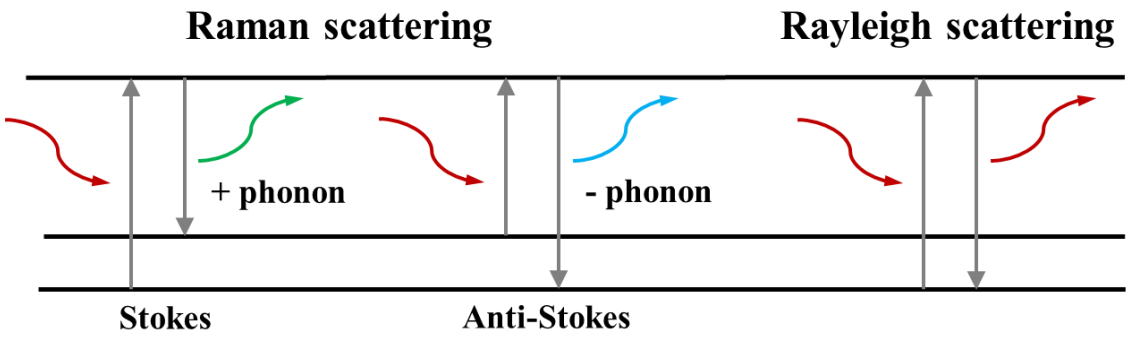

Figure 2.6. Scheme of the physical process in Raman and Rayleigh scattering.

An additional Raman scattering phenomenon of great interest can be the pre-resonant Raman scattering. Pre-resonant Raman scattering leads to a strong enhancement of the Raman signal, and sometimes, but not always, is achieved when the excitation source is closely matched to a fundamental energy value in the material,

such as the bandgap. Figure 2.7 shows the Raman scattering spectra of ZnS measured under 514 and 325 nm laser radiation (pre-resonant) excitation conditions. In the first case, normal Raman scattering occurs with a main peak at 348 cm^{-1}. With 325 nm excitation, ZnS is in pre-resonant conditions, and the signal is greatly enhanced, so that even second (697 cm^{-1}) and third resonance orders (1045 cm^{-1}) of the main peak are visible. This enhancement is especially useful in cases where the phase is present in small quantities as a secondary phase, as it will be seen in the next chapter. It is important to note that the acquisition time between the two spectra is 2-3 orders of magnitude shorter in the pre-resonant case.

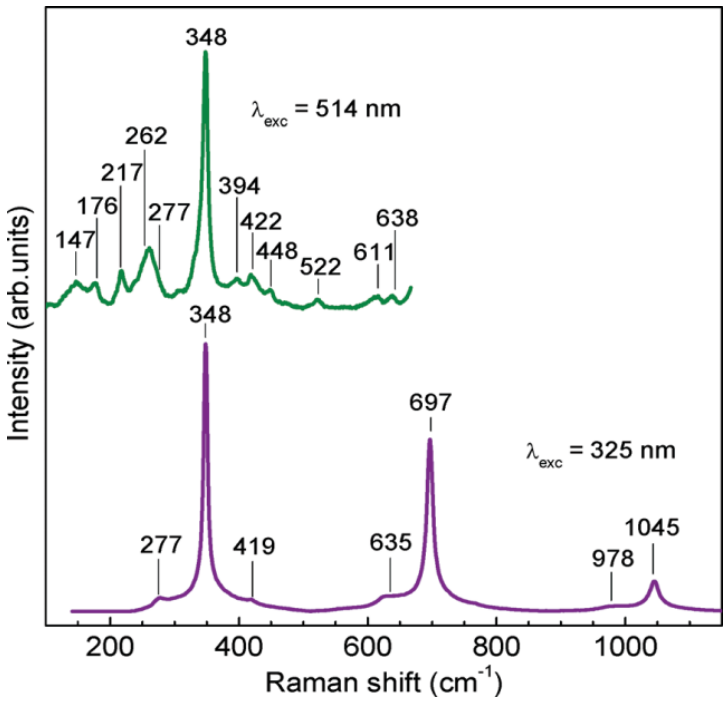

Figure 2.7. Raman spectra of ZnS powder with 514 nm excitation (top spectra) and 325 nm excitation (bottom spectra) laser wavelengths; note that measurement acquisition times when using 325 nm excitation are 2-3 orders of magnitude shorter when compared with 514 nm excitation [18].

In this thesis, the measurements were performed at the Institut de Recerca en Energia de Catalunya (IREC) in Barcelona. Raman spectra were obtained with a Horiba Jobin Yvon LabRam HR800-UV equipment matched with an Olympus metallographic microscope. Backscattering measurements were done with three different excitation wavelengths (532, 325, and 785 nm) focusing the laser spot onto the single crystal and bulk compounds to detect possible secondary phases (Figure 2.8). The use of different excitation wavelengths allows for the selective enhancement of the secondary phases modes and the activation of different Cu_2ZnSnS_4 (CZTS)

modes. Note that the main peak is found at 338 cm^{-1} for CZTS. The laser spot size is of the order of 1-2 μm, but in order to integrate the potential secondary phases, a spot raster facility that extends the analysis to an area of 30 μm x 30 μm has been used. In all Raman measurements, the power density for all excitation wavelengths has been kept below 16 kW/cm^2 to avoid thermal effects. All spectra have been calibrated using a Si single crystal as reference and imposing the Raman shift for the main Si band at 520 cm^{-1}. Simultaneous fittings of spectra with Lorentzian curves have allowed the identification of the peaks attributed to their optical modes.

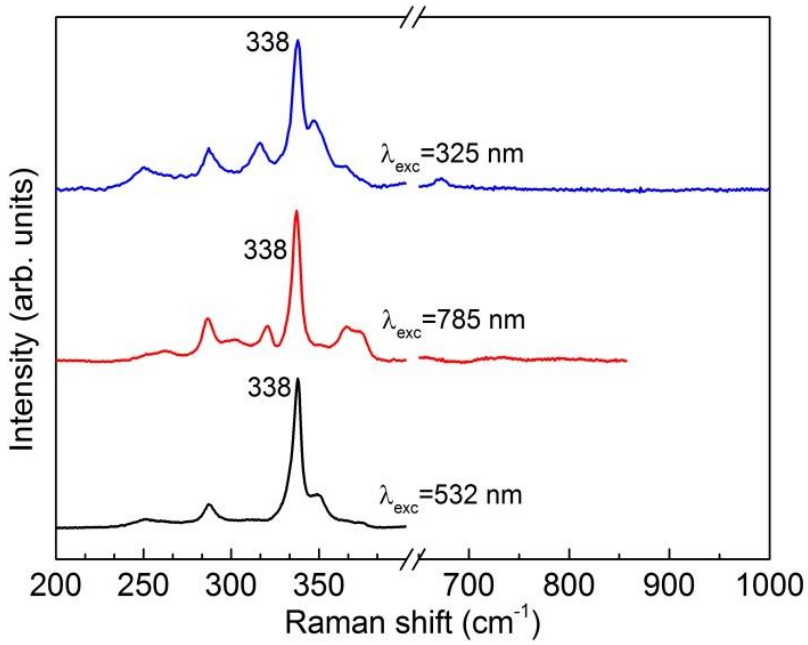

Figure 2.8. Raman scattering spectra of CZTS single crystal with 325, 785 and 532 nm excitation wavelength (from top to bottom).

2.5. Electrical characterization: Temperature dependence conductivity

Nowadays, there are several methods to obtain the conductivity parameters. Among them, there are three methods accepted by the ASTM (American Society for Testing and Materials): the two- and four-points methods, and the Van der Pauw method. In this work, the conductivity was measured varying the temperature and using the Van der Pauw configuration [19].

The Van der Pauw method is widely used because of its accurate measurements and flexibility in the size and shape of the samples. Regarding the two and four points

methods, the Van der Pauw configuration has the advantage that samples should not be cut in a specific way but it is necessary to accomplish certain conditions:

- The sample must be polished and the surface must be free of porosities.
- The sample thickness should be constant.

In this method four contacts are used, as shown in Figure 2.9.

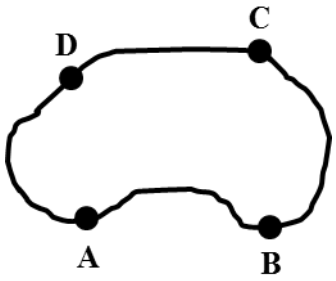

Figure 2.9. Schematic view of Van der Paw configuration on an irregular sample.

Considering a flat sample of a conducting material of arbitrary shape with successive contacts A, B, C and D fixed at arbitrary places along the sample (see Figure 2.9), the resistance $R_{AB,CD}$ ($\rho = R\,d$) is defined as the potential difference V_D-V_C between the contacts D and C per current unit through the contacts A and B. The current enters the sample through the contact A and leaves it through the contact B[19]. The $R_{BC,DA}$ is defined in a similar way. The resistivity might be extracted from the van der Pauw formula:

$$e^{\frac{-\pi d R_{AB,CD}}{\rho}} + e^{\frac{-\pi d R_{BC,DA}}{\rho}} = 1$$

Equation 2-14

where, d is the thickness, ρ is the resistivity and $R_{AB,CD}$ and $R_{BC,DA}$ are defined as:

$$R_{AB,CD} = \frac{V_D - V_C}{I_{AB}}$$

Equation 2-15

$$R_{BC,DA} = \frac{V_A - V_D}{I_{BC}}$$

Equation 2-16

The conductivity of the samples was extracted from the resistivity values.

In this thesis, the measurements were done in the Academy of Sciences of Moldova at the Institute of Applied Physics in Chisinau. The temperature dependence of the resistivity, $\rho(T)$, was measured between 10 and 300 K by the Van der Pauw method. To produce the contacts, In:Ga alloy was used to avoid the sample heating and because of its good ohmic contact. The sample was placed in a closed circle helium cryostat to control the temperature.

The Hot-Probe method was also used as a simple efficient way to distinguish between n-type and p-type conduction using a heated probe and a standard multimeter. The experiment is done by attaching a couple of cold and hot probes to the semiconductor surface. Both probes are wired to a sensitive electrometer whose positive terminal is connected to the hot probe and the negative terminal to the cold probe. While the cold and hot probes are applied to an n-type semiconductor, positive voltage readout is obtained in the meter, whereas for a p-type semiconductor, negative voltage is obtained [20].

2.6. Characterization of solar cells

2.6.1. Single diode equivalent circuit model for solar cells [21]

A single-junction PV cell that is not illuminated behaves very similarly to a semiconductor diode. The single diode model is a basic equivalent circuit to represent a single solar cell. Figure 2.10 shows a single diode model equivalent circuit, where R_s is the series resistance, R_{sh} is the shunt or parallel resistance, I_{ph} represents the photo-generated current in the cell, I_D represents the voltage-dependent current lost due to the recombination and I_{sh} represents the current lost due to the shunt resistance.

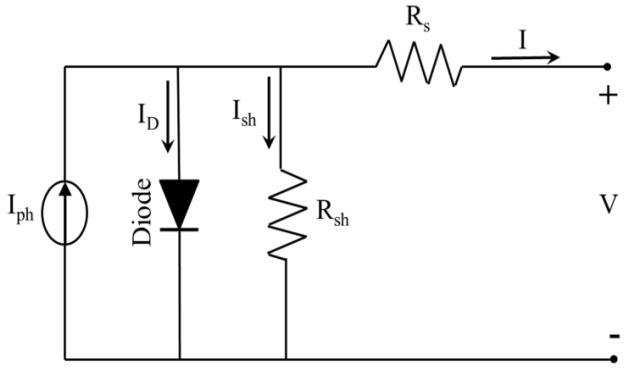

Figure 2.10. Single-diode model equivalent circuit

The conventional equation below describes the I_D modeled using the Shockley equation for an ideal diode:

$$I_D = I_0 \left[exp\left(\frac{qV_D}{nkT}\right) - 1 \right]$$

Equation 2-17

where *n* is the diode ideality factor, I_0 is the saturation current, *k* is the Boltzmann's constant, *q* is the elementary charge and V_D is the voltage across the diode. The ideality factor, which usually ranges from 1 to 2 but might be higher in certain cases, is determined according to the fabrication process and the semiconductor material.

When the photovoltaic junction is illuminated, it will produce a photo-generated current, I_{ph}. An ideal cell is depicted as a current generator that is linked to a parallel diode with an I–V characteristic, writing the shunt current as:

$$I_{sh} = \frac{V_{pv} + IR_S}{R_{sh}}$$

Equation 2-18

where V_{pv} is the PV output voltage, and combining Equation 2-17 and Equation 2-18 results in the complete describing equation for the single diode model for a solar cell:

$$I = I_{ph} - I_0 \left[exp\left(\frac{qV_D}{nkT}\right) - 1 \right] - \frac{V_{pv} + IR_S}{R_{sh}}$$

Equation 2-19

A simple theoretical definition is presented by Equation 2-19 because it does not consider the impact caused by the presence of the electrodes, one above and another below the semiconductor layer, which are required to accumulate the charges that cover the intercepting surface to some extent.

A single diode model provides a good compromise between accuracy and simplicity and this model has been used widely. The effectiveness of the single-diode model has been proven, particularly in the simulation of PV modules with power converters.

The ideality factor (*n*) accounts for the different mechanisms responsible for moving carriers across the junction. The parameter *n* is 1 if the transport process is purely due to diffusion of the carriers, and approximately 2 if the primary process is controlled by the recombination in the depletion region.

Series and shunt resistances (R_S and R_{Sh}, respectively) represent the various ohmic losses that happen in the cell. On one hand, the series resistance represents the resistances introduced by cell solder bonds, cell metallization, and semiconductor resistance. On the other hand, the shunt resistance represents any possible imperfection in the *pn* junction like high-conductivity paths, which could produce short circuits or losses through the edge of the solar cell. Finally, the photo-generated current, I_{ph}, must be determined. Usually, it is assumed that I_{ph} would be equal to I_{SC}.

2.6.2. Current density - Voltage

J-V measurements were carried out to determine the photovoltaic parameters that define a solar cell device. Figure 2.11 shows the J-V curves of a $Cu_2ZnSn(S,Se)_4$ solar cell [22].This is a measure of the output current as a function of the applied bias voltage, both in dark and under illumination conditions. The dark curve shows the standard diode behavior with an exponential turn-up at forward bias. The light curve is shifted down by the light-generated current.

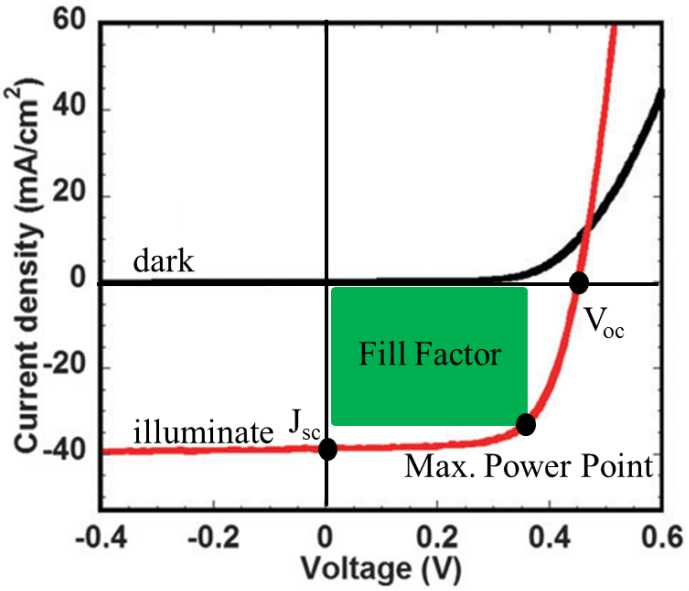

Figure 2.11. J-V curve in dark and under illumination of a $Cu_2ZnSn(S,Se)_4$ solar cell. The photovoltaic parameters are indicated in the graph [22].

The photovoltaic parameters are illustrated in Figure 2.11. The short-circuit current density, J_{sc}, is the current density at zero bias and relates to the maximum current measured. It is often assumed to be the same as the light-generated current, though this assumption is frequently violated when the light-generated current is voltage dependent. The open-circuit voltage, V_{oc}, is the voltage at which the current is zero. The maximum-power point is the point at which the output power density, $|J \cdot V|$ is maximized in the power-generating quadrant. It is also defined the maximum-power current density and voltage, J_{mp} and V_{mp}, respectively. A third parameter, fill factor FF, helps for the definition of the efficiency or performance of a solar cell and can be defined as:

$$FF = \frac{J_{mp}V_{mp}}{J_{sc}V_{oc}}$$

Equation 2-20

The most important parameter of a photovoltaic device is the efficiency. This is defined as the ratio between the power out and the power in. For a solar cell, the output power is the electrical power at the maximum-power point of the J-V curve. The input power is the solar power shining on the cell, which is defined by the AM1.5 spectrum conditions for terrestrial applications (AM0 for space applications). The spectrum has an integrated irradiance of 100 mW/cm^2. The efficiency can be written as:

$$\eta = \frac{J_{sc}V_{oc}FF}{P_{in}}$$

Equation 2-21

where η is the efficiency or performance and P_{in} is the light power incident on the cell.

The I-V characteristics were measured using a Sun 3000 class solar simulator (Abet Technologies Inc., Milford, Connecticut, USA). The measurements were carried out in standard test conditions: AM1.5 spectrum with 100 mW/cm^2 of irradiance at 298 K at IREC.

2.6.3. External Quantum Efficiency

The external quantum efficiency (EQE) is a measure of the ratio of the number of electrons collected out of the cell to the number of incident photons on the cell. It gives valuable information about optical losses and limited information about the electronic properties of the cell. Figure 2.12 shows a typical EQE spectrum for a $Cu_2ZnSn(S,Se)_4$ cell with an efficiency of 11.8% [22]. At long wavelengths the EQE gives information about the absorber layer. At short wavelengths, the EQE response is dominated by the CdS absorption. The band gap energy of CdS is around 2.4 eV (520 nm), so absorption increases strongly below this point.

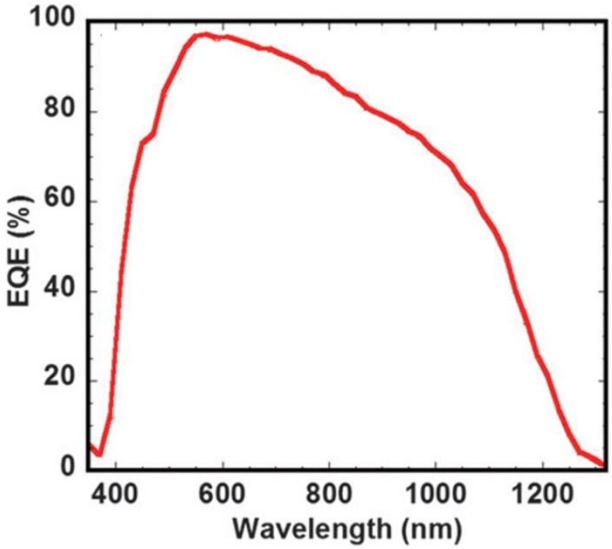

Figure 2.12. External quantum efficiency (EQE) versus Wavelength of $Cu_2ZnSn(S,Se)_4$ cell [22]

The short-circuit current can be calculated from QE measurements:

$$J_{sc} = q \int QE(\lambda) N_{ph}(\lambda) d\lambda$$

Equation 2-22

where q is the elemental charge and N_{ph} is the number of photons at each wavelength in the solar spectrum. This provides a second way of calculating J_{sc}, which can be used as a cross-comparison with the value obtained from J-V measurements.

External quantum efficiency (EQE) measurements were performed using a Bentham PVE300 system (Bentham Instruments Ltd., Berkshire, UK) calibrated with a Si and Ge photodiode at IREC.

2.7. References

[1] J. Heath, Energy Dispersive Spectroscopy, Essent. Knowl. Briefings. Second Edi (2015) 32.

[2] D. Henry, J. Goodge, Wavelength-dispersive X-ray spectroscopy (WDS), Geochemical Instrum. Anal. (2012) 1–6. http://serc.carleton.edu/research_education/geochemsheets/wds.html.

[3] S.-H. Chen, M. Kotlarchyk, Interactions of Photons and Neutrons with Matter, 2007.

[4] A.B. Martín-Rojo, M. González, F.L. Tabarés, Glow Discharge Emission Spectrometry (GDOES): Introducción Teórica, Aspectos Generales y Aplicabilidad en el Marco del Programa Technofusion, 2013.

[5] T. Nelis, J. Pallosi, Glow Discharge as a Tool for Surface and Interface Analysis, Appl. Spectrosc. Rev. 41 (2006) 227–258. doi:10.1080/05704920600620345.

[6] V. Pecharsky, P.Y. Zavalij, Fundamentals of Powder Diffraction and Structural Characterization of Materials, 2005. doi:10.1007/978-0-387-09579-0.

[7] S. Schorr, C. Stephan, T. Törndahl, R. Mainz, X-Ray and Neutron Diffraction on Materials for Thin-Film Solar Cells, in: Adv. Charact. Tech. Thin Film Sol. Cells, 2011: pp. 347–364. doi:10.1002/9783527636280.

[8] B.D. Cullity, Elements of X-ray Diffraction, 1978.

[9] V.F. Sears, Neutron scattering lengths and cross sections, Neutron News. 3 (1992) 26–37. doi:10.1080/10448639208218770.

[10] D.M. North, J.E. Enderby, P.A. Egelstaff, The structure factor for liquid metals I. The application of neutron diffraction techniques, J. Phys. C Solid State Phys. 1 (1968) 784–794. doi:10.1088/0022-3719/1/3/329.

[11] H.M. Rietveld, A profile refinement method for nuclear and magnetic structures, J. Appl. Crystallogr. 2 (1969) 65–71. doi:10.1107/S0021889869006558.

[12] J. Rodríguez-Carvajal, An introduction to the prgram FullProf, n.d. https://www.ill.eu/sites/fullprof/php/tutorials.html.

[13] P.Y. Yu, M. Cardona, Fundamentals of Semiconductors, 4th ed., 2010.

[14] J.G. Albornoz, R. Serna, M. León, Optical properties and electronic structure of polycrystalline $Ag_{1-x}Cu_xInSe_2$ alloys, J. Appl. Phys. 97 (2005) 1–7. doi:10.1063/1.1899243.

[15] P. Lautenschlager, M. Garriga, S. Logothetidis, M. Cardona, Interband critical points of GaAs and their temperature dependence, Phys. Rev. B. 35 (1987) 9174–9189. doi:10.1103/PhysRevB.35.9174.

[16] R. Caballero, I. Victorov, R. Serna, J.M. Cano-Torres, C. Maffiotte, E. Garcia-Llamas, J.M. Merino, M. Valakh, I. Bodnar, M. León, Band-gap engineering of $Cu_2ZnSn_{1-x}Ge_xS_4$ single crystals and influence of the surface properties, Acta Mater. 79 (2014) 181–187. doi:10.1016/j.actamat.2014.06.040.

[17] M. León, S. Levcenko, R. Serna, G. Gurieva, A. Nateprov, J.M. Merino, E.J. Friedrich, U. Fillat, S. Schorr, E. Arushanov, Optical constants of Cu_2ZnGeS_4 bulk crystals, J. Appl. Phys. 108 (2010) 1–5. doi:10.1063/1.3500439.

[18] A. Fairbrother, V. Izquierdo-Roca, X. Fontané, M. Ibáñez, A. Cabot, E. Saucedo, A. Pérez-Rodríguez, ZnS grain size effects on near-resonant Raman scattering: optical non-destructive grain size estimation, CrystEngComm. 16 (2014) 4120–4125. doi:10.1039/c3ce42578a.

[19] L.J. van der Pauw, A method of measuring specific resistivity and Hall effect of discs of aribtrary shape, Philips Res. Reports. 13 (1958) 1–11. doi:citeulike-article-id:8438442.

[20] G. Golan, A. Axelevitch, B. Gorenstein, V. Manevych, Hot-Probe method for evaluation of impurities concentration in semiconductors, Microelectronics J. 37 (2006) 910–915. doi:10.1016/j.mejo.2006.01.014.

[21] A.M. Humada, M. Hojabri, S. Mekhilef, H.M. Hamada, Solar cell parameters extraction based on single and double-diode models: A review, Renew. Sustain. Energy Rev. 56 (2016) 494–509. doi:10.1016/j.rser.2015.11.051.

[22] H. Xin, S.M. Vorpahl, a D. Collord, I.L. Braly, a R. Uhl, B.W. Krueger, D.S. Ginger, H.W. Hillhouse, Lithium-doping inverts the nanoscale electric field at the

grain boundaries in $Cu_2ZnSn(S,Se)_4$ and increases photovoltaic efficiency, Phys. Chem. Chem. Phys. 17 (2015) 23859–23866. doi:10.1039/c5cp04707b

PART I: BULK CHARACTERIZATION

Chapter 3

Synthesis and Fundamental Properties of $Cu_2ZnSn_{1-y}Ge_yS_4$ and $Cu_2ZnSn_{1-y}Ge_ySe_4$ Bulk Compounds

This chapter presents the synthesis of bulk compounds and the study of the chemical composition, structural, optical and vibrational properties, and electrical characterization of the single crystals and polycrystalline compounds of $Cu_2ZnSn_{1-y}Ge_yS_4$ (CZTGS) and $Cu_2ZnSn_{1-y}Ge_ySe_4$ (CZTGSe). All details about the characterization techniques were described in Chapter 2.

3.1. Synthesis of bulk compounds

In this work, the bulk material has been synthesized by three methods, Bridgman method, solid state reaction (SS) and Chemical Vapor Transport deposition (CVT).

3.1.1. Synthesis of Cu_2ZnSnS_4 (CZTS) by Solid State reaction (SS)

Based on the phase diagram reported in [1], the initial weight of each pure element (99.9999 % purity from Alfa Aesar company) was selected to conduct the SS synthesis to obtain Cu_2ZnSnS_4 (CZTS). The solid state reaction is based on the diffusion of the fundamental metallic elements, binary or ternary compounds under isothermal conditions. The essential factors which permit such a reaction are the diffusion behavior of one element or compound into the other, and the endothermic reaction in the final alloy. The latter provides the necessary chemical driving force for the reaction. In addition, the reaction to form the CZTS compound must be carried out at sufficiently low temperatures to avoid to some extent the formation of undesired secondary phases [2], although, it is known that it is very difficult to suppress the presence of secondary phases in the synthesis process of these compounds.

Three different approaches were studied to achieve the single phase CZTS compound. In all approaches, the synthesis process was performed in a sealed vacuum ampoule. The ampoule was located in a vertical furnace and was heated up to 1023 K for at least 145 h. The heating and cooling rates were adjusted to 50 K/h, as illustrated in Figure 3.1. After the first synthesis, the compound was grinded in an agate mortar and the heating and cooling cycles were repeated to improve the chemical and structural homogeneity. In the heating process, it was carefully considered the speed of the heating ramp to prevent from explosions of the ampoules due to the high sulfur vapor pressure.

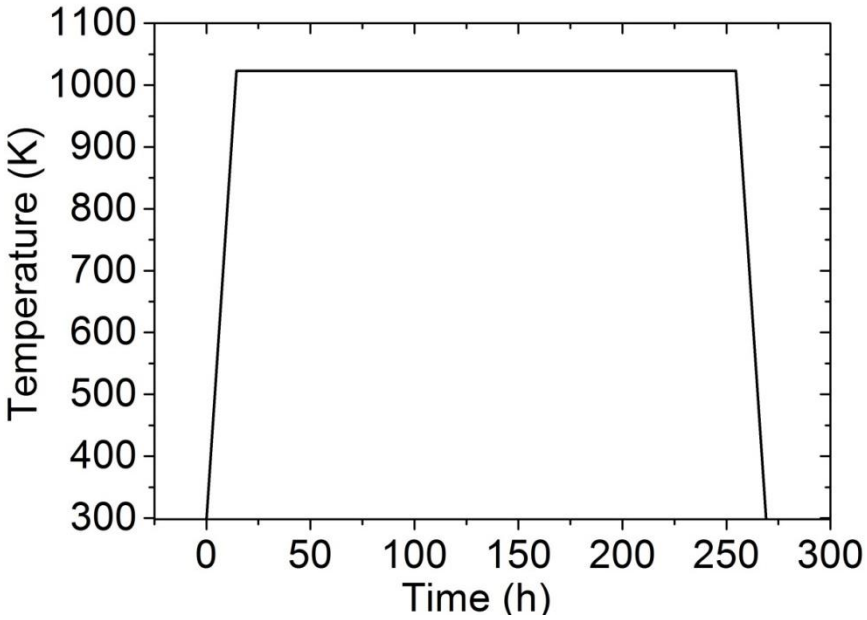

Figure 3.1. Synthesis process profile used in the Solid State reaction process.

In the first approach the polycrystalline CZTS compound was synthesized from its constituent elements Cu, Zn, Sn and S, weighed in stoichiometric proportion (2:1:1:4) and sealed in a quartz ampoule at a base pressure of 10^{-5} mbar. Additionally, it was used a 40% excess of S in the initial mixture of the elements in order to compensate for the poor S incorporation in the compound. This excess of sulfur in the initial mixture facilitates the formation of single phase CZTS [3]. The left image of the Figure 3.2 shows the CZTS compound after the synthesis process. In this image it can be observed the presence of inhomogeneities due to the presence of secondary phases. In the right image of the Figure 3.2, it can be seen clearly how the inhomogeneity was suppressed after the second cycle, which might be indicative that a single phase CZTS compound was achieved.

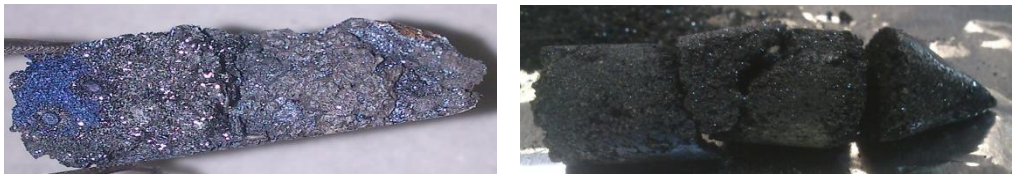

Figure 3.2. CZTS compound after the synthesis from the pure elements (left) and after the homogenization process (right).

The second and the third approaches were based in the solid state reaction of Cu_2S, SnS_2, ZnS binary compounds and Cu_2SnS_3 ternary compound, respectively, to obtain the final CZTS compound.

In the second approach, the CZTS compound was synthesized from the Cu_2S, SnS_2 and ZnS binary compounds. These Cu_2S and SnS_2 were previously synthesized in our laboratory, while commercially available ZnS binary compound (99.99 % purity from Alfa Aesar company) was used. The Cu_2S and SnS_2 were synthesized from their constituent elements Cu, Sn and S, weighed in stoichiometric proportion and sealed in a quartz ampoule at a base pressure of 10^{-5} mbar. The Cu_2S was synthesized by the following process: heated up with a ramp of 2 K/h until 1023 K, this temperature was kept constant for 120 h, then it was cooled down with a ramp of 5 K/h until 723 K for 12 h and finally it was cooled down at room temperature with a ramp of 10 K/h. Additionally, it was performed a homogenization process in which it was heated up until 1073 K for 12 h with a ramp of 50 K/h and then, it was cooled down naturally. Figure 3.3 shows the final Cu_2S ingot after the synthesis and homogenization process. To obtain the SnS_2 binary compound, it was necessary the previous synthesis of SnS. The SnS was synthesized from its constituent elements Sn and S by the following process: heated up with a ramp of 10 K/h until 523 K and kept at this temperature for 96 h, then it was heated up until 1073 K for 24 h with a ramp of 5 K/h and finally it was cooled down with a ramp of 5 K/h until room temperature. The homogenization process was done by following these steps: heated up with a ramp of 20 K/h until 648 K, immediately it was heated up until 693 K for 72 h with a ramp of 10 K/h and the final heating ramp of 2 K/h was used to achieve the maximum temperature at 783 K for 72 h; finally, it was cooled down naturally. Once we have the SnS compound, it was added the necessary amount of sulfur to obtain the stoichiometric portion 1:2 of Sn and S, respectively, and it was sealed in a quartz ampoule under vacuum. The synthesis process of this compound was exactly the same that for the SnS compound but the homogenization process was different. The homogenization process consisted of a ramp of 2 K/h until 385 K and immediately it was heated up until 923 K for 120 h with a ramp of 10 K/h; the cooling down process was done with a quenching with liquid nitrogen. Figure 3.4 shows after the synthesis and homogenization process the SnS compound with a partially embedded quartz ampoule, and also it shows the SnS_2 compound which presents a particular orange color. It can be observed that the SnS_2 is homogeneous in all the volume thanks to the cross section image.

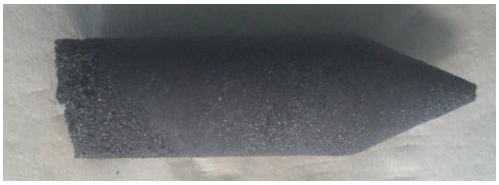

Figure 3.3. Cu_2S compound after synthesis and homogenization process.

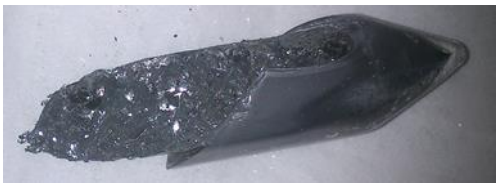

Figure 3.4. SnS compound (above), cross section and longitudinal image of the SnS_2 ingot (below) after the synthesis and homogenization process.

Once we have the binary compound it is necessary to ascertain the correct weighed of each binary compound and the synthesis temperature to obtain the CZTS. To perform this task, it was fundamental to consider the isothermal section of the Cu_2S–SnS_2–ZnS system at 670 K of Figure 3.5 (already shown in Chapter 1) and the phase diagrams of Figure 3.6 and Figure 3.7.

Figure 3.5 shows with more detail the isothermal section of the Cu_2S–SnS_2–ZnS system at 670 K. This figure is fundamental to know how to synthesize the CZTS compound. In the center of the Figure 3.5, it is highlighted with a red circle the formation area where the CZTS compound takes place. In each corner it is highlighted the Cu_2S, SnS_2 and ZnS binary compounds with a red solid rectangle, and also the A and B points corresponding to 50% molar fraction of ZnS. The line that connects the Cu_2S corner and the A point is the section of the phase diagram presented in Figure 3.6 and the line that connects the SnS_2 corner and the B point is the section of the phase diagram presented in Figure 3.7. Furthermore, in Figure 3.5 it is highlighted the Cu_2SnS_3 ternary compound, which is connected with the ZnS corner and its phase diagram will be discussed below in the third synthesis approach.

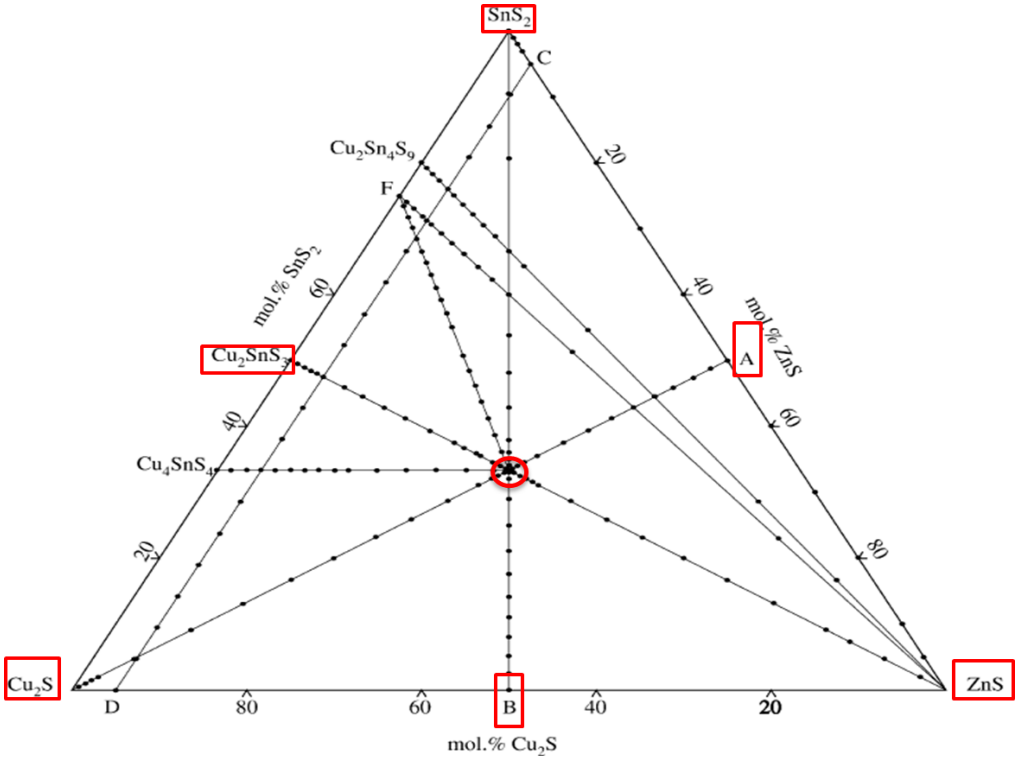

Figure 3.5. Isothermal section of the Cu_2S–SnS_2–ZnS system at 670 K, extracted from [1].

As mentioned above, Figure 3.6 shows the phase diagram of the Cu_2S–A section. The Cu_2ZnSnS_4 compound is located in the region 11 under the δ Greek letter. Also, it is necessary to take into account the phase diagram of the SnS_2-B section (Figure 3.7), where the CZTS compound is located in region 15 under the δ Greek letter. At the end, all three binary compounds, Cu_2S, SnS_2 and ZnS, are interrelated because the A point is a 50% molar mixture of SnS_2 and ZnS and the B point is a 50% molar mixture of Cu_2S and ZnS. As a consequence, the polycrystalline CZTS compound was synthesized from Cu_2S, SnS_2 and ZnS binary compound, weighed in stoichiometric proportion 1:1:1 and sealed in a quartz ampoule at a base pressure of 10^{-5} mbar. As mentioned before, this last synthesis was produced in a vertical furnace and the ampoule was heated up to 1023 K for 7 days. The heating and cooling rates were adjusted to 50 K/h, as illustrated in Figure 3.1. Moreover, it was performed a homogeneity process with the same temperatures and ramp mentioned for the synthesis during 24 days. It was required this amount of time due to the amount of the mixture (15 grams). In this way, it was possible to complete the diffusion of the binary compounds to achieve the CZTS formation. Figure 3.8 shows the Cu_2SnZnS_4 after the synthesis and homogenization process. As it can be seen at naked eye, the compound was homogenous.

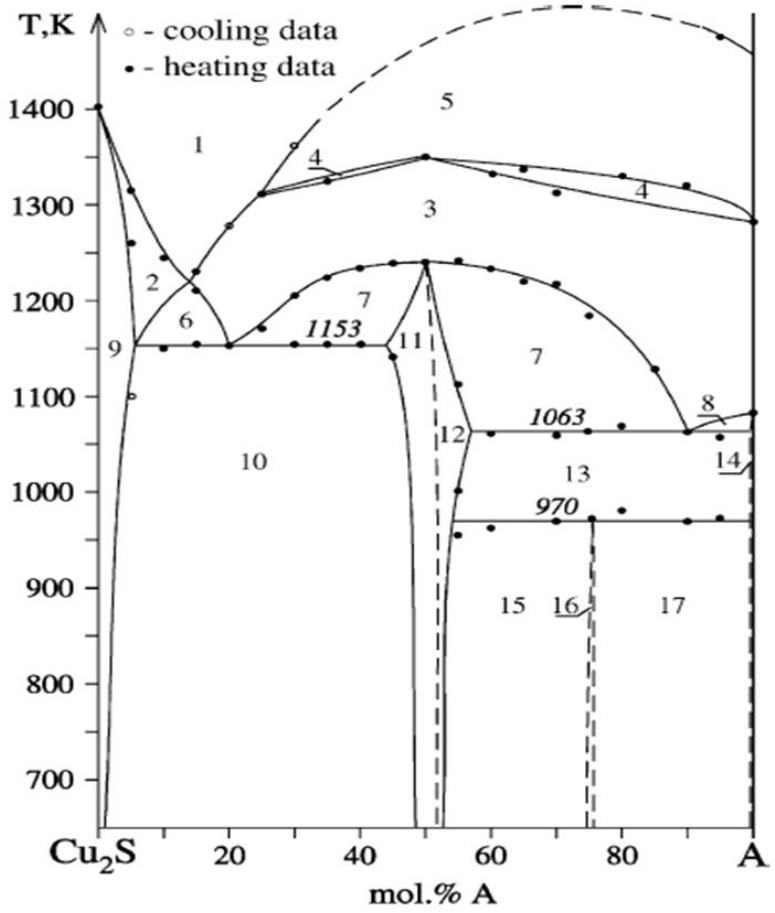

Figure 3.6. Phase diagram of the Cu_2S–A section: (1) L, (2) L + α, (3) L + β′, (4) L + β + β′, (5) L + β, (6) L + α + β′, (7) L + β′+ δ, (8) L + β′+ γ, (9) α, (10) α + δ, (11) δ, (12) β′+ δ, (13) β′+ γ + δ, (14) β′+ γ, (15) β′+ δ + $Cu_2ZnSn_3S_8$, (16) β′+ $Cu_2ZnSn_3S_8$, (17) β′+ γ + $Cu_2ZnSn_3S_8$; where α, β', γ, δ are solid solution regions of Cu_2S, LT-ZnS, SnS_2 and Cu_2ZnSnS_4, respectively [1].

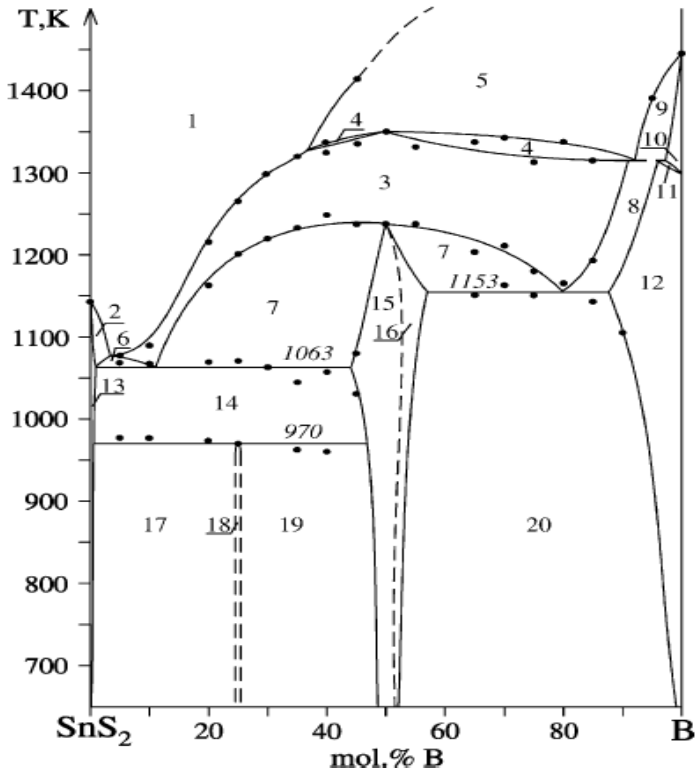

Figure 3.7. Phase diagram of the SnS_2–B section: (1) L, (2) L + γ, (3) L + β′, (4) L + β + β′, (5) L + β, (6) L + β′ + γ, (7) L + β′ + δ, (8) L + α + β′, (9) L + α + β, (10) α + β, (11) α + β + β′, (12) α + β, (13) γ, (14) γ + δ, (15) δ, (16) β′+ δ, (17) γ + $Cu_2ZnSn_3S_8$, (18) $Cu_2ZnSn_3S_8$, (19) δ + $Cu_2ZnSn_3S_8$, (20) α+β′+δ; where α, β', γ, δ are solid solution regions of Cu_2S, LT-ZnS, SnS_2 and Cu_2ZnSnS_4, respectively [1].

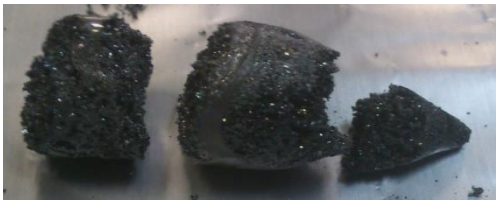

Figure 3.8. Cu_2ZnSnS_4 compound from binary compounds synthesis and after the homogenization process.

In the third and last approach to synthesize the CZTS compound, Cu_2SnS_3 and ZnS were used as starting reactive. This Cu_2SnS_3 ternary compound was previously synthesized while commercially available ZnS binary compound from Alfa Aesar was used. The Cu_2SnS_3 was synthesized following the phase diagram of Figure 3.9. This phase diagram is the tie-line from Cu_2S to SnS_2 of the isothermal section of the Cu_2S–SnS_2–ZnS system at 670 K (Figure 3.5). The Cu_2SnS_3 ternary compound is located in the phase diagram of the Figure 3.9 at 50% molar of SnS_2. To synthesize the ternary

compound, it was used the previous synthesized binary compounds Cu_2S and SnS_2, mentioned above, in the same stoichiometric weighted proportion and it was sealed in a quartz ampoule at a base pressure of 10^{-5} mbar. The Cu_2SnS_3 was synthesized following the presented process in Figure 3.1 and explained above. No homogenization process was needed for this compound.

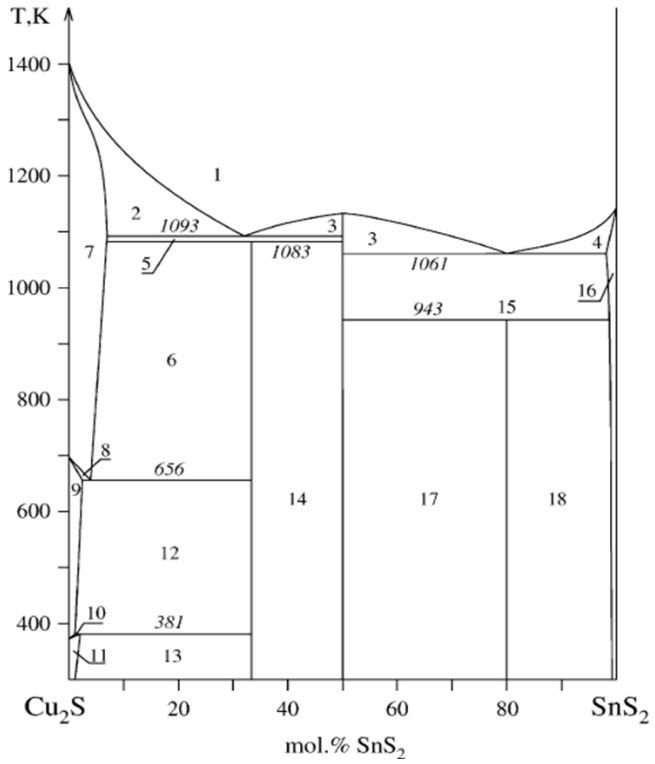

Figure 3.9. Phase diagram of the Cu_2S–SnS_2 system: (1) L, (2) L + α, (3) L + Cu_2SnS_3, (4) L + γ, (5) Cu_2SnS_3 + α, (6) Cu_4SnS_4 + α, (7) α, (8) α + α', (9) α´, (10) α´ + α´´, (11) α´´, (12) Cu_4SnS_4 + α´, (13) Cu_4SnS_4 + α´´, (14) Cu_2SnS_3 + Cu_4SnS_4, (15) Cu_2SnS_3 + γ, (16) γ, (17) Cu_2SnS_3 + $Cu_2Sn_4S_9$, (18) $Cu_2Sn_4S_9$ + γ; where α, β', γ, δ are solid solution regions of Cu_2S, LT-ZnS, SnS_2 and Cu_2ZnSnS_4, respectively [1].

Once the Cu_2SnS_3 ternary compound was synthesized, it was mixed with commercial ZnS following the phase diagram of Figure 3.10. Cu_2ZnSnS_4 was synthesized from Cu_2SnS_3 and ZnS compounds, weighed in stoichiometric proportion 1:1 and it was sealed in a quartz ampoule at a base pressure of 10^{-5} mbar. As mentioned before, this last synthesis was produced in a vertical furnace and was heated up to 1023 K for 24 days. The heating and cooling rates were adjusted to 50 K/h, as illustrated in Figure 3.1. No homogenization process was needed after the synthesis. As it can be seen in Figure 3.11,

the CZTS ingot shows a homogenous appearance after the synthesis from the Cu_2SnS_3 ternary and ZnS binary compounds.

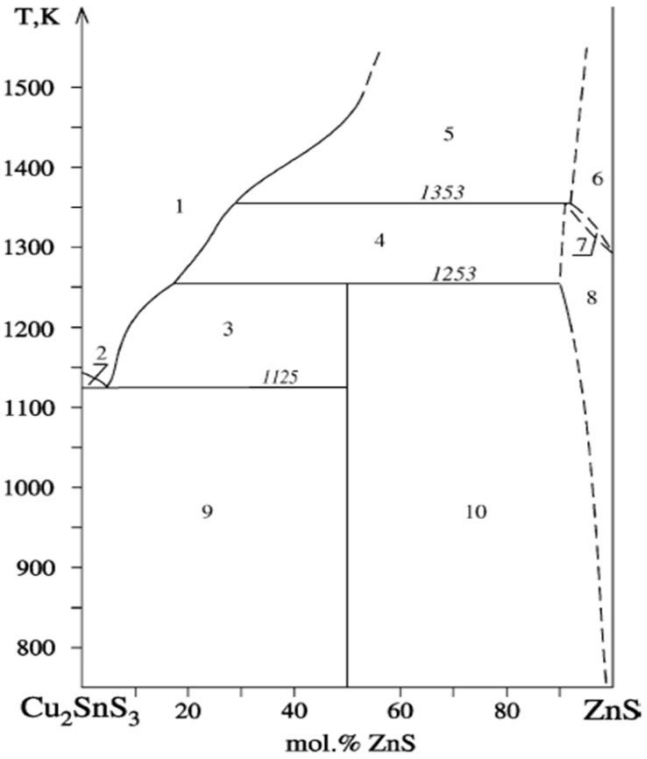

Figure 3.10. Phase diagram of the Cu_2SnS_3–ZnS system: (1) L; (2) L + Cu_2SnS_3;(3) L + Cu_2ZnSnS_4; (4) L + β'; (5)L + β; (6) β; (7) β + β'; (8) β'; (9) Cu_2SnS_3 + Cu_2ZnSnS_4; (10) β'+Cu_2ZnSnS_4; where β'is a solid solution region LT-ZnS [1].

Figure 3.11. Cu_2ZnSnS_4 compound synthesized from Cu_2SnS_3 ternary and ZnS binary compounds.

3.1.2. Synthesis of $Cu_2ZnSn_{1-y}Ge_yS_4$ and $Cu_2ZnSn_{1-y}Ge_ySe_4$ compounds by the Bridgman method

Polycrystalline bulk kesterite compounds with different Ge/Sn ratios were grown by a modified Bridgman method (Figure 3.12), using constituents with purities ≥ 99.999%. The growth was carried out in an evacuated quartz ampoule introduced in a vertical furnace, followed by a heating ramp up to 1173 K avoiding overpressures. A quartz stick was welded to the quartz ampoule, which was used as a holder to apply a vibration moment while the compound was liquid. In this way, the formation of the desired

compound was accelerated. The ampoule was then cooled down and an ulterior homogenization process was applied at 973 K for 7 days. The synthesis and growth temperature of the bulk kesterite compounds were selected in accordance with the Cu_2ZnSnS_4, $Cu_2ZnSnSe_4$, Cu_2ZnGeS_4 and $Cu_2ZnGeSe_4$ phase diagram reported in [1,4–6] respectively. At the initial stage, the temperature was risen at the rate of 2.5 K/min up to 700 K, then it was applied a plateau of 2 h with the vibration system on. In this way, the volatile substances like sulfur or selenium can react easily with the other elements. Again, the temperature was risen up until 800 K with a ramp rate of 1.7 K/min, and then it was applied the same plateau of 2 h with the vibration to ease the reaction between the elements. The final temperature of 1173 K was reached with 1.7 K/min ramp rate and the ampoule was kept at this temperature for 2 h with the vibration on. After that, the furnace was naturally cooled down.

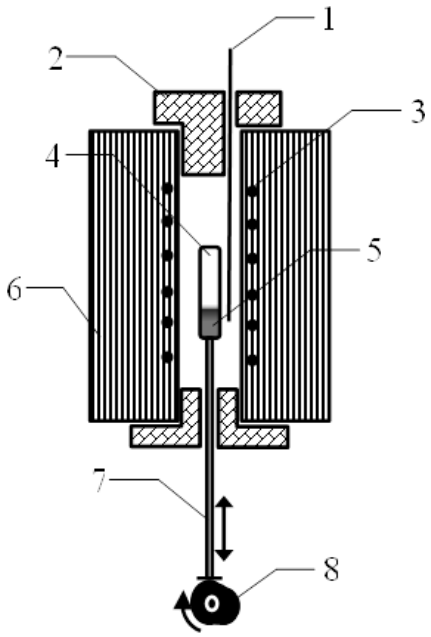

Figure 3.12. Scheme of the vertical furnace for bulk kesterite synthesis by modified Bridgman method. 1) Thermocouple, 2) Insulating plug, 3) Resistance/Heater, 4) Quartz ampoule, 5) Starting constituents, 6) Insulator, 7) Quartz stick and 8) Vibration axis system.

3.1.3. Synthesis of $Cu_2ZnSn_{1-y}Ge_yS_4$ and $Cu_2ZnSn_{1-y}Ge_ySe_4$ single crystals by Chemical Vapor Transport deposition (CVT)

Using the CVT technique, $Cu_2ZnSn_{1-y}Ge_yS_4$ and $Cu_2ZnSn_{1-y}Ge_ySe_4$ single crystals were synthesized [7]. The previously synthesized polycrystalline kesterite compounds (section 3.1.2) were grinded and used as source material for the CVT synthesis.

The CVT process was performed in a quartz ampoule with two sections (see Figure 3.13.a). The source material was loaded in the section 1 and in the section 2, 5 mg cm^{-3} of iodine were loaded in a capillary vessel and a magnetic hammer was placed inside (Figure 3.13b). Then, the two-section ampoule was evacuated at around 10^{-3} Pa and sealed (Figure 3.13c). Once the ampoule was evacuated, the capillary with the iodine was broken by the magnetic hammer and the section 2 was heated to transfer the iodine in gas form towards the section 1 of the ampoule. Finally, the two section ampoules were sealed to obtain two independent ones (Figure 3.13d). The section 1 ampoule was ready to place it in a furnace with two independent heating zones to perform the single crystals synthesis. Iodine was used as transport agent. The temperature at the crystallization zone was kept at 970 K, around 80 K lower than the temperature at the reaction zone (1050 K), and both were maintained for 8 days. Upon the end of the process, the ampoule was pushed out from the furnace around 4 cm towards the hot extreme. As a consequence, the iodine was transferred from the surface grown crystals to the cooler extreme end of the ampoule.

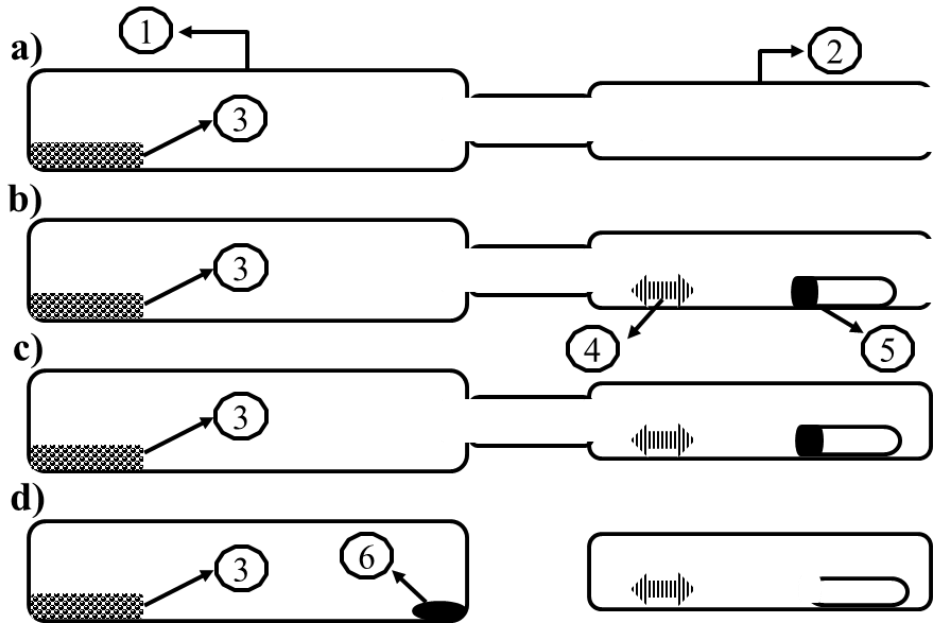

Figure 3.13. Sequence of operation schema to prepare the ampoule to perform the synthesis of the single crystals.1 and 2 are the section 1 and section 2 of the ampoule, respectively; 3 is the initial material; 4 is the magnetic hammer; 5 is the quartz capillary within iodine; and 6 is the iodine transferred.

The growing process of the single crystals can be explained with the following reactions:

1) Initially in the hot zone, the iodine interacts with the starting material and as a consequence the formation of the iodides of copper, zin and tin takes place via the next reaction:

$$Cu_2ZnSnS_{4(bulk)}+2I_{2(gas)} \rightarrow 2CuI_{(gas)}+ ZnI_{(gas)}+SnI_{(gas)}+2S_{2(gas)}$$

2) The constituted iodides were transferred to the crystallization zone (cooler zone) due to the temperature gradient along the ampoule, where the growth of the single crystals occurs:

$$2CuI_{(gas)}+ ZnI_{(gas)}+SnI_{(gas)}+2S_{2(gas)} \rightarrow Cu_2ZnSnS_{4(single\ crystals)}+2I_{2(gas)}$$

3) The released iodine was transferred to the reaction zone and again it was involved in the formation of iodides and the final single crystal growth process.

Similarly, these reactions and single crystals formation happened in the other kesterite structures like $Cu_2ZnSn_yGe_{1-y}S_4$ and $Cu_2ZnSn_yGe_{1-y}Se_4$.

Figure 3.14 shows a picture of different $Cu_2ZnSn_{1-y}Ge_yS_4$ single crystals growth by chemical vapor transport deposition. From this image, it is possible to have an idea about the dimensions of the single crystals comparing with the ruler below them.

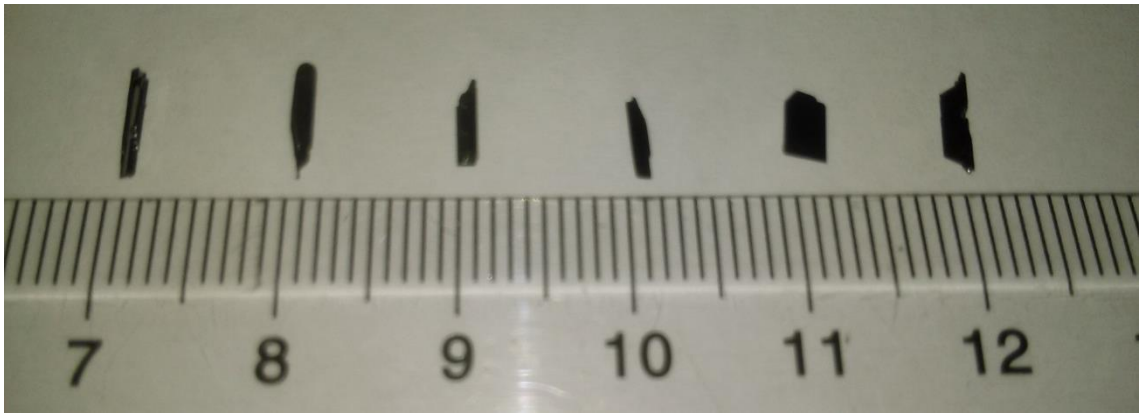

Figure 3.14. $Cu_2ZnSn_{1-y}Ge_yS_4$ single crystals growth by Chemical Vapor Transport deposition. Under there is a ruler as a dimensional reference.

3.2. Composition of bulk compounds

This section presents the chemical composition measurements performed by two independent methods, EDX and WDX. The section is divided in two parts. The first part shows the chemical composition of the sulfur and selenium single crystals synthesized by CVT and the second one presents the chemical composition of the sulfur and selenium polycrystalline compounds synthesized by Bridgman method and solid state reaction.

3.2.1. Single crystals chemical composition

Tables 3.1 and 3.2 show the composition of $Cu_2ZnSn_yGe_{1-y}S_4$ and $Cu_2ZnSn_yGe_{1-y}Se_4$ single crystals respectively as measured by EDX and WDX. The relative error of the concentration values is 1% maximum. In most of the cases, the compositions obtained by EDX and WDX are consistent. In all the cases, the *x*=[Ge/(Ge+Sn)] atomic ratio are similar and they agree with the desired nominal values of the *y* ratio (the *x* atomic ratio is the experimental value of the *y* values present in the chemical formula $Cu_2ZnSn_{1-y}Ge_yS_4$ or $Cu_2ZnSn_{1-y}Ge_ySe_4$). The main deviations between both chemical composition techniques are present in the copper and zinc cations. These differences might be explained due to the different calibration standards used in each specific equipment or the presence of inhomogeneous composition in the sample. In the next section, the *x* ratio will be a key aspect in the following analyses of the structural, optical and vibrational properties.

In Table 3.1, it can be observed that most of the sulfur single crystals show a cooper and zinc rich composition as can be observed in the Cu/(Zn+IV) and Zn/IV ratios, where IV is the sum of Sn and Ge. Ge concentration was varied intentionally to investigate the effect of the Ge addition into the CZTS and CZTSe. The sulfur single crystals show a near stoichiometric composition as can be observed in the S/M ratio.

In Table 3.2, it can be seen that most of the selenium single crystals show a cooper rich and zinc poor composition as can be observed in the Cu/(Zn+IV) and Zn/IV ratios. The selenium single crystals show that they are poor in selenium respects the cations as can be seen in the Se/M ratio.

Table 3.1. Composition of sulfur single crystals measured by EDX and WDX (*Italics*). Note: M= Cu + Zn + Sn + Ge; IV = Sn + Ge

Sample	Cu (at%)	Zn (at%)	Sn (at%)	Ge (at%)	S (at%)	Cu / (Zn+IV)	Zn/IV	x=[Ge/IV]	S/M
Cu_2ZnGeS_4	26.95	11.38	0.00	11.08	50.59	1.20	1.03	1.00	1.02
Cu_2ZnGeS_4	*25.69*	*12.52*	*0.00*	*11.26*	*50.51*	*1.08*	*1.11*	*1.00*	1.02
$Cu_2ZnSn_{0.1}Ge_{0.9}S_4$	24.81	11.78	0.85	9.80	51.32	1.09	1.11	0.92	1.09
$Cu_2ZnSn_{0.3}Ge_{0.7}S_4$	27.18	11.90	3.39	8.48	49.05	1.14	1.00	0.71	0.96
$Cu_2ZnSn_{0.3}Ge_{0.7}S_4$	*25.50*	*12.72*	*3.37*	*7.89*	*50.50*	*1.06*	*1.13*	*0.70*	1.02
$Cu_2ZnSn_{0.5}Ge_{0.5}S_4$	24.62	12.07	5.63	6.77	50.91	1.01	0.97	0.55	1.04
$Cu_2ZnSn_{0.5}Ge_{0.5}S_4$	*25.48*	*12.73*	*6.02*	*5.52*	*50.52*	*1.05*	*1.10*	*0.48*	1.02
$Cu_2ZnSn_{0.7}Ge_{0.3}S_4$	26.49	11.78	9.17	3.55	49.00	1.08	0.93	0.28	0.96
$Cu_2ZnSn_{0.9}Ge_{0.1}S_4$	24.77	13.13	11.29	1.04	49.77	0. 97	1.06	0.08	0.99
Cu_2ZnSnS_4	24.48	12.13	12.71	0.00	50.68	0.98	0.95	0	1.03

Table 3.2. Composition of selenium single crystals measured by EDX and WDX (*Italics*). Note: M= Cu + Zn + Sn + Ge; IV = Sn + Ge

Sample	Cu (at%)	Zn (at%)	Sn (at%)	Ge (at%)	Se (at%)	Cu/ (Zn+IV)	Zn/IV	x=[Ge/IV]	Se/M
$Cu_2ZnGeSe_4$	26.56	12.59	0.00	12.80	48.05	1.05	0.98	1.00	0.92
$Cu_2ZnGeSe_4$	*27.38*	*12.11*	*0.09*	*11.03*	*49.14*	*1.18*	*1.09*	*0.99*	0.97
$Cu_2ZnSn_{0.3}Ge_{0.7}Se_4$	27.16	12.06	3.68	8.93	48.17	1.10	0.96	0.70	0.93
$Cu_2ZnSn_{0.3}Ge_{0.7}Se_4$	*27.13*	*11.95*	*3.57*	*7.93*	*49.16*	*1.16*	*1.04*	*0.69*	0.97
$Cu_2ZnSn_{0.5}Ge_{0.5}Se_4$	27.71	11.65	5.46	6.98	48.20	1.15	0.94	0.56	0.93
$Cu_2ZnSn_{0.7}Ge_{0.3}Se_4$	27.39	11.85	9.10	3.70	47.95	1.11	0.93	0.29	0.92
$Cu_2ZnSn_{0.7}Ge_{0.3}Se_4$	*25.05*	*14.05*	*7.73*	*3.66*	*47.33*	*0.98*	*1.23*	*0.32*	0.94
$Cu_2ZnSnSe_4$	24.90	12.89	14.00	0.00	48.21	0.93	0.92	0.00	0.93

3.2.2. Polycrystalline compounds chemical composition

Table 3.3 and Table 3.4 display the composition of $Cu_2ZnSn_yGe_{1-y}S_4$ and $Cu_2ZnSn_yGe_{1-y}Se_4$ polycrystalline compounds respectively as measured by EDX and WDX. The same behavior as described above for single crystals is observed for polycrystalline compounds; the ratio *x*=[Ge/(Ge+Sn)] measured by EDX and WDX are similar and they agree with the desired nominal values of the *y* ratio. The main deviations between both chemical composition techniques are present in the copper and zinc cations. In the next sections of this chapter, the fundamental properties of these compounds will be analyzed.

In Table 3.3, it can be observed that depending on the measured technique, the samples show copper poor or copper rich composition, as can be seen in the Cu/(Zn+IV) ratio, which means that the copper has a near stoichiometric composition. Moreover, most of the samples show zinc poor composition, as can be observed in the Zn/IV ratios.

In Table 3.4, it can be seen that the most sulfur single crystals show a cooper rich and zinc poor composition, as can be observed in the Cu/(Zn+IV) and Zn/IV ratios.

Furthermore, in both cases, the single crystals show a near stoichiometric composition as can be observed in the S/M and Se/M ratio.

Table 3.3. Composition of sulfur polycrystalline compounds measured by EDX and WDX (*Italics*). Note: M= Cu + Zn + Sn + Ge; IV = Sn + Ge

Sample	Cu (at%)	Zn (at%)	Sn (at%)	Ge (at%)	S (at%)	Cu / (Zn+IV)	Zn/IV	*x*=[Ge/IV]	S/M
Cu_2ZnGeS_4	24.64	12.01	0.00	11.92	51.43	1.01	1.01	1.00	1.06
Cu_2ZnGeS_4	*25.56*	*12.43*	*0.00*	*11.19*	*50.77*	*1.08*	*1.11*	*1.00*	1.03
$Cu_2ZnSn_{0.5}Ge_{0.5}S_4$	24.62	12.08	5.63	6.77	50.90	0.97	0.97	0.55	1.04
$Cu_2ZnSn_{0.5}Ge_{0.5}S_4$	*25.98*	*11.99*	*6.04*	*6.78*	*49.15*	*1.05*	*0.94*	*0.53*	0.97
$Cu_2ZnSn_{0.7}Ge_{0.3}S_4$	25.12	12.27	8.78	3.62	50.21	0.99	0.99	0.29	1.01
Cu_2ZnSnS_4	24.55	11.39	13.38	0.00	50.68	0.85	0.85	0.00	1.03
Cu_2ZnSnS_4	*25.64*	*11.49*	*13.19*	*0.00*	*49.65*	*1.04*	*0.87*	*0.00*	0.99

Table 3.4. Composition of selenium polycrystalline compounds measured by EDX and WDX (*Italics*).
Note: M= Cu + Zn + Sn + Ge; IV = Sn + Ge

Sample	Cu (at%)	Zn (at%)	Sn (at%)	Ge (at%)	Se (at%)	Cu / (Zn+IV)	Zn/IV	x=[Ge/IV]	Se/M
$Cu_2ZnGeSe_4$	26.81	11.62	0.00	12.66	48.91	1.10	0.92	1.00	0.96
$Cu_2ZnGeSe_4$	*24.80*	*15.02*	*0.00*	*10.23*	*49.90*	*0.98*	*1.46*	*1.00*	*1.00*
$Cu_2ZnSn_{0.3}Ge_{0.7}Se_4$	26.57	11.37	4.46	8.80	48.80	1.08	0.86	0.66	0.95
$Cu_2ZnSn_{0.3}Ge_{0.7}Se_4$	*24.87*	*13.01*	*3.25*	*8.44*	*50.41*	*1.01*	*1.11*	*0.72*	*1.02*
$Cu_2ZnSn_{0.5}Ge_{0.5}Se_4$	26.32	11.62	6.70	6.62	48.74	1.06	0.87	0.50	0.95
$Cu_2ZnSn_{0.5}Ge_{0.5}Se_4$	*26.91*	*11.87*	*6.21*	*5.65*	*49.31*	*1.13*	*1.00*	*0.48*	*0.97*
$Cu_2ZnSn_{0.7}Ge_{0.3}Se_4$	26.97	10.96	9.30	3.50	49.27	1.14	0.86	0.27	0.97
$Cu_2ZnSn_{0.7}Ge_{0.3}Se_4$	*26.53*	*12.18*	*9.02*	*3.21*	*49.02*	*1.09*	*1.00*	*0.26*	*0.96*
$Cu_2ZnSnSe_4$	25.66	12.07	12.38	0.00	49.89	1.05	0.97	0.00	1.00
$Cu_2ZnSnSe_4$	*25.76*	*12.59*	*12.63*	*0.00*	*48.96*	*1.02*	*1.00*	*0.00*	*0.96*

Table 3.5 shows the chemical composition measured by EDX of the three different approaches to achieve the CZTS compound presented in section 3.1.1. It can be seen that the approach by binary compounds was unsuccessful. It was not possible to achieve the formation of the CZTS quaternary compound. Instead, it was formed a similar ternary compound to Cu_2SnS_3 from the compositional results. The other two approaches gave a successful formation of the CZTS compound. In both approaches, ZnS was detected as secondary phase, and also, in the ternary and binary compound approach, it was detected Cu_2S. The final compositions of both were Cu-poor and Zn-rich. In spite of the presence of secondary phases, both compounds were used as a source material for the flash and thermal evaporation to obtain absorber thin films, which will be presented in chapter 4.

Table 3.5. Chemical composition of the Cu_2ZnSnS_4 compounds synthesized with different approaches measured by EDX.

CZTS approach	Cu (at%)	Zn (at%)	Sn (at%)	S (at%)	Cu / (Zn+Sn)	Zn/Sn	S/M
From pure elements	23.19	15.89	11.7	49.23	0.84	1.35	0.97
	--	46.69	-	53.31	--	--	--
From binary compounds	29.69	--	19.38	50.94	1.53	--	1.03
From ternary and binary compound	23.57	19.71	10.35	46.37	0.78	1.90	0.87
	61.54	--	--	38.46	--	--	--
	--	44.9	--	51.99	--	--	--

3.3. Structural properties of kesterite compounds

In this section, diffraction measurements by X-rays and neutrons are presented. This section is divided in two parts, first for the single crystals and second for the polycrystalline compounds investigated.

3.3.1. Single crystals X-ray and neutron diffraction measurements

In Figure 3.15 and Figure 3.16, it is presented the X-ray diffraction (XRD) and neutron diffraction (ND) patterns, respectively, of $Cu_2ZnSn_{1-x}Ge_xS_4$ (CZTGS) and $Cu_2ZnSn_{1-x}Ge_xSe_4$ (CZTGSe). In both figures it can be observed how the peaks are shifted to higher angles when the amount of germanium increases. This phenomenon is clearer in the case of the XRD patterns (Figure 3.15) and especially for the main Bragg peak 112. Furthermore, the XRD patterns fit with the Miller indexes of the kesterite structure and the presence of secondary phases was not observed.

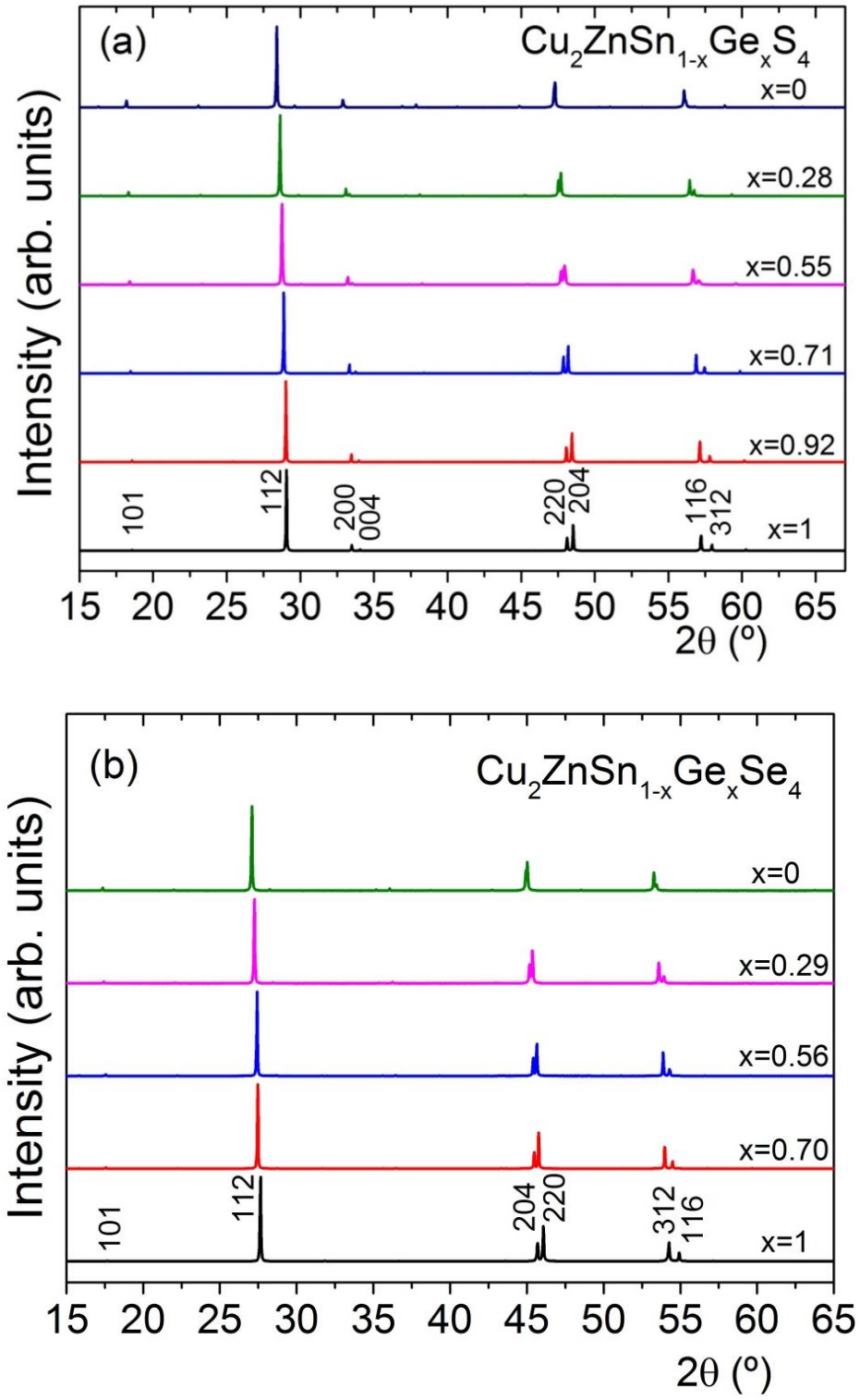

Figure 3.15. X-ray diffraction patterns of CZTGS (a) and CZTGSe (b) single crystals with indication of the Miller indexes of kesterite structure for the most intense peaks.

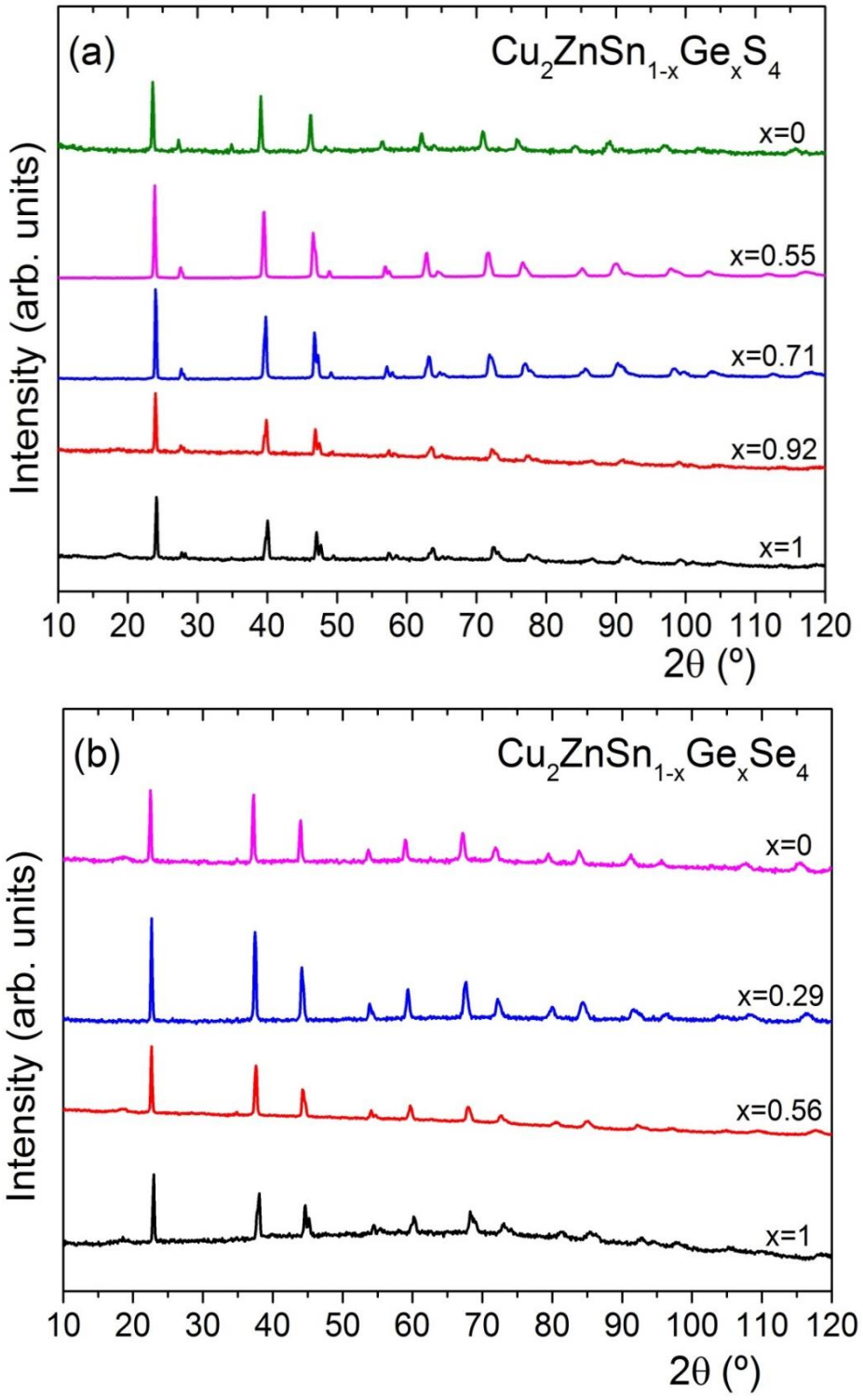

Figure 3.16. Neutron diffraction patterns of CZTGS (a) and CZTGSe (b) single crystals.

3.3.1.1. Simultaneous refinement of single crystals

The Rietveld refinement was done simultaneously with the X-Ray data and Neutron data obtained in D1B at ILL (Grenoble) using the FullProf software. This was done because the amount of powder of these single crystal compounds was small (around 1 gram) which produces higher background in the diffraction patterns than usual. As a consequence, it was used a X-ray diffraction pattern together with a neutron diffraction pattern in the refinement to be able to extract more reliable information. The advantage of this refinements was the high quality of the single crystal samples like high crystallinity and absence of secondary phases. In this way, it was possible to extract valuable structural information combining both data. A couple of examples of simultaneously refinements are shown in Figure 3.17 and Figure 3.18 for one of the sulfur single crystals and other one of the selenium single crystals, respectively.

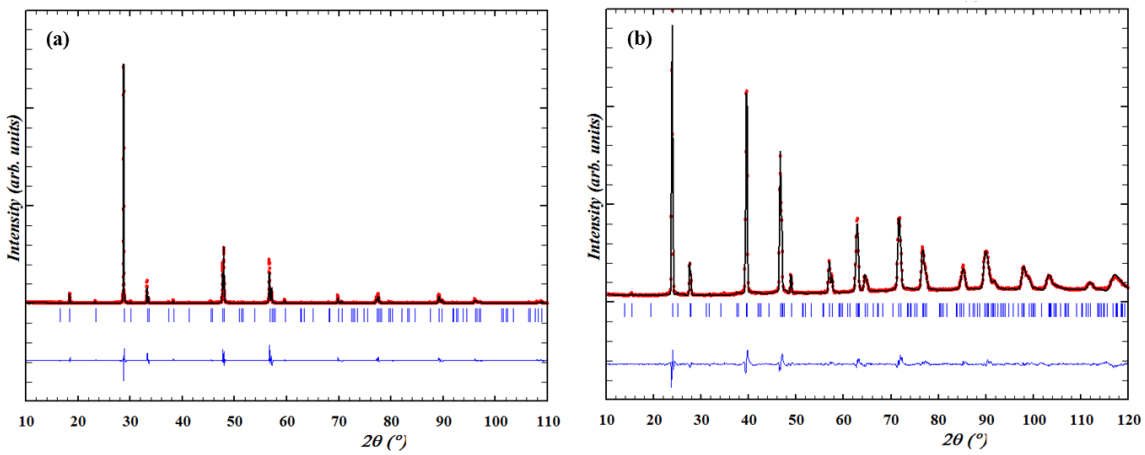

Figure 3.17. Example of the simultaneous Rietveld refinement of the X-Ray pattern (a) and Neutron pattern (b) of the $Cu_2ZnSn_{0.5}Ge_{0.5}S_4$ sample. In red, the observed profile; in black, the calculated profile after the refinement fitting; the blue vertical lines are the theoretical Bragg reflections for the kesterite structure; and the horizontal blue line shows the difference between the observed and calculated profiles.

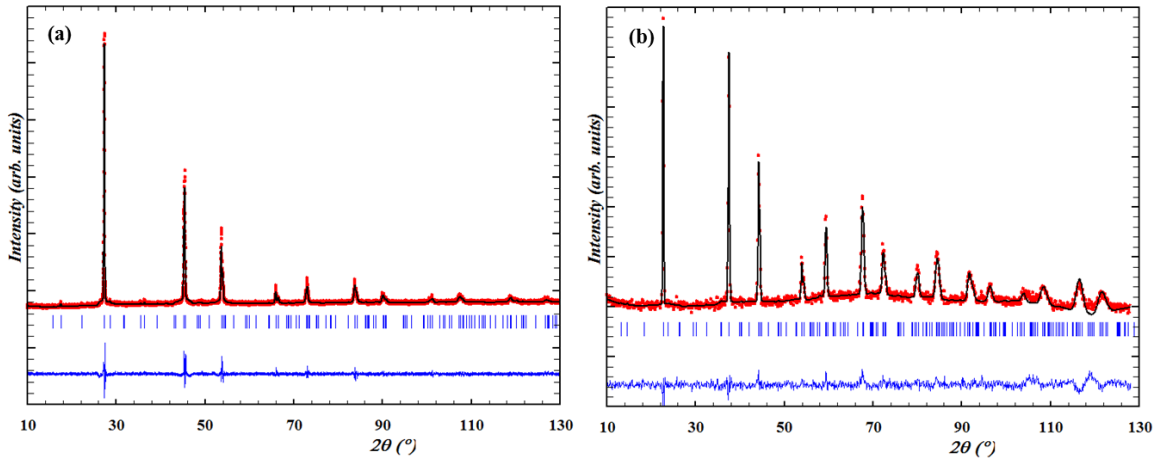

Figure 3.18. Example of the simultaneous Rietveld refinement of the X-Ray pattern (a) and Neutron pattern (b) of the $Cu_2ZnSn_{0.7}Ge_{0.3}Se_4$ sample. In red, the observed profile; in black, the calculated profile after the refinement fitting; the blue vertical lines are the theoretical Bragg reflections for the kesterite structure; and the horizontal blue line shows the difference between the observed and calculated profiles.

The refinement was done with chemical constrains defined by the WDX and EDX chemical composition. As it was mentioned in the introduction, the stannite and kesterite structures are similar, and that was the reason to refine the experimental data also considering the stannite crystal structure and space group I-42m and it was not possible to dismiss this structure because the refinement parameters were not enough different than the ones obtained using the kesterite structure and space group I-4. To conclude about the correct structure after the refinement, the spectroscopic ellipsometry characterization of the same single crystals was taken into account [8], which is also presented in the section 3.4. In [8], it was clear that the band-gap for sulfur single crystals was well defined and fits properly with the kesterite structure. In the case of the selenium single crystals, except $Cu_2ZnGeSe_4$, they also showed the kesterite structure (section 3.4). For these reasons, the final crystal structure considered for all these samples in this work has been the kesterite type structure with space group I-4. In the appendix I, it can be found all the simultaneous refinement patterns and the refined parameters for each sample.

In Table 3.6 and Table 3.7, it is shown the lattice constants (a, c, c/2a) and agreement parameters (R_{Bragg}, χ^2) obtained after the simultaneous refinement of X-ray and neutron diffraction data of CZTGS and CZTGSe single crystals, respectively. The R_{Bragg} factor measures the agreement between the integrated intensities at the Bragg positions calculated from a crystallographic model and those observed and integrated experimentally, and it depends on the fit of the structural parameters. χ^2, also called

goodness of fit, is defined as the ratio between the expected and weighted profile R factors: $\chi^2=(Rwp/Rexp)^2$. The lattice parameters of the Cu_2ZnGeS_4, Cu_2ZnSn_4, $Cu_2ZnGeSe_4$ and $Cu_2ZnSnSe_4$ compounds can be compared with theoretical calculations and experimental data from the literature, as it was presented in the introduction. The lattice parameters of Cu_2ZnSnS_4 and $Cu_2ZnSnSe_4$ obtained by the refinements fit perfectly with the calculated and experimental data of the literature for the kesterite structure [9–11]. In the case of Cu_2ZnGeS_4 and $Cu_2ZnGeSe_4$, there is less information and references of these compounds. As it was mentioned above, it was assigned a space group of the kesterite structure to perform the refinement of the Cu_2ZnGeS_4, while for $Cu_2ZnGeSe_4$ was assigned the space group of the stannite structure. Curiously, if these lattice parameters are compared with the literature, it gives out that the lattice parameters of Cu_2ZnGeS_4 are close to the stannite structure (a= 5.328 Å, c= 10.741 Å (calculated) [12]; a= 5.342 Å, c= 10.540 Å (experimental) [5]), and the ones of $Cu_2ZnGeSe_4$ are close to the kesterite structure (a= 5.602 Å, c= 11.259 Å (calculated); a= 5.606 Å, c= 11.040 Å (experimental) [12]), just the opposite structures and space group assigned for the refinements in this work. These are clear examples that it is very difficult to distinguish between these two structures and at certain point it did not define the final result of the refinements, at least for the lattice parameters.

Table 3.6. Tetragonal lattice constants (a,c), tetragonal distortion (c/2a), agreement parameters (R_{Bragg}, χ^2) for the CZTGS single crystals obtained after simultaneous Rietveld refinement of the neutron and X-ray diffraction data. Note: Standard deviations in last place digits are indicated in brackets. XRD=X-ray diffraction; ND=Neutron diffraction;* means measured by XRD.

Sample	a (Å)	c (Å)	c/2a	R_{Bragg}		χ^2
				ND	XRD	
Cu_2ZnGeS_4	5.34283 (5)	10.51436(13)	0.984(2)	8.50	10.14	2.57
$Cu_2ZnSn_{0.1}Ge_{0.9}S_4$	5.34873(7)	10.5415(16)	0.985(3)	8.69	9.61	2.90
$Cu_2ZnSn_{0.3}Ge_{0.7}S_4$	5.36634(8)	10.59697(19)	0.987(3)	8.26	9.79	3.49
$Cu_2ZnSn_{0.5}Ge_{0.5}S_4$	5.39145(7)	10.66399(24)	0.990(3)	6.40	9.29	7.31
$Cu_2ZnSn_{0.7}Ge_{0.3}S_4$*	5.40219(7)	10.73159(16)	0.993(3)	---	10.84	3.50
Cu_2ZnSnS_4	5.43322(8)	10.83583(21)	0.997(3)	8.84	5.12	1.33

Table 3.7. Tetragonal lattice constants (a,c), tetragonal distortion (c/2a), agreement parameters (RBragg, $\chi 2$) of the CZTGSe single crystals obtained after simultaneous Rietveld refinement of the neutron and X-ray diffraction data. Note: Standard deviations in last place digits are indicated in brackets. XRD=X-ray diffraction; ND=Neutron diffraction.

Sample	a (Å)	c (Å)	c/2a	R_{Bragg}		χ^2
				ND	XRD	
$Cu_2ZnGeSe_4$ ST	5.60845(7)	11.04398(16)	0.985(2)	17.45	6.42	3.03
$Cu_2ZnSn_{0.5}Ge_{0.5}Se_4$	5.64221(8)	11.17333(18)	0.990(3)	7.80	4.52	4.71
$Cu_2ZnSn_{0.7}Ge_{0.3}Se_4$	5.65921(22)	11.22958(62)	0.992(4)	13.29	5.03	1.72
$Cu_2ZnSnSe_4$	5.69558(7)	11.34561(18)	0.996(2)	10.59	5.19	2.40

In Figure 3.19 and Figure 3.20 there are plotted the tetragonal lattice constants a, c and the tetragonal distortion defined as c/2a, presented in Table 3.6 and Table 3.7, respectively. In these figures, it is shown the linear fits of the lattice parameters and the tetragonal distortion. Moreover, in each plot there is the linear function of the fittings. The linear functions for the sulfur single crystals are:

$$a(\text{Å}) = 5.430(1) - 0.089(2)x$$
$$c(\text{Å}) = 10.830(6) - 0.317(9)x$$
$$c/2a = 0.9972(4) - 0.0130(6)x$$

Equation 3-1

Furthermore, the linear functions for the selenium single crystals are:

$$a(\text{Å}) = 5.690(5) - 0.084(8)x$$
$$c(\text{Å}) = 11.33(1) - 0.29(2)x$$
$$c/2a = 0.9960(3) - 0.01129(5)x$$

Equation 3-2

As can be seen in the Equation 3-1 and Equation 3-2 the slopes of the lattice parameters and the tetragonal distortion are very similar between the sulfur and selenium single crystals. In addition, in all the plots there is a linear decrease when tin (Sn) is substituted by germanium (Ge) following the Vegard's law [13]. Indeed, Vegard's law is fulfilled when the atomic ratio *x*=[Ge/(Ge+Sn)] changes. The tetragonal lattice constants decrease

when the amount of germanium increases because the ionic radii of the germanium (53 pm)[14] is smaller than that of the tin (69 pm) [14].

In the case of sulfur single crystals, the parameters to evaluate the quality of the refinements (R_{Bragg} and χ^2) show a similar behavior for all the compounds, with R_{Bragg} around 8 for most of the neutron diffraction data and 10 for the X-ray diffraction data refinements. Selenium single crystals show a R_{Bragg} average of 12.28 and 5.19 from neutron diffraction and X-ray diffraction data, respectively. The higher R_{Bragg} ND values of $Cu_2ZnGeSe_4$ and $Cu_2ZnSnSe_4$ might be due to a high background. The goodness of fit parameter (χ^2) is below 4 for both, sulfur and selenium single crystals. In the case of $Cu_2ZnSn_{0.5}Ge_{0.5}S_4$, which shows a χ^2 over 7, it might be related to the random disorder between Sn and Ge cations, which would be reasonable because it is the intermediate composition. It has been important to combine the X-ray and neutron diffraction data to do the Rietveld refinements because XRD cannot distinguish between the isoelectronic cations Cu^+, Zn^{2+} and Ge^{4+} due to the similar X-ray scattering factors of these cations. On the other hand, neutron diffraction can distinguish between these isolectronic cations because the coherent neutron scattering lengths are enough different (b_{Cu}=7.718(4) fm, b_{Zn}=5.680(5) fm, b_{Ge}=8.185(20) fm [15]). As a consequence, it is possible to use both data (X-ray and neutron) to extract more reliable structural information.

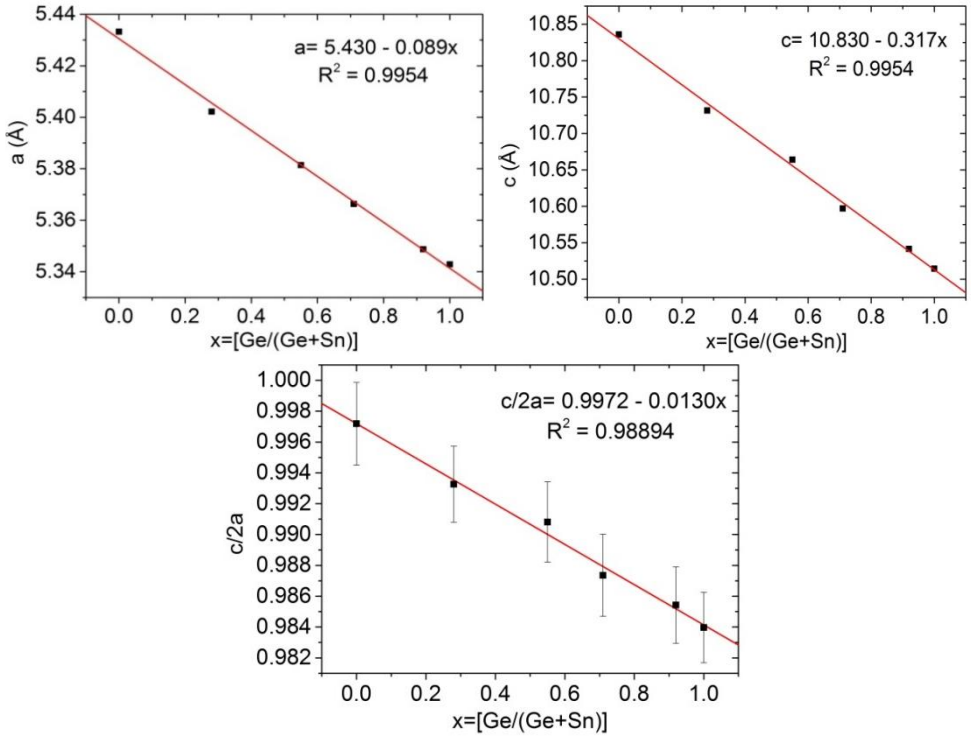

Figure 3.19. Tetragonal lattice constant a, c and tetragonal distortion c/2a of sulfur single crystals. Note: Error bars are included but some of them are not distinguishable in the plots. Linear fittings and R-factors are also included in the plots.

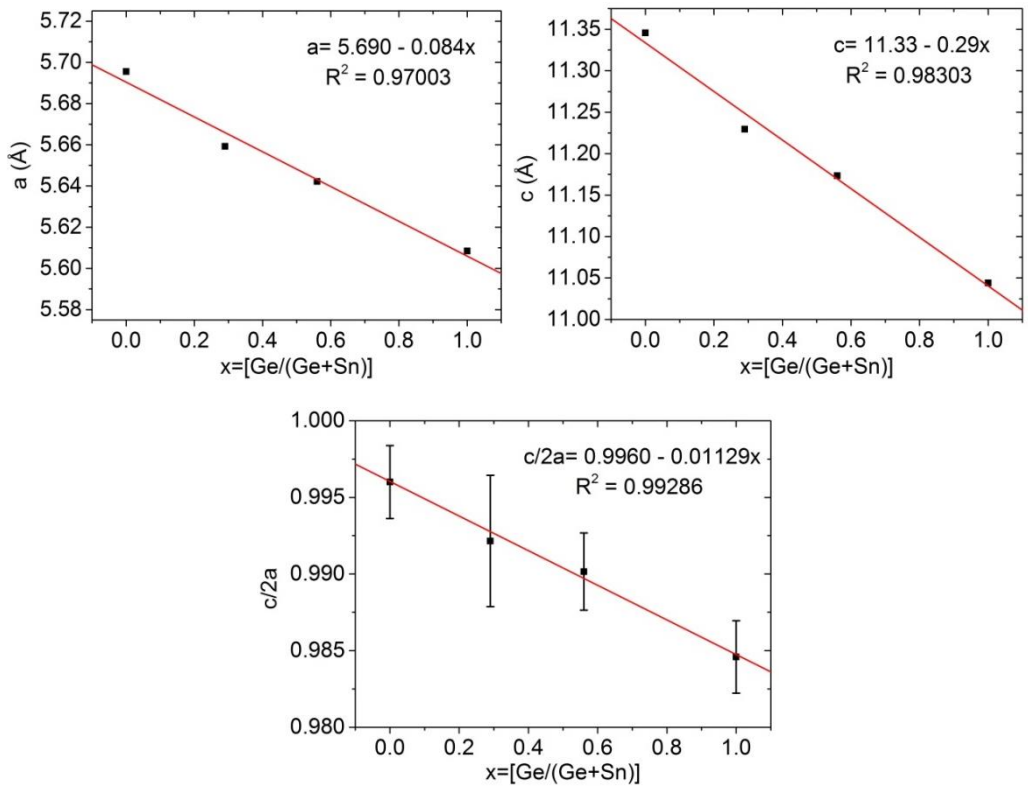

Figure 3.20. Tetragonal lattice constant a, c and tetragonal distortion c/2a of selenium single crystals. Note: Error bars are included but some of them are not distinguishable in the plots. Linear fittings and R-factors are also included in the plots.

Table 3.8 and Table 3.9 present the anion coordinates (X,Y,Z) and the cation-anion distances values plotted versus the *x*=[Ge/(Ge+Sn)] ratio in Figure 3.21 and Figure 3.22 for sulfur and selenium single crystals, respectively. The position of the anion (sulfur) (XYZ) affects directly the cation (Cu,Zn,Sn,Ge) - anion (S) distance. There is not a clear evolution in the cation-anion distances but in the most cases there is a tendency to decrease the distance cation-anion when the amount of germanium increases. This decrease can be observed clearly in the plots of S8i-Ge/Sn2b and Se8i-Ge/Sn2b from Figure 3.21 and Figure 3.22, respectively. This behavior is mainly explained as it is mentioned before, because the ionic radii of the germanium (53 pm) [14] is smaller than the atomic radius of tin (69 pm) [14], which makes possible to reduce the cation-anion distances. Another option could be an ionic hybridization when the germanium replaces the tin atoms and decrease the interatomic distances. This ionic hybridization could be present for the compound with *x*=0.55 and 0.71 where it seems that the anion has a "lateral" translation because there is a tendency that when the anion-cation distance of Ge(2b) and Cu(2c) increases, the anion-cation distance of Zn(2d) and Cu(2a) decreases, and the other way around.

The values extracted for the $Cu_2ZnSn_{0.7}Ge_{0.3}S_4$ sample were obtained only from the Rietveld refinement of the X-ray diffraction data because the amount of powder of this sample was not enough to perform neutron diffraction measurements.

Table 3.8. Anion coordinates (X, Y, Z) and cation-anion distances of the sulfur single crystals obtained from Rietveld refinement of the neutron and X-ray diffraction data. Note: Standard deviations in last place digits are indicated in brackets. Ge2b-S8i is equivalent to Sn2b-S8i; * means measured by XRD.

Sample	X	Y	Z
Cu_2ZnGeS_4	0.26232(47)	0.26574(47)	0.12036(51)
$Cu_2ZnSn_{0.1}Ge_{0.9}S_4$	0.26718(55)	0.26019(55)	0.12017(48)
$Cu_2ZnSn_{0.3}Ge_{0.7}S_4$	0.26197(330)	0.27072(225)	0.12090(60)
$Cu_2ZnSn_{0.5}Ge_{0.5}S_4$	0.26469(131)	0.23646(163)	0.12869(74)
$Cu_2ZnSn_{0.7}Ge_{0.3}S_4$*	0.26556(153)	0.23406(176)	0.12885(43)
Cu_2ZnSnS_4	0.23269(113)	0.25859(132)	0.13173(39)
Sample	**Cu2a-S8i (Å)**	**Cu2c-S8i (Å)**	**Zn2d-S8i (Å)**	**Ge2b-S8i (Å)**
Cu_2ZnGeS_4	2.363(4)	2.321(4)	2.341(4)	2.187(4)
$Cu_2ZnSn_{0.1}Ge_{0.9}S_4$	2.363(4)	2.358(4)	2.315(4)	2.191(4)
$Cu_2ZnSn_{0.3}Ge_{0.7}S_4$	2.394(13)	2.315(12)	2.370(13)	2.187(12)
$Cu_2ZnSn_{0.5}Ge_{0.5}S_4$	2.352(8)	2.390(8)	2.213(8)	2.345(8)
$Cu_2ZnSn_{0.7}Ge_{0.3}S_4$*	2.360(6)	2.411(6)	2.212(6)	2.362(6)
Cu_2ZnSnS_4	2.386(6)	2.227(6)	2.393(7)	2.422(6)

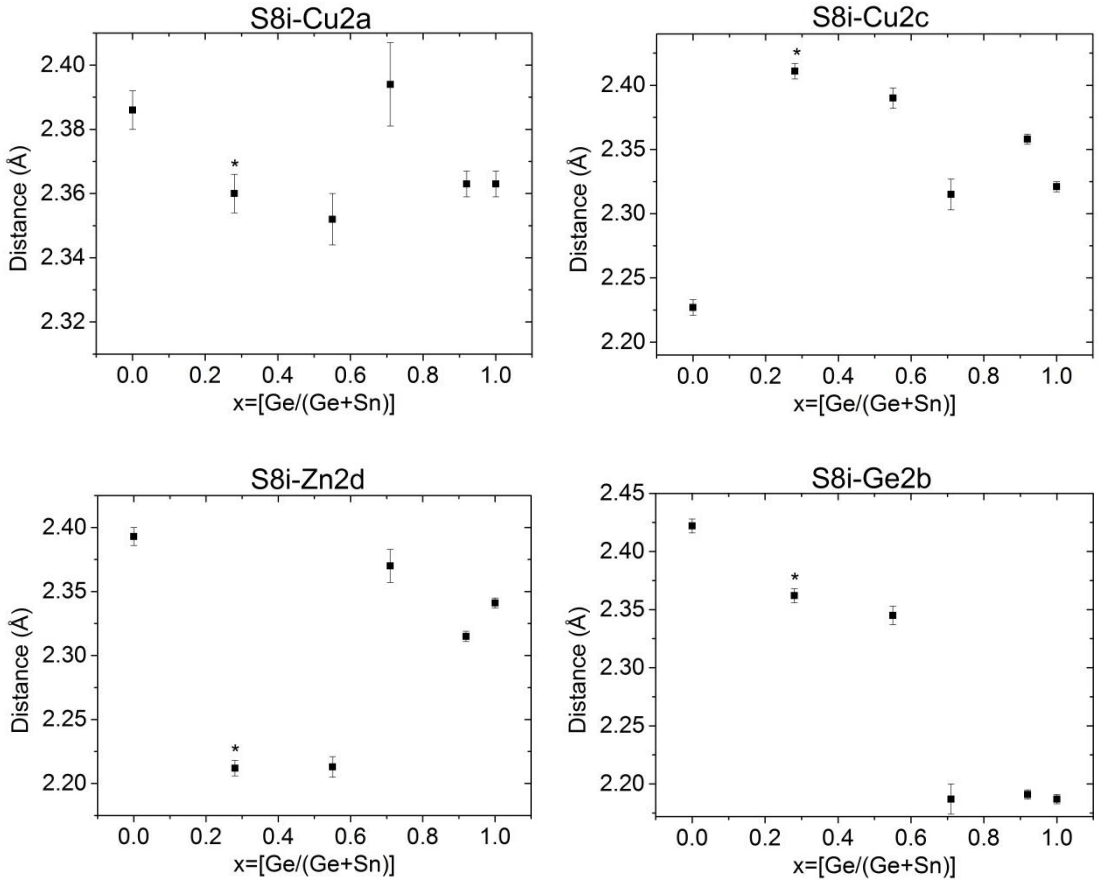

Figure 3.21. Sulfur single crystals cation-anion distance: Cu2a-S8i, Cu2c-S8i, Zn2d-S8i, and Ge2b-S8i. Note: Ge2b-S8i is equivalent to Sn2b-S8i; * means measured by XRD.

Table 3.9. Anion coordinates (X, Y, Z) and cation-anion distances of the selenium single crystals obtained from the simultaneous Rietveld refinement of the neutron and X-ray diffraction data. Note: Standard deviations in last place digits are indicated in brackets. ST=Stannite structure; Ge2b-S8i is equivalent to Sn2b-S8i.

Sample	X	Y	Z
$Cu_2ZnGeSe_4$ ST	0.25744(22)	0.25744(22)	0.12522(35)
$Cu_2ZnSn_{0.5}Ge_{0.5}Se_4$	0.25780(83)	0.24271(72)	0.12677(35)
$Cu_2ZnSn_{0.7}Ge_{0.3}Se_4$	0.25172(204)	0.25730(218)	0.12917(64)
$Cu_2ZnSnSe_4$	0.26614(42)	0.24763(68)	0.13032(19)

Sample	Cu2a-S8i (Å)	Cu2c-S8i (Å)	Zn2d-S8i (Å)	Ge2b-S8i (Å)
$Cu_2ZnGeSe_4$ ST	2.369(3)	2.416(3)	2.416(3)	2.466(3)
$Cu_2ZnSn_{0.5}Ge_{0.5}Se_4$	2.446(5)	2.374(5)	2.474(5)	2.449(5)
$Cu_2ZnSn_{0.7}Ge_{0.3}Se_4$	2.443(10)	2.434(11)	2.401(11)	2.501(11)
$Cu_2ZnSnSe_4$	2.455(3)	2.638(3)	2.491(3)	2.544(3)

Figure 3.22 shows similar behavior but less clear for the compounds with *x*=0.56 and 0.70. It might be explained because in this case the anion is Se instead of S, which should be taken into account. It seems that an ionic hybridization could explain that the anion has a "lateral" translation because there is a tendency that when the anion-cation distance of Ge(2b) and Cu(2c) increases, the anion-cation distance of Zn(2d) and Cu(2a) decreases and the other way around.

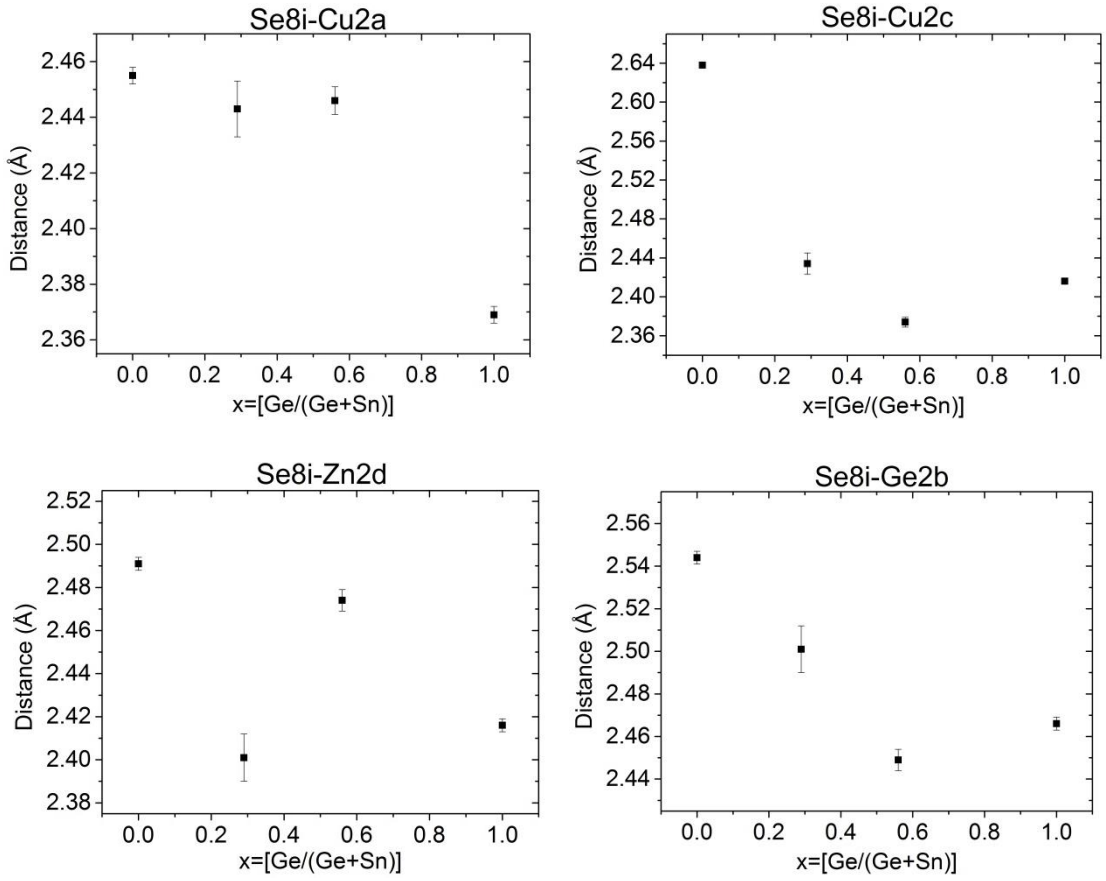

Figure 3.22. Selenium single crystals cation-anion distance: Cu2a-Se8i, Cu2c-Se8i, Zn2d-Se8i, and Ge2b-Se8i. Note: Ge2b-S8i is equivalent to Sn2b-S8i.

Table 3.10 shows the cation substitution reaction and the intrinsic point defects [16,17] obtained because of the chemical composition. In Figure 3.23 it can be seen that, after the compositions shown in Table 3.1, the most sulfur single crystals are in the region F-type [17], but the CZTS sample, which is a mix of A-type and C-type regions. In these regions, the following defects should be present: "$Zn_{Sn,Ge}^{2+} + 2Cu_i^+$" or "$Cu_{Sn,Ge}^{+} + Cu_i^+ + Zn_i^{2+}$" for F-type, "$Zn_{Cu}^{2+} + V_{Cu}$" for A-type, and "$2Cu_{Zn}^{+} + Sn_{Zn}^{4+}$" for C-type. On the other hand, Figure 3.24 shows that selenium single crystals are placed in the A-C, B, D and F regions

after Table 3.2. For B and D-type regions, it should be present the "$2Zn_{Cu}^{2+} + Zn_{Sn,Ge}^{2+}$" "$2Cu_{Zn}^{+} + Cu_{i}^{+}$" defects, respectively. To verify that these defects were present in the samples, it was compared the site occupancy factors (s.o.f.) refinements (Table 3.11 and Table 3.12) to identify qualitatively whether the cation point defects types defined in the Table 3.10 fit with sulfur and selenium single crystals compositional measurements and subsequent Rietveld refinements. For sulfur single crystals (Table 3.11), the F-type (Cu-rich, Zn-rich, (Sn,Ge)-const.) samples show the presence of the antisite defect $Zn_{Sn,Ge}^{2+}$ in all the samples, and in some of them it appears an excess of copper which matches with the presence of the interstitial defect $2Cu_{i}^{+}$. Both defects combined are the fingerprint of the defects in the F-type region. Continuing with the sulfur single crystals, in the case of A, C-type (A=Cu-poor, Zn-rich, (Sn,Ge)-const; C= Cu-rich, Zn-poor, (Sn,Ge)-rich) samples, it appears a defect of Cu which might be related with the vacancy defect V_{Cu}, and/or the antisite defect Zn_{Cu}^{2+}. These two defects are related with the A-type region, so it is possible to discard the presence of C-type defects related. These correlation of the theoretical defect prediction [16,17] (Table 3.11) with the composition of the samples have been also confirmed in the case of selenium single crystals as it can be observed in Table 3.12.

Table 3.10. Cation substitution reactions and their intrinsic point defects corresponding with the chemical composition [16,17].

Type	Composition	Cation substitution reaction	Intrinsic point defects
A	Cu-poor/Zn-rich/(Sn,Ge)-const.	$2Cu^{+} \rightarrow Zn^{2+}$	$Zn_{Cu}^{2+}+V_{Cu}$
B	Cu-poor/Zn-rich/(Sn,Ge)-poor	$2Cu^{+}+Sn^{4+} \rightarrow 3Zn^{2+}$	$2Zn_{Cu}^{2+} + Zn_{Sn,Ge}^{2+}$
C	Cu-rich/Zn-poor/(Sn,Ge)-rich	$3Zn^{2+} \rightarrow 2Cu^{+}+Sn^{4+}$	$2Cu_{Zn}^{+}+Sn_{Zn}^{4+}$
D	Cu-rich/Zn-poor/(Sn,Ge)-const.	$Zn^{2+} \rightarrow 2Cu^{+}$	$Cu_{Zn}^{+} + Cu_{i}^{+}$
F	Cu-rich/Zn-rich/(Sn,Ge)-const.	$Sn^{4+} \rightarrow Zn^{2+}+2Cu^{+}$	$Zn_{Sn,Ge}^{2+} + 2Cu_{i}^{+}$ or $Cu_{Sn,Ge}^{+} + Cu_{i}^{+} + Zn_{i}^{2+}$

Comparing Tables 3.11 and 3.12 and considering the last column with the occupation factors of the observed defects, the amount of them present in the sulfur single crystals is higher, in some cases one order of magnitude, than the ones present in the selenium single

crystals. The quality parameters of the refinements (R_{Bragg} and χ^2) were kept without any remarkable change when the intrinsic point defects were introduced in the analysis.

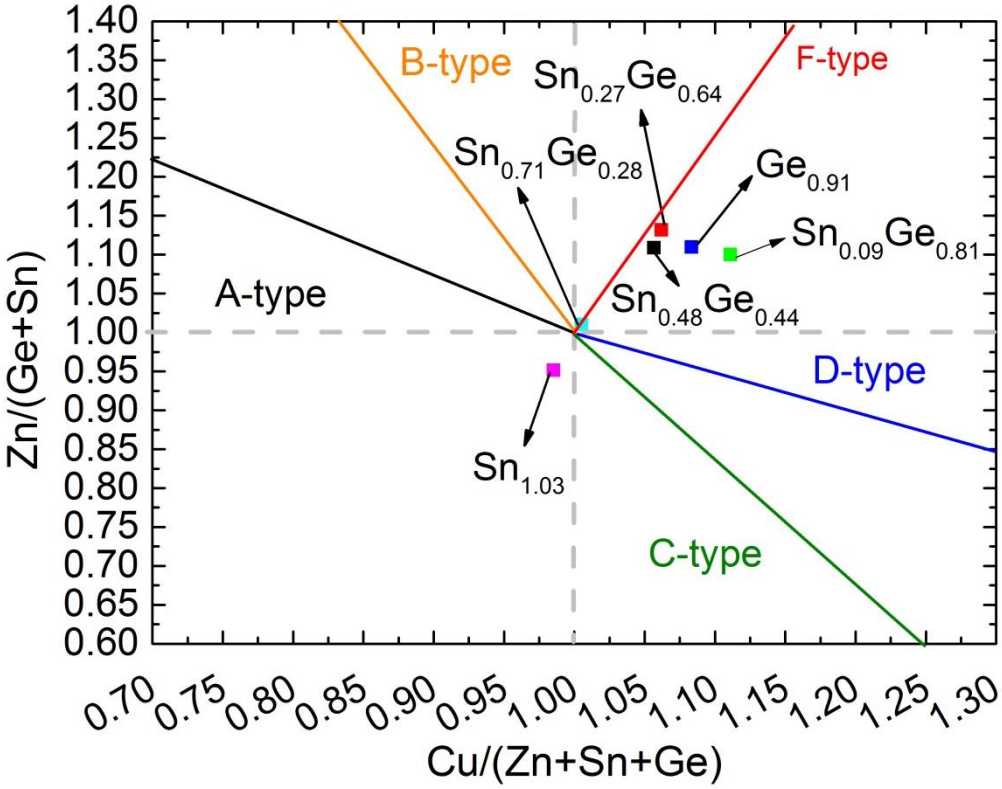

Figure 3.23. Cation ratio plot Cu/(Zn+Ge+Sn) vs. Zn/(Ge+Sn) showing the different chemical composition of the sulfur single crystals and their types A to F [17].

Table 3.11. Site occupancy factors (s.o.f.) by cations obtained from Rietveld refinement of cation position of sulfur single crystals following the most lightly defect presented in Table 3.10.

	Sample	Cu 2a s.o.f.	Cu 2c s.o.f.	Zn 2d s.o.f.	Sn 2b s.o.f.	Ge 2b s.o.f.	$Zn^{2+}_{Sn,Ge}$
F-Type	$Cu_{2.08}Zn_{1.01}Ge_{0.91}S_4$	1.00000	1.05146	0.90603	---	0.94268	0.06384
	$Cu_{2.10}Zn_{1.00}Sn_{0.09}Ge_{0.81}S_4$	1.00000	1.00000	1.12001	0.10634	0.82634	0.02634
	$Cu_{2.06}Zn_{1.03}Sn_{0.27}Ge_{0.64}S_4$	1.03462	1.00000	1.12356	0.29490	0.66490	0.03490
	$Cu_{2.05}Zn_{1.02}Sn_{0.48}Ge_{0.44}S_4$	1.00000	1.00000	1.00158	0.49860	0.45860	0.02860
A,C-Type	Sample	Cu 2a s.o.f.	Cu 2c s.o.f.	Zn 2d s.o.f.	Sn 2b s.o.f.	Ge 2b s.o.f.	Zn^{2+}_{Cu}
	$Cu_{1.98}Zn_{0.98}Sn_{1.03}S_4$	0.91540	0.86827	0.95879	0.93126	---	0.02236

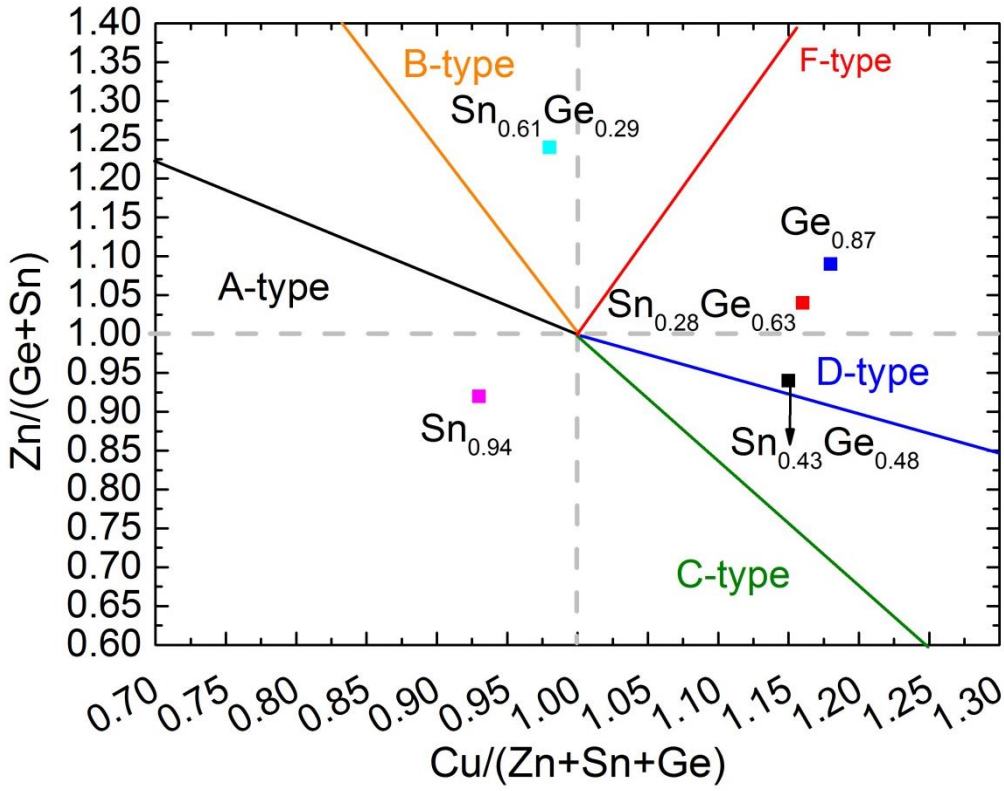

Figure 3.24. Cation ratio plot Cu/(Zn+Ge+Sn) vs. Zn/(Ge+Sn) showing the different chemical composition of the selenium single crystals and their types A to F [17].

Table 3.12. Site occupancy factors (s.o.f.) by cations obtained from simultaneous Rietveld refinement of cation position of the selenium single crystals following the most lightly defect presented in Table 3.10.

D-Type	**Sample**	**Cu 2a s.o.f.**	**Cu 2c s.o.f.**	**Zn 2d s.o.f.**	**Sn 2b s.o.f.**	**Ge 2b s.o.f.**	Cu^{+}_{Zn}	
		1.03258	0.98514	1.02855	--	0.86547	0.00547	
F-Type		**Cu 2a s.o.f.**	**Cu 2c s.o.f.**	**Zn 2d s.o.f.**	**Sn 2b s.o.f.**	**Ge 2b s.o.f.**	$Cu^{2+}_{Sn,Ge}$	
	$Cu_{2.16}Zn_{0.96}Ge_{0.87}Se_4$	1.03711	0.98523	1.00837	--	0.87000	0.01959	
D-Type	**Sample**	**Cu 2a s.o.f.**	**Cu 2c s.o.f.**	**Zn 2d s.o.f.**	**Sn 2b s.o.f.**	**Ge 2b s.o.f.**	Cu^{+}_{Zn}	
	$Cu_{2.19}Zn_{0.90}Sn_{0.43}Ge_{0.48}Se_4$	1.00000	0.97189	0.90606	0.43000	0.48000	0.01110	
B-Type	**Sample**	**Cu 2a s.o.f.**	**Cu 2c s.o.f.**	**Zn 2d s.o.f.**	**Sn 2b s.o.f.**	**Ge 2b s.o.f.**	Zn^{2+}_{Cu}	$Zn^{2+}_{Sn,Ge}$
	$Cu_{1.09}Zn_{1.12}Sn_{0.61}Ge_{0.29}Se_4$	1.00000	0.97265	1.00466	0.60983	0.2893	0.00265	0.00983
C-Type	**Sample**	**Cu 2a s.o.f.**	**Cu 2c s.o.f.**	**Zn 2d s.o.f.**	**Sn 2b s.o.f.**	**Ge 2b s.o.f.**	Zn^{2+}_{Cu}	
	$Cu_{2.00}Zn_{1.06}Sn_{0.94}Se_4$	0.94717	0.92863	0.96571	0.94000	--	0.00675	

In summary, it has been shown how the theoretical defect prediction [16,17] (Table 3.11) match with the site occupancy refinements performed and the compositions measured by WDX and/or EDX. For the sulfur single crystals, the A,C-type mixture has been determined by the chemical composition measurements while the presence of Zn_{Cu}^{2+} and $Zn_{Sn,Ge}^{2+}$ defects was obtained by the refinements. This means that the sample that shows the A,C-type mixture is mostly A-type because C-type defects were not found.. For some of the selenium single crystals, the B-type sample was found, consistent with the observed presence of Zn_{Cu}^{2+} and $Zn_{Sn,Ge}^{2+}$ defects; in some other samples, C-type and D-type regions have been found, with the presence of Zn_{Cu}^{2+} and Cu_{Zn}^{+} defects, respectively. In the case of the $Cu_2ZnGeSe_4$, it appears to be a mixture of F and D-type regions and two defects were found, Cu_{Zn}^{+} and $Cu_{Sn,Ge}^{2+}$, respectively, but the amount of $Cu_{Sn,Ge}^{2+}$ defects was one order of magnitude higher than the amount of Cu_{Zn}^{2+} defects, and therefore it could be concluded that this sample is mostly D-type.

3.3.2. Cu_2ZnSnS_4 polycrystalline compounds synthesized with different approaches

Figure 3.25 shows the X-ray diffraction patterns of the Cu_2ZnSnS_4 polycrystalline compounds synthesized with three different approaches. In the pure elements approach, the characteristic Miller indexes of the kesterite structure are indicated. Moreover, there are indicated the secondary phase peaks of ZnS and Cu_2SnS_3 with Δ and α, respectively. In most of the cases these secondary phases overlap with the kesterite peaks. Here, they are included in the plot because they were detected by EDX and due to the increment on the broadening of the peaks overlapped. Despite EDX measurements did not detect the presence of kesterite phase in the binary approach alloy, in the XRD pattern it appears the kesterite peaks plus Cu_2SnS_3 secondary phases. Most of the Cu_2SnS_3 peaks overlap with the kesterite peaks but a couple of peaks were detected and assigned to this compound at around $2\theta=31^o$ and 42^o. In the ternary and binary approaches, it was not possible to identify the Cu_2S peaks detected by EDX. The Σ letter indicates the aluminum peaks from the aluminum holder used to perform the XRD measurement. To avoid the presence of these peaks, all the rest of the XRD measurements were performed on carbon holders, which have no peak reflections.

Through the inhomogeneity of these samples and the presence of secondary phases, these powders were not further characterized and they were used as a source material to make absorber thin films (chapter 4).

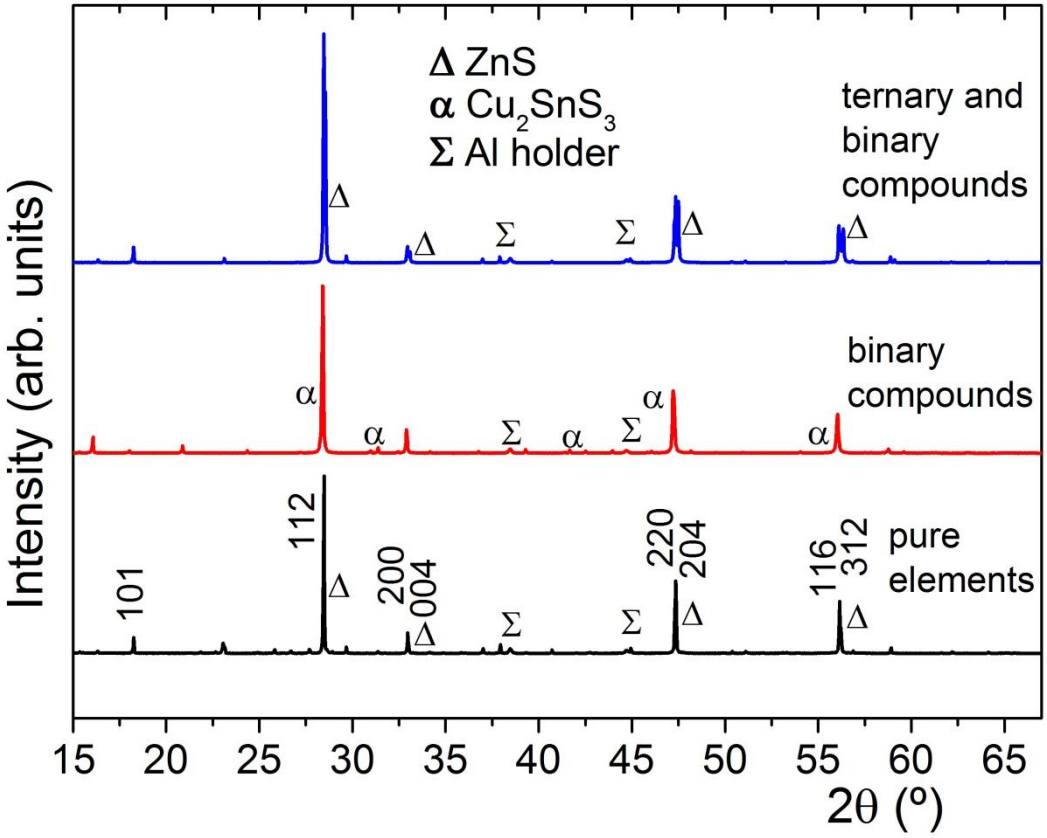

Figure 3.25. X-ray diffraction patterns of Cu_2ZnSnS_4 polycrystalline compounds synthesized with different approaches with indication of the Miller indexes for the most intense peaks of the kesterite structure. Note: the Greeks letters Δ, α, Σ indicates the ZnS, Cu_2SnS_3secondary phase peaks and the Aluminum peaks due to the holder, respectively.

3.3.3. $Cu_2ZnSn_yGe_{1-y}S_4$ and $Cu_2ZnSn_yGe_{1-y}Se_4$ polycrystalline compounds X-ray and Neutron Diffraction measurements

Figure 3.26 shows the X-ray diffraction patterns of sulfur (a) and selenium (b) compounds. In the diffraction pattern of Cu_2ZnGeS_4, several extra peaks appear related with undesired secondary phases. For this reason, the CZGS sample was discarded in the neutron diffraction measurements. In Figure 3.27 the Neutron diffractograms of CZTGS (a) and CZTGSe (b) compounds are plotted. The polycrystalline compounds show less crystallinity and homogeneity in composition than the single crystals and the presence of Zn(S,Se) secondary phases, which will be discussed below. In the case of the

polycrystalline compounds, the amount of the powders was much higher (more than 3 grams) than in the case of single crystals (around 1 gram). This fact made feasible to perform the refinements with only the neutron diffraction data because the higher amount of the powders gave clear peaks with less background, which can be clearly observed at the higher angles when compared the single crystals (Figure 3.16, Figure 3.17, Figure 3.18) with the polycrystalline (Figure 3.27, Figure 3.28) neutron diffraction patterns. As a consequence, it was not necessary to perform simultaneous refinements with X-ray and neutron data to extract reliable structural information. For this reasons, the Rietveld refinement was done only on the Neutron data obtained at HZB.

In Figure 3.26 and Figure 3.27 it can be observed how the peaks are shifted to higher angles when the amount of germanium increases. This phenomenon is clearer in the case of the XRD patterns (Figure 3.26) and especially for the main peak 112, as observed for the single crystals. In the Cu_2ZnGeS_4 pattern, it was detected several extra peaks not related to the kesterite structure. This fact was fundamental to discard this compound for neutron measurements. Since the neutron beam time was limited, it was used for other compounds that presented better X-ray patterns.

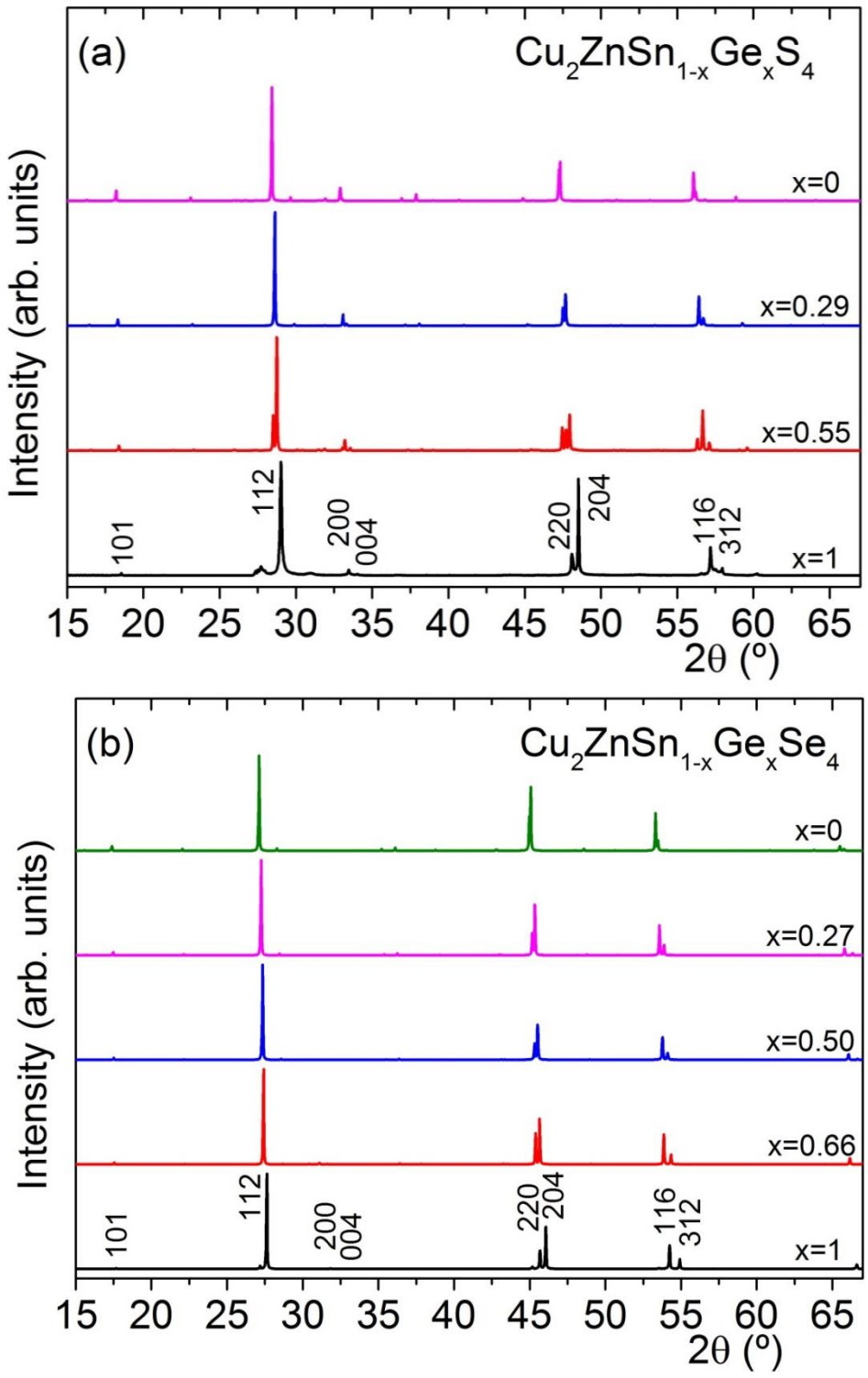

Figure 3.26. X-ray diffraction patterns of CZTGS (a) and CZTGSe (b) polycrystalline compounds with indication of the Miller indexes of kesterite structure for the most intense peaks.

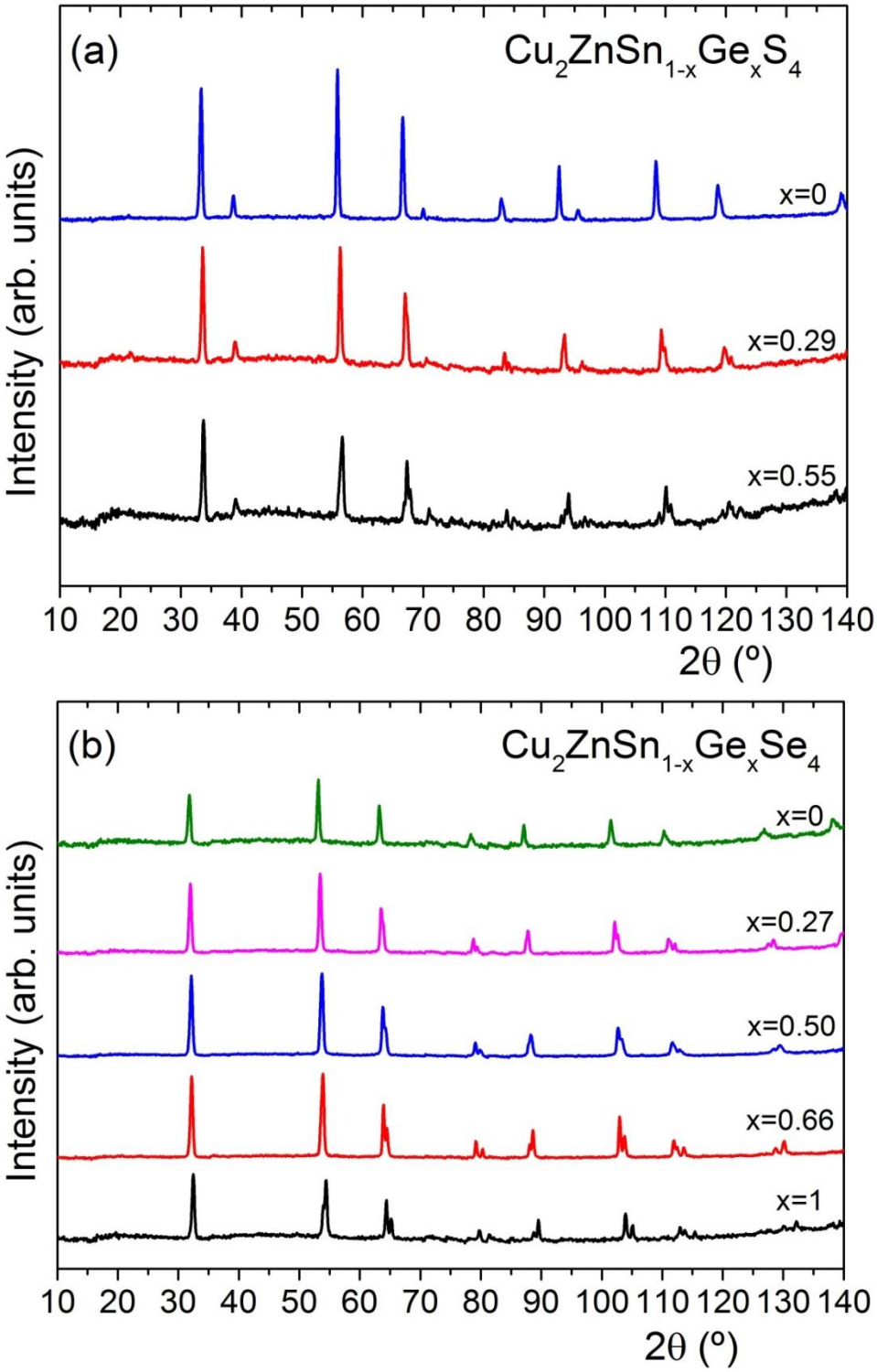

Figure 3.27. Neutron diffraction patterns of CZTGS (a) and CZTGSe (b) polycrystalline compounds.

Figure 3.28 is an example of the refined neutron patterns of Cu_2ZnSnS_4 (a) $Cu_2ZnSn_{0.3}Ge_{0.7}S_4$ (b) with the kesterite and Zn(S,Se) phases.

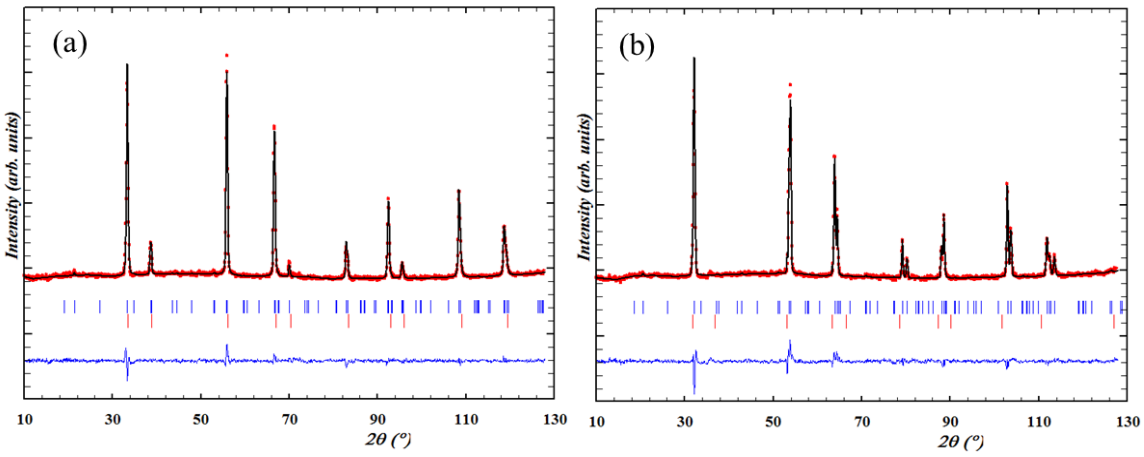

Figure 3.28. Examples of neutron patterns refined of polycrystalline compounds by Rietveld method, Cu_2ZnSnS_4 (a) and $Cu_2ZnSn_{0.3}Ge_{0.7}Se_4$ (b). In red is the data acquisition, in black the refinement fitting, the blue vertical lines are the theoretical Bragg reflections for the kesterite structure, the red vertical lines are the theoretical Bragg reflections of Zn(S,Se) secondary phases and the horizontal blue line is the difference between the data acquisition and refinement fitting.

3.3.3.1. Refinement of $Cu_2ZnSn_yGe_{1-y}S_4$ and $Cu_2ZnSn_yGe_{1-y}Se_4$ polycrystalline compounds

From these refinements, the cell parameters were extracted for the sulfur compounds (Table 3.13) and selenium compounds (Table 3.14), as well as the agreement parameters (R_{Bragg} and χ^2). In both cases, most of the compounds were refined considering two phases, kesterite (KS) and Zn(S,Se), except the $Cu_2ZnSn_{0.7}Ge_{0.3}S_4$ and $Cu_2ZnGeSe_4$. The Rietveld refinement and the agreement parameter improved sensitively in the moment that the secondary phases (Zn(S,Se)) were included in the refinement. In the most of sulfur and selenium polycrystalline compounds, the goodness of fit parameter (χ^2) are below 2. Also, the R_{Bragg} agreement parameter ranges from 4 to 14, which gives an idea about the inhomogeneity of the polycrystalline compounds. The R_{Bragg} of the single crystals showed less divergence due to the higher homogeneity and crystallinity of these compounds compared to the polycrystalline compounds. All the parameters and patterns related to these refinments are presented in the Appendix I.

Figure 3.29 and Figure 3.30 show the lattice constants (a,c) and tetragonal distortion (c/2a) of the sulfur and selenium polycrystalline compounds, respectively. Following is

the linear function of the lattice constants and tetragonal distortion fittings for the sulfur polycrystalline compounds:

$$a(\text{Å}) = 5.4320(8) - 0.091(2)x$$
$$c(\text{Å}) = 10.830(1) - 0.314(3)x$$
$$c/2a = 0.99686(4) - 0.0122(1)x$$

Equation 3-3

These values obtained in these fitting are very close to the ones presented in the sulfur single crystals (see Equation 3-1). Also, these similarities are present in the selenium single crystals (see Equation 3-2) and the selenium polycrystalline compounds as can be seen in the next fittings:

$$a(\text{Å}) = 5.695(3) - 0.085(5)x$$
$$c(\text{Å}) = 11.351(8) - 0.30(1)x$$
$$c/2a = 0.9967(5) - 0.0116(8)x$$

Equation 3-4

Furthermore, all the plots follow a linear decrease when the tin (Sn) is substituted by germanium (Ge) following the Vegard's law [13]. These behaviors are analogue to the single crystal samples and it is due to the same reasoning, the lattice constants decrease when the amount of germanium increase because the ionic radii of the germanium (53 pm) [14] is smaller than the atomic radius of tin (69 pm) [14]. All the refined parameters and the neutron diffraction patterns are presented in Appendix I.

Table 3.13. Tetragonal lattice constants (a,c), tetragonal distortion (c/2a), refinement parameters (R_{Bragg}, χ^2) of the sulfur polycrystalline compounds obtained from Rietveld refinement of the Neutron diffraction data.

Note: Standard deviations in last place digits are indicated in brackets. KS=Kesterite structure; SF=Secondary phase (ZnS); ND=Neutron diffraction.

Sample	a (Å)	c (Å)	c/2a	R_{Bragg}		χ^2
				KS	SF	
$Cu_2ZnSn_{0.5}Ge_{0.5}S_4$	5.38244(18)	10.65808(56)	0.997(3)	13.55	9.62	1.58
$Cu_2ZnSn_{0.7}Ge_{0.3}S_4$	5.40493(12)	10.73787(38)	0.993(3)	9.17	--	1.86
Cu_2ZnSnS_4	5.432390(9)	10.83048(34)	0.997(3)	4.76	4.04	1.85

Table 3.14. Tetragonal lattice constants (a,c), tetragonal distortion (c/2a), refinement parameters (R_{Bragg}, χ^2) of the selenium polycrystalline compounds obtained from Rietveld refinement of the neutron diffraction data. Note: Standard deviations in last place digits are indicated in brackets. KS=Kesterite structure; SF=Secondary phase (ZnSe); ND=Neutron diffraction.

Sample	a (Å)	c (Å)	c/2a	R_{Bragg}		χ^2
				KS	SF	
$Cu_2ZnGeSe_4$	5.60899(15)	11.04369(45)	0. 984(4)	10.29	--	1.65
$Cu_2ZnSn_{0.3}Ge_{0.7}Se_4$	5.64122(9)	11.1571(24)	0.989(3)	9.28	21.15	2.65
$Cu_2ZnSn_{0.5}Ge_{0.5}Se_4$	5.64813(13)	11.19741(41)	0.991(3)	7.91	7.68	3.47
$Cu_2ZnSn_{0.7}Ge_{0.3}Se_4$	5.66936(10)	11.25967(36)	0.993(3)	13.29	5.03	1.72
$Cu_2ZnSnSe_4$	5.69598(26)	11.35021(96)	0.996(5)	14.27	12.09	1.43

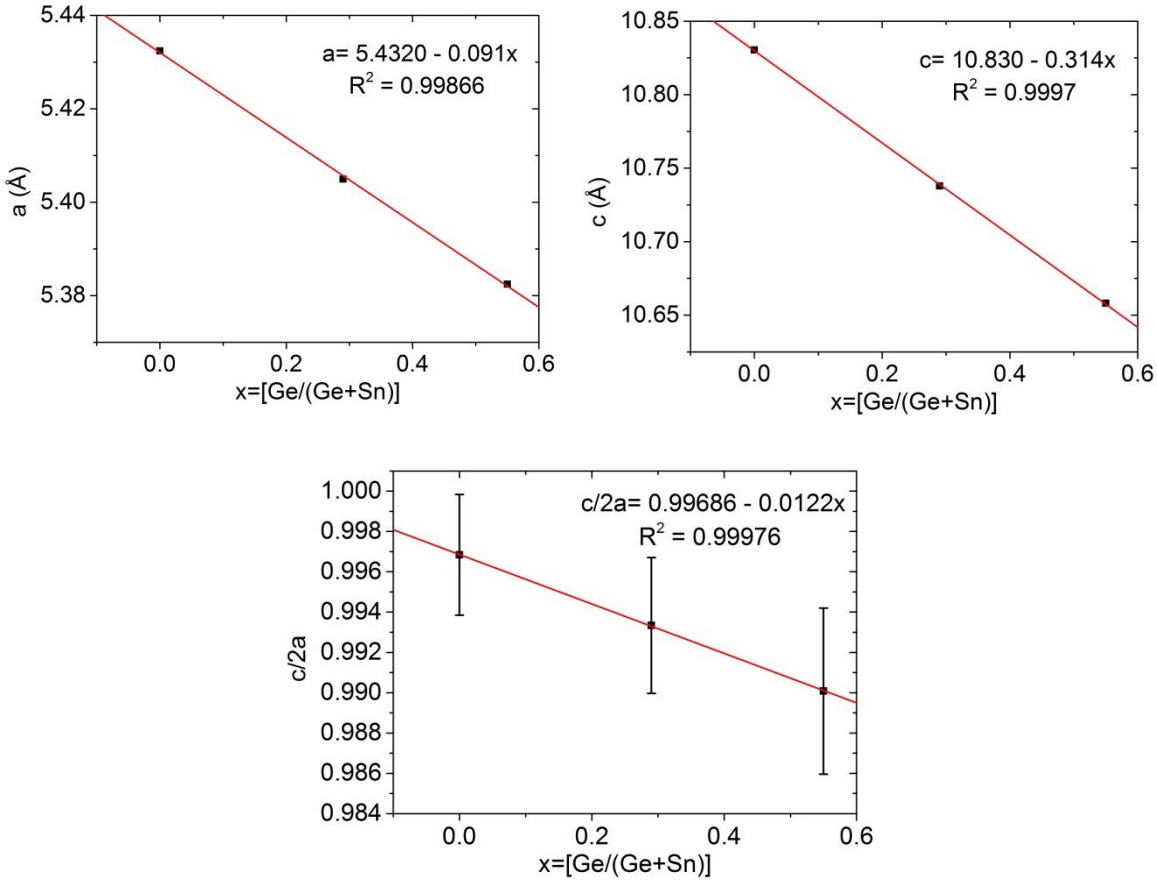

Figure 3.29. Tetragonal lattice constant a, c and tetragonal distortion c/2a of sulfur polycrystalline compounds. Note: Error bars are included but some of them are not distinguishable in the plots. Linear fittings and R-factors are also included in the plots.

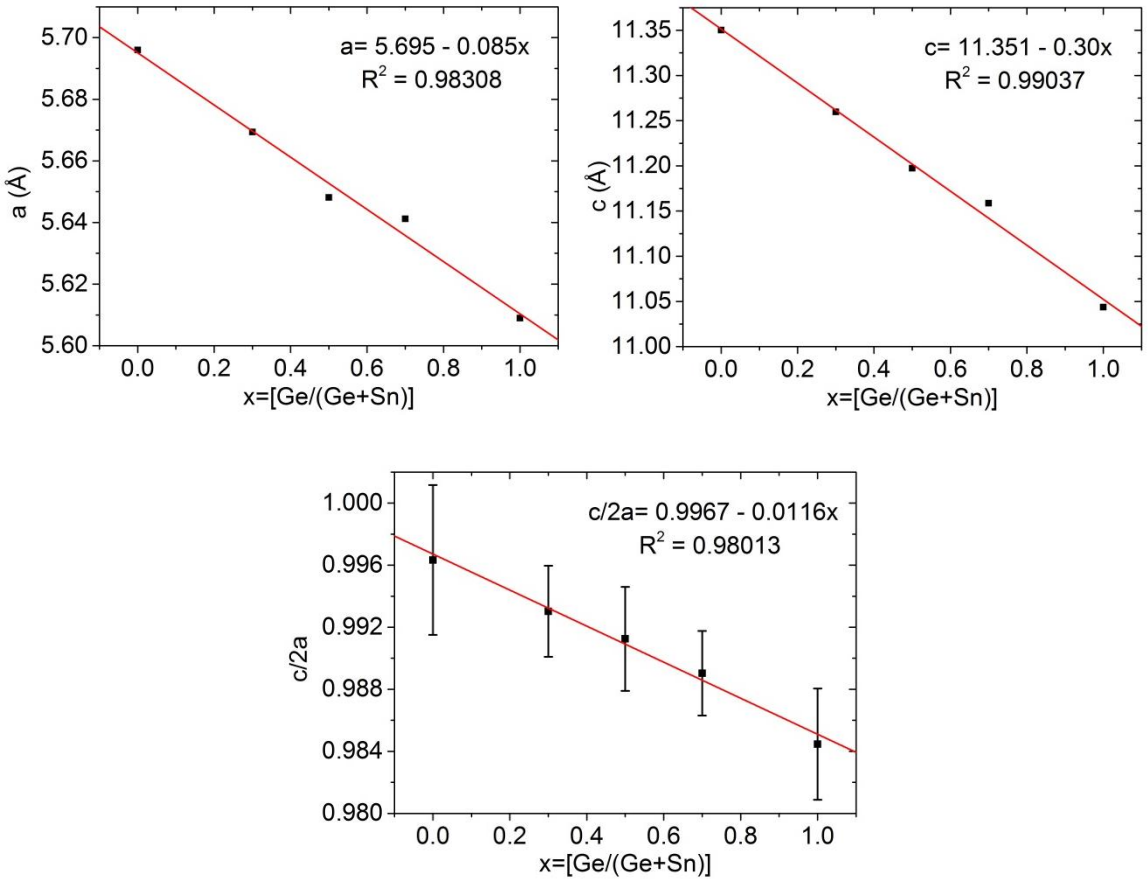

Figure 3.30. Tetragonal lattice constant a, c and tetragonal distortion c/2a of selenium polycrystalline compounds. Note: Error bars are included but some of them are not distinguishable in the plots. Linear fittings and R-factors are also included in the plots.

Table 3.15 and Table 3.16 present the anion coordinates (X,Y,Z) and the cation-anion distances values plotted versus the *x*=[Ge/(Ge+Sn)] ratio in Figure 3.21 and Figure 3.22 for sulfur and selenium single crystals, respectively. As it was mentioned for sulfur single crystals, there is not a clear evolution in the cation-anion distances but it seems there is a tendency to decrease the distance cation-anion when the amount of germanium increases. This decrease is clearly observed in the plots of the anion-germanium distances (see Figure 3.21 and Figure 3.32). The reason of this behavior is attributed to the difference in the germanium and tin ionic radii (53 pm and 69 pm [14], respectively), which makes likely the reduction of the cation-anion distances. Another option mentioned above, it could be the ionic hybridization in the moment that germanium is changed for tin atoms and decrease the interatomic distances. Similar behavior is present for sulfur polycrystalline and single crystals, it seems that the anion has a "lateral" translation. There is a tendency that when the sulfur-cation distance of Ge(2b) and Cu(2a) increase the sulfur-cation distance of Zn(2d) and Cu(2c) decrease and contrariwise.

Table 3.15. Anion coordinates (X, Y, Z) and cation-anion distances of the sulfur polycrystalline obtained from Rietveld refinement of the neutron and X-ray diffraction data. Note: Standard deviations in last place digits are indicated in brackets. Ge2b-S8i is equivalent to Sn2b-S8i.

Sample	X	Y	Z
$Cu_2ZnSn_{0.5}Ge_{0.5}S_4$	0.24098(1318)	0.23988(1440)	0.12142(730)
$Cu_2ZnSn_{0.7}Ge_{0.3}S_4$	0.24481(980)	0.27450(787)	0.11397(545)
Cu_2ZnSnS_4	0.24252(400)	0.24562(400)	0.12803(258)

Sample	Cu2a-S8i (Å)	Cu2c-S8i (Å)	Zn2d-S8i (Å)	Ge2b-S8i (Å)
$Cu_2ZnSn_{0.5}Ge_{0.5}S_4$	2.24(8)	2.35(8)	2.35(8)	2.36(8)
$Cu_2ZnSn_{0.7}Ge_{0.3}S_4$	2.24461(4)	2.36491(4)	2.40605(4)	2.33131(4)
Cu_2ZnSnS_4	2.33(3)	2.32(3)	2.34(4)	2.40(3)

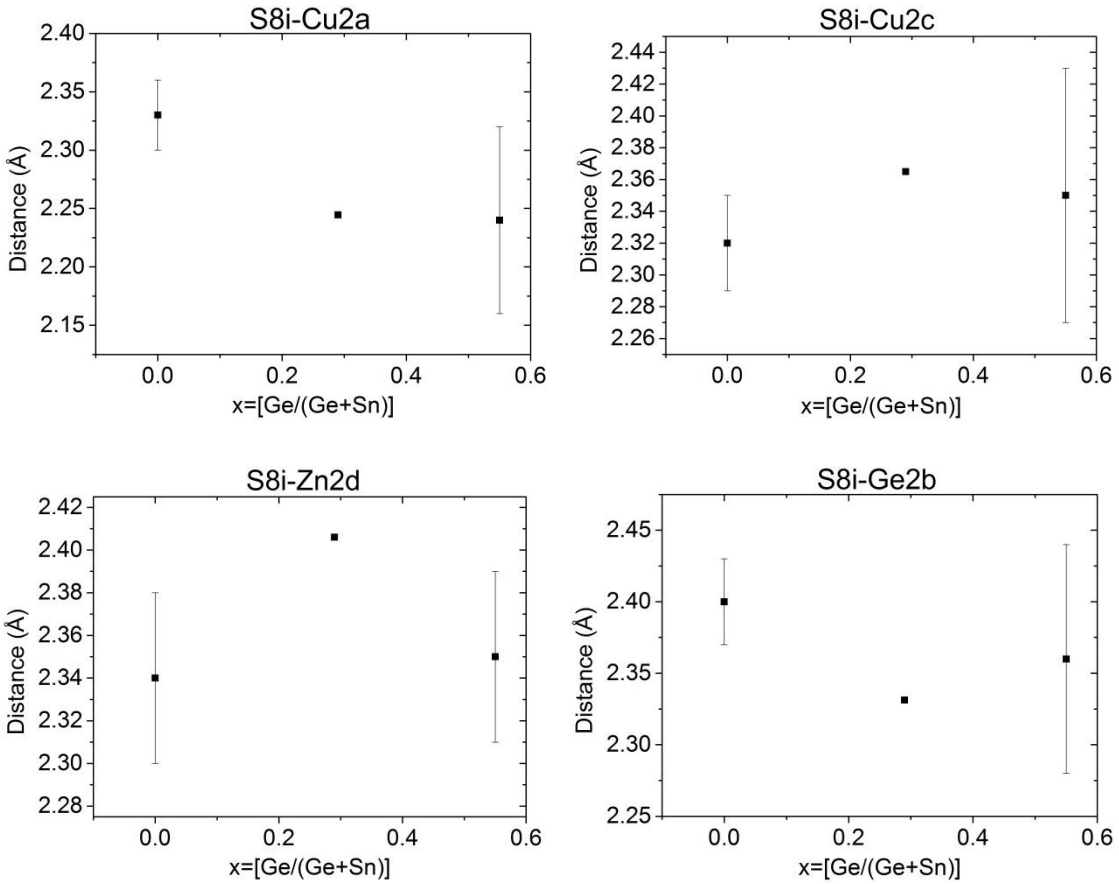

Figure 3.31. Sulfur polycrystalline cation-anion distance: Cu2a-Se8i, Cu2c-Se8i, Zn2d-Se8i, and Ge2b-Se8i. Note: Ge2b-S8i is equivalent to Sn2b-S8i.

Table 3.16. Anion coordinates (X, Y, Z) and cation-anion distances of the selenium single crystals obtained from the simultaneous Rietveld refinement of the neutron and X-ray diffraction data. Note: Standard deviations are indicated in last place in brackets. ST=Stannite structure; Ge2b-S8i is equivalent to Sn2b-S8i.

Sample	X	Y	Z
$Cu_2ZnGeSe_4$	0.25199(259)	0.23330(259)	0.12219(246)
$Cu_2ZnSn_{0.3}Ge_{0.7}Se_4$	0.25744(94)	0.25857(94)	0.12564(94)
$Cu_2ZnSn_{0.5}Ge_{0.5}Se_4$	0.26967(1681)	0.26137(925)	0.12629(152)
$Cu_2ZnSn_{0.7}Ge_{0.3}Se_4$	0.25398(1250)	0.25008(527)	0.13044(88)
$Cu_2ZnSnSe_4$	0.26545(1055)	0.24557(594)	0.12987(209)

Sample	Cu2a-S8i (Å)	Cu2c-S8i (Å)	Zn2d-S8i (Å)	Ge2b-S8i (Å)
$Cu_2ZnGeSe_4$	2.448(19)	2.375(19)	2.498(19)	2.350(19)
$Cu_2ZnSn_{0.3}Ge_{0.7}Se_4$	2.386(8)	2.427(8)	2.435(8)	2.490(8)
$Cu_2ZnSn_{0.5}Ge_{0.5}Se_4$	2.35(7)	2.46(7)	2.40(7)	2.55(7)
$Cu_2ZnSn_{0.7}Ge_{0.3}Se_4$	2.47(5)	2.43(5)	2.40 (5)	2.50(5)
$Cu_2ZnSnSe_4$	2.46(5)	2.37(5)	2.50(5)	2.53(5)

Figure 3.32 shows a similar behavior than the ones presented for the selenium single crystals, but in this case it seems that all the anion-cation distance of the compounds are interrelated maybe because the ionic hybridization is present in all the compounds. This hybridization behavior might explain that the anion has a “lateral” translation because there is a tendency that when the selenium-cation distance of Ge(2b) and Cu(2c) increases, the selenium-cation distance of Zn(2d) and Cu(2a) decreases and inversely.

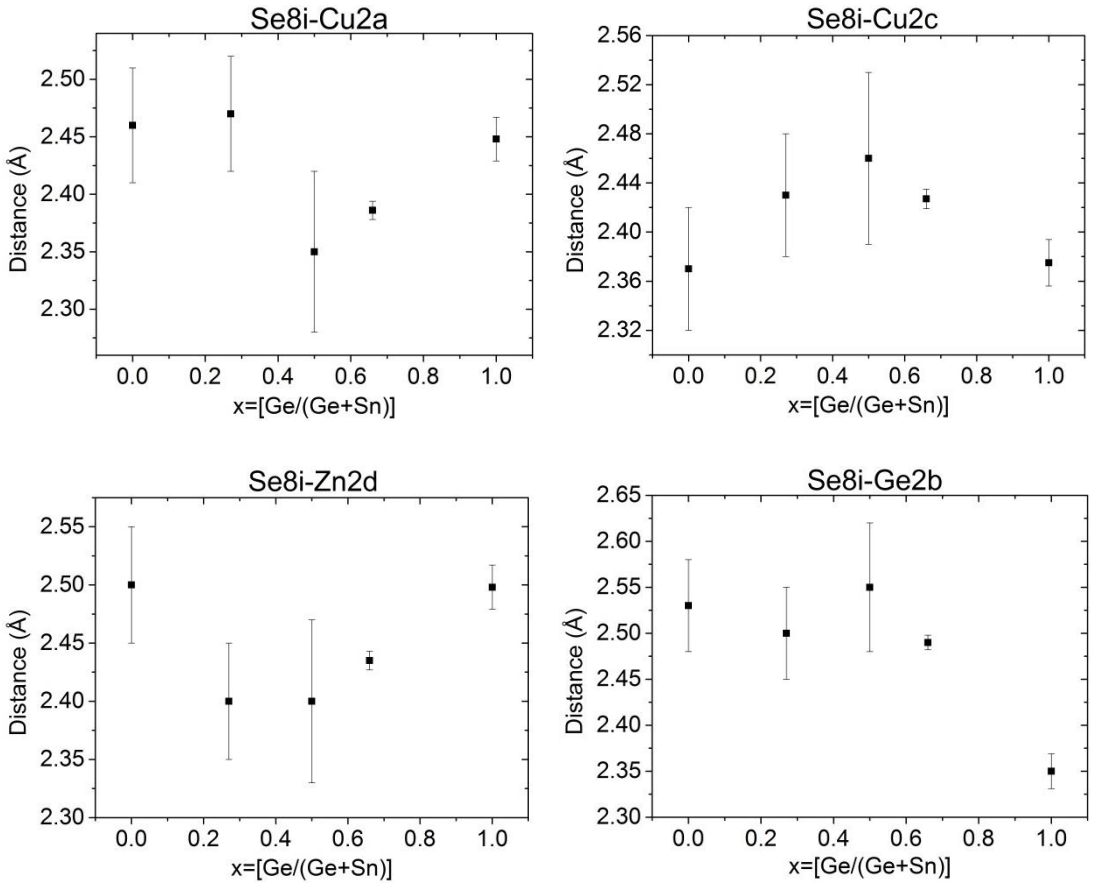

Figure 3.32. Selenium polycrystalline cation-anion distance: Cu2a-Se8i, Cu2c-Se8i, Zn2d-Se8i, and Ge2b-Se8i. Note: Ge2b-S8i is equivalent to Sn2b-S8i.

3.4. Optical properties of kesterite compounds

In this section, there are two sub-sections. The first one shows the spectroscopic ellipsometry measurements of the sulfur and selenium single crystals synthesized by CVT and the second one presents the spectroscopic ellipsometry measurements of the sulfur and selenium polycrystalline compounds synthesized by the Bridgman method. In each section, the results are presented and discussed.

3.4.1. Single crystals measured by Spectroscopic ellipsometry [8]

Figure 3.33 and Figure 3.34 show the experimental spectral dependence of the dielectric functions of the different $Cu_2ZnSn_{1-y}Ge_yS_4$ and $Cu_2ZnSn_{1-y}Ge_ySe_4$ single crystals, respectively.

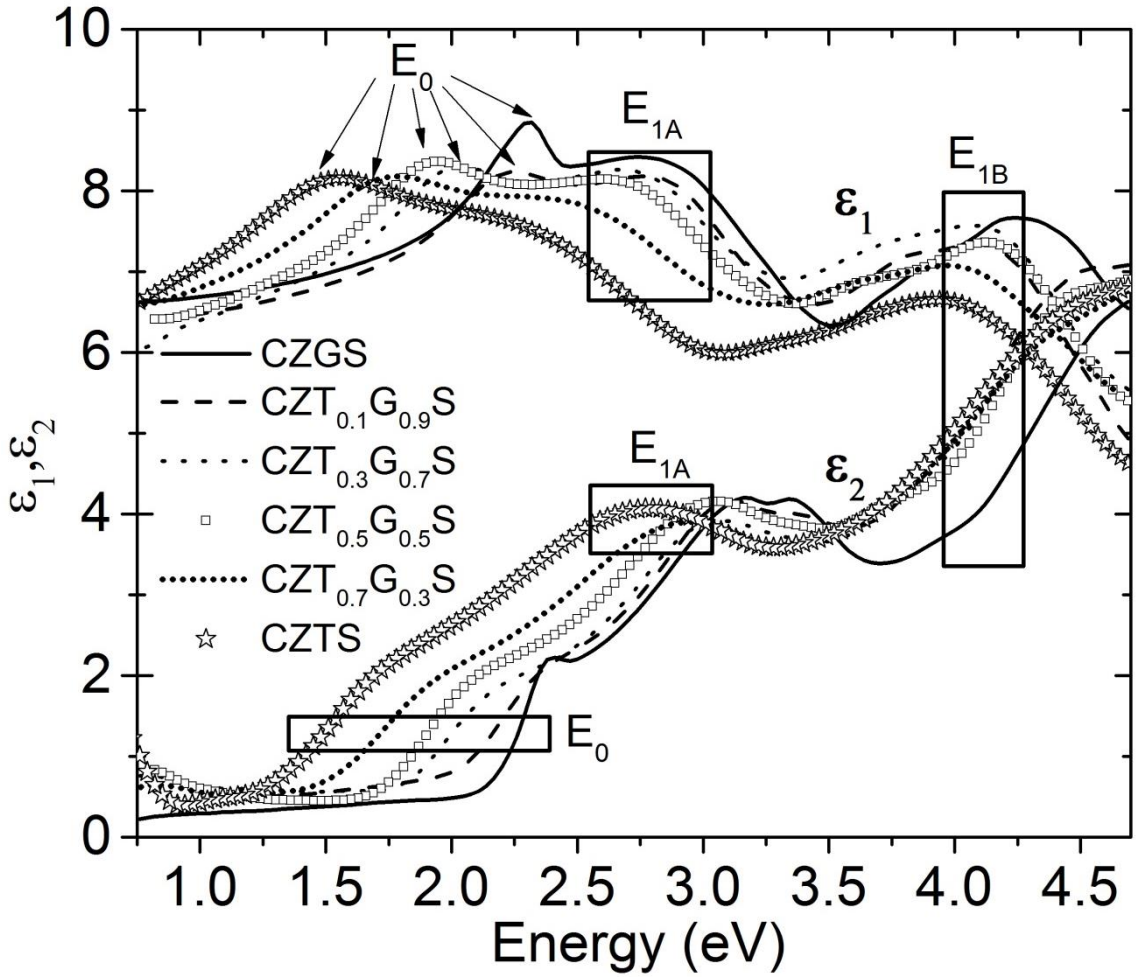

Figure 3.33. Experimental spectral dependence of real ($\varepsilon_1(E)$) and imaginary ($\varepsilon_2(E)$) parts of the dielectric function $\varepsilon(E)$ of $Cu_2ZnSn_{1-y}Ge_yS_4$ single crystals. The spectra exhibit three CP structures, E_0, E_{1A} and E_{1B} for each compound.

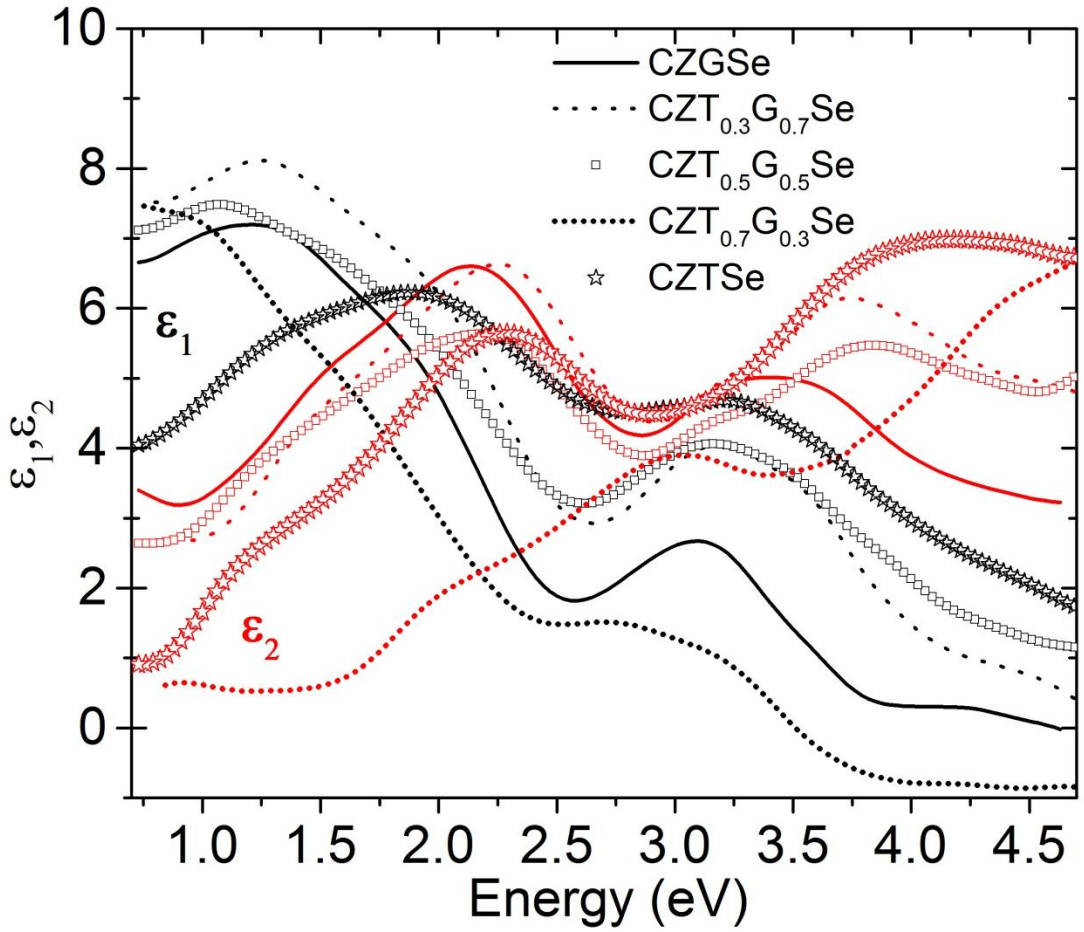

Figure 3.34. Experimental spectral dependence of real ($\varepsilon_1(E)$) and imaginary ($\varepsilon_2(E)$) part of the dielectric function $\varepsilon(E)$ of $Cu_2ZnSn_{1-y}Ge_ySe_4$ single crystals.

Figure 3.33 shows in the spectra clear interband critical points (CP) structures analyzed in terms of standard analytic line shapes:

$$\varepsilon(\omega) = C - Aexp^{i\Phi}(\omega - E + i\Gamma)^m$$

Equation 3-5

where A is the amplitude, E is the energy threshold, Γ is the boarding, and Φ is the excitonic phase angle [18]. These parameters are determined by fitting the numerically obtained second derivative spectra $d^2\varepsilon(E)/dE^2$ of the experimental $\varepsilon(E)$ to Equation 3-5. The exponent m has the value -½ for one-dimensional, 0 for two-dimensional, and ½ for three-dimensional critical points. From the CPs, information on the energy separation of valence and conduction bands can be obtained. Previously, calculations based on different features observed in complex dielectric constants have been reported in CZTS [19] and CZGS [20] single crystals. Here the $\varepsilon(E)$ spectra show three CPs structures: E_0, E_{1A} and E_{1B}. Analogous procedures were done after Figure 3.34. In this case the interband critical points (CP) were not highlighted to avoid confusion in the plot.

To obtain the CP's energies, the $\varepsilon(E)$ spectra were smoothed by fast Fourier transform filtering before fitting $d^2\varepsilon(E)/dE^2$. Figure 3.35 and Figure 3.37 exhibit the second derivatives of the real and imaginary parts of the dielectric functions and their fittings by using Equation 3-5. The fittings have been done taking into account CPs of 3D-type for the fundamental absorption edge $E_0=E_g$ and 2D-type for the second, E_{1A}, and third, E_{1B}, transition energies.

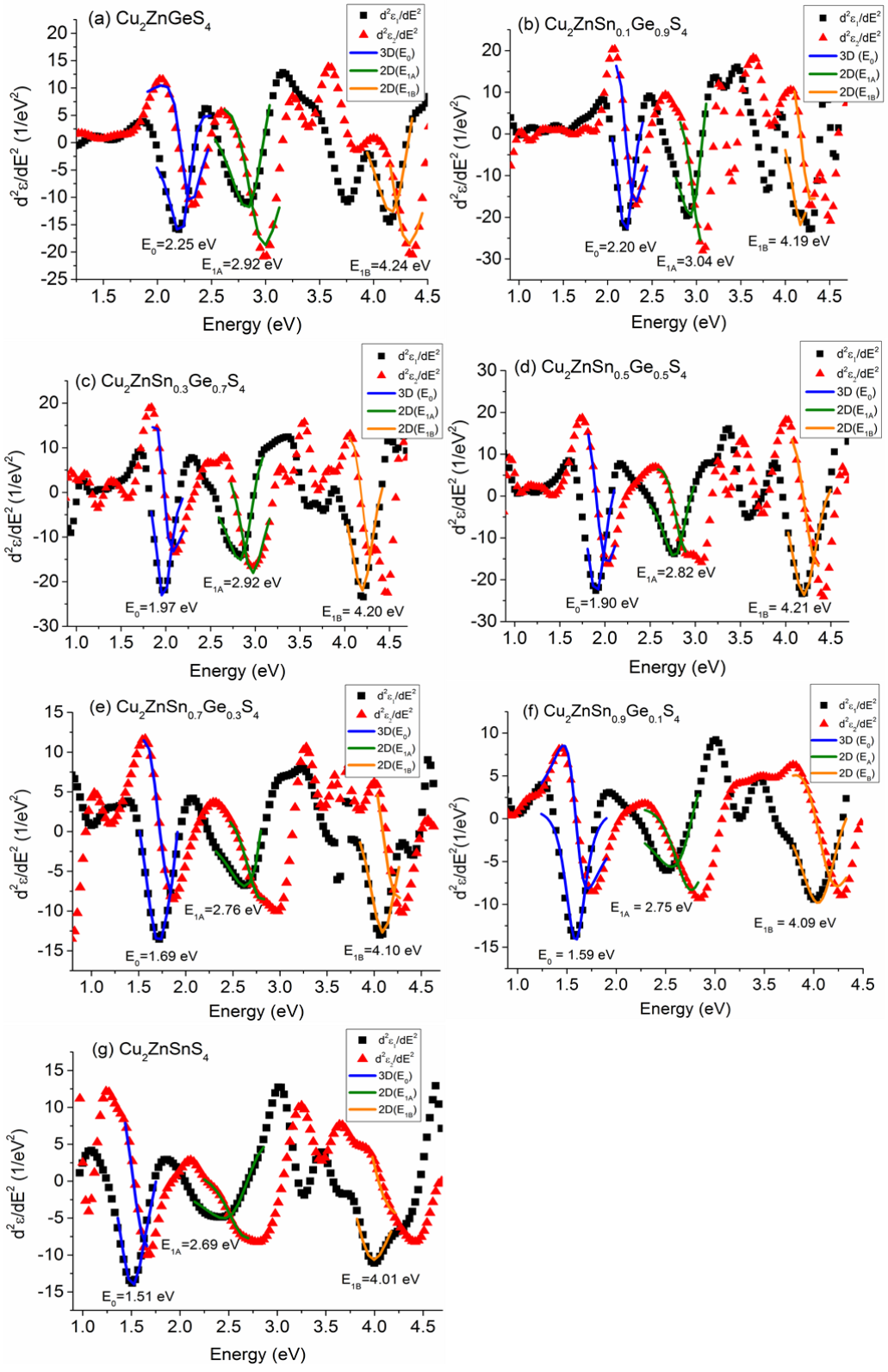

Figure 3.35. (a), (b), (c), (d), (e), (f), (g) Second derivative spectra of the experimental real and imaginary dielectric functions and the fitting based on Equation 3-5 to obtain the transition energies of sulfur single crystals. E_0, E_{1A} and E_{1B} values are given.

Table 3.17 shows the energy threshold of the fundamental absorption edge E_0 = 2.25 eV for Cu_2ZnGeS_4 (CZGS), which is in good agreement with the 2.27 eV of the kesterite CZGS theoretical calculations [21] and that obtained experimentally in single crystals by ellipsometry [20]. In the case of the selenide single crystal $Cu_2ZnGeSe_4$ (CZGSe) (Table 3.18 and the red triangle in Figure 3.38), it was noticed a change in the tendency of the fundamental absorption edge compared with the other selenium single crystals. This is because CZGSe presents a different structure which affects directly to the fundamental absorption edge E_0 = 1.33eV, which is the E_0 value for the stannite structure as reported in [10,22] by theoretical calculations. Except this precise compound CZGSe, all the other compounds were identified to crystallize in the kesterite structure, as it will be explained below in this section.

The E_0 threshold is assigned to the electronic transition at the Γ(000) point, corresponding to a direct transition from the valence-band maximum (VBM) to the conduction-band minimum (CBM). In this work, for the CZGS kesterite compound, the energies of the second threshold E_{1A} and the third E_{1B} are 2.92 eV and 4.24 eV respectively. Also for the CZGSe stannite compound, the energies of the second threshold E_{1A} and the third E_{1B} are 1.86 eV and 3.08 eV respectively. These energies are very close to those reported from theoretical band structure studies in [21] for CZGS and in [10] for CZGSe, which correspond to the transitions at the high critical points *N(A)*: 2Π/a (0.5 0.5 0.5), *T(Z)*: 2Π/a (0 0 0.5) and Γ_2:(0 0 0) of the first Brillouin zone for the E_{1A}, E_{1B} and E_0 transitions, respectively.

The partial substitution of Ge by Sn leads to a decrease of the E_0 values, as displayed in Table 3.17 and Table 3.18. Figure 3.36 and Figure 3.38 display the variation of the fundamental energy E_0 with the experimental [Ge/(Sn+Ge)] atomic ratio and its linear fitting for sulfides and selenides, respectively. Following is presented the band gap linear fitting of the sulfur single crystals:

$$E_0 = 1.50(1) + 0.73(2)x$$

Equation 3-6

Also, it is shown the band gap linear fitting of the selenium single crystals:

$$E_0 = 0.91(3) + 0.69(5)x$$

Equation 3-7

In both cases the band gap evolution follows the Vegard's law, as already observed for $Cu_2ZnSn_{1-y}Ge_ySe_4$ [23]. In Figure 3.38, two points for x=1 (CZGSe) are shown, the red triangle (1.33 eV) is the one measured in this work but it did not follow the linear fitting because it refers to the stannite structure, and the higher point (1.60 eV) with the star on top, that was extracted from literature [10] and it refers to the kesterite structure value like all the other measured points of selenium compound. The x=1 (CZGSe) point extracted from the literature in Figure 3.38 has been used to perform a linear fitting and useful to assure that the rest of the samples follow the kesterite structure tendency. Moreover, in [10], a theoretical calculated value of 1.32 eV band-gap and experimentally in [24] by spectrophotometry a value of 1.29 eV was obtained for the $Cu_2ZnGeSe_4$ with the stannite structure, which fits properly with the one that has been measured by spectroscopic ellipsometry in this work. The fact that only with spectroscopic ellipsometry it was detected the $Cu_2ZnGeSe_4$ as stannite structure might be related with this specific single crystal. This technique requires a big enough area to reflect the light to perform the measurement (section 2.3), and in $Cu_2ZnGeSe_4$ single crystals synthesis, only one single crystal was enough big to perform this measurement (the other were too small to obtain any result). This single crystal was reserved exclusively to perform spectroscopic ellipsometry while the rest were used in the other characterization techniques (diffraction (section 3.3) and Raman (section 3.5) measurements). This single crystal was measured several times to assure that the band gap energy value obtained was reliable. Lately, it was performed Raman measurements in the single crystal characterized by ellipsometry (section 3.4) and the other measured by Raman (section 3.5). It was found that there were remarkable differences. For the Raman spectra measured with 532 nm excitation wavelengths, some intensity changes in the 170-180 cm^{-1} region as well as the presence of an extra peak around 196 cm^{-1} for the ellipsometry single crystal were found. The Raman measurement with the 785 nm excitation wavelength showed the same intensity changes in the 170-180 cm^{-1} region and the existence of extra peaks around 190 and 236 cm^{-1}. These changes in the spectrums are related to the coupling modification of the excitation wavelength with the band gap energy. This might be due to the coexistence of both stannite and kesterite structures. In Appendix II shows both Raman spectra with the different excitation wavelengths and the indicated changes.

It has to be mentioned, that theoretical works [21] suggest that Zn does not have an important role in the change of the band gap energy, so the deviation from a linear

increase of E_0 with the Ge content may be related to the different Cu concentration of the samples. The reason of this deviation may be originated in the Cu-S p-d coupling that determines the VBM level, and the Cu-poor samples show higher band gaps due to the decrease in the VBM [21,25,26]. The phenomena of the "vacancy compound" for Cu-poorer thin films, increasing E_0, have been widely used in the chalcopyrite compound to improve their efficiency like in the case of CISe/CdS interface [27]. The composition of the kesterite plays an important role because the highest performance obtained for CZTSSe-based solar cells are obtained for Cu-poor kesterite layers.

Table 3.17. Transition energies E_0, E_{1A} and E_{1B} values of $Cu_2ZnSn_{1-y}Ge_yS_4$ (y = 0.1, 0.3, 0.5, 0.7, 0.9 and 1) single crystals.

Sample	E_0 (±0.03) (eV)	E_{1A} (±0.03) (eV)	E_{1B} (±0.03) (eV)
Cu_2ZnGeS_4	2.25	2.92	4.24
$Cu_2ZnSn_{0.1}Ge_{0.9}S_4$	2.20	3.04	4.19
$Cu_2ZnSn_{0.3}Ge_{0.7}S_4$	1.98	2.92	4.20
$Cu_2ZnSn_{0.5}Ge_{0.5}S_4$	1.90	2.82	4.21
$Cu_2ZnSn_{0.7}Ge_{0.3}S_4$	1.69	2.76	4.10
$Cu_2ZnSn_{0.9}Ge_{0.1}S_4$	1.59	2.75	4.09
Cu_2ZnSnS_4	1.51	2.69	4.01

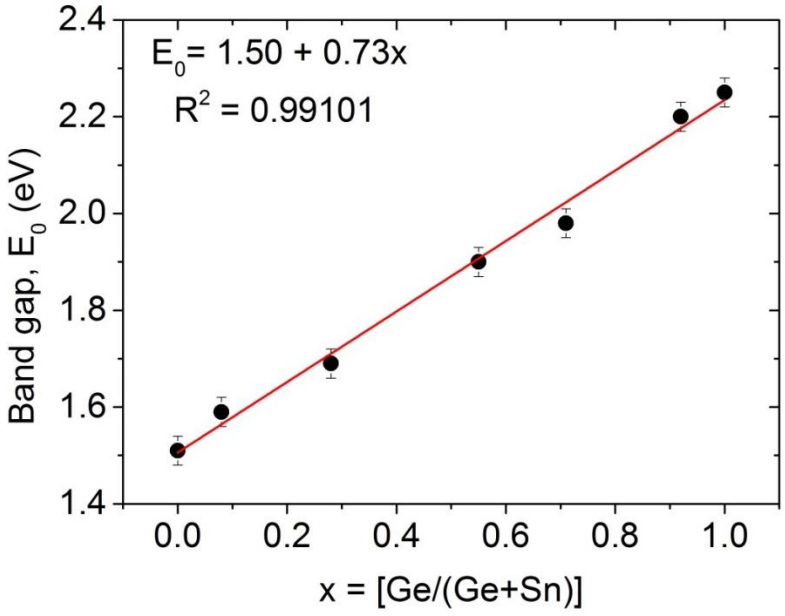

Figure 3.36. Variation of the fundamental band gap energy with the x= [Ge/(Sn+Ge)] atomic ratio values of $Cu_2ZnSn_{1-x}Ge_xS_4$ (x= 0.08, 0.28, 0.55, 0.71, 0.92 and 1) single crystals. The solid line represents the linear fit of the experimental data.

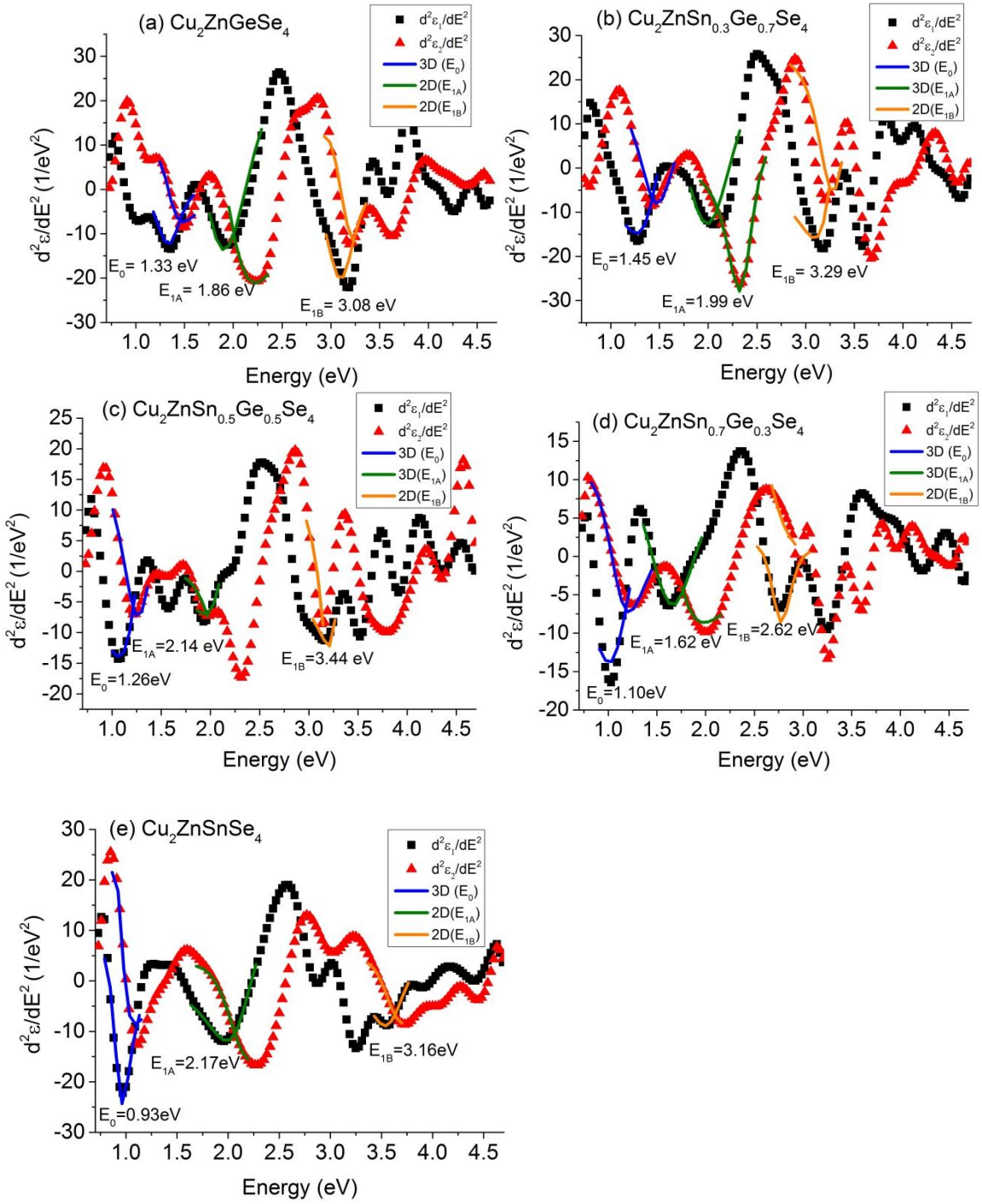

Figure 3.37. (a), (b), (c), (d), (e) Second derivative spectra of the experimental real and imaginary dielectric functions and the fitting based on Equation 3-5 to obtain the transition energies of selenium single crystals. E_0, E_{1A} and E_{1B} values are given.

Table 3.18. Transition energies E_0, E_{1A} and E_{1B} values of $Cu_2ZnSn_{1-y}Ge_ySe_4$ (y = 0, 0.3, 0.5, 0.7 and 1) single crystals.

Sample	E_0 (±0.03) (eV)	E_{1A} (±0.03) (eV)	E_{1B} (±0.03) (eV)
$Cu_2ZnGeSe_4$	1.33	1.86	3.08
$Cu_2ZnSn_{0.3}Ge_{0.7}Se_4$	1.45	1.99	3.29
$Cu_2ZnSn_{0.5}Ge_{0.5}Se_4$	1.26	2.14	3.44
$Cu_2ZnSn_{0.7}Ge_{0.3}Se_4$	1.10	1.62	2.62
$Cu_2ZnSnSe_4$	0.93	2.17	3.16

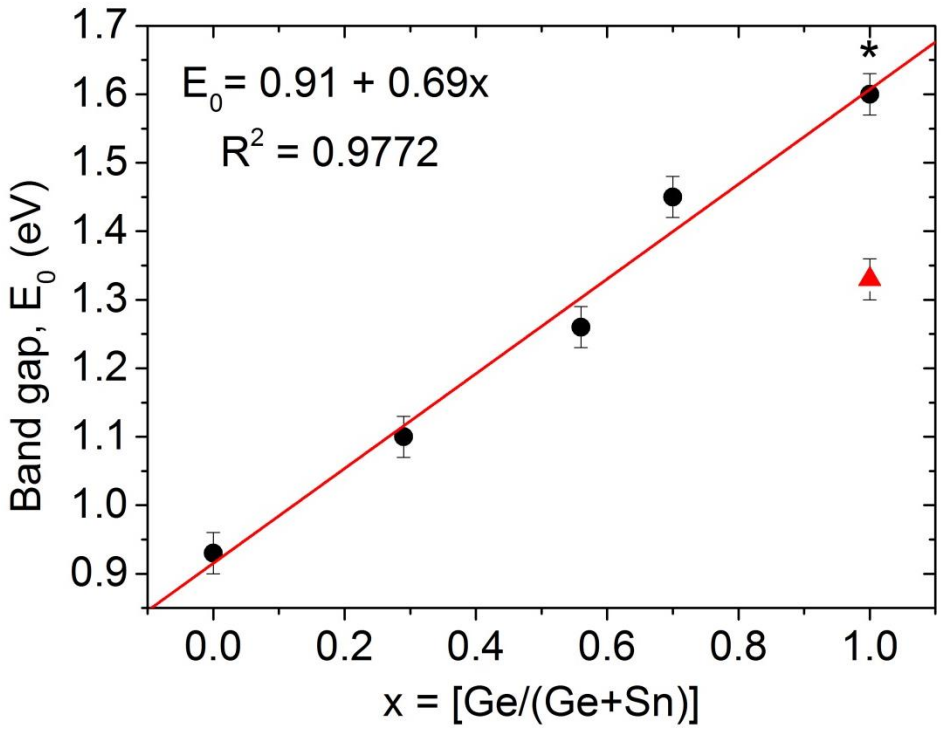

Figure 3.38. Variation of the fundamental band gap energy with the x= [Ge/(Sn+Ge)] atomic ratio values of $Cu_2ZnSn_{1-x}Ge_xSe_4$ (x= 0, 0.27, 0.50, 0.66 and 1) single crystals. The solid line represents the linear fit of the experimental data. Note: the point with the * on top is from literature [10], the red triangle is the E_0 of stannite CZGSe compound measured.

3.4.2. Polycrystalline compounds measured by Spectroscopic ellipsometry

Figure 3.39 and Figure 3.41 exhibit the second derivatives of the real and imaginary parts of the dielectric functions and their fittings by using Equation 3-5 of the CZTGS and CZTGSe samples, respectively. The fittings have been done again taking into account CPs of 3D-type for the fundamental absorption edge E_0=E_g and 2D-type for the second, E_{1A}, and third, E_{1B}, transition energies.

The fundamental absorption edge $E_0=E_g$ of the sulfur polycrystalline compounds have similar values than the ones obtained for the sulfur single crystals (Table 3.19). Moreover, the selenium polycrystalline compounds and the selenium single crystals values of the fundamental absorption edge (Table 3.20) are similar in the extremes composition, CZGSe and CZTSe. On the other hand, the intermediate selenium polycrystalline compounds show differing values in the fundamental absorption edge; although the samples were polished, these differences in the fundamental absorption edge might be due to the presence of grain boundaries in the surface; this grain boundaries might promote the oxidation in these boundaries which could not be possible to remove it with the standard polishing [18,28]. As it can be seen, the number of the samples is substantially less than the samples presented in the single crystals section. The reason for this is the presence of secondary phases in the polycrystalline samples, which makes impossible to perform appropriate measurements to achieve reliable energy transition values for the CZTGS or CZTGSe samples.

The partial substitution of Ge by Sn leads to a decrease of the E_0 values, as displayed in Table 3.19 and Table 3.20, as it was previously observed for the single crystals.

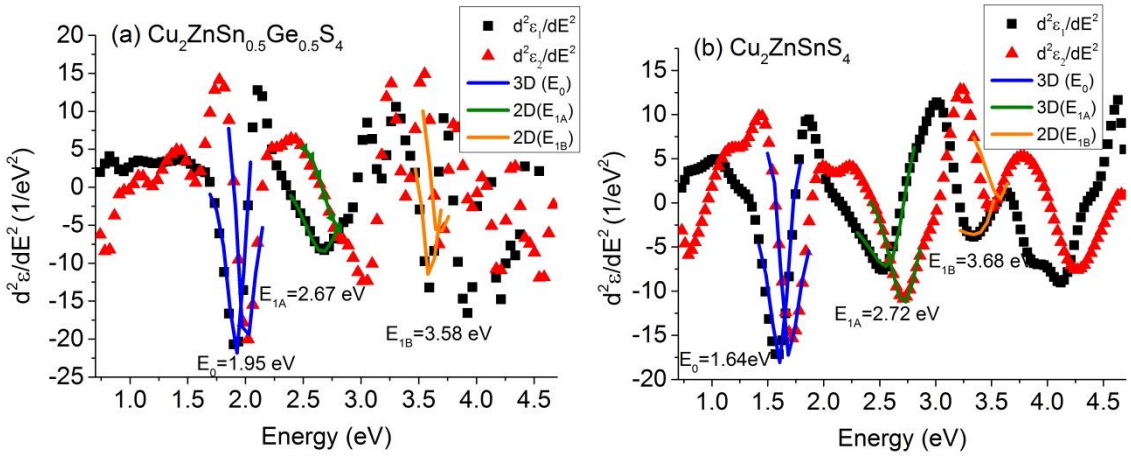

Figure 3.39. (a), (b) Second derivative spectra of the experimental real and imaginary dielectric functions and the fitting based on Equation 3-5 to obtain the transition energies of sulfur polycrystalline compounds. E_0, E_{1A} and E_{1B} values are given.

Table 3.19. Transition energies E_0, E_{1A} and E_{1B} values of $Cu_2ZnSn_{1-y}Ge_yS_4$ (y = 0 and 0.5) polycrystalline compounds.

Sample	E_0 (±0.03) (eV)	E_{1A} (±0.03) (eV)	E_{1B} (±0.03) (eV)
$Cu_2ZnSn_{0.5}Ge_{0.5}S_4$	1.95	2.67	3.58
Cu_2ZnSnS_4	1.64	2.72	3.68

Figure 3.40 and Figure 3.42 display the variation of the fundamental energy E_0 with the experimental [Ge/(Sn+Ge)] atomic ratio for sulfides and selenides polycrystalline samples, respectively, and the linear fitting for the latter ones:

$$E_0 = 0.91(4) + 0.35(5)x$$

Equation 3-8

The *Y* axis intersection is the same than for the selenium single crystals (see Equation 3-7) but the slope is almost the half. The reason of this difference is easy to understand since the band gap value considered for the $Cu_2ZnGeSe_4$ single crystal was 1.60 eV, extracted from the literature, instead the 1.33 eV measured experimentally which corresponded to a mixture of stannite-kesterite structures and it was out of range to perform a linear suitable adjustment (see Figure 3.38). Meanwhile, linear fitting of the selenium polycrystalline compounds band gap energy was done with 1.25 eV for the $Cu_2ZnGeSe_4$, which affects directly to the slope of the fitting. Furthermore, Vegard's law is fulfilled when the atomic ratio x=[Ge/(Ge+Sn)] changes for the selenium compounds. There is no linear fitting for the sulfur polycrystalline compounds because there were only two samples measured.

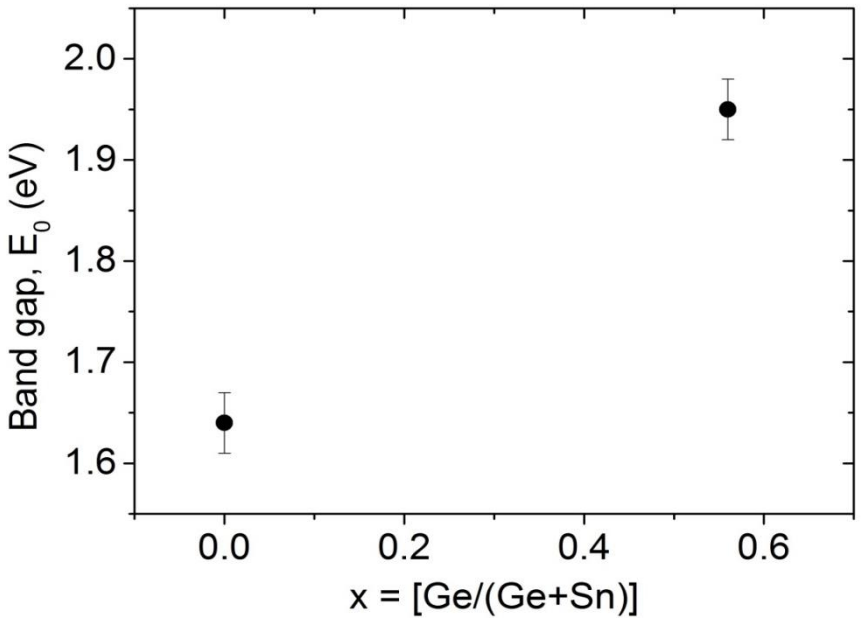

Figure 3.40. Variation of the fundamental band gap energy with the *x*= [Ge/(Sn+Ge)] atomic ratio values of $Cu_2ZnSn_{1-x}Ge_xS_4$ (*x*= 0 and 0.55).

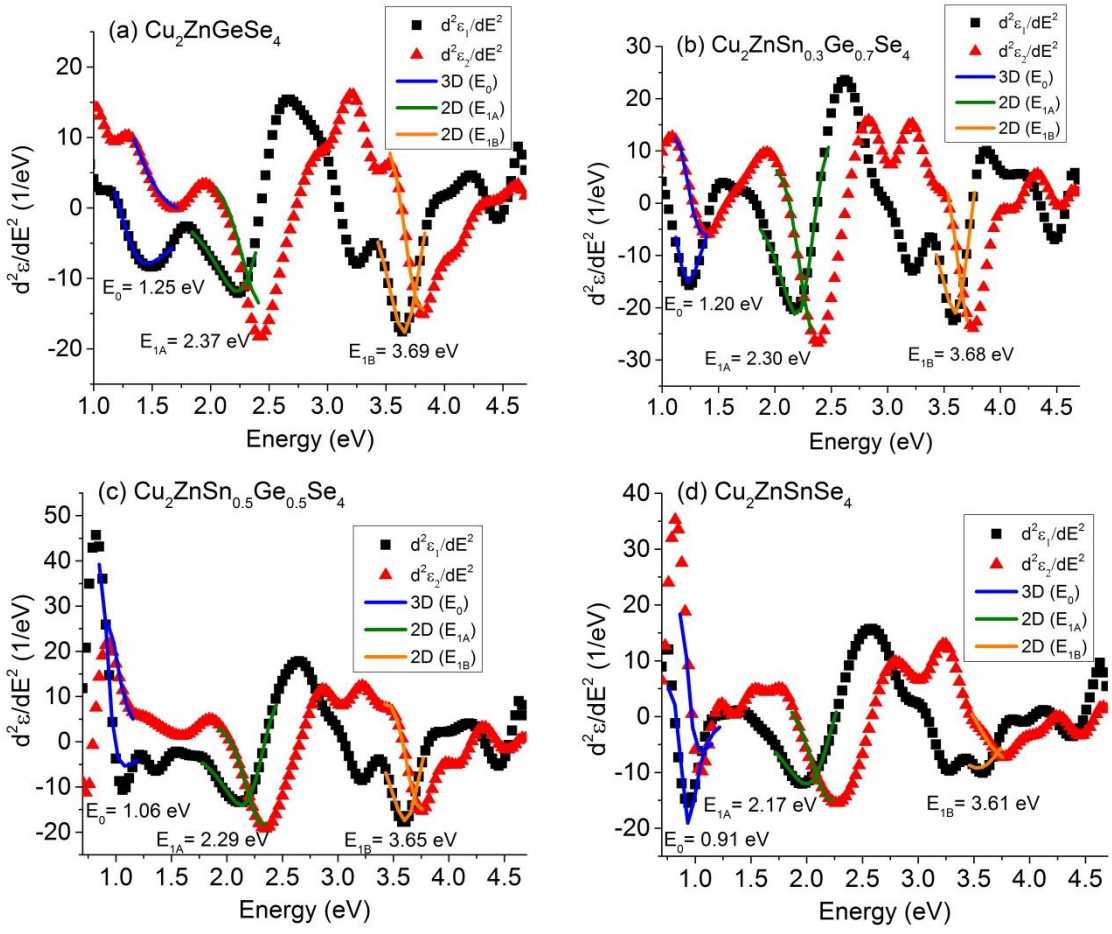

Figure 3.41. (a), (b), (c), (d) Second derivative spectra of the experimental real and imaginary dielectric functions and the fitting based on Equation 3-5 to obtain the transition energies of selenium polycrystalline compounds. E_0, E_{1A} and E_{1B} values are given.

Table 3.20. Transition energies E_0, E_{1A} and E_{1B} values of $Cu_2ZnSn_{1-y}Ge_ySe_4$ (y = 0, 0.3, 0.5 and 1) single crystals.

Sample	E_0 (±0.03) (eV)	E_{1A} (±0.03) (eV)	E_{1B} (±0.03) (eV)
$Cu_2ZnGeSe_4$	1.25	2.37	3.69
$Cu_2ZnSn_{0.3}Ge_{0.7}Se_4$	1.20	2.03	3.68
$Cu_2ZnSn_{0.5}Ge_{0.5}Se_4$	1.06	2.29	3.65
$Cu_2ZnSnSe_4$	0.91	2.17	3.61

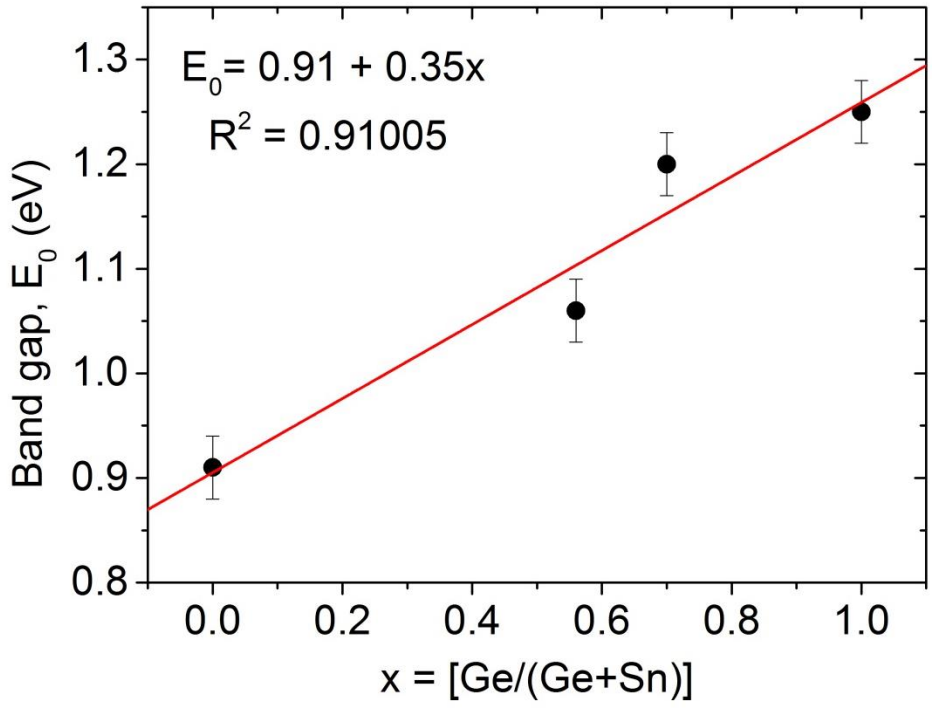

Figure 3.42. Variation of the fundamental band gap energy with the x= [Ge/(Sn+Ge)] atomic ratio values of $Cu_2ZnSn_{1-x}Ge_xSe_4$ (x= 0 , 0.50, 0.66 and 1) single crystals. The solid line represents the linear fit of the experimental data.

3.5. Vibrational properties by Raman spectroscopy

In this section, it will be presented the Raman spectra of the CZTGS, CZTGSe single crystals and polycrystalline and its discussion.

3.5.1. **Single crystals** [29]

The Raman spectra of the CZTGS single crystals are presented in Figure 3.43. The position of the peaks was deduced from Lorentzian curves deconvolution of the experimental spectra excited with three different laser lines (532 nm (Figure 3.43(a)), 633 nm (Figure 3.43(b)) and 785 nm (Figure 3.43(c))). To perform measurements with three different wavelengths gives the advantage that the excitation wavelength matches different electronic transitions of the crystal, so the vibrational modes associated with the excited electronic state are greatly enhanced and it makes easier to identify low intensity modes. Here, the shift of all peaks to higher wavenumbers with the increase of the Ge content is clear.

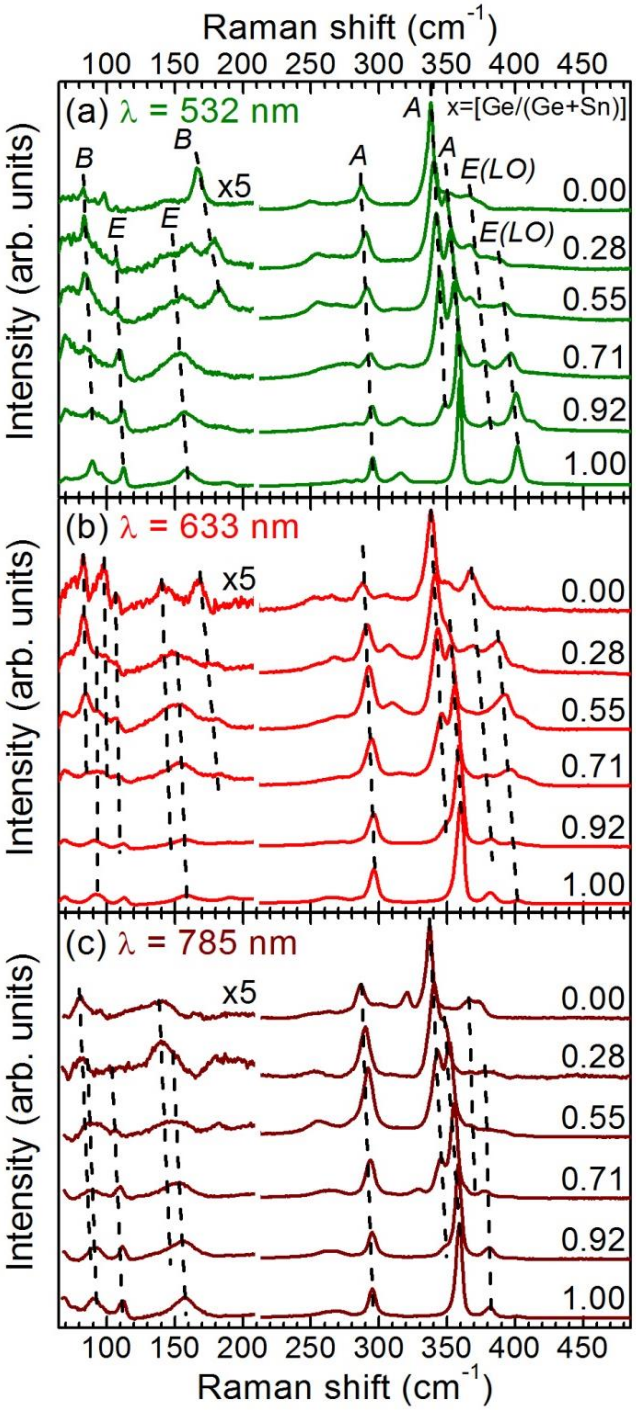

Figure 3.43. Raman spectra of CZTGS single crystals measured with different excitation wavelengths marked in the graphs. The numbers in the spectra indicate the *x*=[Ge/(Ge+Sn)] value according to EDX chemical composition measurements. The intensity of the spectra in the low wavenumber range (< 200 cm-1) has been magnified for convenience. Black dashed lines in the figures are used as a visual guide and their symmetry modes are indicated in the 532 nm excitation wavelength.

Figure 3.44 shows the shifts of the Raman modes of the most relevant peaks, after the Lorentzian deconvolution of the spectra, with the [Ge/(Ge+Sn)] ratio. It is important to take into account that the Raman modes symmetry indicated in Figure 3.44 is valid only

in case of pure compounds and corresponds to the results obtained from polarization measurements in Cu_2ZnSnS_4 [30] and Cu_2ZnGeS_4 [31] single crystals.

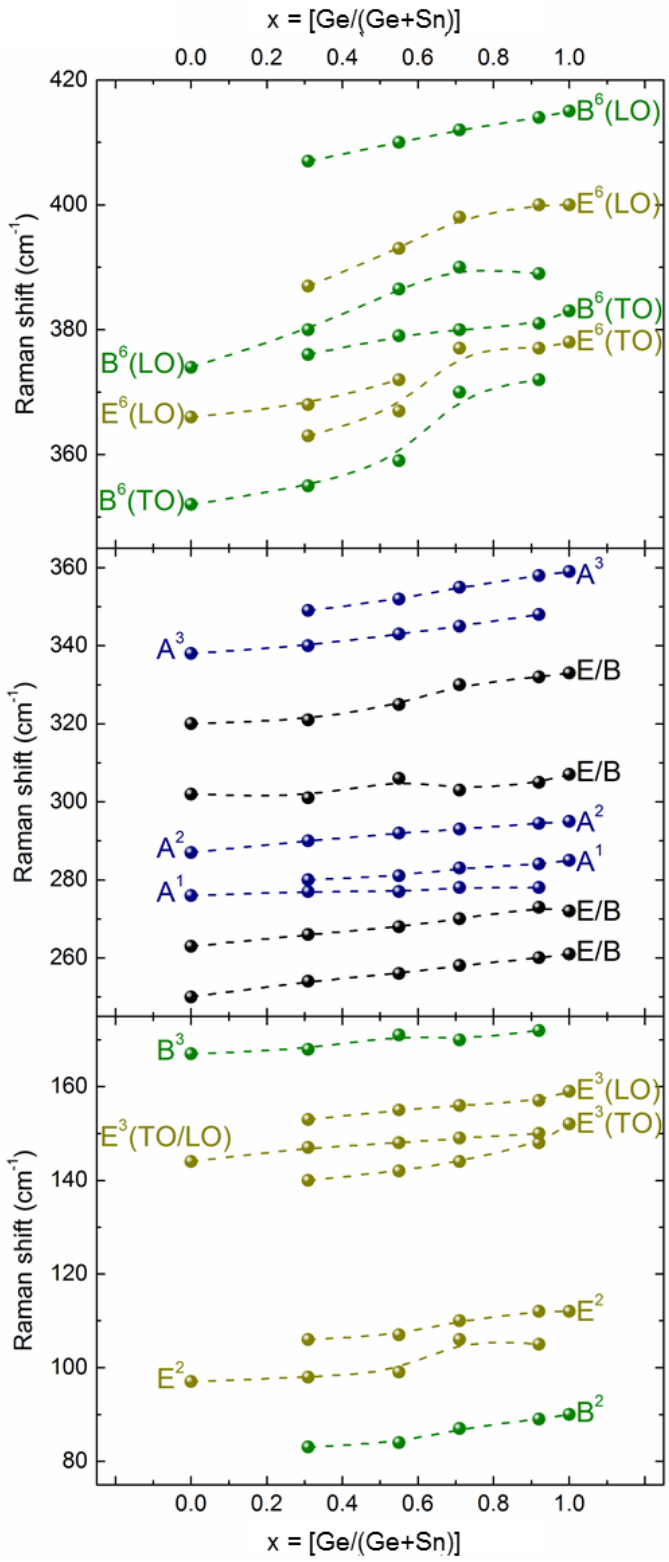

Figure 3.44. Shift of Raman peaks in the CZTGS single crystals. The symmetry mode is indicated only for pure compounds and correlates with the results in [30] and [31]. The TO/LO splitting is indicated only when it is significant.

As it was mentioned in the previous section, the CZTSSe and CZGeSSe compounds, crystalizing in the tetragonal Bravais lattice, can be associated to kesterite or stannite type structures. These structures are hardly distinguishable from the XRD diffractograms, being much easier to differentiate them from the Raman scattering study. As it was mentioned in the introduction, according to unit cell group analysis, the irreducible representation of the zone center (Γ point) phonon modes for stannite and kesterite type structures differs in the number of possible A_1 or A modes ($2A_1$ modes for stannite and $3A$ modes for kesterite). Also, there are other differences in other related modes to distinguish these two structural types. However, the utility of these modes to distinguish both structures is compromised because of their usual low intensity. Previously, based on polarized Raman scattering investigations of single crystals, it was shown that for all four pure compounds CZTS(Se) and CZGS(Se), the second most intense band consisting on two peaks could be a clear indication for the kesterite type structure in quaternary compounds [30–32]. Taking into account these aspects, it will follow the analysis and discussion of the results to identify the type of structure.

As shown in Figure 3.43 and Figure 3.44, the most intense peak (338 cm^{-1} in CZTS and 359 cm^{-1} in CZGeS) as well as the less intense *A* symmetry peak (276 cm^{-1} in CZTS and 285 cm^{-1} in CZGeS) show the two mode behavior (i.e., splitting of the peak in two). On the other hand, the second most intense *A* symmetry peak (287 cm^{-1} in CZTS and 295 cm^{-1} in CZGeS) presents the one mode behavior. In [31], the anion motion for three different *A* symmetry modes in CZGeS compound was presented, which exhibits strong differences in their motion orientation as will be explain with more detail below. This fact could explain the different one or two mode behavior of the *A* symmetry modes in the CZTGS single crystals.

The Raman spectra of the CZTGSe single crystals measured under the laser lines 532, 633 and 785 nm are shown in Figure 3.45. In the spectra, two intense peaks in the range 160–210 cm^{-1} are associated to the *A*-like symmetry modes, and clearly exhibit one-mode behavior. The position of the peaks was deduced from Lorentzian curves deconvolution of the experimental spectra excited with three different laser lines. An increasing blue shift with the [Ge/(Ge+Sn)] ratio for all peaks was found, similar to that found in the sulfur compounds, and it is presented in Figure 3.46. Here, the symmetry of the peaks is indicated only in the case of the pure compounds and corresponds to the results obtained from polarization measurements in $Cu_2ZnSnSe_4$ and $Cu_2ZnGeSe_4$ single crystals [32].

Excluding the *A*-like symmetry peaks, the rest of the modes, marked as *E* or *B* symmetry modes in Figure 3.46, exhibited two mode behavior, which denotes the strong influence of Sn and Ge cation vibrations in their nature. It should be underlined that the *B* symmetry peak at the lowest wavenumber (74 cm^{-1} in CZGSe) is supposed to have also a two mode behavior, and correlates with the *B* symmetry mode of CZTSe, which cannot be observed here because of the filter cut.

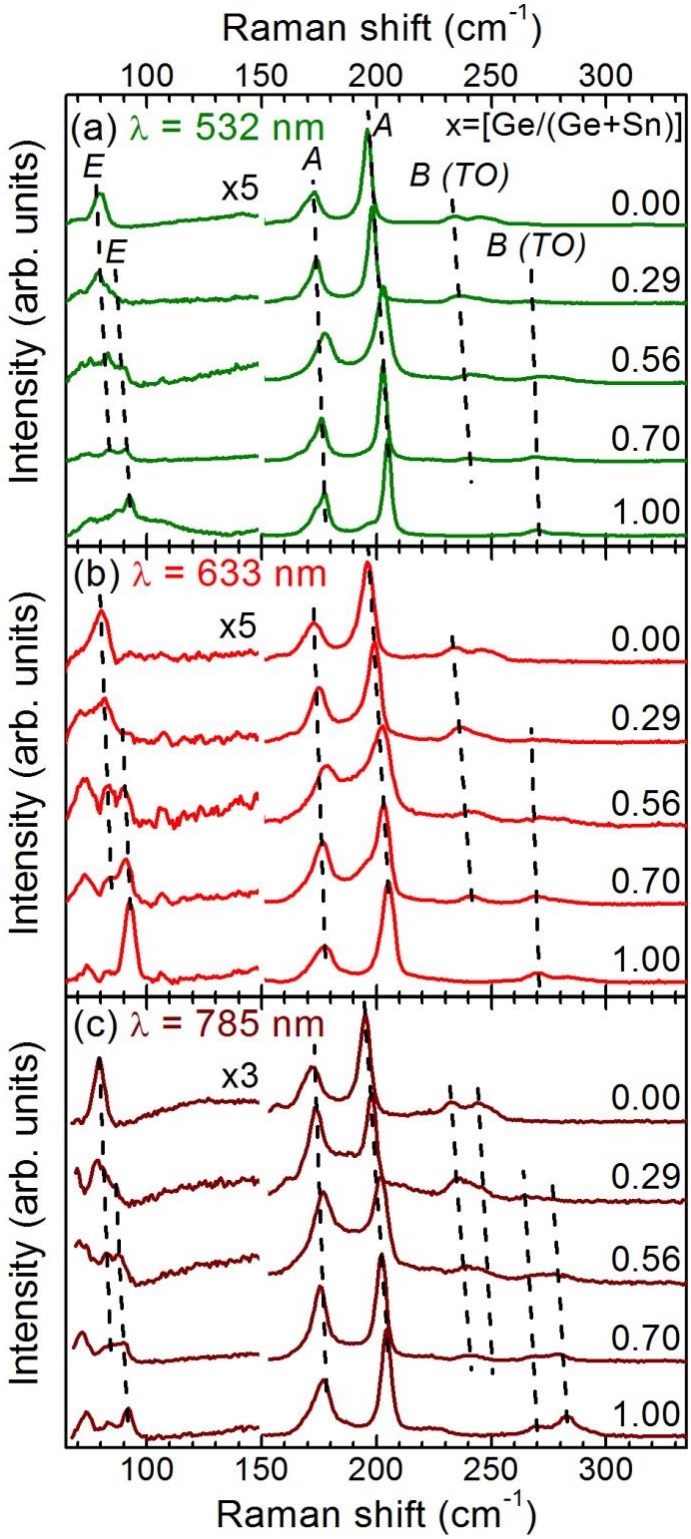

Figure 3.45. Raman spectra of CZTGSe single crystals measured with different excitation wavelengths marked in the graphs. The numbers in the spectra indicate the *x*=[Ge/(Ge+Sn)] value according to EDX chemical composition measurements. The intensity of the spectra in the low wavenumber range (< 200 cm-1) has been magnified for convenience. Black dashed lines in the figures are used as a visual guide and their symmetry modes are indicated in the 532 nm excitation wavelength. The intensity of the spectra in the low wavenumber range (< 150 cm^{-1}) has been magnified for convenience. Black dashed lines in the figures are used as a visual guide and their symmetry modes are indicated in the 532 nm excitation wavelength.

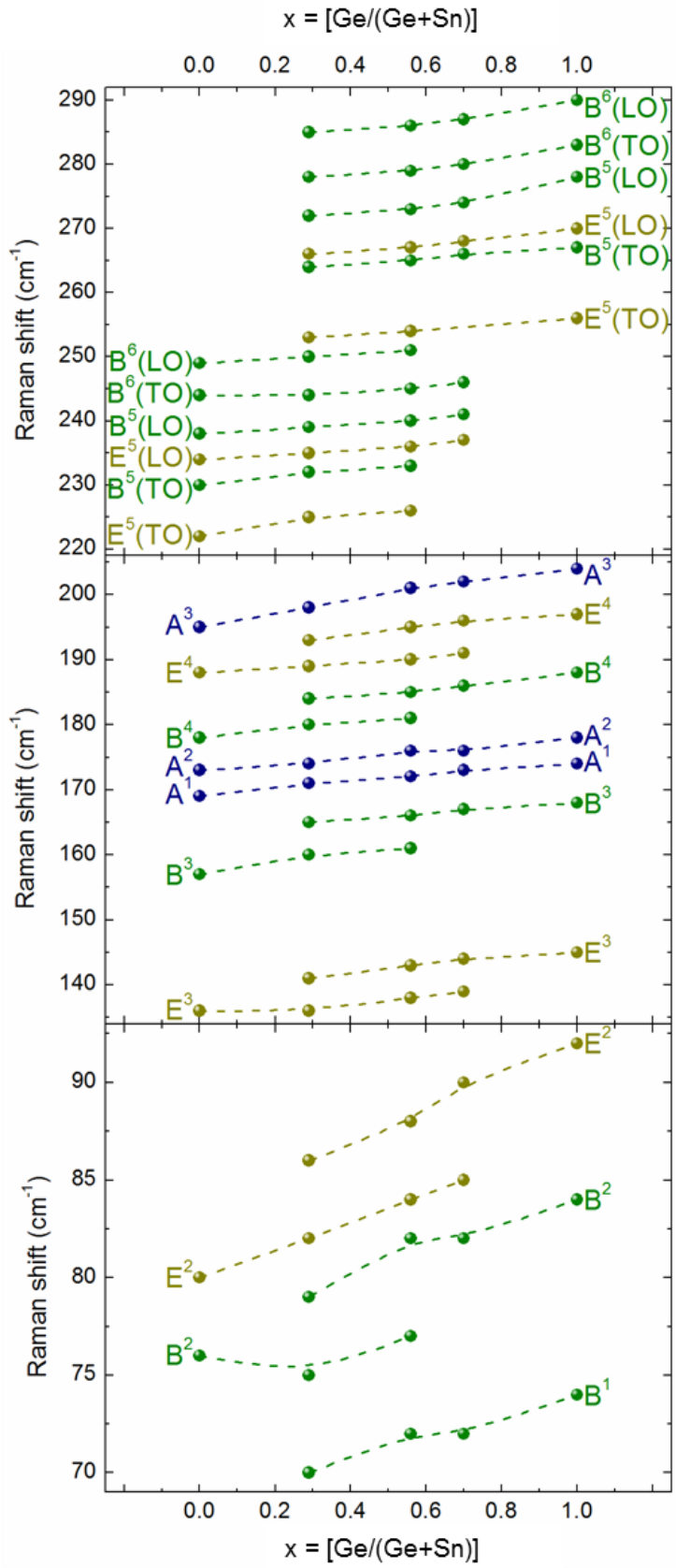

Figure 3.46. Shift of the Raman peaks in the CZTGSe single crystals. The symmetry is indicated only for pure compounds and correlates with results in [32]. The *TO/LO* splitting is indicated only when it is significant.

For the CZTGSe single crystals, the only resonant conditions are achieved for the pure CZGSe compound under NIR excitation (Figure 3.45(c)), which is supported by a small enhancement of the high frequency polar modes in the respective spectra. The band gap of the compound decreases when the Ge content diminishes [20,33], which leads to the necessity of using a higher wavelength laser to induce the resonant conditions.

The values of full width at half maximum (FWHM) for the most intense *A* symmetry peaks for pure CZTSe and CZGSe were quite similar. They are in the range 4–6 cm^{-1}, and increase up to 7–9 cm^{-1} in the sample with [Ge/(Ge+Sn)] = 0.55. Nevertheless, such a small increase of the FWHM in the single crystals could not be interpreted as an evidence of any structural change. As it was previously published in [34] for $Cu_2(Zn,Fe)SnS_4$ single crystals, a clear broadening of the main peaks in the transition from stannite to kesterite structure was observed; more specifically, the broadening of the peaks for these compounds was three times bigger than the ones observed in our compounds. Taking into account this fact and the linear shift of the peaks with the change in the *x*=[Ge/(Ge+Sn)] ratio, we can conclude that all the selenium solid solutions present a kesterite-like structure.

The difference of two and one A symmetry mode behavior in CZTGS and CZTGSe single crystals, respectively, could be explained in terms of the difference in the anion masses. Thus, the motion of the atoms of sulfur, being more than two times lighter than Ge atoms and more than three times lighter than Sn atoms, would be more affected by the cations replacement in the lattice. In the case of the selenium atoms, they have closer mass values to Ge and Sn ones, which are almost indifferent to the cation substitution, resulting only in small shifts of the modes, which was also theoretically predicted [9].

However, here an additional effect could be responsible for the different *A* mode behavior in S and Se content compounds. In chalcopyrite compounds, it was shown a simple method for calculation of the Raman modes frequency using the mass and force constants between cations and anions [35]. For the sulfur content compound, the force constant was found to be more than 15 % higher than in the selenide ones [36]. This could lead to some preferential occupation of the Ge cations in the crystal lattice of single crystals, resulting in the formation of Sn-S and Ge-S subsystems. The idea of this preferential occupation is based on the possibility that when a Sn atom is replaced by Ge, the next Ge atom will not take a random position, but a position near to the first

replacement or in a symmetric position and the third Ge atom replacement will be affected from the other previous two replacements. This would occur repeatedly and finally, this influence or interaction in the follow Ge replacements will create a non-random distribution in the CZTS structure, but a subsystem of Ge atoms [37–39]. These changes in the surroundings of sulfur atoms creates a Sn-S and a Ge-S subsystem because the preferential occupation. These subsystems have different vibrational frequency and could lead to a two-mode behavior of the *A* symmetry modes.

As it can be also seen from Figure 3.44, not only the most intense peak exhibits the two mode behavior. Here, it is interesting to analyze the peaks at 144 cm^{-1} in CZTS, and at 152 cm^{-1} and 158 cm^{-1} in CZGS, attributed to the *E* symmetry mode and split into the Transverse Optical (*TO*) and Longitudinal Optical (*LO*) components in the case of the CZGS compound. For the CZTS compound, the split was not observed, which is in good correlation with theoretical calculations [9] where such a split was only of 0.5 cm^{-1}. As a result, we observed a shift of the two CZGS-related peaks and a shift of the only one CZTS-related peak for the intermediate compounds. The coexistence of two *TO* and *LO* peak at almost the same position at 144 cm^{-1} could suggest that both components of the corresponding *E* symmetry mode have the two mode behavior in CZTGS intermediate compounds.

Some of the peaks in Figure 3.44 (black dots) were not correlated to any peaks of other pure compounds and are shown as having one mode behavior only for convenience. Due to their low intensity and strong overlap with neighbors in all measured spectra, their analysis is not simple. For instance, the peak at 250 cm^{-1} in the CZTS compound, most probably involves two peaks found from polarization measurements, at 248 cm^{-1} (*B(TO)* symmetry) and 250 cm^{-1} (*E(TO)* symmetry) [30]. The first of them could correlate with the *B* symmetry peak at 261 cm^{-1} for the CZGS compound and they most probably have double mode behavior for the intermediate compounds. The last is also supported by the wide shape of the peaks: the FWHM was found to be 15–18 cm^{-1} for them while it did not exceed 12 cm^{-1} for the pure Ge/Sn compounds. Some additional low intensity peaks were also found in the Raman spectra and they are not presented in Figure 3.44. Most of them are only detected in one or two samples of the single crystals. It could be also possible that these peaks were artifacts, appearing in the Raman spectra because of the broadening of the real peaks and their strong overlapping. Nevertheless, a more complicate nature

cannot be excluded for them, e.g. multiphonon, Fermi resonance [40], mutual vibrations of Sn and Ge atoms, etc.

As it is shown in Figure 3.43, the Raman spectra of CZTGS single crystals are much dependent on the used excitation wavelength than the CZTGSe single crystals. This is related to the change in the resonant conditions with the different [Ge/(Ge+Sn)] ratios. The resonant conditions for the pure CZGS compound are achieved when the green excitation wavelength is used [31], while for the pure CZTS compound the near infra-red (NIR) laser is in resonant conditions [30]. Assuming a linear band gap change with the change of the [Ge/(Ge+Sn)] ratio, the resonant conditions for the sample with [Ge/(Ge+Sn)] ≈ 0.5 should appear with the red laser. As a consequence, several enhancements of high frequency polar modes were found because of the use of different excitation wavelengths. This effect should be taken into account and used for future quality control of CZTGS layers as well as in the complete thin film solar cells to detect the presence of secondary phases.

The full width at the half maximum (FWHM) of the *A* symmetry modes was slightly higher for CZTS than for CZGS compounds, varying in the range 5–8 cm^{-1} and 3–5 cm^{-1}, respectively, depending on the different excitation wavelengths. As it was mentioned above, the selenium compounds presented a similar FWHM behavior. Therefore, all the sulfur single crystals are kesterite-like structure.

3.5.2. Polycrystalline compounds

Figure 3.47 and Figure 3.48 show the Raman spectra of the sulfur and selenium polycrystalline compounds, respectively, measured with 514 nm excitation wavelength. The splitting of the A^3 symmetry mode from 339 cm^{-1} for Cu_2ZnSnS_4 to 340 and 351 cm^{-1} for $Cu_2ZnSn_{1-x}Ge_xS_4$, their values and the shift of sulfur polycrystalline compounds coincide exactly with the values obtained from the Raman spectra of sulfur single crystals (Figure 3.44) when the *x* ratio (*x*=[Ge/(Ge+Sn)]) increases. This analogy also happens with the selenium polycrystalline compounds (Figure 3.48) and selenium single crystals (Figure 3.46); in this case there is only one *A* symmetry peak which shifts from 196 cm^{-1} to 202 cm^{-1} when the amount of germanium increases. Moreover, the peaks indicated in the Figure 3.47 and Figure 3.48 are also present in their analogous single crystals compounds.

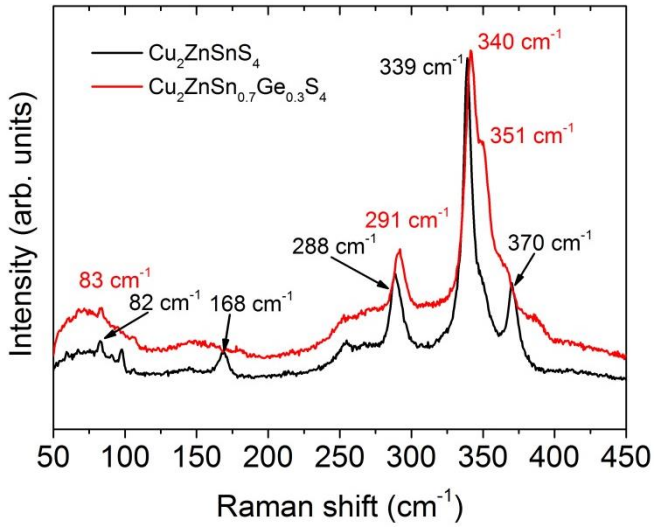

Figure 3.47. Raman spectra of Cu_2ZnSnS_4 (black line) and $Cu_2ZnSn_{0.7}Ge_{0.3}S_4$ (red line) polycrystalline compounds measured with 514 nm excitation wavelengths. The main peaks are indicated with their frequencies.

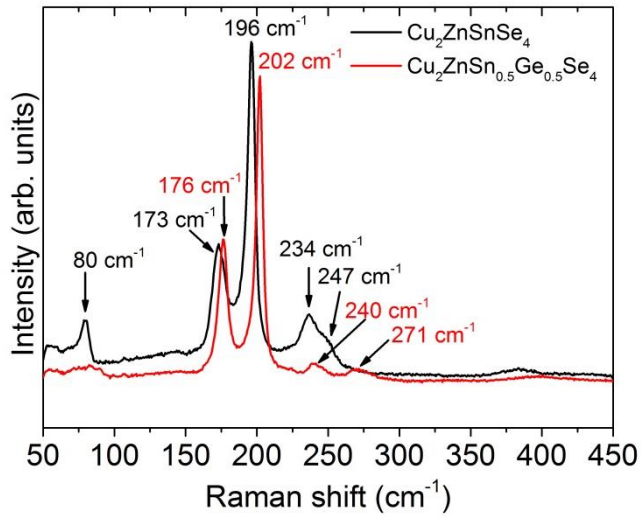

Figure 3.48. Raman spectra of $Cu_2ZnSnSe_4$ (black line) and $Cu_2ZnSn_{0.5}Ge_{0.5}Se_4$ (red line) polycrystalline compounds measured with 514 nm excitation wavelengths. The main peaks are indicated with their frequencies.

3.5.2.1. Secondary phases detection

It is interesting to reveal the usefulness of the Raman spectroscopy as a secondary phase detector technique. Figure 3.49 shows the Raman spectrum of CZTS polycrystalline compound synthesized from pure elements (section 3.1.1) measured with 514 nm excitation wavelength with the different contributions derived from the mathematical adjustment by Lorentzian curves of the different peaks. In each CZTS peak is indicated

the frequency of the plot adjusted by Lorentzian curves, and in parenthesis is the symmetry mode [41]. The presence of binary compounds is likely in these polycrystalline compounds because of their reaction issues in the synthesis process [42–44]. There are several secondary phases easy to identify with 514 nm excitation wavelength because their peaks do not overlap with the kesterite peaks structures like SnS, Sn_2S_3 and SnS_2. The peaks of SnS are placed in the region of 100-200 cm^{-1} and SnS_2 and Sn_2S_3 are in pre-resonance conditions with green light (514 nm), which are easy to detect in any CZTS Raman spectra [45,46]. In addition, there are the Cu_xSe and Cu_xS binary compounds which are not a problem to detect because the presence of their intense peaks occurs at low frequencies; furthermore the main peaks at higher frequencies do not overlap with other peaks from neither kesterite nor other secondary phases [41,47]. There are other secondary phases more complicated to detect, like monoclinic Cu_2SnS_3 (CTS) and ZnS when the kesterite (CZTS) samples are measured with 514 nm excitation wavelength. This is due to the overlapping and/or the low intensity of the main modes with this specific excitation wavelength (514 nm, green light). In the case of CTS, the spectrum is characterized by the main peaks at 290 cm^{-1} and 352 cm^{-1}, which is difficult to identify because these peaks are close to the main peaks of CZTS [45]. Moreover, there is the ZnS secondary phase, where the main Raman peak is located at 348 cm^{-1}, having a low intensity with green excitation wavelength and partially overlapping with CZTS [45]. To solve these problems with both secondary phases (CTS and ZnS), ultraviolet excitation wavelength (325 nm), which creates pre-resonant conditions, was used. The 325 nm excitation wavelengths are closer to the band gap of these secondary phases which allows detecting small amounts of these compounds in presence of CZTS. Figure 3.50 shows a clear example of Cu_2SnS_3 detection with 325 nm excitation wavelength for the CZTS polycrystalline compound synthesized with binary compounds (section 3.1.1). Moreover, Figure 3.51 is another example of the detection of ZnS with 325 nm excitation wavelength for the CZTS polycrystalline compound synthesized with pure elements (section 3.1.1). In both cases (Figure 3.50 and Figure 3.51) the Raman measurements were done in pre-resonant conditions. In the case of the ZnS, the enhancement of the signal by the pre-resonant conditions is large enough to observe the main peak at 349cm^{-1} and the presence of other two peaks at 696 and 1046 cm^{-1} corresponding to the 2^{nd} and 3^{rd} order modes, respectively.

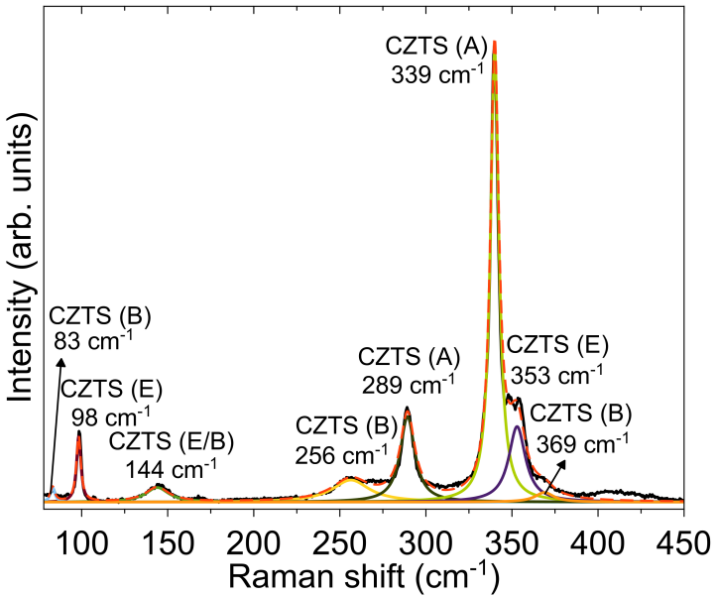

Figure 3.49. Raman spectrum of CZTS polycrystalline compound (black line) measured with 514 nm excitation wavelength with the different contributions derived from the mathematical adjustment by Lorentzian curves of the different peaks (colored lines), the orange dashed line is the sum of the Lorentzian curves. In each CZTS peak is indicated the frequency of the plot adjusted by Lorentzian curves and in parenthesis is the symmetry mode [41].

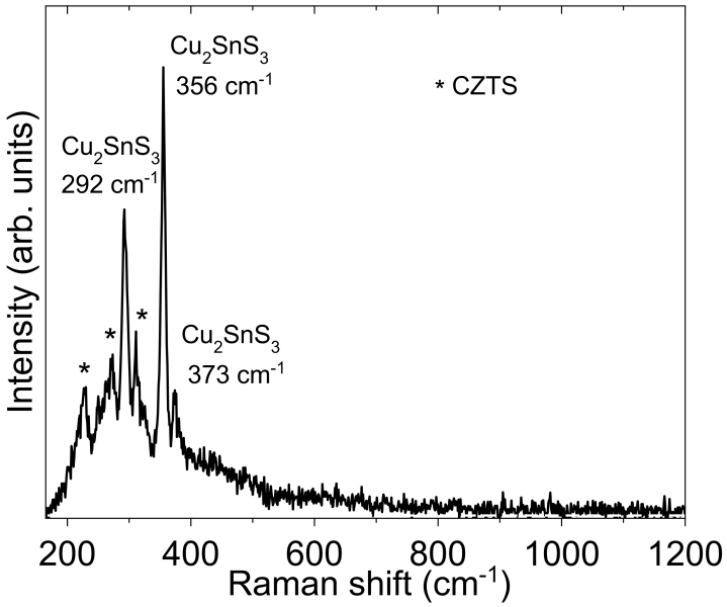

Figure 3.50. Raman spectrum of CZTS polycrystalline compound synthesized with binary compounds measured with 325 nm excitation wavelength. Note: the CZTS peaks are indicated with a * and the Cu2SnS3 peaks are indicated with its frequency.

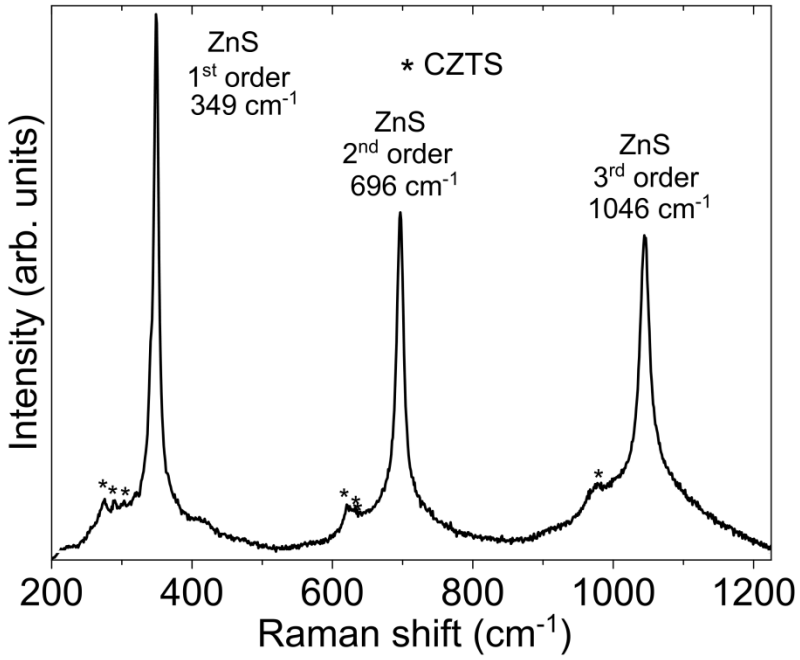

Figure 3.51. Raman spectrum of CZTS polycrystalline compound synthesized with pure elements measured with 325 nm excitation wavelength. Note: the CZTS peaks are indicated with a * and The ZnS peaks are indicated with its frequency.

3.6. Electrical characterization of kesterite compounds

This section presents the conductivity versus temperature measurements of sulfur and selenium single crystals.

3.6.1. Conductivity versus temperature measurements

3.6.1.1. Single crystals

All single crystals were determined p-type by Seebeck measurements using a heated probe and a standard multimeter as it was explained in chapter 2, section 2.5.

The conductivity, $\sigma(T)$, was extracted from I/V measurements using the van der Pauw configuration in the temperature interval from 10 to 300 K. The contacts were made with Indium-Gallium alloy.

The temperature dependence of the conductivity is shown in Figure 3.52 and Figure 3.53 for CZTGS and CZTGSe, respectively. Two distinct behaviors are explicitly observed in two different temperature ranges. Therefore, it seems that different transport mechanisms can take place for these CZGTS and CZTGSe single crystals.

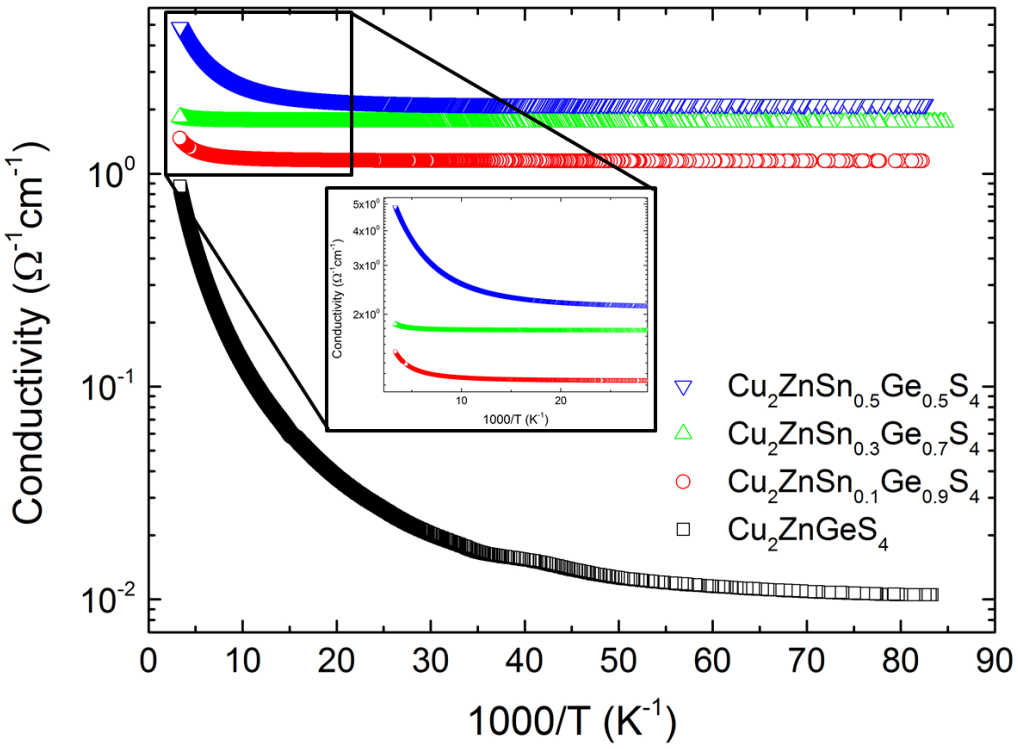

Figure 3.52. Temperature dependence of conductivity of $Cu_2ZnSn_{1-y}Ge_yS_4$ (CZTGS) single crystals

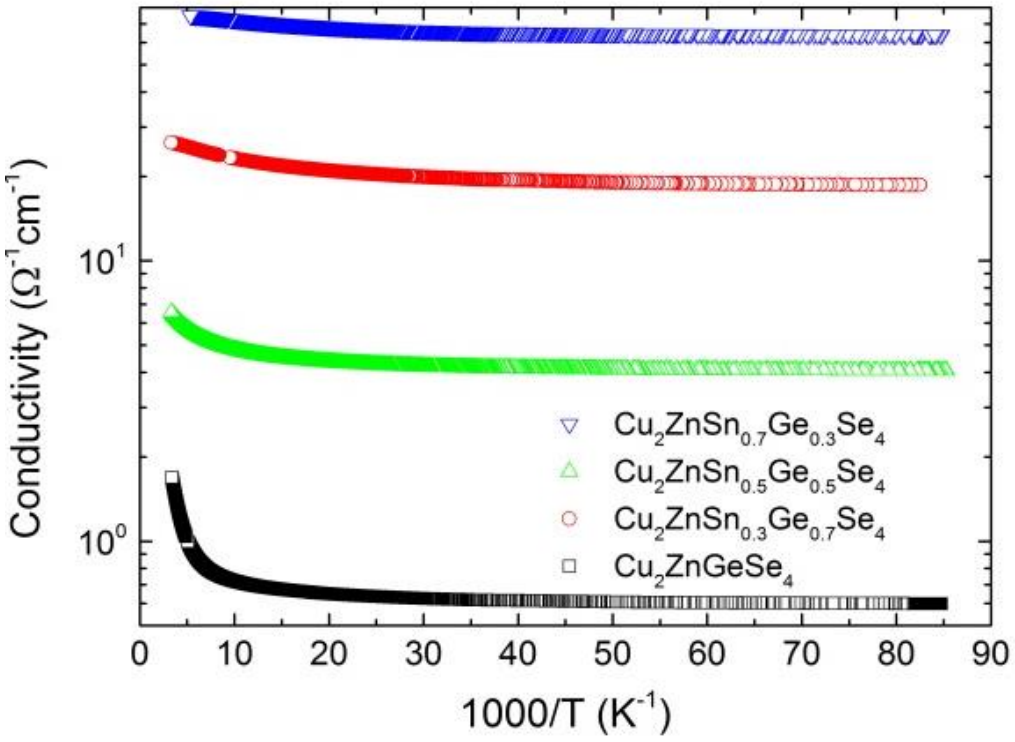

Figure 3.53. Temperature dependence of conductivity of $Cu_2ZnSn_{1-y}Ge_yS_4$ (CZTGSe) single crystals

The conductivity data σ can be quantitatively described by the equation:

$$\sigma(T)=\sigma_1 exp\left(-\left[T_0/T\right]^{1/4}\right)+\sigma_2 exp\left(-E_2/k_bT\right)+\frac{\sigma_3}{T^{1/2}}exp\left(-E_3/k_bT\right)$$

Equation 3-9

where σ_1, σ_2, σ_3 are pre-factors, T_0 is the Mott characteristic temperature, k_b is the Boltzmann constant, E_2 is the nearest neighbor hopping activation energy and E_3 is the grain boundary barrier energy.

The first term of Equation 3-9 denotes the Mott variable range hopping (*M-VRH*) on defects transport and the second term is the thermal activation (*TA*) conduction process. Transition from the *TA* to the *M-VRH* conduction regime takes place when it becomes energetically favorable for electrons to jump beyond the nearest-neighboring sites. Such situation is stimulated usually by lowering the temperature or increasing the microscopic disorder. The third term is related to the thermionic emission (*TE*) across grain boundaries. Here, the third term on the grain boundaries barrier is neglected because of the single crystal nature of the CZTGS and CZTGSe samples in this study. Then, Equation 3-9 is rewritten to Equation 3-10.

$$\sigma(T) = \sigma_1 exp\left(-\left[T_0/T\right]^{1/4}\right)+\sigma_2 exp\left(-E_2/k_bT\right)$$

Equation 3-10

The experimental data were fitted with both possible models, *M-VRH* and *TA*. It appears that the *TA* model applies better in the high temperature range down to 120 K and the M-*VRH* model applies better at lower interval temperatures from 120 K. Figure 3.54 and Figure 3.55 displays the variation of $ln\sigma$ vs $1000/T$ in the temperature range 120-300 K. As it follows from the second term of Equation 3-10, Equation 3-11, the plots of $ln\sigma$ vs $1000/T$ in the interval of the thermal activation conduction process should be represented by linear functions. Therefore, the activation energies E_2 can be determined from the linear fits of these plots. Equation 3-11 is given by:

$$\sigma(T) = \sigma_2 \exp\left(-E_2/k_bT\right)$$

Equation 3-11

After a visual inspection of the curves and regarding the correlation factors of the fittings, in most of the CZGTS compounds two linear fits with two different slopes were applied, the first one in the range of 310-215 K and the second between 160-120 K approximately. However, the experimental data have been fitted by only one linear fit in most of the CZTGSe single crystals with the exception of $Cu_2ZnGeSe_4$ that displays a different behavior.

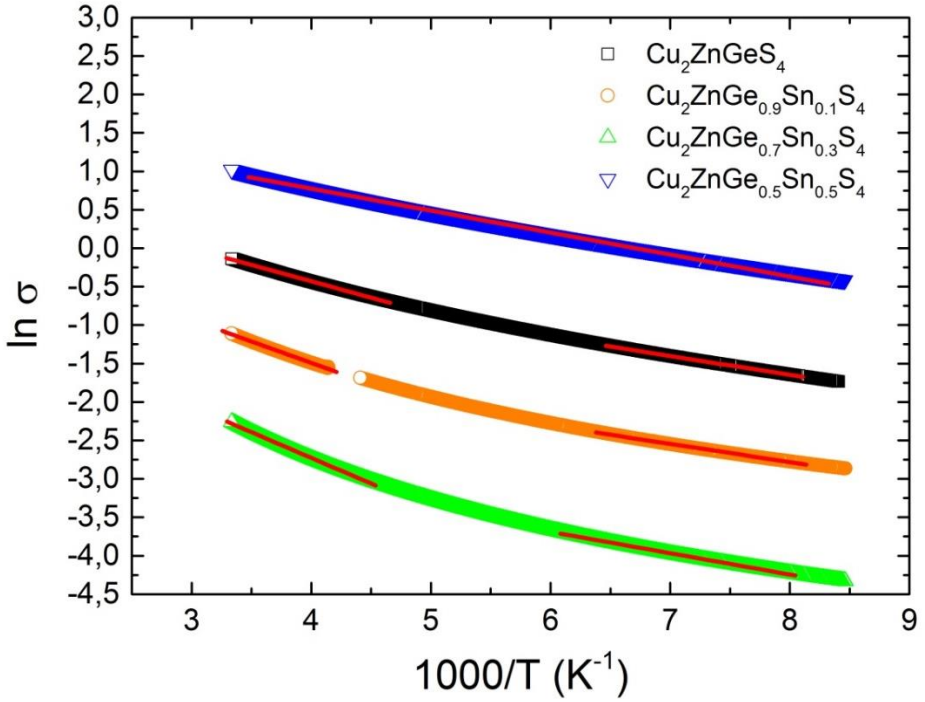

Figure 3.54. ln σ versus 1000/T. The red lines are the linear fits following the Equation 3-11.

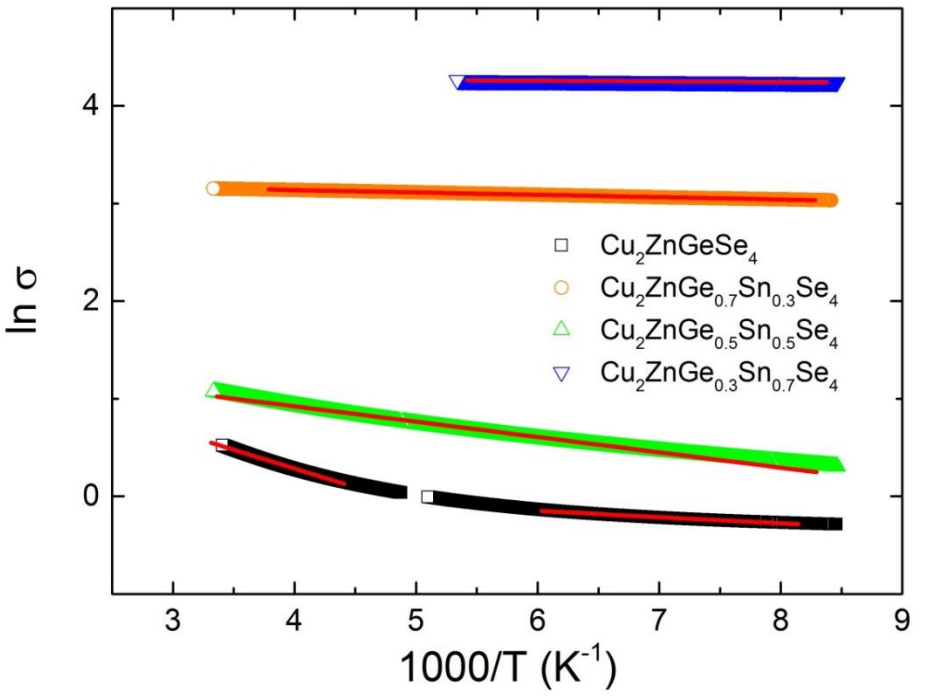

Figure 3.55. ln σ versus 1000/T. The red lines are the linear fits following the Equation 3-11.

Table 3.21 shows the activation energies E_2 obtained for the different CZTGS samples. The E_2 values at the highest temperatures when two slopes can be considered show an increase when the Ge content is decreasing. On other hand, the E_2 values in the lower range of the high temperature region appear to decrease when the Ge content is increasing. These behaviors may be due to the presence of different Germanium defects. Up to our knowledge, no activation energies of Germanium related defects in the kesterite compound have been already determined, making more difficult to discern the kind of defects present in these samples.

Table 3.21. Fitting parameters for the temperature dependent conductivity in CZTGS single crystals.

Sample	Thermal activation		
	$T_{initial}$	T_{final}	E_2 (meV)
Cu_2ZnGeS_4	215	311	36.76
	123	155	21.30
$Cu_2Zn\ Sn_{0.1}Ge_{0.9}S_4$	237	307	48.06
	123	157	20.41
$Cu_2Zn\ Sn_{0.3}Ge_{0.7}S_4$	220	310	57.52
	124	164	23.90
$Cu_2Zn\ Sn_{0.5}Ge_{0.5}S_4$	120	312	25.74

Table 3.22 shows the activation energies E_2 obtained for the CZTGSe samples. In this case, no correlation between the activation energy and Germanium content was found, apart from the lower obtained values compared to the case of the CZGTS samples.

Table 3.22. Fitting parameters for the temperature dependent conductivity in CZTGSe samples

Sample	Thermal activation		
	$T_{initial}$	T_{final}	E_2 (meV)
$Cu_2ZnGeSe_4$	227	302	33.18
	123	166	5.73
$Cu_2Zn\ Sn_{0.3}Ge_{0.7}Se_4$	124	301	2.11
$Cu_2Zn\ Sn_{0.5}Ge_{0.5}Se_4$	121	298	13.52
$Cu_2Zn\ Sn_{0.7}Ge_{0.3}Se_4$	121	288	2.09

Figure 3.56 and Figure 3.57 show the variation of $ln\sigma$ with $T^{-1/4}$ in the temperature interval of 12-120 K. As mentioned above, the Mott variable range hopping fits better to the experimental results in this lower temperature range. According to [48], the experimental data were linearly fitted using Equation 3-12:

$$\sigma(T) = \sigma_1 \exp\left(-\left[T_0/T\right]^{1/4}\right)$$

Equation 3-12

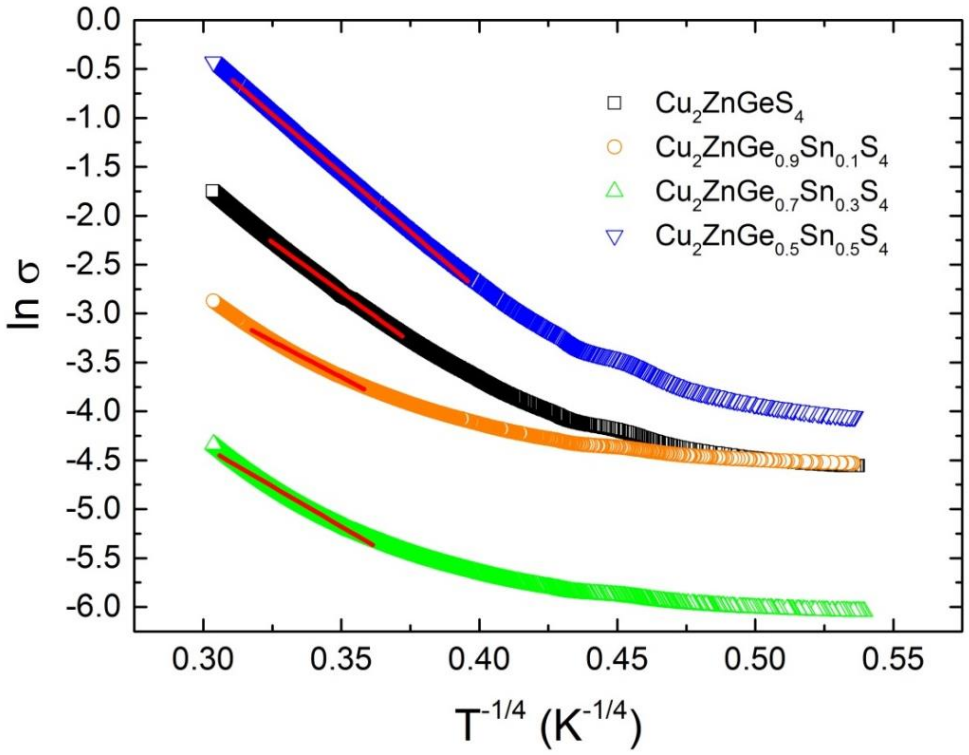

Figure 3.56. $ln\sigma$ versus $T^{-1/4}$ of $Cu_2ZnSn_{1-y}Ge_yS_4$ single crystals. The red lines are fitting by Mott *VRH* conduction mechanism by Equation 3-12.

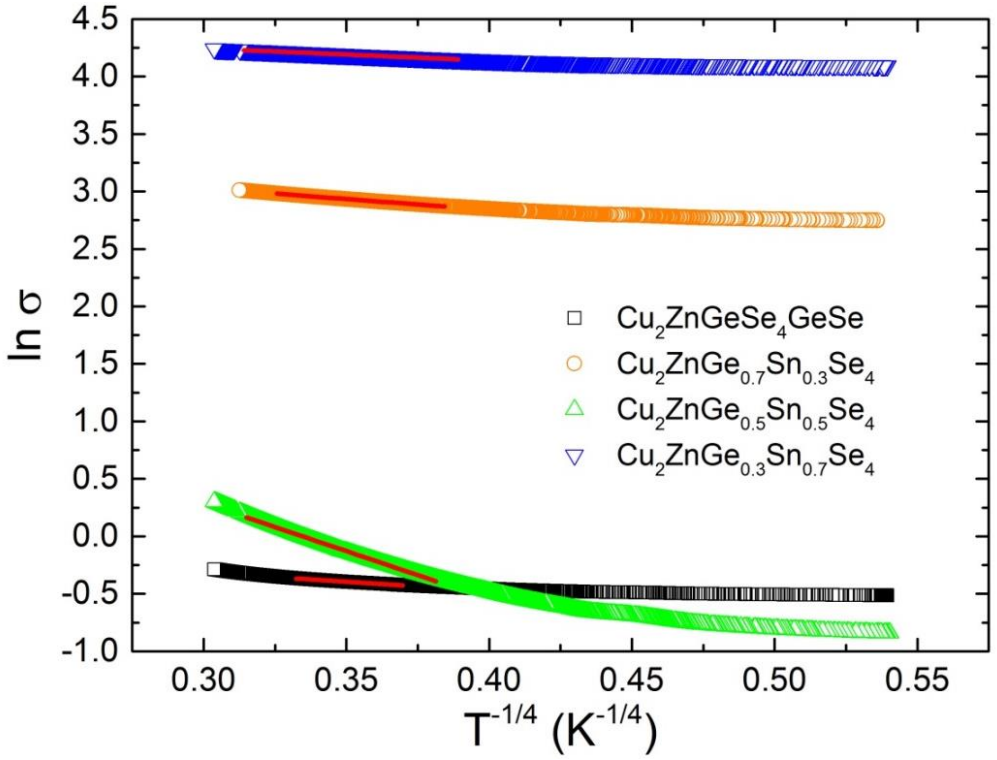

Figure 3.57. *lnσ* versus $T^{-1/4}$ of $Cu_2ZnSn_{1-y}Ge_yS_4$ single crystals. The red lines are fitting by Mott *VRH* conduction mechanism by Equation 3-12.

Table 3.23 and Table 3.24 shows the characteristic parameters of the Mott *VHR* conduction mechanism. T_v and T_m values are also included, which refer to the initial and final fitting temperature ranges respectively. T_0 is the characteristic *M-VRH* temperature, extracted from the fittings done following Equation 3-12, and the parameter *W* is the width of the acceptor band $W = (Tv^3T_0)^{1/4}$ [49–51] .

Table 3.23. Mott Fitting parameters of the temperature dependent conductivity for CZTGS samples

Sample	**M-VRH**			
	T_0 (K)	**T_v**	**T_m**	**W (meV)**
Cu_2ZnGeS_4	$17.40x10^4$	52.20	90.43	34.18
$Cu_2Zn\ Sn_{0.1}Ge_{0.9}S_4$	$4.75x10^4$	60.73	98.33	27.68
$Cu_2Zn\ Sn_{0.3}Ge_{0.7}S_4$	$7.33x10^4$	56.64	114.22	29.28
$Cu_2Zn\ Sn_{0.5}Ge_{0.5}S_4$	$33.51x10^4$	40.71	107.28	33.42

Table 3.24. Mott Fitting parameters of the temperature dependent conductivity for CZTGSe samples.

Sample	M-VRH			
	T_0 (K)	T_v	T_m	W (meV)
$Cu_2ZnGeSe_4$	5.39	53.51	81.85	2.60
$Cu_2Zn\ Sn_{0.3}Ge_{0.7}Se_4$	12.38	45.80	88.84	2.85
$Cu_2Zn\ Sn_{0.5}Ge_{0.5}Se_4$	4892.88	47.30	101.53	13.00
$Cu_2Zn\ Sn_{0.7}Ge_{0.3}Se_4$	1.25	43.61	102.74	1.55

In the Mott *VRH* interval, the band width of the band acceptor (*W*) has been found to vary between 27 to 34 meV for CZTGS, being similar to that reported in [49,50] for the CZTS compound. From the literature [48,50], it was proposed that the Cu_{Zn} defect was the most probable source of acceptors with a similar *W* values. In this work, it was determined in the section 3.3.1 of the structural properties characterization by Rietveld refinements that the predominant defect in the samples was $Zn^{2+}_{Sn,Ge}$ (see Table 3.12). For this reason, here it is proposed that the band acceptor (*W*) determined for the CZGTS is due to the $Zn^{2+}_{Sn,Ge}$ defect. For CZTGSe, there is more divergence in the band acceptor width, from 1.5 to 13 meV. In this case, it is more difficult to achieve a conclusion because from the structural properties characterization (section 3.1.1) it appears more than one type of defects (see Table 3.13). The *W* values might be related to the Cu_{Zn} or Zn^{2+}_{Cu} defects. The higher widths of the acceptor band (*W*) in CZGTS are attributed to the enhanced microscopic disorder in these compounds with respect to CZGTSe ones. Moreover, the higher values of the CZGTS compound match with the higher amount of defects present than in the case of CZGTSe compounds, presented in the section 3.1.1. Indeed, the amount of the defects in CZGTS was higher, in some cases one order of magnitude, than the ones determined for CZGTSe. This relation also happens in the band width of the acceptor band (*W*). The values of T_0, the Mott characteristic temperature, are inversely related to the density (DOS) of localized states near the Fermi level [52]. CZTGS samples show higher T_0 than those of CZTGSe, probably indicating that there is less density of localized states near the Fermi level for CZTGS compounds [53].

3.7. References

[1] I.D. Olekseyuk, I.V. Dudchak, L.V. Piskach, Phase equilibria in the Cu_2S–ZnS–SnS_2 system, J. Alloys Compd. 368 (2004) 135–143. doi:10.1016/j.jallcom.2003.08.084.

[2] R.B. Schwarz, W.L. Johnson, Formation of an Amorphous Alloy by Solid-State reactuion of pure polycrystalline metals, Phys. Rev. Lett. 51 (1983) 415–418.

[3] V. Kheraj, K.K. Patel, S.J. Patel, D.V. Shah, Synthesis and characterisation of Copper Zinc Tin Sulphide (CZTS) compound for absorber material in solar-cells, J. Cryst. Growth. 362 (2013) 174–177. doi:10.1016/j.jcrysgro.2011.10.034.

[4] I. V. Dudchak, L. V. Piskach, Phase equilibria in the Cu_2SnSe_3 –$SnSe_2$ –ZnSe system, J. Alloys Compd. 351 (2003) 145–150.

[5] O. V Parasyuk, L. V Piskach, Y.E. Romanyuk, I.D. Olekseyuk, V.I. Zaremba, V.I. Pekhnyo, Phase relations in the quasi-binary Cu_2GeS_3–ZnS and quasi-ternary Cu_2S–Zn(Cd)S–GeS_2 systems and crystal structure of Cu_2ZnGeS_4, J. Alloys Compd. 397 (2005) 85–94. doi:http://dx.doi.org/10.1016/j.jallcom.2004.12.045.

[6] Y.E. Romanyuk, O. V Parasyuk, Phase equilibria in the quasi-ternary Cu_2Se–ZnSe–$GeSe_2$ system, J. Alloys Compd. 348 (2003) 195–202.

[7] I. V. Bodnar, Growth and Properties of $CuAlS_{2x}Se_{2(1–x)}$ Single Crystals, Inorg. Mater. 38 (2002) 647–651. doi:10.1023/A:1016271804632.

[8] E. Garcia-Llamas, J.M. Merino, R. Serna, X. Fontané, I.A. Victorov, A. Pérez-Rodríguez, M. León, I.V. Bodnar, V. Izquierdo-Roca, R. Caballero, Wide band-gap tuning $Cu_2ZnSn_{1–x}Ge_xS_4$ single crystals: Optical and vibrational properties, Sol. Energy Mater. Sol. Cells. (2015) 1–7. doi:10.1016/j.solmat.2015.12.021.

[9] A. Khare, B. Himmetoglu, M. Johnson, D.J. Norris, M. Cococcioni, E.S. Aydil, Calculation of the lattice dynamics and Raman spectra of copper zinc tin chalcogenides and comparison to experiments, J. Appl. Phys. 111 (2012) 083707/1-9. doi:10.1063/1.4704191.

[10] D. Chen, N.M. Ravindra, Electronic and optical properties of Cu_2ZnGeX_4 (X=S,

Se and Te) quaternary semiconductors, J. Alloy Compd. 579 (2013) 468–472. doi:10.1016/j.jallcom.2013.06.048.

[11] S. Siebentritt, S. Schorr, Kesterites — a challenging material for solar cells, Prog. Photovoltaics Res. Appl. 20 (2012) 512–519. doi:10.1002/pip.2156.

[12] S. Chen, A. Walsh, X.G. Gong, S.H. Wei, Classification of lattice defects in the kesterite Cu_2ZnSnS_4 and $Cu_2ZnSnSe_4$ earth-abundant solar cell absorbers, Adv. Mater. 25 (2013) 1522–1539. doi:10.1002/adma.201203146.

[13] L. Vegard, Die Konstitution der Mischkristalle und die Raumfüllung der Atome, Zeitschrift Für Phys. 5 (1921) 17–26. doi:10.1007/BF01349680.

[14] R.D. Shannon, Revised Effective Ionic Radii and Systematic Studies of Interatomie Distances in Halides and Chaleogenides, Acta Crystallogr. A32 (1976) 751–767. doi:10.1107/S0567739476001551.

[15] V.F. Sears, Neutron scattering lengths and cross sections, Neutron News. 3 (1992) 26–37. doi:10.1080/10448639208218770.

[16] A. Lafond, L. Choubrac, C. Guillot-Deudon, P. Deniard, S. Jobic, Crystal structures of photovoltaic chalcogenides, an intricate puzzle to solve: The cases of CIGSe and CZTS materials, Zeitschrift Fur Anorg. Und Allg. Chemie. 638 (2012) 2571–2577. doi:10.1002/zaac.201200279.

[17] L.E. Valle Rios, K. Neldner, G. Gurieva, S. Schorr, Existence of off-stoichiometric single phase kesterite, J. Alloys Compd. 657 (2016) 408–413. doi:10.1016/j.jallcom.2015.09.198.

[18] P. Lautenschlager, M. Garriga, S. Logothetidis, M. Cardona, Interband critical points of GaAs and their temperature dependence, Phys. Rev. B. 35 (1987) 9174–9189. doi:10.1103/PhysRevB.35.9174.

[19] S. Levcenko, G. Gurieva, M. Guc, A. Nateprov, Optical constants of Cu_2ZnSnS_4 bulk crystals, Mold. J. Phys. Sci. 8 (2009) 173–177.

[20] M. León, S. Levcenko, R. Serna, G. Gurieva, A. Nateprov, J.M. Merino, E.J. Friedrich, U. Fillat, S. Schorr, E. Arushanov, Optical constants of Cu_2ZnGeS_4 bulk

crystals, J. Appl. Phys. 108 (2010) 1–5. doi:10.1063/1.3500439.

[21] S. Chen, X.G. Gong, A. Walsh, S.H. Wei, Electronic structure and stability of quaternary chalcogenide semiconductors derived from cation cross-substitution of II-VI and I-III-VI_2 compounds, Phys. Rev. B - Condens. Matter Mater. Phys. 79 (2009) 1–10. doi:10.1103/PhysRevB.79.165211.

[22] S. Chen, X.G. Gong, A. Walsh, S.H. Wei, Crystal and electronic band structure of Cu_2ZnSnX_4 (X=S and Se) photovoltaic absorbers: First-principles insights, Appl. Phys. Lett. 94 (2009) 1–3. doi:10.1063/1.3074499.

[23] M. Morihama, F. Gao, T. Maeda, T. Wada, Crystallographic and optical properties of $Cu_2Zn(Sn_{1-x}Ge_x)Se_4$ solid solution, Jpn. J. Appl. Phys. 53 (2014) 1–6. doi:10.7567/JJAP.53.04ER09.

[24] M. Schleich, A. Wold, Optical and Electrical Properties of Quaternary Chalcogenides, Mater. Res. Bull. 12 (1977) 111–114. doi:10.1016/0025-5408(77)90150-7.

[25] S.H. Han, A.M. Hermann, F.S. Hasoon, H.A. Al-Thani, D.H. Levi, Effect of Cu deficiency on the optical properties and electronic structure of $CuInSe_2$ and $CuIn_{0.8}Ga_{0.2}Se_2$ determined by spectroscopic ellipsometry, Appl. Phys. Lett. 85 (2004) 576–578. doi:10.1063/1.1776616.

[26] S. Levcenko, M. León, G. Gurieva, R. Serna, J.M. Merino, E.J. Friedrich, E. Arushanov, I. V. Bodnar, Comparative study of tetragonal $Cu_2In_7Se_{11.5}$ and trigonal $CuIn_5Se_8$ by spectroscopic ellipsometry, Mater. Chem. Phys. 125 (2011) 77–81. doi:10.1016/j.matchemphys.2010.08.074.

[27] D. Schmid, M. Ruckh, F. Grunwald, H.W. Schock, Chalcopyrite/defect chalcopyrite heterojunctions on the basis of $CuInSe_2$, J. Appl. Phys. 73 (1993) 2902.

[28] J.G. Albornoz, R. Serna, M. León, Optical properties and electronic structure of polycrystalline $Ag_{1-x}Cu_xInSe_2$ alloys, J. Appl. Phys. 97 (2005) 1–7. doi:10.1063/1.1899243.

[29] E. Garcia-Llamas, M. Guc, I.V. Bodnar, X. Fontané, R. Caballero, J.M. Merino, M. León, V. Izquierdo-Roca, Multiwavelength excitation Raman scattering of $Cu2ZnSn_{1-x}Ge_x(S,Se)_4$ solid solution in single crystals for earth abundant photovoltaic application, J. Alloys Compd. (2016) Accepted.

[30] M. Guc, S. Levcenko, I.V. Bodnar, V. Izquierdo-roca, X. Fontane, L.V. Volkova, E. Arushanov, A. Pérez-Rodríguez, Polarized Raman scattering study of kesterite type Cu_2ZnSnS_4 single crystals, Sci. Rep. 5 (2016) 19414/1-7. doi:10.1038/srep19414.

[31] M. Guc, A.P. Litvinchuk, S. Levcenko, V. Izquierdo-Roca, X. Fontané, M.Y. Valakh, E. Arushanov, A. Pérez-Rodríguez, Optical phonons in the wurtzstannite Cu_2ZnGeS_4 semiconductor: Polarized Raman spectroscopy and first-principle calculations, Phys. Rev. B. 89 (2014) 1–7. doi:10.1103/PhysRevB.89.205205.

[32] M. Guc, S. Levcenko, V. Izquierdo-Roca, X. Fontané, E. Arushanov, A. Pérez-Rodríguez, Polarized Raman scattering analysis of $Cu_2ZnSnSe_4$ and $Cu_2ZnGeSe_4$ single crystals, J. Appl. Phys. 114 (2013) 1–9. doi:10.1063/1.4830028.

[33] M. León, S. Levcenko, R. Serna, I. V. Bodnar, A. Nateprov, M. Guc, G. Gurieva, N. Lopez, J.M. Merino, R. Caballero, S. Schorr, A. Perez-Rodriguez, E. Arushanov, Spectroscopic ellipsometry study of $Cu_2ZnSnSe_4$ bulk crystals, Appl. Phys. Lett. 105 (2014) 061909–1/4. doi:10.1063/1.4892548.

[34] X. Fontané, V. Izquierdo-Roca, E. Saucedo, S. Schorr, V.O. Yukhymchuk, M.Y. Valakh, A. Perez-Rodriguez, J.R. Morante, Vibrational properties of stannite and kesterite type compounds: Raman scattering analysis of $Cu_2(Fe,Zn)SnS_4$, J. Alloys Compd. 539 (2012) 190–194. doi:10.1016/j.jallcom.2012.06.042.

[35] H. Neumann, Lattice vibrations in $A^IB^{III}C^{VI}_2$ chalcopyrite compounds, Helv. Phys. Acta. 58 (n.d.) 337–346. http://cat.inist.fr/?aModele=afficheN&cpsidt=8441551 (accessed June 12, 2016).

[36] C. Rincón, M. Quintero, C. Power, E. Moreno, E. Quintero, J.A. Henao, M.A. Macías, M. Morocoima, Raman spectra of $Cu_2B^{II}C^{IV}X_4{}^{VI}$ magnetic quaternary semiconductor compounds with tetragonal stannite type structure, J. Appl. Phys.

117 (2015). doi:10.1063/1.4921438.

[37] M. Ishii, K. Shibata, H. Nozaki, Anion Distributions and Phase Transitions in $CuS_{1-x}Se_x$(x= 0-1) Studied by Raman Spectroscopy, J. Solid State Chem. 105 (1993) 504–511. doi:http://dx.doi.org/10.1006/jssc.1993.1242.

[38] A. Khare, B. Himmetoglu, M. Cococcioni, E.S. Aydil, First principles calculation of the electronic properties and lattice dynamics of $Cu_2ZnSn(S_{1-x}Se_x)4$, J. Appl. Phys. 111 (2012) 123704/1-8. doi:10.1063/1.4728232.

[39] M. Dimitrievska, H. Xie, A. Fairbrother, X. Fontané, G. Gurieva, E. Saucedo, A. Pérez-Rodríguez, S. Schorr, V. Izquierdo-Roca, Multiwavelength excitation Raman scattering of $Cu_2ZnSn(S_xSe_{1-x})_4$ ($0 \leq x \leq 1$) polycrystalline thin films: Vibrational properties of sulfoselenide solid solutions, Appl. Phys. Lett. 105 (2014) 031913/1-5. doi:10.1063/1.4891333.

[40] M.Y. Valakh, A.P. Litvinchuk, V.M. Dzhagan, V.O. Yukhymchuk, A.M. Yaremko, Y.A. Romanyuk, M. Guc, I. V Bodnar, A. Pérez-Rodríguez, D.R.T. Zahn, Fermi resonance in the phonon spectra of quaternary chalcogenides of the type Cu_2ZnGeS_4., J. Phys. Condens. Matter. 28 (2016) 065401/7. doi:10.1088/0953-8984/28/6/065401.

[41] X. Fontané, L. Calvo-Barrio, V. Izquierdo-Roca, E. Saucedo, A. Pérez-Rodriguez, J.R. Morante, D.M. Berg, P.J. Dale, S. Siebentritt, In-depth resolved Raman scattering analysis for the identification of secondary phases: Characterization of Cu_2ZnSnS_4 layers for solar cell applications, Appl. Phys. Lett. 98 (2011) 1–3. doi:10.1063/1.3587614.

[42] Q. Guo, G.M. Ford, W.C. Yang, B.C. Walker, E.A. Stach, H.W. Hillhouse, R. Agrawal, Fabrication of 7.2% efficient CZTSSe solar cells using CZTS nanocrystals, J. Am. Chem. Soc. 132 (2010) 17384–17386. doi:10.1021/ja108427b.

[43] H. Katagiri, K. Jimbo, S. Yamada, T. Kamimura, W.S. Maw, T. Fukano, T. Ito, T. Motohiro, Enhanced conversion efficiencies of Cu_2ZnSnS_4-based thin film solar cells by using preferential etching technique, Appl. Phys. Express. 1 (2008)

041201–1/2. doi:10.1143/APEX.1.041201.

[44] D.B. Mitzi, O. Gunawan, T.K. Todorov, K. Wang, S. Guha, The path towards a high-performance solution-processed kesterite solar cell, Sol. Energy Mater. Sol. Cells. 95 (2011) 1421–1436. doi:10.1016/j.solmat.2010.11.028.

[45] X. Fontané, Caracterización por espectroscopia Raman de semiconductores Cu_2ZnSnS_4 para nuevas tecnologías fotovoltaicas, 2013.

[46] X. Fontane, V. Izquierdo-Roca, A. Fairbrother, M. Espindola-Rodriguez, S. Lopez-Marino, M. Placidi, T. Jawhari, E. Saucedo, A. Perez-Rodriguez, Selective detection of secondary phases in $Cu_2ZnSn(S,Se)_4$ based absorbers by pre-resonant Raman spectroscopy, 2013 IEEE 39th Photovolt. Spec. Conf. 4 (2013) 2581–2584. doi:10.1109/PVSC.2013.6745001.

[47] T.K. Todorov, J. Tang, S. Bag, O. Gunawan, T. Gokmen, Y. Zhu, D.B. Mitzi, Beyond 11% effi ciency: Characteristics of State-of-the-Art $Cu_2ZnSn(S,Se)_4$ Solar Cells, Adv. Energy Mater. 3 (2013) 34–38. doi:10.1002/aenm.201200348.

[48] A. Nagaoka, H. Miyake, T. Taniyama, K. Kakimoto, K. Yoshino, Correlation between intrinsic defects and electrical properties in the high-quality Cu_2ZnSnS_4, Appl. Phys. Lett. 103 (2013) 1–4.

[49] M. Guc, R. Caballero, K.G. Lisunov, N. López, E. Arushanov, J.M. Merino, M. León, Disorder and variable-range hopping conductivity in Cu_2ZnSnS_4 thin films prepared by flash evaporation and post-thermal treatment, J. Alloys Compd. 596 (2014) 140–144. doi:10.1016/j.jallcom.2014.01.177.

[50] K.G. Lisunov, M. Guk, A. Nateprov, S. Levcenko, V. Tezlevan, E. Arushanov, Features of the acceptor band and properties of localized carriers from studies of the variable-range hopping conduction in single crystals of p-Cu_2ZnSnS_4, Sol. Energy Mater. Sol. Cells. 112 (2013) 127–133. doi:10.1016/j.solmat.2013.01.027.

[51] K.G. Lisunov, M. Guc, S. Levcenko, D. Dumcenco, Y.S. Huang, G. Gurieva, S. Schorr, E. Arushanov, Energy spectrum of near-edge holes and conduction mechanisms in $Cu_2ZnSiSe_4$ single crystals, J. Alloys Compd. 580 (2013) 481–486. doi:10.1016/j.jallcom.2013.06.156.

[52] N.F. Mott, E.A. Davis, Electronic processes in non-crystalline materials, 1971. doi:10.1016/0040-6090(72)90068-5.

[53] V. Kosyak, M.A. Karmarkar, M.A. Scarpulla, Temperature dependent conductivity of polycrystalline Cu_2ZnSnS_4 thin films, Appl. Phys. Lett. 100 (2012) 1–6.

PART II: THIN FILMS CHARACTERIZATION

Chapter 4

Device Fabrication and Characterization

This chapter presents the fabrication of the thin films by two rapid deposition processes, flash and thermal evaporation. Moreover, it shows different thermal treatments changing plateau times and heating rates, the chemical composition evolution of the thin films after different chemical etchings and sulfurization/sulfoselenization processes, and the fabrication of the solar cells. Finally, it is characterized the solar cells by J-V and EQE measurements.

4.1. Thin films deposition

4.1.1. Flash evaporation

The flash evaporation is a rapid deposition process and appropriate when attempting to evaporate compounds whose constituent elements have very different vapor pressure as it could be the case to obtain kesterite thin films. Figure 4.1 shows a picture of the flash evaporation equipment used in this work. The powder material was introduced inside the vibration container. This container had a vibration speed selector, which made possible the control of the rate with which the powder material came into the hot crucible, thus controlling the deposition rate of the thin film. The powder passed through the quartz tube to transfer it to the hot molybdenum crucible. The temperature of the crucible was around 1273 K, which produced an instantaneous evaporation of the powder onto the substrates. The system was equipped with a quartz microbalance to in-situ control the thickness of the thin film deposited on the substrate. All the system was closed under a steel bell to be able to perform vacuum. The base pressure was of the order of 10^{-6} mbar.

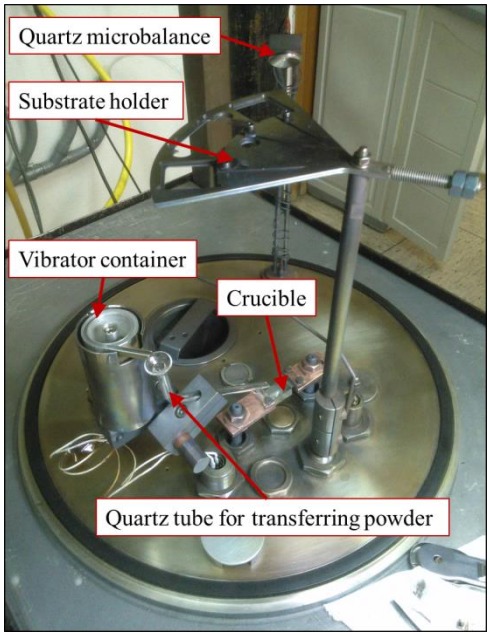

Figure 4.1. Flash evaporation system

The quaternary, ternary and binary bulk compounds synthesized by solid state reaction, detailed in section 3.1.1 were used as evaporation material to perform the flash deposition. Before flash evaporation, these compounds were grinded to a grain size range of 100-200 µm and introduced in the container shown in Figure 4.1.

Thin films were grown onto molybdenum coated soda-lime glass substrates by flash evaporation at different nominal substrate temperatures, T_{sub}, between 373 and 573 K. The thicknesses of the kesterite thin films were between 0.5 and 1 μm approximately.

Table 4.1 shows the substrate temperatures and the composition of the films and the source materials.The source material and the most of the films show Cu-poor, Sn-poor and Zn-rich composition. As it can be seen, there are substantial composition differences between the samples, despite the initial source material was the same. The reason of this fact might be due to the unreliable control of the evaporation rate, which affects the vacuum pressure inside the chamber. This change in the pressure affected directly to the rate and the way how the evaporated elements were incorporated in the substrate. This scenario most likely affected directly the final composition of the thin films and made impossible to achieve a fine control of the thin film deposition; as can be seen in EF3, EF4 and EF6, EF7 with the same substrate temperature of 478 K and 573 K, respectively. Although the substrate temperature and the source material are the same for EF3, EF4 and EF6, EF7, respectively, the final composition between EF3 and EF4 are clearly different as well as in the case of EF6 and EF7 (see Table 4.1).

Table 4.1. Chemical composition measured by EDX of source material and the thin films as grown by flash evaporation. Also, it is indicated the substrate temperature (T_{sub}).

Sample name	**T_{sub} (K)**	**Cu (at%)**	**Zn (at%)**	**Sn (at%)**	**S (at%)**	**Cu / (Zn+Sn)**	**Zn/Sn**	**S/M**
Source material	--	**23.19**	**15.89**	**11.7**	**49.23**	**0.84**	**1.35**	**0.97**
EF1	300	16.49	17.61	12.02	53.89	0.56	1.47	1.17
EF2	373	16.77	16.45	15.33	50.41	0.53	1.07	1.04
EF3	478	11.67	11.53	27.46	51.20	0.30	0.42	1.01
EF4	478	14.40	7.67	24.42	53.47	0.45	0.31	1.15
EF5	573	18.83	10.91	15.74	55.29	0.71	0.69	1.22
Source material	--	**23.57**	**19.71**	**10.35**	**46.37**	**0.78**	**1.90**	**0.86**
EF6	573	15.44	16.15	16.49	52.31	0.47	0.98	1.09
EF7	573	25.23	18.44	8.5	48.14	0.94	2.17	0.92

4.1.2. Thermal evaporation

The vacuum system used for the thermal evaporation is the same than that used for the flash evaporation (see Figure 4.1). Now, neither the container nor the quartz tube were used for these growth processes. The compounds were grinded to a grain size range of 100-200 μm and the powders were placed directly inside the Molybdenum crucible with a maximum of five grams of the precursor material. The powders were thermally evaporated at nominal substrate temperatures between 373 and 523 K onto Mo coated soda-lime glass. The crucible was heated up progressively, keeping the evaporation rate between 10 and 30 Å/s until 1393 K. The base pressure was of 10^{-6} mbar. The thicknesses of the kesterite thin films were between 0.5 and 1.5 μm approximately. This deposition process presents the advantage that in only 12 minutes it was possible to grow 1.5 μm of kesterite thin films, reducing the costs considerably [1].

Table 4.2 shows the chemical composition of the source material and the as-grown thin films by thermal evaporation. Moreover, it is indicated the substrate temperature at which the thin film was grown. In the ET1 sample, 100 mg of commercial ZnS were added to the source material to ensure a Zn-rich thin film. Using this equipment, a preferential re-evaporation of Zn was observed during the flash evaporation process independent of the evaporation source used; this is related to the high partial vapor pressure of Zn [2]. Unfortunately, the final composition of ET1 shows a Zn poor thin film, although, the final ET1 composition was better than ET2. ET2 sample shows a very low content of zinc and copper. ET7 source material was obtained thanks to Kai Neldner from HZB (Berlin). It is clear that none of them present a suitable composition (Cu-poor, Zn-rich [3]) to achieve a good efficiency but it is expected to improve the composition by thermal treatments and chemical etchings as it will be explained in section 4.2. The effect of the thermal treatments was studied in more detailed with samples ET4, ET6 and ET7. The inability to reproduce similar compositions of the samples using the same source material is due to the lack of reproducibility of this evaporation technique. The main problem detected was that a small amount of humidity inside the powder made the evaporation process unstable, because of the transition of the water to vapor state when the powders were heated up. The vapor expanded suddenly inside the powder and changed the evaporation ratio

and, as a consequence, the vacuum pressure of the chamber. At the end, these changes affected directly to the final composition because the source material was not evaporated homogeneously.

Table 4.2. Chemical composition measured by EDX of source material and the as-grown thin films by thermal evaporation. Also, it is indicated the substrate temperature (T_{sub}).

Sample name	T_{sub} (K)	Cu (at%)	Zn (at%)	Sn (at%)	S (at%)	Cu / (Zn+Sn)	Zn/Sn	S/M
Source material	--	**23.19**	**15.89**	**11.7**	**49.23**	**0.84**	**1.35**	**0.97**
ET1	603	23.36	9.11	14.24	51.39	1.00	0.64	1.10
ET2	603	17.41	6.63	25.44	50.18	0.54	0.26	1.01
Source material	--	**23.57**	**19.71**	**10.35**	**46.37**	**0.78**	**1.90**	**0.86**
ET3	523	28.80	11.84	13.07	47.35	1.16	0.91	0.88
ET4	623	36.21	16.78	4.17	42.84	1.73	4.02	0.75
ET5	623	27.44	18.63	8.84	45.09	1.00	2.11	0.82
ET6	623	42.09	8.02	8.36	41.53	2.57	0.96	0.71
Source material	--	**27.27**	**14.39**	**15.81**	**42.53**	**0.90**	**0.91**	**0.74**
ET7	523	28.85	13.54	14.37	43.25	1.03	0.94	0.76

4.2. Thermal treatments

As-evaporated samples were annealed at 823 K for one hour in Ar atmosphere (P~100 Pa) in a partially closed graphite container placed inside a quartz tube furnace. Elemental sulfur (120 mg) was supplied by placing the desired amount into the graphite box prior to heating. Different plateau times (30 and 60 minutes) and heating rates (2, 5, 10 and 20 K/minute) were used for the thermal treatments, and the samples were cooled down naturally until room temperature.

The flash evaporated samples were used to understand how the plateau time affects the composition and the thermal evaporation samples were used to understand how the different heating rates affect the thin film composition.

Table 4.3 shows the changes in chemical composition of the as-grown thin films by flash evaporation exposed to different thermal treatments via variation of the plateau time at the maximum temperature. As it can be seen, in the first thermal treatment with a plateau of 30 minutes, there was a general re-evaporation of all the elements and inclusion of the sulfur anion inside the thin film. The 60 minutes' plateau was applied in EF1, EF2, EF3 and EF4 samples and it can be observed a decrease in the amount of Cu and Sn. At this temperature of the thermal treatments a loss of Sn due to the SnS re-evaporation was expected, as it was reported in [2]. The Zn element diminishes clearly in the EF3 and EF4 samples and more slightly in the EF1 sample comparing with the as-grown thin film composition. In EF2 sample, the amount of Zn increased with respect to the initial composition. As a general tendency, the thermal treatments produced a decrease of the cation amounts and an increase of the anion amount. Moreover, the impact in the initial composition of the different plateau times (30 and 60 minutes) was not significant. In other words, the plateau time was not a critical aspect in the chemical composition changes. In both plateaus of 30 and 60 minutes, the cations re-evaporation followed the same tendency.

Table 4.3. Chemical composition measured by EDX of as-grown thin films by flash evaporation and after the thermal treatments. Also, it is indicated the different plateau times.

Sample name	Plateau time (min)	Cu (at%)	Zn (at%)	Sn (at%)	S (at%)	Cu / (Zn+Sn)	Zn/Sn	S/M
EF1	As-grown	16.49	17.61	12.02	53.89	0.56	1.47	1.17
	30	13.90	16.12	9.97	59.06	0.53	1.62	1.48
	60	14.71	17.00	10.62	57.66	0.53	1.60	1.36
EF2	As grown	16.77	16.45	15.33	50.41	0.53	1.07	1.04
	30	15.11	15.67	10.06	59.47	0.59	1.56	1.46
	60	14.48	17.04	10.29	59.80	0.53	1.66	1.43
EF3	As-grown	11.67	11.53	27.46	51.20	0.30	0.42	1.01
	30	9.72	8.78	21.70	60.74	0.32	0.40	1.51
	60	9.57	8.53	22.04	58.40	0.31	0.39	1.45
EF4	As-grown	14.40	7.67	24.42	53.47	0.45	0.31	1.15
	30	13.24	8.83	19.43	58.79	0.47	0.45	1.42
	60	12.45	6.80	18.86	61.85	0.49	0.36	1.62
EF5	As-grown	18.83	10.91	15.74	55.29	0.71	0.69	1.22
	30	16.92	11.02	12.44	60.30	0.72	0.89	1.49

Table 4.4 shows the variation of the chemical composition of the as-grown thin films by thermal evaporation with different thermal treatments changing the heating rates. As it can be seen, there were not relevant differences between the different heating rates (2, 5, 10 and 20 K/min). In all four heating rates, there were the same tendency of re-evaporation of Cu and increase of the Zn and Sn contents, doubling the amount of Sn in ET4 and almost in ET6 after the thermal treatments. In all the thermal treatments the amount of sulfur increased in the final chemical composition. The impact of the change of the heating rates in the final composition was not significant.

Table 4.4. Chemical composition measured by EDX of as grown thin films by thermal evaporation and after the thermal treatments. Also, it is indicated the different heating rates.

Sample name	Heating rate (K/min)	Cu (at%)	Zn (at%)	Sn (at%)	S (at%)	Cu / (Zn+Sn)	Zn/Sn	S/M
ET4	As-grown	36.21	16.78	4.17	42.84	1.73	4.02	0.75
	2	14.47	24.46	8.66	52.40	0.44	2.82	1.10
	10	15.77	22.80	8.95	52.50	0.50	2.55	1.10
	20	15.68	23.05	9.06	52.21	0.49	2.54	1.09
ET6	As-grown	42.09	8.02	8.36	41.53	2.57	0.96	0.71
	10	23.66	9.84	13.61	52.88	1.01	0.72	1.12
ET7	As-grown	28.85	13.54	14.37	43.25	1.03	0.94	0.76
	2	20.68	11.84	16.08	51.40	0.74	0.74	1.06
	5	20.82	11.71	16.19	51.29	0.75	0.72	1.05
	10	20.82	11.33	15.35	52.5	0.78	0.74	1.11

4.3. Chemical Etching and Thermal treatments

The selected sample to apply the chemical etching, thermal treatments and finally the layer deposition of the window to finish the device was ET6 because the absorber layer was the thickest with 2 μm, and different etchings and thermal treatments were investigated in this set of evaporated samples. It is reported that the minimum thick of the absorber layer must be 1.5 μm to avoid the recombination process at the back contact of the solar cell [4]. Furthermore, this sample shows similar values of Sn and Zn and it was expected to reduce the amount of Cu by chemical etchings. Initially, it was performed a comparison between the chemical composition measured of the Cu_2ZnSnS_4 (ET6 absorber layer) by EDX and XRF. As it can be seen in Table 4.5 and mentioned above, the composition presented is not the appropriated to have a good device performance [3] because of a very Cu-rich composition and low concentrations of Zn and Sn. Moreover, there is a clear discrepancy in the chemical composition measurements by both techniques. This difference might be produced by the use of different internal calibration standards or by the intrinsic features of these techniques. The XRF was calibrated with measurements by inductively-coupled plasma-optical emission spectroscopy (ICP-OES)

and the EDX was calibrated with an internal standard calibration. Due to this unexplained uncertainty, it was decided to consider exclusively the measurements by XRF, being used directly after chemical and thermal treatments. For these reasons and from now on, all the chemical composition measurements presented here will be those performed by XRF.

Table 4.5. Chemical composition measurements of ET6 (Cu_2ZnSnS_4) sample by EDX and XRF

Technique	Cu (at%)	Zn (at%)	Sn (at%)	S (at%)	Cu / (Zn+Sn)	Zn/Sn	S/M
EDX	42.09	8.02	8.36	41.53	2.57	0.96	0.71
XRF	31.20	10.05	13.43	45.32	1.33	0.75	0.83

As mentioned in the introduction, kesterite is a complex material and with a narrow single-phase existence zone in the phase diagram. Moreover, to obtain the highest conversion efficiency the composition condition must be off-stoichiometry with Cu-poor, Zn-rich and Sn-poor composition [5]. As a consequence, secondary phases like ZnS, CuS, Cu_2SnS_3 and SnS are likely to form in the as-grown absorbers and have already been reported in several papers [6–9]. The presence of secondary phases has a detrimental effect on the performance of the final device, as it has been observed in [10]. If these secondary phases are present along the thickness of the film, the negative effect cannot be avoided, and indeed prevention is probably the only solution by selecting the best deposition and annealing conditions. On the other hand, if they are present at the surface, it is possible to remove them by chemical etching. The most common etchings for kesterite are KCN, HCl and $(NO_4)_2S$ to remove Cu_xS, ZnS and SnS_x, respectively [11–15]. Table 4.6 summarizes the etching routes with the concentration, temperature and exposure time used to remove the different secondary phases and their etching reactions.

Table 4.6. Etching procedures to remove secondary phases. Note: v= volume; w = weight (s) = solid; (aq) = aqueous; (l) = liquid; (g) = gas and (so) = soluble.

Secondary phase	Etching routes	Etching reactions	Ref.
Cu_xS ($1 \leq x \leq 2$)	2−10% (w/v) KCN, RT, 0.5−30 min	*2CuS(Se)(s) + 5KCN(aq) + 2KOH(aq)* ⇄ **$2KCu(CN)_2(aq) + 2K_2S(Se)(aq) + KCNO(aq) + H_2O(l)$**	[11–13]
ZnS	5−10% (v/v) HCl, 75°C, 5−10 min	*2HCl(aq) + ZnS(s)* ⇄ **$ZnCl_2(aq) + H_2S(g)$**	[14]
SnS_x ($1 \leq x \leq 2$)	4−22% (w/w) $(NO_4)_2S$, RT, 0.5-10 min	$SnS(s)+2S(aq) = SnS_2(s)$ → *$2NH_4(aq)$+ SnS_2(s)* ⇄ **$(NH_4)_2SnS_2$ (so)**	[15]

After the etching of the samples, either a sulfurization or a selenization process under Ar atmosphere was performed. These thermal treatments are useful to improve the crystallization [10] of the samples and to assure that the anion atomic positions were fully occupied. Moreover, a partial substitution of sulfur by selenium, also called sulfoselenization took also place. This sulfoselenization converts CZTS into CZTSSe. The addition of Se reduces the band gap of the kesterite absorber and normally leads to better device performance [6,8,16–19].

For these processes, a graphite box was used (Figure 4.2(a)). The samples were located together with 50 mg of S or Se powder (Alfa Aesar, 99.995% and 99.999% respectively) and 5 mg of Sn powder (Alfa Aesar, 99.999%) inside the crucible. The annealing step was performed in a three zones tubular furnace (Figure 4.2(b)) capable of working in vacuum (10^{-4} mbar) and inert gas atmosphere (Ar) [20].

Figure 4.2. Graphite box with samples and sulfur inside (a) and graphite box inside the tubular furnace (b).

The sulfurization was done at 823 K for 45 minutes under argon pressure of 1 bar (Figure 4.3(a)). The selenization or sulfoselenization thermal treatment applied was a two-step process (Figure 4.3(b)). The first treatment was carried out at 723 K for 30 minutes and the subsequent second treatment at 823 K for 15 minutes, and reaching the maximum argon pressure of 1 bar. For both treatments, the heating rate was of 20 K/min and cooling was allowed to occur naturally down to room temperature; approximately it took 2 h to cool down below 373 K.

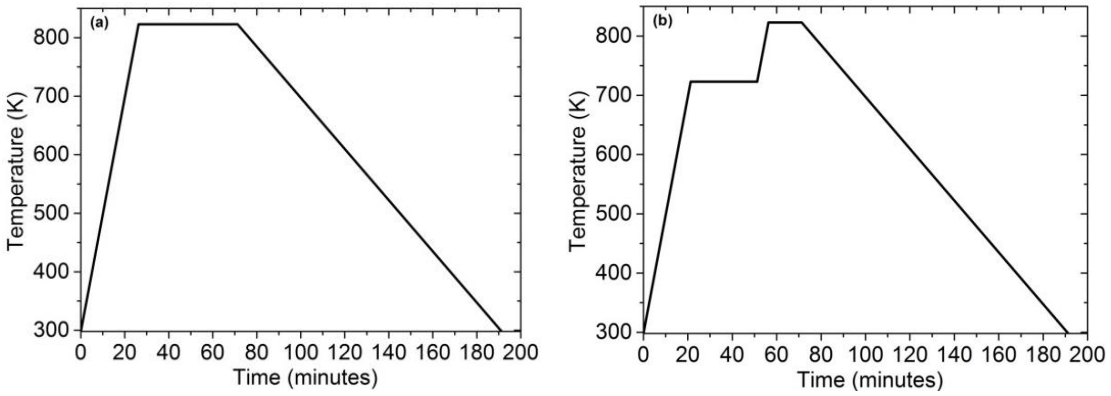

Figure 4.3. Sulfurization thermal treatment profile (TT1) (a) and selenization / sulfoselenization thermal treatment profile (TT2) (b)

Table 4.7 and Table 4.8 show the evolution of the chemical composition with the different etchings and the final thermal treatments. As it can be seen, the initial composition was Cu and Sn-rich and Zn-poor. These initial compositions are the opposite of the desired composition (Cu-poor and Zn-rich) [3]. For this reason, it is of paramount importance to apply the suitable etchings and thermal treatments to obtain the most appropriated chemical composition. It can be seen that after the KCN etchings (10% (w/v) KCN at room temperature) there is a decrease of the Cu content meanwhile the Zn

and the Sn ones increased. Afterwards, it was applied the $(NH_4)_2S$ etching which decreased the amount of Sn. In both etching steps the effect obtained was the expected. The total time in the last etching step with $(NH_4)_2S$ in Table 4.8 was 3 minutes longer than in the Table 4.7 because after the first 5 minutes the amount of Sn was higher and Zn was still lower than Sn. After the 3 minutes extra, the Zn concentration was higher than the Sn content and it still kept a Cu-poor composition. As it can be seen, in each chemical etching the thickness of the absorber layer decreases as the chemical etching removes layers from the surface. The last step was the thermal treatment, in the case of the sample of Table 4.7 a sulfurization thermal treatment (TT1) was carried out and in the case of Table 4.8 it was performed a sulfoselenization thermal treatment (TT2). In both cases, the final composition was Cu-poor and Zn-rich as those used to obtain high performance devices.

Table 4.7. Chemical composition measurements of Cu_2ZnSnS_4 by XRF after each etching process and the sulfurization thermal treatment (TT1) and the thickness (d) of the kesterite absorbent. Note: the times in the chemical etching are consecutives and additives.

Etching / Exposure time and thermal treatment	**d (µm)**	**Cu (at%)**	**Zn (at%)**	**Sn (at%)**	**S (at%)**	**Cu / (Zn+Sn)**	**Zn/Sn**	**S/M**
None (Initial)	1.91	31.20	10.05	13.43	45.32	1.33	0.75	0.83
KCN / 5 sec.	1.62	24.04	11.58	16.63	47.74	0.85	0.70	0.91
KCN / 1 sec.	1.40	21.45	13.52	19.00	46.03	0.66	0.71	0.85
$(NH_4)_2S$ / 2 min.	1.32	20.60	13.95	16.58	48.87	0.67	0.84	0.96
$(NH_4)_2S$ / 2 min.	1.14	22.30	15.68	13.28	48.74	0.77	1.18	0.95
$(NH_4)_2S$ / 1 min.	1.02	21.83	17.12	12.57	48.48	0.74	1.36	0.94
TT1(S)	1.01	21.28	17.48	12.25	48.99	0.72	1.43	0.96

Table 4.8. Chemical composition measurements of Cu_2ZnSnS_4 by XRF after each etching process, plus the sulfoselenization thermal treatment (TT2) and the thickness (d) of the kesterite absorbent. Note: the times in the chemical etching are consecutives and additives

Etching / Exposure Time and thermal treatment	d (µm)	Cu (at%)	Zn (at%)	Sn (at%)	S (at%)	Se (at%)	Cu / (Zn+Sn)	Zn/Sn	S/M	Se/M	S/ (S+Se)
None (Initial)	1.91	31.20	10.05	13.43	45.32	--	1.33	0.75	0.83	--	--
KCN / 5 sec.	1.79	24.75	11.64	15.69	47.92	--	0.91	0.74	0.92	--	--
KCN / 1 sec.	1.68	21.81	12.50	17.15	48.54	--	0.74	0.73	0.94	--	--
$(NH_4)_2S$ / 5 min.	1.41	20.82	14.42	15.05	49.71	--	0.71	0.96	0.99	--	--
$(NH_4)_2S$ / 3 min.	1.18	22.60	16.42	13.16	47.82	--	0.77	1.25	0.91	--	--
TT2(SSe)	1.25	21.61	15.63	13.72	9.53	39.51	0.74	1.14	0.19	0.78	0.19

4.4. Fabrication of the photovoltaic solar cell: Buffer, Window and Contact layer deposition

The completion of the device and the molybdenum deposition were performed at the Catalonia Institute for Energy Resarch (IREC) in Barcelona during a research stay. The Molybdenum (Mo) back contact was deposited onto the soda-lime glass by direct current (DC) magnetron sputtering prior to the deposition of the CZTS absorber layer. To finish the device it is necessary to deposit the buffer and window layers, and the metallic grids to enhance the current collection. Figure 4.4 shows the scheme of a kesterite thin film solar cell and all the necessary layers of a finished device.

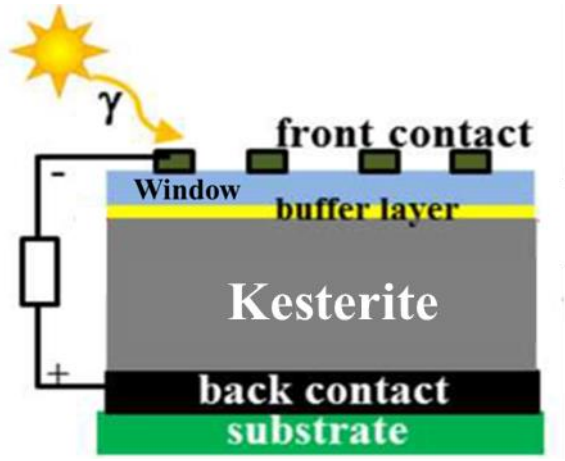

Figure 4.4. Scheme of a complete kesterite thin film device.

The CdS buffer layer was deposited by chemical bath deposition, followed by DC-pulsed sputtering deposition of 50 nm i-ZnO and 350 nm of DC-pulsed In_2O_3:SnO_2 (ITO) bilayer (CT100 Alliance Concept, Cran-Gevrier, France) [21]. For device characterization, individual solar cells of 3×3 mm^2 were isolated using a manual microdiamond scriber (MR200,OEG, Frankfurt, Germany) with a scribed line width of 20 μm, thus avoiding the necessity of the metallic grid deposition (front contact) onto the ITO surface.

4.5. Characterization of the device

4.5.1. Glow Discharge Optical Emission Spectroscopy (GDOES) and Raman measurements

The ET7 sample (see Table 4.4.) was used to perform GDOES measurements of the CdS/CZTS/Mo/glass structure to investigate the distribution of the elements through the absorber film. Figure 4.5 shows the GDOES depth profiles for the samples annealed with 2 K/min (a) and 10 K/min (b) heating rates. Sn is preferentially segregated at the back interface in both cases since a higher Sn concentration next to the Mo back contact is detected for the absorber annealed at higher heating rates. Moreover, an increased content of S is measured next to the Mo, coinciding with the increased Sn concentration. This might indicate the preferential formation of SnS in the deeper part of the absorber. In addition to that, a strong decrease of the Cu and Zn signals is also observed at the absorber/Mo back interface. Na diffuses from the soda-lime glass into the absorber layer. The positive effect of Na on CIGSe solar cells and the affinity of Na for Cu vacancies is

well known [22]. A higher Na concentration near the back contact coincides with the decreased Cu and increased Sn GDOES signals, especially in the thermal treatment with a 10 K/min heating rate. Generally, Na diffuses from the glass substrate towards the absorber surface. However, here an increased Na GDOES signal is observed near the front half of the CZTS layer in both cases [1].

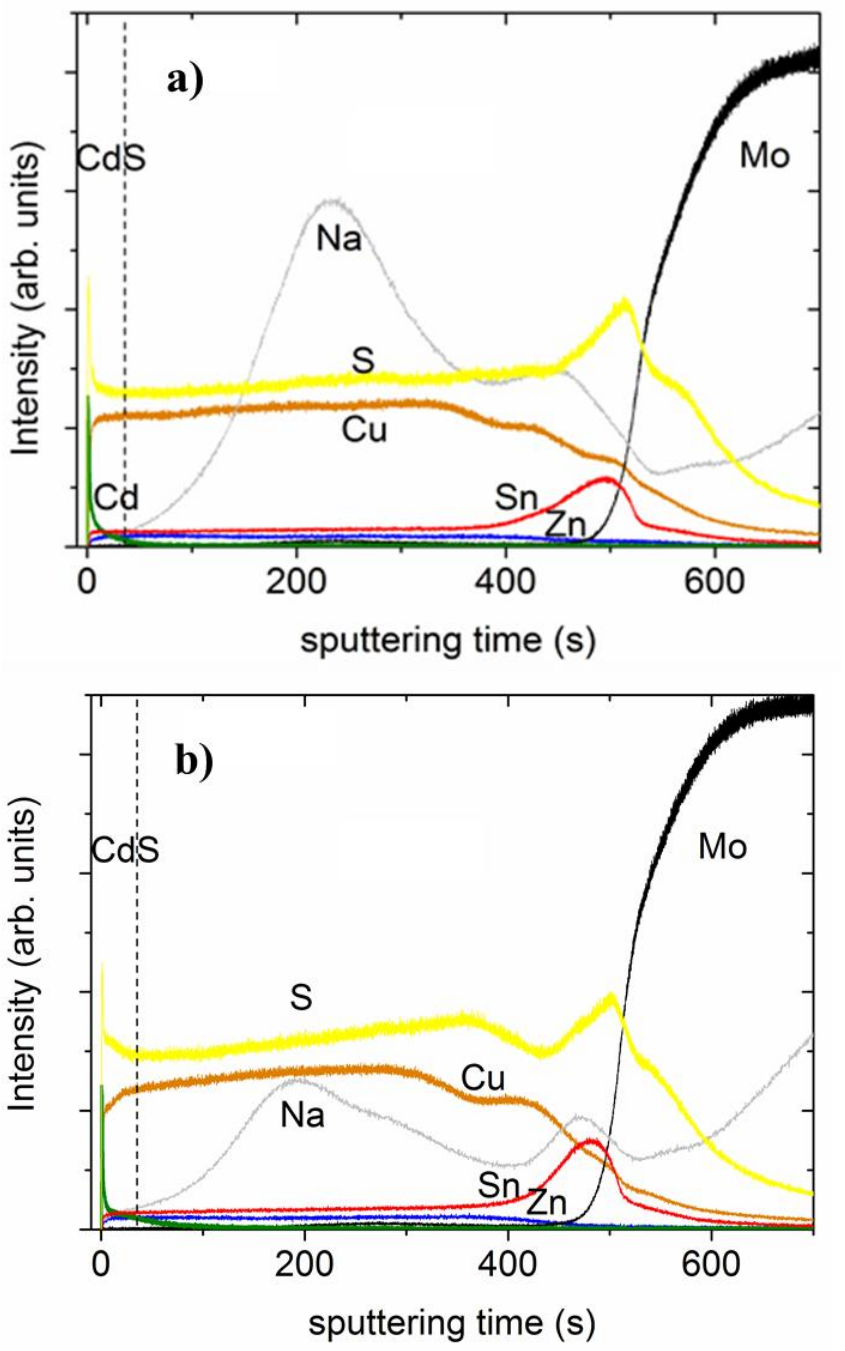

Figure 4.5. GDOES depth profile of CdS/CZTS/Mo structure for CZTS films annealed with a heating rate of 2 K/min (a) and 10 K/min (b) [1]

In order to assure that this SnS secondary phase is not on the absorber surface, Raman measurement was performed on this device. An excitation wavelength of 633 nm was used to avoid the Raman modes of CdS, estimating the penetration depth around 170 nm. As displayed in Figure 4.6, only the characteristic Raman peaks of CZTS were detected [23].

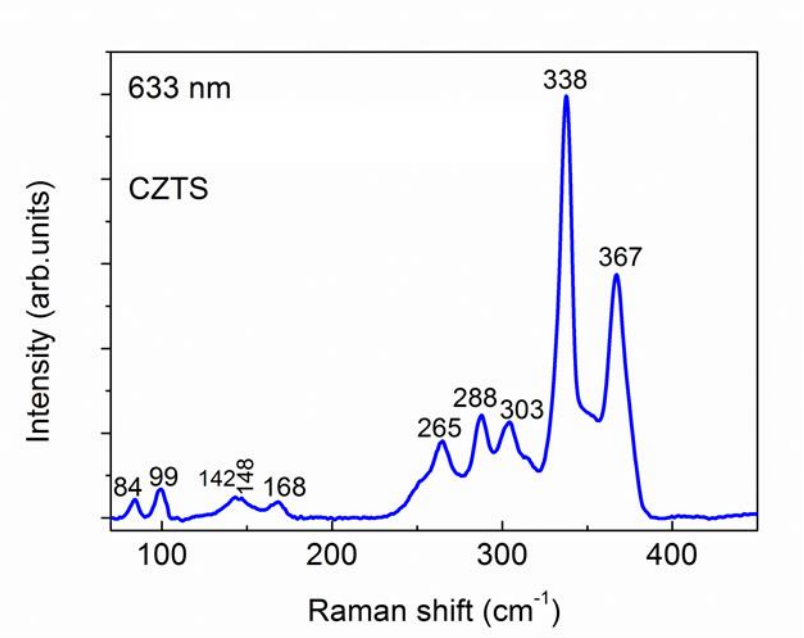

Figure 4.6. Raman spectroscopy of CZTS thin films annealed with 10 K/min heating rate.

4.5.2. Intensity vs Voltage (I-V) and External Quantum Efficiency (EQE) measurements

After all the etchings and thermal treatments processes, CdS was deposited followed by i-ZnO/ITO window bilayer. After that, it was performed the mechanical scribing (Figure 4.7) as it was previously explained.

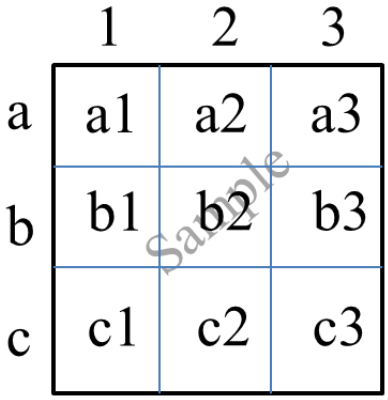

Figure 4.7. Scheme of the thin film sample and its scribed and the nomenclature used to name the samples.

Despite the adequate chemical composition of the Cu_2ZnSnS_4 sample as it is shown in Table 4.7, the performance was not the desired. All the cell efficiencies (η) were below 0.1%, with the exception of the sample ET7 (absorber thickness of 1.5 μm) that achieved 1.1 % efficiency after $(NH4)_2S$ chemical etching (Voc = 336 mV, Jsc = 9.3 mA/cm^2, FF = 33.7 %) [1]. The presence of SnS inside the absorber layer as detected by GDOES is one of the main reasons of this low device performance. The main explanation for the other solar cells might be the thin absorber layer (1 μm), which avoids the generation of enough light-generated carriers and as a consequence, their collection to generate a significant current. However, the existence of secondary phases cannot be ruled out after the GDOES analysis, being another possibility of the very low performance of the device, as mentioned above.

The photovoltaic parameters of CZTSSe solar cells fabricated using the absorber layer after the sulfoselenization treatment are shown in Table 4.9 and displayed in Figure 4.8. It seems that this thermal treatment was a key aspect to achieve a better performance. Figure 4.8 and Figure 4.9 show the J-V and EQE curves, where one can observe the difference between the cells (3 x 3 mm^2) of the same absorber layer. These results indicate the non-uniform deposition character of the absorber layer by thermal evaporation as it was explained in section 4.1.2, not being the best procedure to fabricate high efficiency solar cells. But this was not the intention of this work; the aim of fabricating a whole thin film device was to verify if it was possible to obtain an operation cell with the bulk kesterite material synthesized in this thesis by a rapid and simple evaporation process, as it was explained in chapter 2.

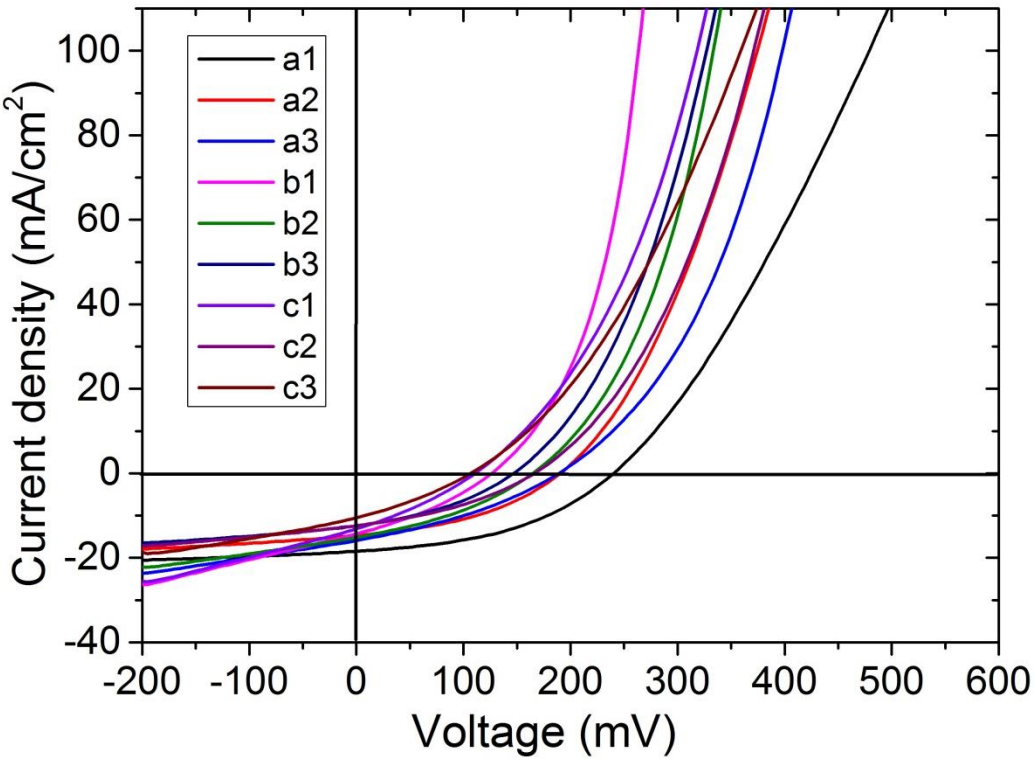

Figure 4.8. J-V curves for $Cu_2ZnSn(S,Se)_4$ cells.

Table 4.9. Photovoltaic parameters of the CZTSSe solar cell devices

Cell name	Voc (mV)	Jsc (mA/cm^2)	FF (%)	η (%)	R_{shunt} ($Ohm*cm^2$)	R_{series} ($Ohm*cm^2$)
a1	239.80	18.86	43.90	1.99	53.76	0.51
a2	190.08	14.89	41.08	1.16	36.43	0.59
a3	188.60	16.15	34.40	1.05	20.27	0.91
b1	175.39	15.14	38.58	1.02	27.98	1.79
b2	164.41	15.27	35.95	0.90	19.79	2.14
b3	146.68	12.26	38.26	0.69	25.14	2.27
c1	125.93	14.22	33.92	0.61	12.99	2.49
c2	110.69	12.82	32.42	0.46	11.37	2.65
c3	88.33	12.25	29.08	0.31	7.90	3.1

As shown in Table 4.9, the best cell has achieved 2 % (a1) of efficiency, being 0.31 % (c3) the lowest efficiency obtained with the sulfoselenization treatment of the absorber layer. The higher efficiency corresponds to the device with all higher PV parameters and

higher shunt resistance. The low efficiencies can be mainly due to the low shunt resistance values that can cause power losses by providing an alternate current path for the light-generated current, leading to a low V_{oc} and fill factor. It can be also seen that the parasitic series resistances are an order of magnitude higher than those reported in [21], explaining the low J_{sc}. Moreover, the ET7 sample measured with GDOES showed the presence of SnS in depth of the absorber layer, and the high content of Sn at the back interface do not allow enhancing the device performance despite the $(NH_4)_2S$ etching. This chemical etching is generally used to remove the SnS secondary phase [15], but it is only effective on the absorber surface. Fernandes et al. [24] also observed the presence of Sn_xS_y phases at the back contact. The lower band gap SnS phase next to the Mo layer could enhance recombination of charge carriers near the back contact [25], reducing the short circuit current. The Sn excess of the as-evaporated sample was not lost during the annealing treatment. The presence of SnS next to the back contact could be explained by the initial formation of SnS during the evaporation of CZTS thin films [1]. Since the absorber thin film of ET7 and the "a1" cell were obtained with the same equipment by thermal evaporation, it might be possible that this SnS phase might be present in the measured cells (Figure 4.8 and Table 4.1) and it would have a negative effect as it is mentioned above. In summary, there are a lot of aspects to improve in the devices here presented, contacts, p-n junction…, ; but as mentioned above, the main point of this chapter is to show a working kesterite cell device.

Figure 4.9 shows the external quantum efficiency (EQE) versus the wavelength for all CZTSSe cells investigated. Analyzing in more detail the EQE curves (Figure 4.9), the first thing that can be inferred is the decrease in the quantum efficiency in the spectral range from 400 to 515 nm, caused by the optical absorption of the CdS buffer layer. Although, all the cells received the same CdS bath deposition, it seems that the thickness of the CdS differs between the cells and that is why each cell has its own behavior in this spectral region. One reason could be the different roughness of the different absorber surfaces that leads to different CdS growth. There is also a clear reduction of the overall EQE due to the reflection at the surface and, mainly, to the low carrier diffusion length. In conclusion, there are issues in all the spectra to be improved, nevertheless the cells worked and achieved almost 2% of efficiency (Table 4.9).

In general, these CZTSSe devices are characterized by a long end tail curve sloping gradually from 520 nm, which might be attributed to high doping densities and short electron diffusion lengths [26]. Moreover, the thickness of the layer might have a crucial role in this particular decrease of the EQE curve from 520 nm, being here of only 1.25 μm. In [4] was reported that a thickness lower than 2 μm might produce a recombination process at the back contact of the solar cell, which affects the EQE spectrum in the higher wavelengths (from 520 to 1200 nm).

For an ideal junction, the EQE can be approximated by [27]

$$EQE = 1 - \frac{exp(\alpha W)}{1+\alpha L_n}$$

Equation 4-1

where α is the absorption coefficient, W is the width of the spatial charge region and L_n is the minority carrier diffusion length. Assuming a short diffusion length, near 0, the product $\alpha L_n < 1$, and then Equation 4-1 reduces to [28]:

$$EQE = 1 - exp(-\alpha W)$$

Equation 4-2

For a direct transition, the dependence of the absorption coefficient on the photon energy is given by

$$\alpha h\nu \propto (h\nu - E_g)^{1/2}$$

Equation 4-3

then, the plot of $[E \ln(1\text{-}EQE)]^2$ against E (Figure 4.10) can be used to extrapolate the electronic bandgap E_g. From this plot, it was determined a bandgap value of 0.98 eV for the best cell. From the literature, the experimental band gap values of CZTSe were 0.8 eV [29], 0.94eV [26], and 1.02eV [30]. Moreover, for CZTSSe there were reported in [31] experimental band gap values of 1.03 eV and 1.21 eV for S/(S+Se) ratios of 0.04 and 0.8, respectively. The bandgap values differences observed between these references and the ones obtained could be due to differences in stoichiometry but also to the presence of additional phases [26].

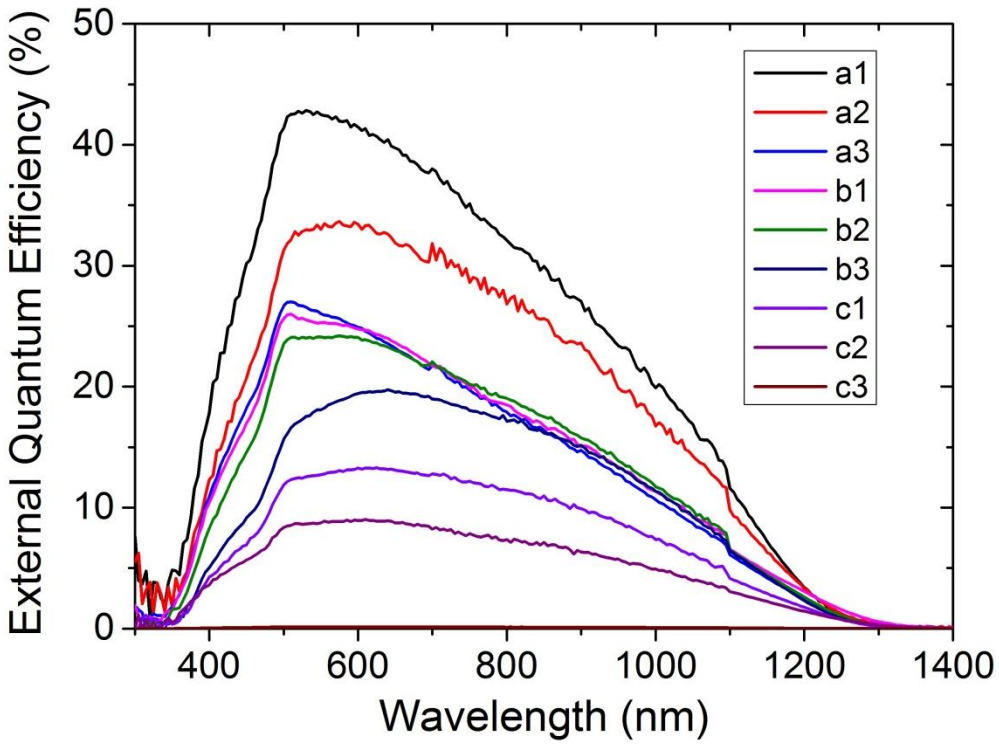

Figure 4.9. External Quantum Efficiency (EQE) vs Wavelength curves for $Cu_2ZnSn(S,Se)_4$ cells.

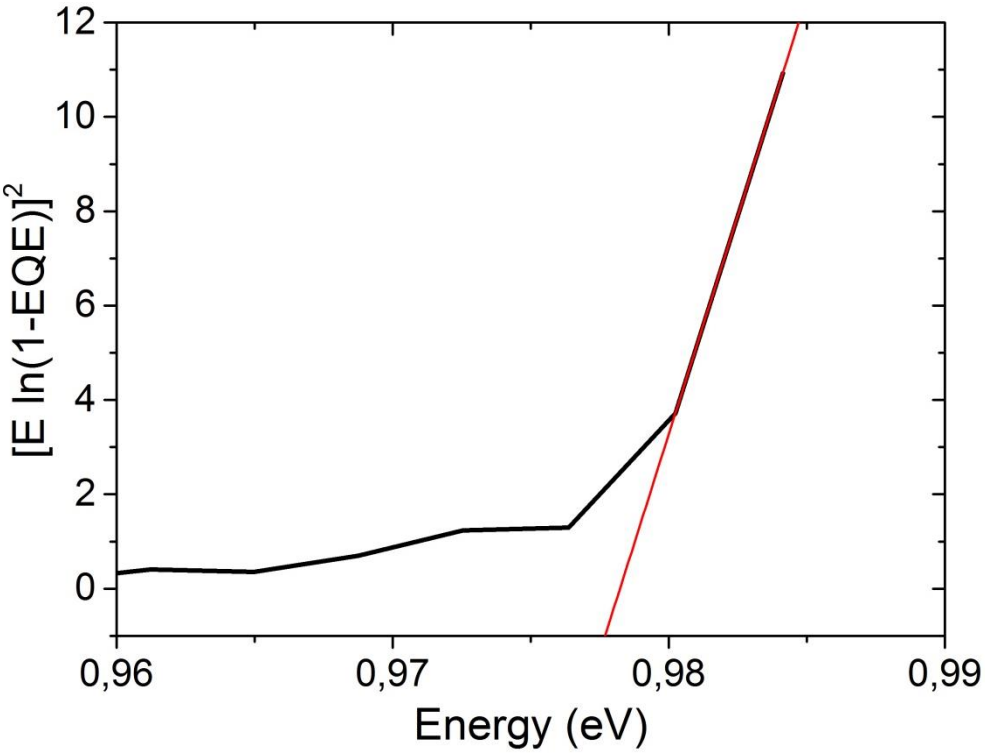

Figure 4.10. Band gap determination of the "a1" (CZTSSe) cell for the plot of $[E\ln(1-EQE)]^2$ versus E.

4.6. References

[1] E. Garcia-Llamas, J.M. Merino, R. Gunder, K. Neldner, D. Greiner, Y. Sánchez, V. Izquierdo-Roca, E. Saucedo, A. Steigert, M. León, S. Schorr, R. Caballero, Cu_2ZnSnS_4 thin film solar cells grown by fast thermal evaporation and thermal treatment, Sol. Energy. (2016). Under review.

[2] R. Caballero, V. Izquierdo-Roca, J.M. Merino, E.J. Friedrich, A. Climent-Font, E. Saucedo, A. Pérez-Rodríguez, M. León, Cu_2ZnSnS_4 thin films grown by flash evaporation and subsequent annealing in Ar atmosphere, Thin Solid Films. 535 (2013) 62–66. doi:10.1016/j.tsf.2012.10.028.

[3] T.K. Todorov, J. Tang, S. Bag, O. Gunawan, T. Gokmen, Y. Zhu, D.B. Mitzi, Beyond 11% effi ciency: Characteristics of State-of-the-Art $Cu_2ZnSn(S,Se)_4$ Solar Cells, Adv. Energy Mater. 3 (2013) 34–38. doi:10.1002/aenm.201200348.

[4] H. Heriche, Z. Rouabah, S. Benabbes, L. Selmani, Thickness optimization of various layers of CZTS solar cell, J. New Technol. Mater. 4 (2014) 27–30.

[5] D.B. Mitzi, O. Gunawan, T.K. Todorov, K. Wang, S. Guha, The path towards a high-performance solution-processed kesterite solar cell, Sol. Energy Mater. Sol. Cells. 95 (2011) 1421–1436. doi:10.1016/j.solmat.2010.11.028.

[6] W. Wang, M.T. Winkler, O. Gunawan, T. Gokmen, T.K. Todorov, Y. Zhu, D.B. Mitzi, Device characteristics of CZTSSe thin-film solar cells with 12.6% efficiency, Adv. Energy Mater. (2013) 1–5. doi:10.1002/aenm.201301465.

[7] K. Timmo, M. Altosaar, J. Raudoja, M. Grossberg, M. Danilson, O. Volobujeva, E. Mellikov, Chemical etching of $Cu_2ZnSn(S,Se)_4$ monograin powder, Photovolt. Spec. Conf. (PVSC), 2010 35th IEEE. (2010) 001982–001985. doi:10.1109/PVSC.2010.5616411.

[8] V. Chawla, B. Clemens, Effect of composition on high efficiency CZTSSe devices fabricated using co-sputtering of compound targets, Photovolt. Spec. Conf. (PVSC), 2012 38th IEEE. (2012) 2990–2992. doi:10.1109/PVSC.2012.6318212.

[9] W.-C. Hsu, I. Repins, C. Beall, C. DeHart, G. Teeter, B. To, Y. Yang, R. Noufi, The effect of Zn excess on kesterite solar cells, Sol. Energy Mater. Sol. Cells. 113

(2013) 160–164. doi:10.1016/j.solmat.2013.02.015.

[10] A. Fairbrother, X. Fontané, V. Izquierdo-Roca, M. Espíndola-Rodríguez, S. López-Marino, M. Placidi, L. Calvo-Barrio, A. Pérez-Rodríguez, E. Saucedo, On the formation mechanisms of Zn-rich Cu_2ZnSnS_4 films prepared by sulfurization of metallic stacks, Sol. Energy Mater. Sol. Cells. 112 (2013) 97–105. doi:10.1016/j.solmat.2013.01.015.

[11] S. Niki, P.J. Fons, A. Yamada, Y. Lacroix, H. Shibata, H. Oyanagi, M. Nishitani, T. Negami, T. Wada, Effects of the surface Cu_2Se phase on the growth and properties of $CuInSe_2$ films, Appl. Phys. Lett. 74 (1999) 1630–1633. doi:10.1063/1.123639.

[12] B.A. Schubert, B. Marsen, S. Cinque, T. Unold, R. Klenk, S. Schorr, H.W. Schock, Cu_2ZnSnS_4 thin film solar cells by fast coevaporation, Prog. Photovolt Res. Appl. 19 (2011) 93–96. doi:10.1002/pip.

[13] L. Weinhardt, O. Fuchs, D. Gross, E. Umbach, C. Heske, N.G. Dhere, A.A. Kadam, S.S. Kulkarni, D. Groß, Surface modifications of $Cu(In,Ga)S_2$ thin film solar cell absorbers by KCN and H_2O_2/H_2SO_4 treatments, J. Appl. Phys. 100 (2006) 024907/1-4. doi:Artn 024907 Doi 10.1063/1.2216367.

[14] A. Fairbrother, E. Garcia-Hemme, V. Izquierdo-Roca, X. Fontané, F.A. Pulgarin-Agudelo, O. Vigil-Galan, A. Perez-Rodriguez, E. Saucedo, Development of a Selective Chemical Etch To Improve the Conversion Efficiency of Zn-Rich Cu_2ZnSnS_4 Solar Cells, J. Am. Chem. Soc. 134 (2012) 8018–8021.

[15] H. Xie, Y. Sánchez, S. López-Marino, M. Espíndola-Rodríguez, M. Neuschitzer, D. Sylla, A. Fairbrother, V. Izquierdo-Roca, A. Pérez-Rodríguez, E. Saucedo, Impact of Sn(S,Se) secondary phases in $Cu_2ZnSn(S,Se)_4$ solar cells: A chemical route for their selective removal and absorber surface passivation, ACS Appl. Mater. Interfaces. 6 (2014) 12744–12751. doi:10.1021/am502609c.

[16] Q. Guo, G.M. Ford, W.C. Yang, B.C. Walker, E.A. Stach, H.W. Hillhouse, R. Agrawal, Fabrication of 7.2% efficient CZTSSe solar cells using CZTS nanocrystals, J. Am. Chem. Soc. 132 (2010) 17384–17386. doi:10.1021/ja108427b.

[17] Y. Sun, Y. Zhang, H. Wang, M. Xie, K. Zong, H. Zheng, Y. Shu, J. Liu, H. Yan, M. Zhu, W. Lau, Novel non-hydrazine solution processing of earth-abundant $Cu_2ZnSn(S,Se)_4$ absorbers for thin-film solar cells, J. Mater. Chem. A. 1 (2013) 6880–6887. doi:10.1039/c3ta10566k.

[18] J. He, L. Sun, S. Chen, Y. Chen, P. Yang, J. Chu, Composition dependence of structure and optical properties of $Cu_2ZnSn(S,Se)_4$ solid solutions: An experimental study, J. Alloys Compd. 511 (2012) 129–132. doi:10.1016/j.jallcom.2011.08.099.

[19] H.S. Duan, W. Yang, B. Bob, C.J. Hsu, B. Lei, Y. Yang, The role of sulfur in solution-processed $Cu_2ZnSn(S,Se)_4$ and its effect on defect properties, Adv. Funct. Mater. 23 (2013) 1466–1471. doi:10.1002/adfm.201201732.

[20] A. Fairbrother, X. Fontané, V. Izquierdo-Roca, M. Placidi, D. Sylla, M. Espindola-Rodriguez, S. Lopez-Mariño, F.A. Pulgarin-Agudelo, O. Vigil-Galan, A. Perez-Rodriguez, E. Saucedo, Secondary phase formation in Zn-rich $Cu_2ZnSnSe_4$-based solar cells annealed in low pressure and temperature conditions, Prog. Photovoltaics Res. Appl. 22 (2014) 479–487. doi:10.1002/pip.2473.

[21] M. Neuschitzer, Y. Sanchez, S. López-Marino, H. Xie, A. Fairbrother, M. Placidi, S. Haass, V. Izquierdo-Roca, A. Perez-Rodriguez, E. Saucedo, Optimization of CdS buffer layer for high-performance $Cu_2ZnSnSe_4$ solar cells and the effects of light soaking: elimination of crossover and red kink, Prog. Photovolt Res. Appl. 23 (2015) 1660–1667. doi:10.1002/pip.2589.

[22] R. Caballero, C.A. Kaufmann, V. Efimova, T. Rissom, V. Hoffmann, H.W. Schock, Investigation of $Cu(In,Ga)Se_2$ thin-film formation during the multi-stage co-evaporation process, Prog. Photovoltaics Res. Appl. 21 (2013) 30–46. doi:10.1002/pip.1233.

[23] M. Dimitrievska, A. Fairbrother, X. Fontané, T. Jawhari, V. Izquierdo-Roca, E. Saucedo, A. Pérez-Rodríguez, Multiwavelength excitation Raman scattering study of polycrystalline kesterite Cu_2ZnSnS_4 thin films, Appl. Phys. Lett. 104 (2014) 1–5. doi:10.1063/1.4861593.

[24] P.A. Fernandes, P.M.P. Salomé, A.F. da Cunha, Study of polycrystalline

Cu_2ZnSnS_4 films by Raman scattering, J. Alloys Compd. 509 (2011) 7600–7606. doi:10.1016/j.jallcom.2011.04.097.

[25] J.J. Scragg, J.T. Watjen, M. Edoff, T. Ericson, T. Kubart, C. Platzer-Bjorkman, A Detrimental Reaction at the Molybdenum Back Contact in $Cu_2ZnSn(S,Se)_4$ Thin-Film Solar Cells, J. Am. Chem. Soc. 134 (2012) 19330–19333. doi:10.1021/ja308862n.

[26] G. Zoppi, I. Forbes, R.W. Miles, P.J. Dale, J.J. Scragg, L.M. Peter, Cu2ZnSnSe4 Thin Film Solar Cells Produced by Selenisation of Magnetron Sputtered Precursors, Prog. Photovoltaics Res. Appl. 17 (2009) 315–319. doi:10.1002/pip.886.

[27] S.S. Hegedus, W.N. Shafarman, Thin-Film Solar Cells: Device Measurements and Analysis, Prog. Photovoltaics Res. Appl. 12 (2004) 155–176. doi:10.1002/pip.518.

[28] K. Takahashi, A. Yoshikawa, A. Sandhu, Wide Bandgap Semiconductors: Fundamental Properties and Modern Photnonic and Electronic Devices, 2007.

[29] T.M. Friedlmeier, N. Wieser, T. Walter, H. Dittrich, H.W. Schock, Heterojunctions based on Cu_2ZnSnS_4 and $Cu_2ZnSnSe_4$ thin films, in: Proc. 14th Eur. Conf. Photovolt. Sci. Eng. Exhib., 1997: pp. 1242–1245.

[30] M. Grossberg, J. Krustok, K. Timmo, M. Altosaar, Radiative recombination in $Cu_2ZnSnSe_4$ monograins studied by photoluminescence spectroscopy, Thin Solid Films. 517 (2009) 2489–2492. doi:10.1016/j.tsf.2008.11.024.

[31] T.K. Todorov, K.B. Reuter, D.B. Mitzi, High-efficiency solar cell with earth-abundant liquid-processed absorber, Adv. Mater. 22 (2010) E156–E159. doi:10.1002/adma.200904155.

Chapter 5

Conclusions

The objective of the present work was the synthesis of $Cu_2ZnSn_{1-y}Ge_y(S,Se)_4$ bulk compounds and the study of the fundamental properties of these compounds. Another objective was the fabrication of solar cells from the material previously synthesized. Next, the main conclusions of this thesis are summarized.

5.1. PART I: Bulk Characterization

5.1.1. Synthesis and chemical composition

- $Cu_2ZnSn_{1-y}Ge_yS_4$ (CZTGS) with y = 0, 0.1, 0.3, 0.5, 0.7, 0.9 and 1, and $Cu_2ZnSn_{1-y}Ge_ySe_4$ (CZTGSe) with y = 0, 0.3, 0.5, 0.7 and 1, single crystals were synthesized by Chemical Vapor Transport (CVT) without secondary phases. CZTGS and CZTGSe in polycrystalline form were synthesized with y = 0, 0.3, 0.5, 0.7 (only for selenium) and 1 by Bridgman and most of them presented Zn(S,Se) as a secondary phase. In all the cases, the *x*= [Ge/(Ge+Sn)] ratios agree with the desired nominal values of *y* .
- The Cu_2ZnSnS_4 (CZTS) compound was also synthesized by solid state reaction (SS) but with three different approaches: from pure elements, from binary compounds, and from ternary and binary compounds. In two of these approaches, CZTS was synthesized successfully, presenting a Cu-poor and Zn-rich composition.

5.1.2. Structural characterization

- For the single crystals, a simultaneous Rietveld refinement of the X-ray and Neutron diffraction experimental data was done. For the polycrystalline compounds, the refinements were carried out only with the neutron diffraction data. For most of the single crystals and polycrystalline compounds, the goodness of fit parameter (χ^2) was below 4
- The tetragonal lattice constants (a, c) and the tetragonal distortion, c/2a, were obtained after the Rietveld refinements. In all the compounds, the tetragonal lattice constants and the tetragonal distortion fulfilled the Vegard's law when the atomic ratio *x*= [Ge/(Ge+Sn)] changes (the *x* atomic ratio is the experimental value of the *y* value present in the chemical formula $Cu_2ZnSn_{1-y}Ge_yS_4$ or $Cu_2ZnSn_{1-y}Ge_ySe_4$). The tetragonal lattice constants decrease when the amount of germanium increases because the ionic radii of the germanium (53 pm) is smaller than the tin one (69 pm).
- The position of the anion (XYZ) and the anion-cation distances were calculated. In all the compounds. It was observed a tendency to decrease the S8i-Ge/Sn2b and Se8i-Ge/Sn2b distances with the increase of the amount of germanium. This behavior is explained due to lower ionic radii of the germanium.

- For the single crystals, the theoretical defect prediction matches with the site occupancy factors after the refinements performed and the compositions measured by WDX and/or EDX. On the one hand, the Zn_{Cu}^{2+} and $Zn_{Sn,Ge}^{2+}$ defects were identified for the sulphide compounds. On the other hand, the Cu_{Zn}^{+}, $Cu_{Sn,Ge}^{+}$, Zn_{Cu}^{2+} and $Zn_{Sn,Ge}^{2+}$ defects were identified for the selenide compounds. Qualitatively, it was found that the amount of defects in the sulphide compounds was higher, in some cases one order of magnitude, than the observed ones in the selenide compounds.

5.1.3. Optical characterization

- The optical properties of $Cu_2ZnSn_{1-y}Ge_y(S,Se)_4$ single crystals and polycrystalline compounds with different Ge contents were investigated by spectroscopic ellipsometry. It was determined the band gap (E_0) and interband (E_{1A} and E_{1B}) transition energies with the change of *x*= [Ge/(Ge+Sn)] ratio. The band gap energy increased linearly with the amount of Ge from 0.93 to 1.60 eV and from 1.51 to 2.25 eV for selenide and sulphide single crystals, respectively. The polycrystalline compounds showed similar values and linear behavior as the single crystals. For all the compounds, the E_0 matched with the theoretical calculation of the kesterite structure; except in the case of $Cu_2ZnSnGeSe_4$ single crystals, for which it appears that the band gap energy (1.33 eV) fitted better for the stannite structure, whose band gap value is smaller than the corresponding one for the kesterite structure (1.60 eV). As a consequence, spectroscopic ellipsometry has proved to be a good non-destructive technique to determine the band gap energy and to distinguish between kesterite and stannite structures. Furthermore, the understanding of the incorporation of Ge into the $Cu_2ZnSn(S,Se)_4$ lattice is fundamental in order to develop efficient bandgap engineering of these compounds towards the fabrication of solar cells with enhanced performance.

5.1.4. Vibrational characterization

- The vibrational properties were studied by Raman spectroscopy using different excitation wavelengths. For all pure single crystals, the kesterite-type structure was determined based on the small broadening of the peaks and the number of observed A symmetry modes. The analysis of the measured Raman spectra at different

excitation wavelengths allowed determining the position of more than 30 peaks in different samples presenting the fingerprint Raman spectra for the single crystals in resonant and non-resonant conditions. All the peaks shifted to higher wavenumbers when increasing the *x*= [Ge/(Ge+Sn)] ratio. In selenium containing compounds, all A symmetry peaks exhibited only one mode behavior. In the case of sulfur containing compounds, most of the peaks showed a two mode behavior, including two A symmetry modes.

- The sulfur and selenium polycrystalline compounds measured by Raman spectroscopy showed a similar behavior than the single crystal compounds. All the peaks shifted to higher wavenumbers when increasing the germanium content. On one hand, in the selenium containing compounds, all A symmetry peaks exhibited only one mode behavior. On the other hand, in the sulfur intermediate compounds it appeared two A symmetry modes.
- It was proved that the Raman spectroscopy was a fine technique to detect undesired secondary phases like ZnS and Cu_2SnS_3 by selecting the proper excitation wavelength to create pre-resonant conditions.

5.1.5. Electrical characterization

- All single crystals were determined p-type by Seebeck measurements using a heated probe and a standard multimeter.
- Two different conduction mechanisms for the single crystals were identified by conductivity versus temperature ($\sigma(T)$) measurements. The thermal activated conduction process dominates at high temperature ranges, between 300 and 120 K, and the Mott variable range hopping fits better with the experimental results at lower temperatures, from 120 K to 12 K.
- A decrease of the thermal activation energies with the Ge content seems to take place in CZGTS samples, while no clear dependence of the activation energy is obtained with the Ge concentration in CZGTSe samples.
- In the Mott *VRH* interval, the band width of the band acceptor (*W*) has been found to vary between 27 and 34 meV for CZTGS. It has been proposed that the $Zn_{Sn,Ge}^{2+}$ defect was the most probable source of acceptors for the CZTGS because this was the predominant defect obtained by the Rietveld refinements of the structural characterization. For CZTGSe, there were more divergences in the band acceptor

width, from 1.5 to 13 meV. In this case, the *W* values might be related to the Cu_{Zn}^{+} or Zn_{Cu}^{2+} antsite. The higher values for the width of the acceptor band (*W*) in CZGTS are attributed to the enhanced microscopic disorder in these compounds with respect to CZGTSe and the higher amount of defects after the Rietveld refinements. Indeed, the amount of the defects in CZGTS was higher, in some cases one order of magnitude, than the ones determined for CZGTSe. Moreover, CZTGS samples show higher T_0 than those of CZTGSe, probably indicating that there is less density of localized states near the Fermi level for CZTGS.

5.2. PART II: Device fabrication and characterization

5.2.1. Thin films deposition

- Two rapid deposition processes were used to obtain thin films of Cu_2ZnSnS_4 (CZTS), by flash evaporation and by thermal evaporation. In both cases, it was achieved the CZTS thin film composition but it was detected a problem of reproducibility. It was not possible to achieve similar final compositions with the same initial source material and substrate temperature.

5.2.2. Thermal treatments

- Two different plateau times, of 30 and 60 minutes, at maximum temperature of the thermal treatments, were carried out. The plateau time is not a critical aspect on the chemical composition changes. In both plateaus, cation re-evaporation happened in the same degree.
- Different thermal treatments changing the heating rates (2, 5, 10 and 20 K/min) were performed. The impact of the change of the heating rates on the final composition was not significant. In all heating rates, there were the same tendency of re-evaporation of Cu and increase of the Zn and Sn contents.
- The chemical etchings were paramount to obtain the desired compositions: Cu-poor and Zn-rich: KCN etchings (10% (w/v) KCN at room temperature) during 6 seconds decreased the Cu content meanwhile the Zn and the Sn concentrations increased. Afterwards, $(NH_4)_2S$ etching for about 7 minutes decreased the amount of Sn.

5.2.3. Characterization of the device

- A higher Sn concentration next to the Mo back contact was detected by GDOES measurements for the absorber annealed at higher heating rates. Moreover, an increased content of S was measured next to the Mo, coinciding with the increased Sn concentration. This might indicate the preferential formation of SnS in depth. Since it was not detected at the surface, as measured by Raman spectroscopy. The presence of this SnS secondary phase in the bulk of the absorber layer is one of the reasons of the limited device performance.
- Most of the CZTS cells shown efficiencies (η) below 0.1%. The main explanation might be the thin absorber layer (1 μm), which avoids the generation of enough light-generated carriers and as a consequence their collection to generate a significant current. However, the existence of secondary phases cannot be ruled out, being another possibility of the very low performance of the devices, as mentioned above.
- 2% was the best efficiency for the CZTSSe solar cells. The sulfoselenization thermal treatment was a key aspect to achieve a better performance than the ones obtained for CZTS. The EQE measurements of the CZTSSe devices were characterized by a long end tail curve sloping gradually from 520 nm, which might be attributed to high doping densities and short electron diffusion lengths. Moreover, the thickness of the layer might have a crucial role in this particular decrease of the EQE curve from 520 nm, being here of only 1.25 μm, which affects the EQE spectrum in the higher wavelengths (from 520 to 1200 nm). It was determined a bandgap value of 0.98 eV for the best cell.

Chapter 6

Conclusiones

El objetivo de este trabajo consistió en la síntesis de los compuestos $Cu_2ZnSn_{1-y}Ge_y(S,Se)_4$ en volumen y el estudio de sus propiedades fundamentales. Un segundo objetivo consistió en la fabricación de células solares con el material sintetizado previamente. Las siguientes son las principales conclusiones de esta tesis.

6.1. PARTE I: Caracterización de los compuestos en volumen

6.1.1. Síntesis y composición química

- Se sintetizaron, sin presencia de fases secundarias, monocristales de $Cu_2ZnSn_{1-y}Ge_yS_4$ (CZTGS) con y = 0, 0.1, 0.3, 0.5, 0.7, 0.9 y 1, y de $Cu_2ZnSn_{1-y}Ge_ySe_4$ (CZTGSe) con y = 0, 0.3, 0.5, 0.7 mediante transporte químico en fase vapor (CVT). También se sintetizaron compuestos policristalinos de las mismas soluciones con y = 0, 0.3, 0,5, 0,7 (sólo para el selenio) y 1 por Bridgman, presentando la mayoría de ellos Zn(S,Se) como fase secundaria. En todos los casos, las distintas relaciones atómicas *x*=[Ge/(Ge+Sn)] medidas estuvieron en concordancia con los valores nominales deseados de *y*.
- El compuesto Cu_2ZnSnS_4 (CZTS) también fue sintetizado por reacción en estado sólido (SS) a través de tres rutas de síntesis diferentes: a partir de elementos puros, a partir de compuestos binarios, y a partir de compuestos ternarios y binarios. En dos de estas rutas se sintetizó el compuesto en fase única, presentando una composición pobre en Cu y rica en Zn.

6.1.2. Caracterización estructural

- En el caso de las muestras monocristalinas, se llevaron a cabo refinamientos Rietveld simultáneos de los datos experimentales de difracción de rayos X y de difracción de neutrones. Para los compuestos policristalinos, los refinamientos se llevaron a cabo sólo con los datos de difracción de neutrones. Para la mayoría de los monocristales y los compuestos policristalinos, el parámetro de la calidad de ajuste (χ^2) fue inferior a 4.
- Los parámetros de red (a,c) y la distorsión tetragonal, c/2a, se obtuvieron mediante los refinamientos Rietveld. En todos los compuestos, estos parámetros y la distorsión tetragonal cumplen la ley de Vegard en función de la relación atómica *x*=[Ge/(Ge+Sn)], y disminuyen con el aumento de la cantidad de germanio debido a que el radio iónico del germanio (53 pm) es menor que el del estaño (69 pm).

- Se calcularon la posición de los aniones (XYZ) y las distancias anión-catión. En todos los compuestos se observó una tendencia a la disminución de las distancias S8i-Ge/Sn2b y Se8i-Ge/Sn2b con el aumento de la cantidad de germanio. Este comportamiento se explicó por el menor radio iónico del germanio.
- En el caso de las muestras monocristalinas, los cálculos teóricos de defectos concuerdan con los factores de ocupación en las posiciones cristalinas obtenidos mediante refinamiento Rietveld y las medidas de WDX y/o EDX. Por un lado, se identificaron los defectos Zn_{Cu}^{2+} and $Zn_{Sn,Ge}^{2+}$ para los compuestos de azufre, y por otro, se identificaron los defectos Cu_{Zn}^{+}, $Cu_{Sn,Ge}^{+}$, Zn_{Cu}^{2+} and $Zn_{Sn,Ge}^{2+}$ para los compuestos de selenio. Cualitativamente, se encontró que la cantidad de defectos en los compuestos de azufre era mayor, en algunos casos un orden de magnitud, que la observada en los compuestos de selenio.

6.1.3. Caracterización óptica

- Las propiedades ópticas de los monocristales y compuestos policristalinos $Cu_2ZnSn_{1-y}Ge_y(S,Se)_4$ con diferentes contenidos de Ge fueron investigados por elipsometría espectroscópica. Se determinó la energía de la banda prohibida (E_0) y las energías de interbanda (E_{1A} y E_{1B}) con el cambio de la relación de *x*= [Ge/(Ge+Sn)]. Se observó que la energía de la anchura de la banda prohibida aumenta linealmente con la cantidad de Ge, de 0.93 hasta 1.60 eV y de 1.51 hasta 2.25 eV para monocristales de selenio y azufre, respectivamente. Los compuestos policristalinos mostraron valores similares y el mismo comportamiento lineal que en el caso de los monocristales. Para todos los compuestos, la E_0 corresponde a los valores obtenidos de los cálculos teóricos para la estructura kesterita; excepto en el caso del monocristal $Cu_2ZnSnGeSe_4$. En este caso, parece que la energía de la anchura de la banda prohibida (1.33 eV) se ajusta mejor a los valores de la estructura estannita, cuyo valor de E_0 es más pequeño que la que corresponde a la estructura de kesterita (1.60 eV). Como consecuencia, la elipsometría espectroscópica ha demostrado ser una buena técnica no destructiva para determinar la energía de anchura de la banda prohibida y para distinguir entre la kesterita y otras estructuras como pudiera ser la estanita. Además, la comprensión de cómo se incorpora el Ge en la red atómica de $Cu_2ZnSn(S,Se)_4$ es fundamental para el

desarrollo de la ingeniería de la banda prohibida y para conseguir la fabricación de células solares con un mejor rendimiento.

6.1.4. Caracterización vibracional

- Las propiedades vibracionales se estudiaron mediante espectroscopia de Raman usando diferentes longitudes de onda de excitación. En el caso de los monocristales cuaternarios, se confirmó la estructura del tipo kesterita, basado en el reducido ensanchamiento de los picos y el número de modos de simetría A observados. El análisis de los espectros de Raman medidos con diferentes longitudes de onda de excitación permitieron determinar la posición de más de 30 picos en diferentes muestras, lo que presenta una huella identificativa de los espectros de Raman para estos compuestos en condiciones resonantes y no resonantes. Se observó que la posición de todos los picos se desplaza hacia números de onda más elevados cuando se aumenta la relación atómica x= [Ge/(Ge+Sn)]. En los compuestos que contienen selenio, todos los picos de simetría A exhibieron solamente un comportamiento unimodal. En el caso de los compuestos que contienen azufre, la mayoría de los picos mostraron un comportamiento bimodal, incluyendo el pico con modo de simetría A.
- Los compuestos de azufre y selenio policristalinos medidos por espectroscopia Raman mostraron un comportamiento similar a los compuestos de monocristales. Todos los picos se desplazan hacia números de onda más elevados al aumentar el contenido de germanio. Por un lado, todos los compuestos que contienen selenio mostraron un solo pico en el modo de simetría A. Por otro lado, en los compuestos intermedios de azufre aparecieron dos modos de simetría A.
- Se demostró que la espectroscopia de Raman es una buena técnica para detectar fases secundarias no deseadas como ZnS y Cu_2SnS_3 mediante la adecuada selección de la longitud de onda de excitación para crear condiciones pre-resonantes

6.1.5. Caracterización eléctrica

- Los monocristales estudiados en este trabajo presentaron conductividad tipo p, determinada mediante mediciones Seebeck utilizando una sonda caliente y un multímetro estándar.

- En estas muestras, se identificaron dos mecanismos de conducción diferentes mediante medidas de conductividad frente a la temperatura (σ(T)). El proceso de conducción activado térmicamente domina en el rango de mayores temperaturas, entre 300 y 120 K, y el de Mott de "hopping" variable encaja mejor con los resultados experimentales a temperaturas más bajas, de 120 K a 12 K. Para las muestras CZTGS parece tener lugar una disminución de las energías de activación térmica con el contenido de Ge, mientras que no se obtiene ninguna dependencia clara de la misma con la concentración de Ge para las muestras CZGTSe. En el intervalo Mott VRH, el ancho de banda del aceptor (*W*) se ha encontrado que varía entre 27 y 34 meV para las muestras CZTGS. Se ha propuesto el defecto $Zn_{Sn,Ge}^{2+}$ como la fuente más probable de aceptores para los compuestos CZTGS porque fue el defecto predominante obtenido a partir de los refinamientos Rietveld en la caracterización estructural de estos compuestos. En el caso de las muestras de la solución CZTGSe hubo más divergencias en el ancho de banda del aceptor, de 1.5 a 13 meV. En este caso, los valores de *W* podrían estar relacionados con los defectos Cu_{Zn}^{+} o Zn_{Cu}^{2+}. Los valores más altos para el ancho de banda del aceptor (*W*) en CZGTS se atribuyeron al aumento del desorden microscópico en estos compuestos con respecto a los CZGTSe, lo cual está respaldado por la mayor cantidad de defectos observada en los refinamientos Rietveld. De hecho, las cantidades de los defectos en CZGTS fueron de un orden de magnitud mayor que los determinados para CZGTSe. Por otra parte, las muestras de CZTGS muestran temperaturas críticas de Mott (T_0) superiores a las de CZTGSe, probablemente indicando que hay menor densidad de estados localizados cerca del nivel de Fermi para CZTGS.

6.2. PARTE II: Caracterización de las láminas delgadas

6.2.1. Deposición de películas delgadas

- Se utilizaron dos tipos de proceso de deposición rápida para obtener películas delgadas de Cu_2ZnSnS_4 (CZTS), por evaporación flash y por evaporación térmica. En ambos casos, se logró la composición deseada de la película pero se detectó un problema de reproducibilidad. No fue posible conseguir composiciones finales similares con el mismo material inicial y misma temperatura de sustrato.

6.2.2. Tratamientos térmicos

- Se llevaron a cabo varios tratamientos térmicos con diferentes tiempos de duración del tratamiento. Los tiempos a la máxima temperatura no fueron un aspecto crítico en los cambios de la composición química de las muestras. En ambos casos, la re-evaporación de cationes ocurrió con el mismo grado.
- Se llevaron a cabo diferentes tratamientos térmicos cambiando las velocidades de calentamiento (2, 5, 10 y 20 K / min). El impacto del cambio de las velocidades de calentamiento en la composición final no fue significativoa. En todos los casos, se observó la misma tendencia de re-evaporación del Cu y un aumento de Zn y Sn.
- Los ataques químicos fueron de suma importancia para obtener las composiciones finales deseadas: pobres en Cu y ricas en Zn. El ataque químico de KCN (10% (p / v) KCN a temperatura ambiente) durante 6 segundos disminuyó el contenido de Cu mientras que las concentraciones de Zn y Sn aumentaron. Los ataques posteriores con $(NH_4)_2S$ durante alrededor de 7 minutos consiguieron reducir la cantidad de Sn.

6.2.3. Caracterización del dispositivo

- Las medidas de GDOES evidenciaron una mayor concentración de Sn junto al contacto trasero de Mo para el absorbente tratado térmicamente a velocidades de calentamiento superiores. Por otra parte, se midió un aumento del contenido de S junto al Mo, coincidiendo con el aumento de la concentración de Sn. Esto podría indicar la formación preferencial de la fase secundaria SnS en profundidad que no fue detectada en la superficie, según la medida que se realizó con espectroscopia de Raman. La presencia de esta fase secundaria SnS en el interior de la capa absorbente es una de las razones del rendimiento limitado del dispositivo.
- La mayoría de las células CZTS mostraron eficiencias (η) por debajo de 0.1%. La principal explicación podría ser que la capa absorbente fuera demasiado fina (1 μm), lo que reduciría la colección de portadores para generar una corriente significativa. Sin embargo, no se puede descartar la existencia de fases secundarias, siendo otra posibilidad que explique la eficiencia tan baja, como ya se mencionó anteriormente.
- 2% fue la mejor eficiencia de las células solares fabricadas con los compuestos CZTSSe tras el tratamiento de sulfoselenización, lo que fue un aspecto clave para lograr un mejor rendimiento que en los dispositivos obtenidos a partir de los

compuestos CZTS. Las mediciones de EQE de los dispositivos CZTSSe se caracterizaron por una curva con una larga cola que descendía de manera gradual a partir de los 520 nm, pudiéndose atribuir a la alta densidad de dopaje y a la corta longitud de difusión de los electrones. Además, el espesor de la capa podría tener un papel crucial en esta particular disminución de la curva EQE a partir de 520 nm, siendo en este caso el espesor de tan sólo de 1.25 μm. Para la mejor célula se determinó un valor de la anchura de la banda prohibida de 0.98 eV.

Appendices

Appendix I: Rietveld refinements

In section 3.3, the structural properties by Rietveld refinements were discussed. In this appendix, all the diffraction patterns and refined parameters for each sample are presented.

I.1. Single crystals refinements by X-ray and neutron diffraction data

I.1.1. Sulfur single crystals

Cu_2ZnGeS_4

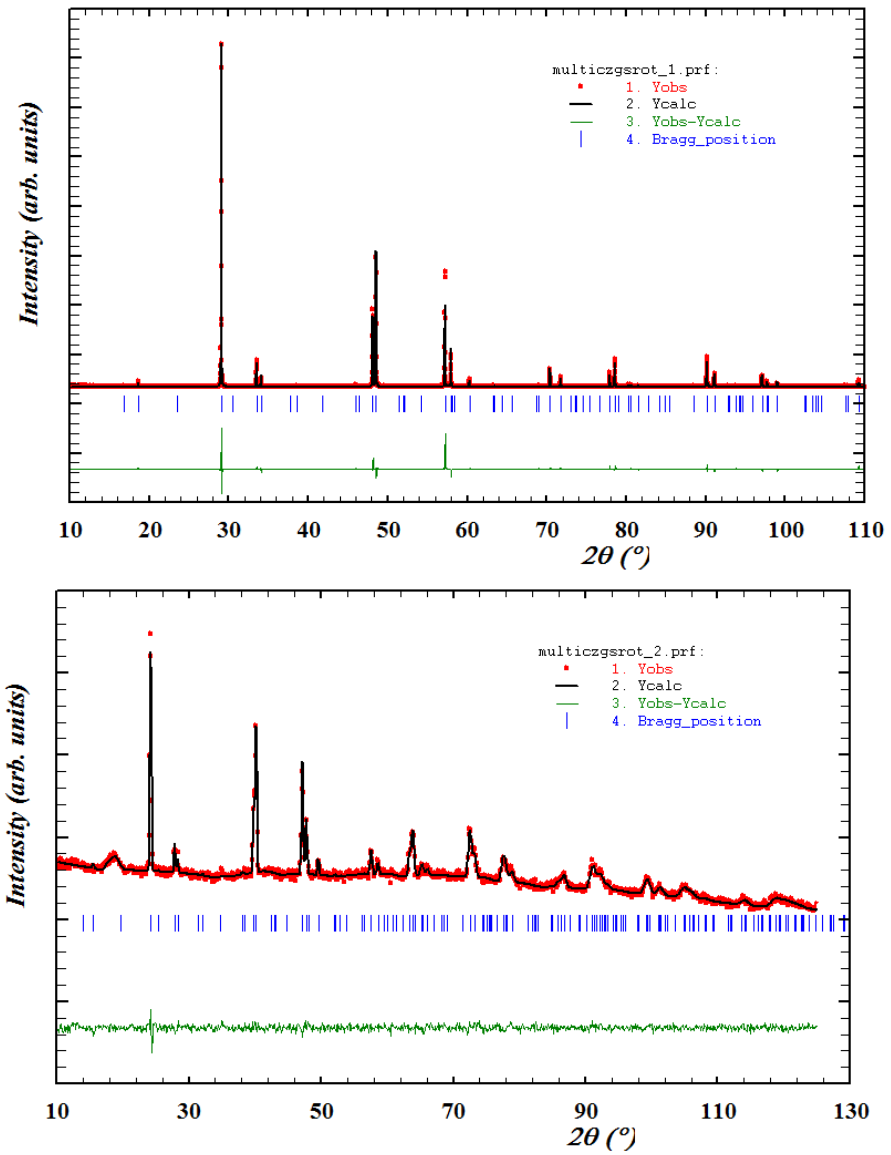

Figure I.1. Simultaneous Rietveld refinement of the X-Ray pattern, above, and Neutron pattern, below, of the Cu_2ZnGeS_4 single crystal.

```
!  Zero    Code    SyCos    Code   SySin    Code  Lambda     Code MORE ->Patt# 1
 -0.02345   41.0  0.00000     0.0  0.00000     0.0 0.000000    0.00   0
!
!  Zero    Code    SyCos    Code   SySin    Code  Lambda     Code MORE ->Patt# 2
 -0.10579   11.0  0.00000     0.0  0.00000     0.0 0.000000    0.00   0
!-------------------------------------------------------------------------------
!  Data for PHASE number:   1  ==> Current R_Bragg for Pattern#  1:     10.14
!  Data for PHASE number:   1  ==> Current R_Bragg for Pattern#  2:     8.50
!-------------------------------------------------------------------------------
CZGS4
!
!Nat Dis Ang Jbt Isy Str Furth         ATZ     Nvk More
   6   0   0   0   0   0   0      12494.1221   0   0
!Contributions (0/1) of this phase to the  2 patterns
 1 1
!Irf Npr Jtyp  Nsp_Ref Ph_Shift for Pattern#  1
   0   5   0       0        0
! Pr1    Pr2    Pr3   Brind.    Rmua   Rmub   Rmuc     for Pattern#  1
  1.000  1.000  2.000  1.000  0.000  0.000  0.000
!Irf Npr Jtyp  Nsp_Ref Ph_Shift for Pattern#  2
   0   7   1       0        0
! Pr1    Pr2    Pr3   Brind.    Rmua   Rmub   Rmuc     for Pattern#  2
  2.000  2.000  0.000  1.000  0.000  0.000  0.000
!
I -4                    <--Space group symbol
!Atom   Typ       X         Y         Z        Biso       Occ     In Fin N_t Spc /Codes
S8i    S       0.26232   0.26574   0.12036   0.00000   4.00000   0   0   0    0
                151.00    161.00    171.00      0.00      0.00
Cu2a   Cu      0.00000   0.00000   0.00000   0.00000   1.00000   0   0   0    0
                  0.00      0.00      0.00      0.00      0.00
Cu2c   Cu      0.00000   0.50000   0.25000   0.00000   1.05146   0   0   0    0
                  0.00      0.00      0.00      0.00      0.00
Ge2b   Ge      0.00000   0.00000   0.50000   0.00000   0.94268   0   0   0    0
                  0.00      0.00      0.00      0.00      0.00
Zn2b   Zn      0.00000   0.00000   0.50000   0.00000   0.06384   0   0   0    0
                  0.00      0.00      0.00      0.00      0.00
Zn2d   Zn      0.00000   0.50000   0.75000   0.00000   0.90603   0   0   0    0
                  0.00      0.00      0.00      0.00      0.00
!-------> Profile Parameters for Pattern #  1
!  Scale        Shape1       Bov       Str1      Str2      Str3   Strain-Model
 0.20384E-04   0.58474   0.18549   0.00000   0.00000   0.00000       0
    11.00000   121.000   101.000     0.000     0.000     0.000
!       U         V         W         X         Y        GauSiz   LorSiz Size-Model
   0.008072  -0.002772   0.003289   0.000000   0.000000   0.000000   0.000000    0
     71.000     81.000     91.000      0.000     0.000      0.000      0.000
!     a         b         c        alpha      beta       gamma      #Cell Info
   5.342830   5.342830  10.514361  90.000000  90.000000  90.000000
   21.00000   21.00000   31.00000   0.00000    0.00000    0.00000
!  Pref1    Pref2      Asy1      Asy2      Asy3      Asy4
  0.15303  0.00000 -0.03276  0.00000  0.00000  0.00000
   131.00     0.00   111.00      0.00      0.00      0.00
!-------> Profile Parameters for Pattern #  2
!  Scale        Shape1       Bov       Str1      Str2      Str3   Strain-Model
 0.31011E-01   0.00000   0.47170   0.00000   0.00000   0.00000       0
    61.00000     0.000   141.000     0.000     0.000     0.000
!       U         V         W         X         Y        GauSiz   LorSiz Size-Model
   1.356573  -0.794750   0.187515   0.000000   0.000000   0.000000   0.000000    0
     51.000     0.000      0.000      0.000     0.000      0.000      0.000
!     a         b         c        alpha      beta       gamma      #Cell Info
   55.342830   5.342830  10.514361  90.000000  90.000000  90.000000
   21.00000   21.00000   31.00000   0.00000    0.00000    0.00000
!  Pref1    Pref2      Asy1      Asy2      Asy3      Asy4       S_L       D_L
  1.00000  0.00000  0.00000  0.00000  0.00000  0.00000  0.00000  0.00000
     0.00     0.00     0.00      0.00      0.00     0.00      0.00      0.00
!  2Th1/TOF1    2Th2/TOF2  Pattern to plot
     10.091     110.000       1
```

$Cu_2ZnSn_{0.1}Ge_{0.9}S_4$

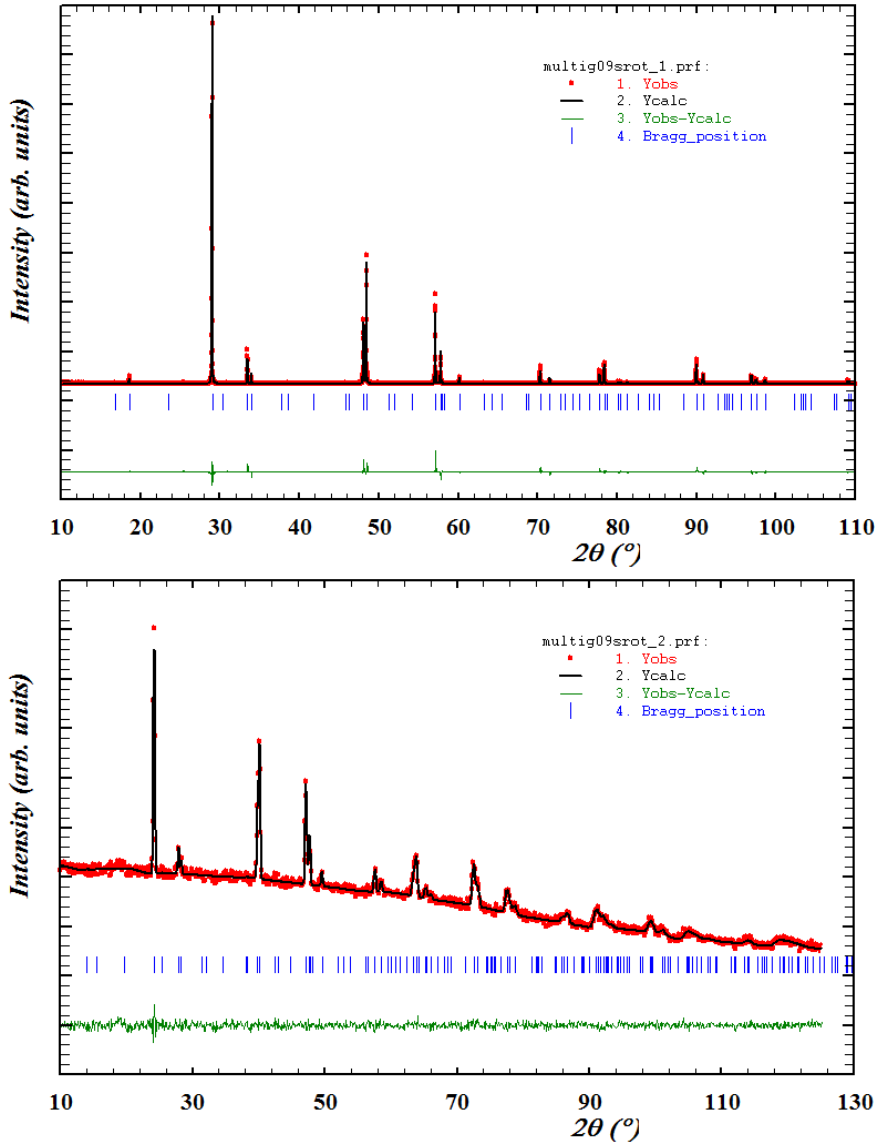

Figure I.2. Simultaneous Rietveld refinement of the X-Ray pattern, above, and Neutron pattern, below, of the $Cu_2ZnSn_{0.1}Ge_{0.9}S_4$ single crystal.

```
!  Zero    Code    SyCos    Code   SySin    Code  Lambda     Code MORE ->Patt# 1
 -0.00984  151.0  0.00000    0.0  0.00000    0.0 0.000000    0.00   0
!
!  Zero    Code    SyCos    Code   SySin    Code  Lambda     Code MORE ->Patt# 2
 -0.24953   51.0  0.00000    0.0  0.00000    0.0 0.000000    0.00   0
!-------------------------------------------------------------------------------
!  Data for PHASE number:   1  ==> Current R_Bragg for Pattern#  1:     9.61
!  Data for PHASE number:   1  ==> Current R_Bragg for Pattern#  2:     8.69
!-------------------------------------------------------------------------------
Cu2ZnGe09Sn01S4
!
!Nat Dis Ang Jbt Isy Str Furth        ATZ     Nvk More
   7   0   0   0   0   0   0      12892.3486   0   1
!Jvi Jdi Hel Sol Mom Ter  N_Domains
   0   3   0   0   0   0      0
!Contributions (0/1) of this phase to the  2 patterns
 1 1
!Irf Npr Jtyp  Nsp_Ref Ph_Shift for Pattern#  1
   0   5   0       0        0
! Pr1    Pr2    Pr3   Brind.    Rmua   Rmub   Rmuc     for Pattern#  1
  1.000  1.000  2.000  1.000  0.000  0.000  0.000
!Irf Npr Jtyp  Nsp_Ref Ph_Shift for Pattern#  2
   0   7   1       0        0
! Pr1    Pr2    Pr3   Brind.    Rmua   Rmub   Rmuc     for Pattern#  2
  1.000  1.000  2.000  1.000  0.000  0.000  0.000
!
! Max_dst(dist) (angles)  Bond-Valence Calc.
      4.0000    160.0000
I -4                     <--Space group symbol
!Atom   Typ       X         Y         Z        Biso       Occ     In Fin N_t Spc /Codes
S8i    S       0.26718   0.26019   0.12017   0.00000   4.00000   0   0   0    0
                171.00    181.00    191.00      0.00      0.00
Cu2a   Cu      0.00000   0.00000   0.00000   0.00000   1.00000   0   0   0    0
                  0.00      0.00      0.00      0.00      0.00
Cu2c   Cu      0.00000   0.50000   0.25000   0.00000   1.00000   0   0   0    0
                  0.00      0.00      0.00      0.00      0.00
Ge2b   Ge      0.00000   0.00000   0.50000   0.00000   0.82634   0   0   0    0
                  0.00      0.00      0.00      0.00      0.00
Sn2b   Sn      0.00000   0.00000   0.50000   0.00000   0.10634   0   0   0    0
                  0.00      0.00      0.00      0.00      0.00
Zn2b   Zn      0.00000   0.00000   0.50000   0.00000   0.02634   0   0   0    0
                  0.00      0.00      0.00      0.00      0.00
Zn2d   Zn      0.00000   0.50000   0.75000   0.00000   1.12001   0   0   0    0
                  0.00      0.00      0.00      0.00      0.00
!-------> Profile Parameters for Pattern #  1
!  Scale        Shape1       Bov       Str1       Str2       Str3   Strain-Model
 0.21003E-04    0.66511    0.47301    0.00000    0.00000    0.00000        0
    11.00000   121.000     61.000      0.000      0.000      0.000
!       U          V          W          X          Y        GauSiz   LorSiz Size-Model
   0.012033  -0.001966   0.002889   0.000000   0.000000   0.000000   0.000000    0
     91.000    101.000    111.000      0.000      0.000      0.000      0.000
!      a          b          c        alpha       beta       gamma       #Cell Info
   5.348730   5.348730  10.541482  90.000000  90.000000  90.000000
   31.00000   31.00000   41.00000    0.00000    0.00000    0.00000
!  Pref1     Pref2      Asy1       Asy2       Asy3       Asy4
  0.01316  0.00000  0.04464  0.01099  0.00000  0.00000
   141.00     0.00   131.00    81.00      0.00      0.00
!-------> Profile Parameters for Pattern #  2
!  Scale        Shape1       Bov       Str1       Str2       Str3   Strain-Model
 0.25136E-01    0.00000    0.92811    0.00000    0.00000    0.00000        0
    21.00000     0.000     71.000      0.000      0.000      0.000
!       U          V          W          X          Y        GauSiz   LorSiz Size-Model
   1.108284  -0.645100   0.166904   0.000000   0.000000   0.000000   0.000000    0
    161.000      0.000      0.000      0.000      0.000      0.000      0.000
!      a          b          c        alpha       beta       gamma       #Cell Info
   5.348730   5.348730  10.541482  90.000000  90.000000  90.000000
   31.00000   31.00000   41.00000    0.00000    0.00000    0.00000
!  Pref1     Pref2      Asy1       Asy2       Asy3       Asy4       S_L        D_L
  1.00000  0.00000  0.00000  0.00000  0.00000  0.00000  0.00000  0.00000
     0.00     0.00     0.00     0.00     0.00     0.00     0.00     0.00
!  2Th1/TOF1    2Th2/TOF2  Pattern to plot
     10.091     110.000       1
```

$Cu_2ZnSn_{0.3}Ge_{0.7}S_4$

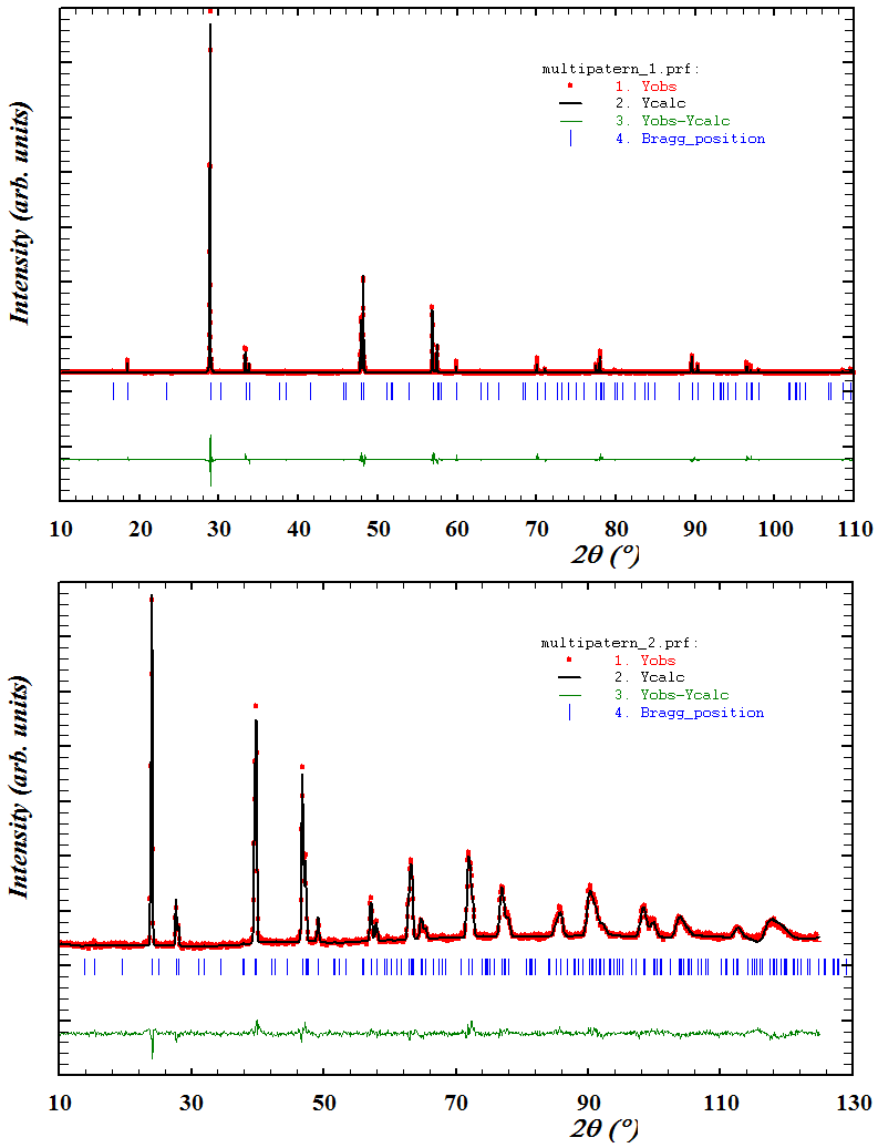

Figure I.3. Simultaneous Rietveld refinement of the X-Ray pattern, above, and Neutron pattern, below, of the $Cu_2ZnSn_{0.3}Ge_{0.7}S_4$ single crystal.

```
!  Zero    Code    SyCos    Code   SySin    Code  Lambda     Code MORE ->Patt# 1
  0.00214   51.0  0.00000     0.0  0.00000     0.0 0.000000    0.00   0
!
!  Zero    Code    SyCos    Code   SySin    Code  Lambda     Code MORE ->Patt# 2
 -0.01671   61.0  0.00000     0.0  0.00000     0.0 0.000000    0.00   0
!-------------------------------------------------------------------------------
!  Data for PHASE number:   1  ==> Current R_Bragg for Pattern#  1:     9.79
!  Data for PHASE number:   1  ==> Current R_Bragg for Pattern#  2:     8.26
!-------------------------------------------------------------------------------
CZSn03Ge07S4
!
!Nat Dis Ang Jbt Isy Str Furth         ATZ     Nvk More
   7   0   0   0   0   0   0      13329.2422   0   0
!Contributions (0/1) of this phase to the  2 patterns
 1 1
!Irf Npr Jtyp  Nsp_Ref Ph_Shift for Pattern#  1
   0   5   0       0       0
! Pr1    Pr2    Pr3   Brind.    Rmua   Rmub   Rmuc     for Pattern#  1
  1.000  1.000  2.000  1.000  0.000  0.000  0.000
!Irf Npr Jtyp  Nsp_Ref Ph_Shift for Pattern#  2
   0   7   1       0       0
! Pr1    Pr2    Pr3   Brind.    Rmua   Rmub   Rmuc     for Pattern#  2
  2.000  2.000  0.000  1.000  0.000  0.000  0.000
!
I -4                     <--Space group symbol
!Atom   Typ       X        Y        Z      Biso       Occ     In Fin N_t Spc /Codes
S8i    S       0.26197  0.27072  0.12090  0.00000   4.00000   0   0   0    0
                151.00   181.00   191.00     0.00      0.00
Cu2a   Cu      0.00000  0.00000  0.00000  0.00000   1.03462   0   0   0    0
                  0.00     0.00     0.00     0.00      0.00
Cu2c   Cu      0.00000  0.50000  0.25000  0.00000   1.00000   0   0   0    0
                  0.00     0.00     0.00     0.00      0.00
Ge2b   Ge      0.00000  0.00000  0.50000  0.00000   0.66490   0   0   0    0
                  0.00     0.00     0.00     0.00      0.00
Sn2b   Sn      0.00000  0.00000  0.50000  0.00000   0.29490   0   0   0    0
                  0.00     0.00     0.00     0.00      0.00
Zn2b   Zn      0.00000  0.00000  0.50000  0.00000   0.03490   0   0   0    0
                  0.00     0.00     0.00     0.00      0.00
Zn2d   Zn      0.00000  0.50000  0.75000  0.00000   1.12356   0   0   0    0
                  0.00     0.00     0.00     0.00      0.00
!-------> Profile Parameters for Pattern #  1
!  Scale        Shape1       Bov       Str1       Str2       Str3   Strain-Model
 0.17927E-04   0.83108   0.86902   0.00000   0.00000   0.00000        0
    11.00000   111.000   101.000     0.000     0.000     0.000
!       U          V          W          X          Y        GauSiz   LorSiz Size-Model
   0.005997   0.002784   0.001716   0.000000   0.000000   0.000000   0.000000    0
     71.000     81.000     91.000      0.000      0.000      0.000      0.000
!      a          b          c        alpha      beta       gamma      #Cell Info
   5.366331   5.366332  10.596955  90.000000  90.000000  90.000000
   31.00000   31.00000   41.00000   0.00000    0.00000    0.00000
!  Pref1    Pref2      Asy1      Asy2      Asy3      Asy4
 -0.27723  0.00000  0.07438 -0.00499  0.00000  0.00000
   121.00     0.00   171.00   161.00      0.00      0.00
!-------> Profile Parameters for Pattern #  2
!  Scale        Shape1       Bov       Str1       Str2       Str3   Strain-Model
 0.31525E-01   0.00000   0.11169   0.00000   0.00000   0.00000        0
    21.00000     0.000   141.000     0.000     0.000     0.000
!       U          V          W          X          Y        GauSiz   LorSiz Size-Model
   1.149212  -0.579693   0.139368   0.000000   0.000000   0.000000   0.000000    0
     131.000      0.000      0.000      0.000      0.000      0.000      0.000
!      a          b          c        alpha      beta       gamma      #Cell Info
   5.366331   5.366332  10.596955  90.000000  90.000000  90.000000
   31.00000   31.00000   41.00000   0.00000    0.00000    0.00000
!  Pref1    Pref2      Asy1      Asy2      Asy3      Asy4       S_L       D_L
  1.00000  0.00000  0.00000  0.00000  0.00000  0.00000  0.00000  0.00000
     0.00     0.00     0.00     0.00     0.00     0.00     0.00     0.00
!  2Th1/TOF1    2Th2/TOF2  Pattern to plot
     10.091      110.000       1
```

$Cu_2ZnSn_{0.5}Ge_{0.5}S_4$

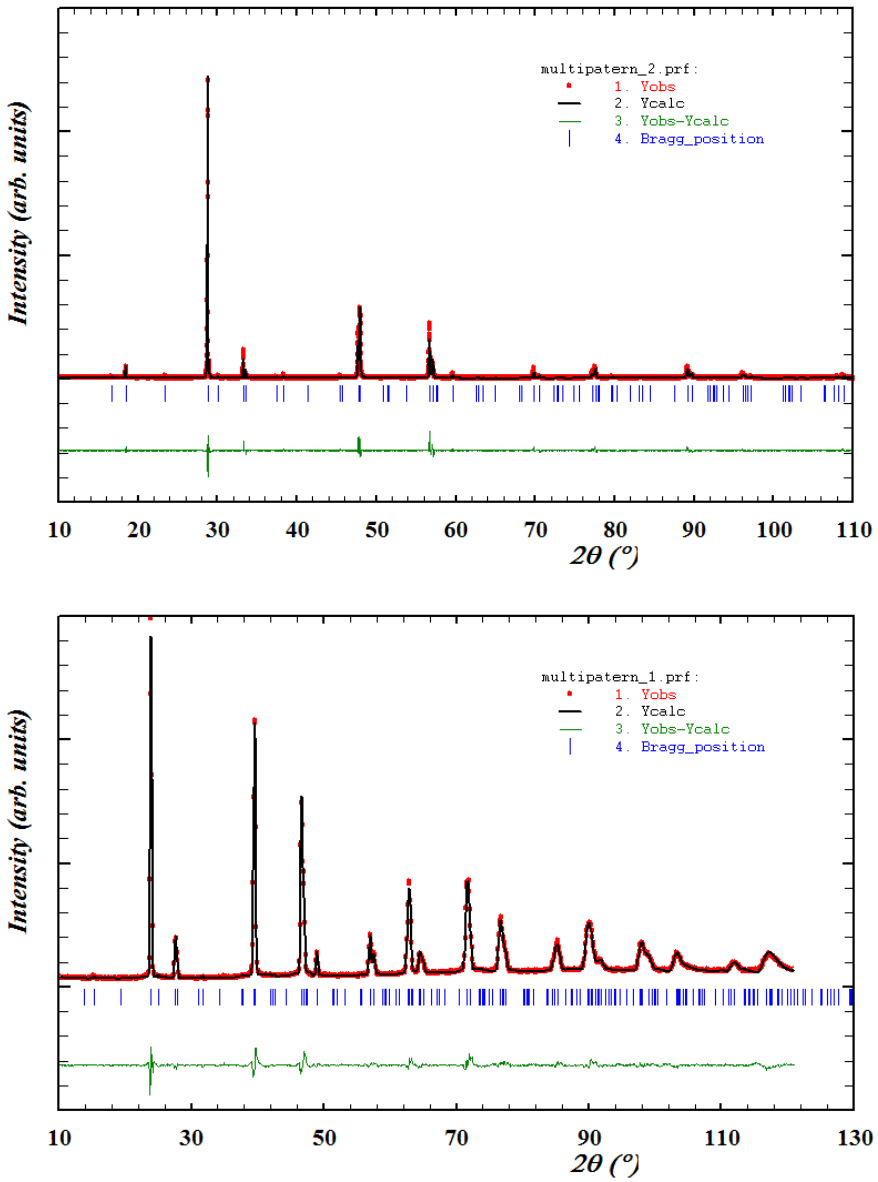

Figure I.4. Simultaneous Rietveld refinement of the X-Ray pattern, above, and Neutron pattern, below, of the $Cu_2ZnSn_{0.5}Ge_{0.5}S_4$ single crystal.

```
!  Zero    Code    SyCos    Code   SySin    Code  Lambda     Code MORE ->Patt# 1
 -0.07755    0.0  0.00000    0.0  0.00000    0.0 0.000000    0.00   0
!
!  Zero    Code    SyCos    Code   SySin    Code  Lambda     Code MORE ->Patt# 2
 -0.03173    0.0  0.00000    0.0  0.00000    0.0 0.000000    0.00   0
!-------------------------------------------------------------------------------
!  Data for PHASE number:   1  ==> Current R_Bragg for Pattern#  1:     6.40
!  Data for PHASE number:   1  ==> Current R_Bragg for Pattern#  2:     9.29
!-------------------------------------------------------------------------------
CZSn05Ge05S4CVT
!
!Nat Dis Ang Jbt Isy Str Furth        ATZ     Nvk More
   7   0   0   0   0   0   0      13284.9219   0   0
!Contributions (0/1) of this phase to the  2 patterns
 1 1
!Irf Npr Jtyp  Nsp_Ref Ph_Shift for Pattern#  1
   0   7    1      0        0
! Pr1    Pr2    Pr3    Brind.    Rmua    Rmub    Rmuc     for Pattern#  1
  1.000  1.000  2.000  1.000  0.000  0.000  0.000
!Irf Npr Jtyp  Nsp_Ref Ph_Shift for Pattern#  2
   0   5    0      0        0
! Pr1    Pr2    Pr3    Brind.    Rmua    Rmub    Rmuc     for Pattern#  2
  1.000  1.000  2.000  1.000  0.000  0.000  0.000
!
82                      <--Space group symbol
!Atom   Typ       X        Y        Z      Biso       Occ     In Fin N_t Spc /Codes
S8g     S       0.26469  0.23646  0.12869  0.00000   4.00000   0   0   0     0
                151.00   161.00   171.00     0.00      0.00
Cu2a    Cu      0.00000  0.00000  0.00000  0.00000   1.00000   0   0   0     0
                  0.00     0.00     0.00     0.00      0.00
Cu2c    Cu      0.00000  0.50000  0.25000  0.00000   1.00000   0   0   0     0
                  0.00     0.00     0.00     0.00      0.00
Ge2b    Ge      0.00000  0.00000  0.50000  0.00000   0.45860   0   0   0     0
                  0.00     0.00     0.00     0.00      0.00
Sn2b    Sn      0.00000  0.00000  0.50000  0.00000   0.49860   0   0   0     0
                  0.00     0.00     0.00     0.00      0.00
Zn2b    Zn      0.00000  0.00000  0.50000  0.00000   0.02860   0   0   0     0
                  0.00     0.00     0.00     0.00      0.00
Zn2d    Zn      0.00000  0.50000  0.75000  0.00000   1.00158   0   0   0     0
                  0.00     0.00     0.00     0.00      0.00
!-------> Profile Parameters for Pattern #  1
!  Scale        Shape1      Bov       Str1      Str2      Str3   Strain-Model
 0.16097       0.00000   0.50071   0.00000   0.00000   0.00000       0
   41.00000      0.000    51.000     0.000     0.000     0.000
!      U          V          W          X          Y        GauSiz   LorSiz Size-Model
   1.119828  -0.645100   0.166904   0.000000 | 0.000000   0.000000   0.000000     0
    111.000      0.000      0.000      0.000      0.000      0.000      0.000
!     a          b          c        alpha      beta       gamma      #Cell Info
   5.391458   5.391458  10.663999  90.000000  90.000000  90.000000
   21.00000   21.00000   31.00000   0.00000    0.00000    0.00000
!  Pref1    Pref2      Asy1      Asy2      Asy3      Asy4      S_L       D_L
  1.00000  0.00000   0.00000   0.00000   0.00000   0.00000   0.00000   0.00000
     0.00     0.00       0.00      0.00      0.00      0.00      0.00      0.00
!-------> Profile Parameters for Pattern #  2
!  Scale        Shape1      Bov       Str1      Str2      Str3   Strain-Model
 0.30658E-04   0.49532   0.80864   0.00000   0.00000   0.00000       0
   11.00000    101.000    91.000     0.000     0.000     0.000
!      U          V          W          X          Y        GauSiz   LorSiz Size-Model
   0.083198   0.003673   0.002293   0.000000   0.000000   0.000000   0.000000     0
     61.000     71.000     81.000      0.000      0.000      0.000      0.000
!     a          b          c        alpha      beta       gamma      #Cell Info
   5.391458   5.391458  10.663999  90.000000  90.000000  90.000000
   21.00000   21.00000   31.00000   0.00000    0.00000    0.00000
!  Pref1    Pref2      Asy1      Asy2      Asy3      Asy4
 -0.05029  0.00000   0.14933   0.00405   0.00000   0.00000
   121.00     0.00     131.00    141.00     0.00      0.00
!  2Th1/TOF1    2Th2/TOF2  Pattern to plot
      10.091      110.000       2
```

$Cu_2ZnSn_{0.7}Ge_{0.3}S_4$

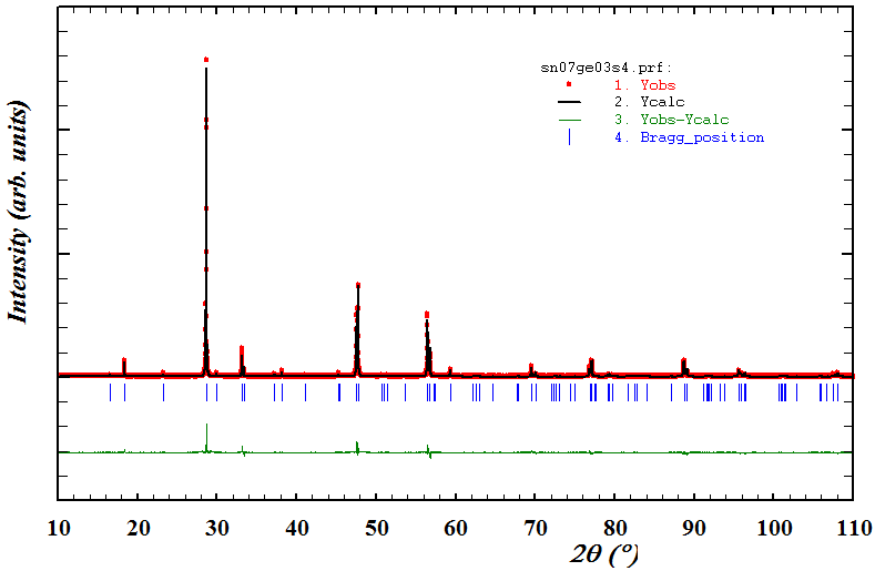

Figure I.5. Rietveld refinement of the X-Ray pattern of the $Cu_2ZnSn_{0.7}Ge_{0.3}S_4$ single crystal.

```
!-------------------------------------------------------------------------------
!  Data for PHASE number:   1  ==> Current R_Bragg for Pattern#  1:    10.84
!-------------------------------------------------------------------------------
CZSn07Ge03S4CVT
!
!Nat Dis Ang Pr1 Pr2 Pr3 Jbt Irf Isy Str Furth       ATZ    Nvk Npr More
   6   0   0 1.0 1.0 2.0   0   0   0   0   0      13609.828   0   5   0
!
82                     <--Space group symbol
!Atom   Typ       X         Y         Z        Biso       Occ     In Fin N_t Spc /Codes
S8g    S       0.26556   0.23406   0.12885  0.00000   4.00000    0   0   0     0
                211.00    221.00    231.00     0.00      0.00
Cu2a   Cu      0.00000   0.00000   0.00000  0.00000   1.00000    0   0   0     0
                  0.00      0.00      0.00     0.00      0.00
Cu2c   Cu      0.00000   0.50000   0.25000  0.00000   1.00000    0   0   0     0
                  0.00      0.00      0.00     0.00      0.00
Ge2b   Ge      0.00000   0.00000   0.50000  0.00000   0.28000    0   0   0     0
                  0.00      0.00      0.00     0.00      0.00
Sn2b   Sn      0.00000   0.00000   0.50000  0.00000   0.71000    0   0   0     0
                  0.00      0.00      0.00     0.00      0.00
Zn2d   Zn      0.00000   0.50000   0.75000  0.00000   1.00000    0   0   0     0
                  0.00      0.00      0.00     0.00      0.00
!-------> Profile Parameters for Pattern #  1
!  Scale        Shape1      Bov       Str1      Str2      Str3   Strain-Model
 0.22385E-04   0.98371   0.00000   0.00000   0.00000   0.00000       0
    41.00000   141.000     0.000     0.000     0.000     0.000
!     U         V         W         X         Y       GauSiz   LorSiz Size-Model
   0.021787  -0.005950   0.003625   0.000000   0.000000   0.000000   0.000000     0
    111.000    121.000    131.000     0.000     0.000     0.000     0.000
!     a         b         c       alpha      beta      gamma      #Cell Info
   5.402189  5.402189  10.731592  90.000000  90.000000  90.000000
   21.00000  21.00000  31.00000    0.00000    0.00000    0.00000
!  Pref1    Pref2      Asy1      Asy2      Asy3      Asy4
 -0.17045  0.00000  0.03681  0.02702  0.00000  0.00000
   181.00     0.00   191.00   201.00     0.00      0.00
!  2Th1/TOF1    2Th2/TOF2  Pattern to plot
      10.091      110.000       1
```

Cu_2ZnSnS_4

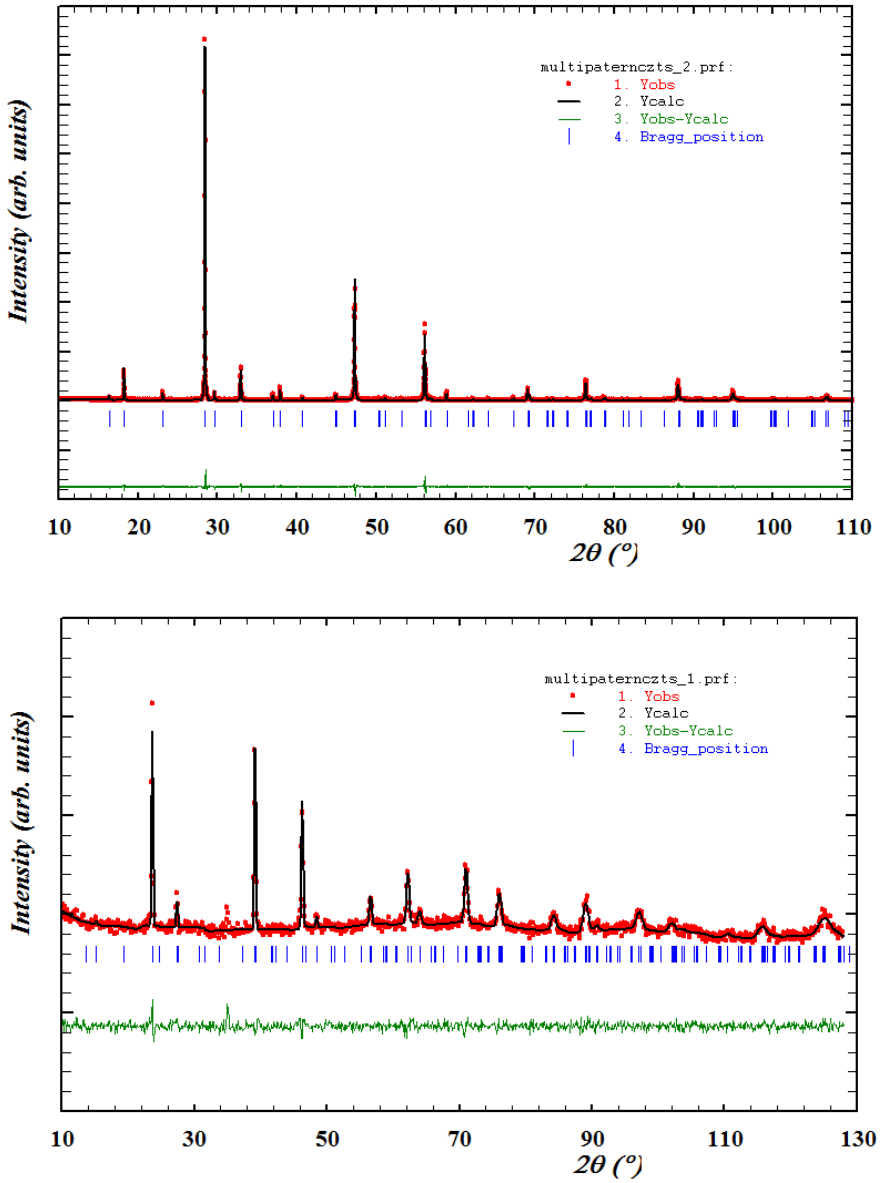

Figure I.6. Simultaneous Rietveld refinement of the X-Ray pattern, above, and Neutron pattern, below, of the Cu_2ZnSnS_4 single crystal.

```
!  Zero    Code    SyCos    Code   SySin    Code  Lambda     Code MORE ->Patt# 1
 -0.12144   11.0  0.00000    0.0  0.00000    0.0 0.000000    0.00   0
!
!  Zero    Code    SyCos    Code   SySin    Code  Lambda     Code MORE ->Patt# 2
 -0.06099   21.0  0.00000    0.0  0.00000    0.0 0.000000    0.00   0
!-------------------------------------------------------------------------------
!  Data for PHASE number:   1  ==> Current R_Bragg for Pattern#  1:      8.84
!  Data for PHASE number:   1  ==> Current R_Bragg for Pattern#  2:      5.12
!-------------------------------------------------------------------------------
CZSnS4
!
!Nat Dis Ang Jbt Isy Str Furth         ATZ     Nvk More
   6   0   0   0   0   0   0      13317.1094    0   0
!Contributions (0/1) of this phase to the  2 patterns
 1 1
!Irf Npr Jtyp  Nsp_Ref Ph_Shift for Pattern#  1
   0   7   1       0       0
! Pr1    Pr2    Pr3   Brind.   Rmua   Rmub   Rmuc     for Pattern#  1
  1.000  1.000  2.000  1.000  0.000  0.000  0.000
!Irf Npr Jtyp  Nsp_Ref Ph_Shift for Pattern#  2
   0   5   0       0       0
! Pr1    Pr2    Pr3   Brind.   Rmua   Rmub   Rmuc     for Pattern#  2
  2.000  0.000  4.000  1.000  0.000  0.000  0.000
!
82                    <--Space group symbol
!Atom   Typ       X        Y        Z      Biso       Occ     In Fin N_t Spc /Codes
S8g    S       0.23269  0.25859  0.13173  0.00000   4.00000   0   0   0    0
                161.00   171.00   181.00     0.00      0.00
Cu2a   Cu      0.00000  0.00000  0.00000  0.00000   0.91540   0   0   0    0
                  0.00     0.00     0.00     0.00      0.00
Cu2c   Cu      0.00000  0.50000  0.25000  0.00000   0.86827   0   0   0    0
                  0.00     0.00     0.00     0.00      0.00
Zn2b   Zn      0.00000  0.50000  0.25000  0.00000   0.02236   0   0   0    0
                  0.00     0.00     0.00     0.00      0.00
Sn2b   Sn      0.00000  0.00000  0.50000  0.00000   0.93126   0   0   0    0
                  0.00     0.00     0.00     0.00      0.00
Zn2d   Zn      0.00000  0.50000  0.75000  0.00000   0.95879   0   0   0    0
                  0.00     0.00     0.00     0.00      0.00
!-------> Profile Parameters for Pattern #  1
!  Scale        Shape1       Bov       Str1       Str2       Str3   Strain-Model
 0.13659E-01   0.00000   0.72801   0.00000   0.00000   0.00000       0
    41.00000     0.000   101.000     0.000     0.000     0.000
!       U         V         W         X         Y       GauSiz   LorSiz Size-Model
   1.407513  -0.794750   0.187515   0.000000   0.000000   0.000000   0.000000    0
     71.000     0.000     0.000     0.000     0.000     0.000     0.000
!     a         b         c       alpha      beta |     gamma      #Cell Info
   5.433220  5.433220  10.835834  90.000000  90.000000  90.000000
   51.00000  51.00000  61.00000   0.00000    0.00000    0.00000
!  Pref1    Pref2      Asy1      Asy2      Asy3      Asy4       S_L       D_L
  1.00000  0.00000  0.00000  0.00000  0.00000  0.00000  0.00000  0.00000
     0.00     0.00     0.00     0.00     0.00     0.00     0.00     0.00
!-------> Profile Parameters for Pattern #  2
!  Scale        Shape1       Bov       Str1       Str2       Str3   Strain-Model
 0.23103E-04   1.01104   1.00773   0.00000   0.00000   0.00000       0
    31.00000   121.000   111.000     0.000     0.000     0.000
!       U         V         W         X         Y       GauSiz   LorSiz Size-Model
   0.015497  0.002833  0.002115   0.000000   0.000000   0.000000   0.000000    0
     81.000    91.000     0.000     0.000     0.000     0.000     0.000
!     a         b         c       alpha      beta      gamma      #Cell Info
   5.433220  5.433220  10.835834  90.000000  90.000000  90.000000
   51.00000  51.00000  61.00000   0.00000    0.00000    0.00000
!  Pref1    Pref2      Asy1      Asy2      Asy3      Asy4
  0.06024  0.00000  0.05277  0.02899  0.00000  0.00000
   151.00     0.00   131.00   141.00     0.00     0.00
!  2Th1/TOF1    2Th2/TOF2  Pattern to plot
     10.091     110.000       1
```

I.1.2. Selenium single crystals

$Cu_2ZnGeSe_4$

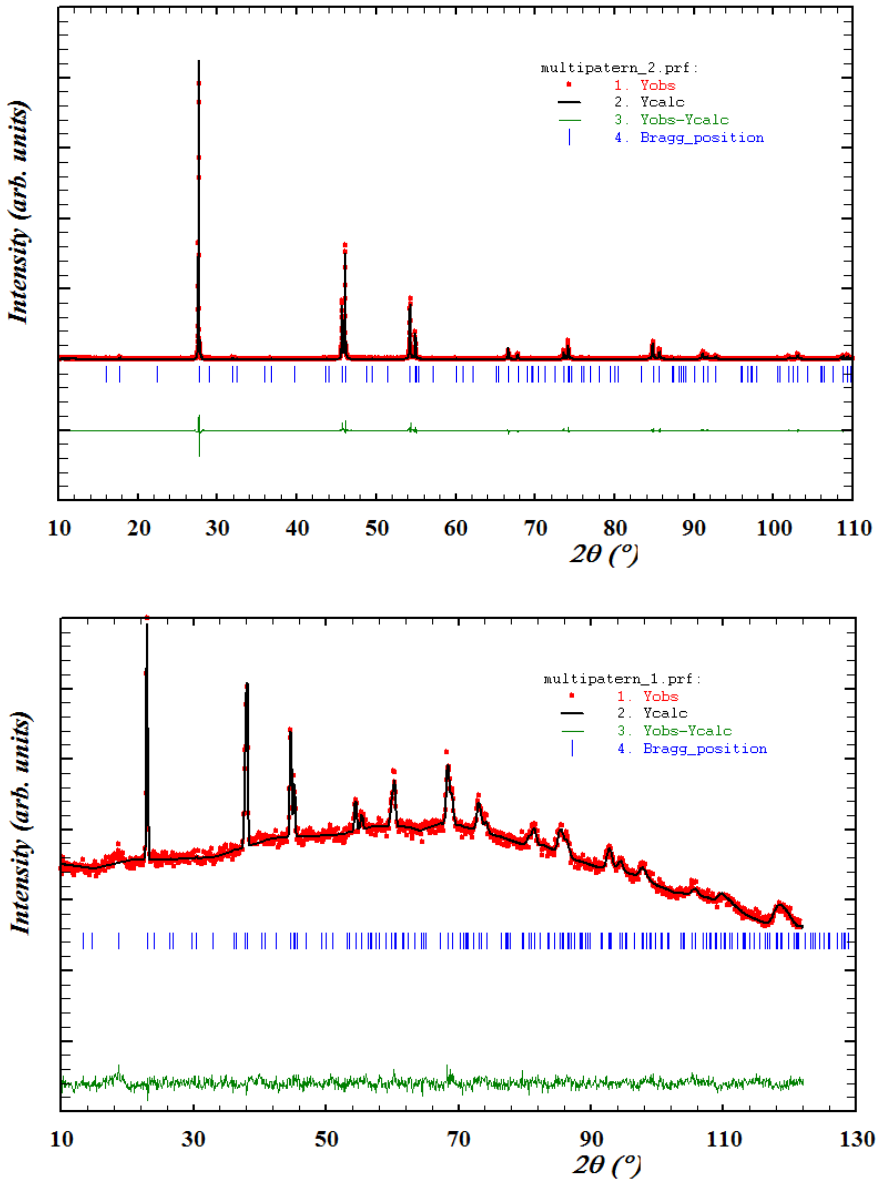

Figure I.7. Simultaneous Rietveld refinement of the X-Ray pattern, above, and Neutron pattern, below, of the $Cu_2ZnGeSe_4$ single crystal.

```
!  Zero    Code    SyCos    Code   SySin    Code  Lambda     Code MORE ->Patt# 1
 -0.03974   51.0  0.00000    0.0  0.00000    0.0 0.000000    0.00   0
!
!  Zero    Code    SyCos    Code   SySin    Code  Lambda     Code MORE ->Patt# 2
 -0.02682   61.0  0.00000    0.0  0.00000    0.0 0.000000    0.00   0
!-------------------------------------------------------------------------------
!  Data for PHASE number:   1  ==> Current R_Bragg for Pattern#  1:    17.45
!  Data for PHASE number:   1  ==> Current R_Bragg for Pattern#  2:     6.42
!-------------------------------------------------------------------------------
GeSeCVT
!
!Nat Dis Ang Jbt Isy Str Furth        ATZ     Nvk More
   6   0   0   0   0   0   0      18383.2988   0   0
!Contributions (0/1) of this phase to the  2 patterns
 1 1
!Irf Npr Jtyp  Nsp_Ref Ph_Shift for Pattern#  1
   0   7    1      0        0
! Pr1    Pr2    Pr3    Brind.    Rmua    Rmub    Rmuc     for Pattern#  1
  1.000  1.000  2.000  1.000  0.000  0.000  0.000
!Irf Npr Jtyp  Nsp_Ref Ph_Shift for Pattern#  2
   0   5    0      0        0
! Pr1    Pr2    Pr3    Brind.    Rmua    Rmub    Rmuc     for Pattern#  2
  1.000  1.000  2.000  1.000  0.000  0.000  0.000
!
82                        <--Space group symbol
!Atom   Typ        X         Y         Z      Biso       Occ     In Fin N_t Spc /Codes
Se8    Se       0.25744   0.25741   0.12522  0.00000   4.00000   0   0   0     0
                171.00    181.00    191.00     0.00      0.00
Cu2a   Cu       0.00000   0.00000   0.00000  0.00000   1.03258   0   0   0     0
                  0.00      0.00      0.00     0.00      0.00
Cu2d   Cu       0.00000   0.50000   0.75000  0.00000   0.98514   0   0   0     0
                  0.00      0.00      0.00     0.00      0.00
Ge2b   Ge       0.00000   0.00000   0.50000  0.00000   0.86547   0   0   0     0
                  0.00      0.00      0.00     0.00      0.00
Cu2b   Cu       0.00000   0.00000   0.50000  0.00000   0.00547   0   0   0     0
                  0.00      0.00      0.00     0.00      0.00
Zn2c   Zn       0.00000   0.50000   0.25000  0.00000   1.02855   0   0   0     0
                  0.00      0.00      0.00     0.00      0.00
!-------> Profile Parameters for Pattern #  1
!  Scale          Shape1       Bov        Str1       Str2       Str3   Strain-Model
 0.91686E-02    0.00000    0.44610    0.00000    0.00000    0.00000        0
    41.00000      0.000    161.000      0.000      0.000      0.000
!       U          V          W          X          Y        GauSiz   LorSiz Size-Model
   1.189194  -0.579693   0.139368   0.000000   0.000000   0.000000   0.000000     0
    141.000      0.000      0.000      0.000      0.000      0.000      0.000
!     a          b          c        alpha      beta       gamma      #Cell Info
   5.608457   5.608457  11.043987  90.000000  90.000000  90.000000
   21.00000   21.00000   31.00000    0.00000    0.00000    0.00000
!  Pref1    Pref2      Asy1      Asy2      Asy3      Asy4       S_L       D_L
  1.00000  0.00000  0.00000  0.00000  0.00000  0.00000  0.00000  0.00000
     0.00     0.00     0.00     0.00     0.00     0.00     0.00     0.00
!-------> Profile Parameters for Pattern #  2
!  Scale          Shape1       Bov        Str1       Str2       Str3   Strain-Model
 0.25080E-04    0.96432    0.40930    0.00000    0.00000    0.00000        0
    11.00000    101.000    151.000      0.000      0.000      0.000
!       U          V          W          X          Y        GauSiz   LorSiz Size-Model
   0.031717  -0.003791   0.002380   0.000000   0.000000   0.000000   0.000000     0
     71.000     81.000     91.000      0.000      0.000      0.000      0.000
!     a          b          c        alpha      beta       gamma      #Cell Info
   5.608457   5.608457  11.043987  90.000000  90.000000  90.000000
   21.00000   21.00000   31.00000    0.00000    0.00000    0.00000
!  Pref1    Pref2      Asy1      Asy2      Asy3      Asy4
  0.02632  0.00000  0.01818  0.02624  0.00000  0.00000
   111.00     0.00   121.00   131.00     0.00     0.00
!  2Th1/TOF1    2Th2/TOF2  Pattern to plot
     10.091     110.000       2
```

$Cu_2ZnSn_{0.5}Ge_{0.5}Se_4$

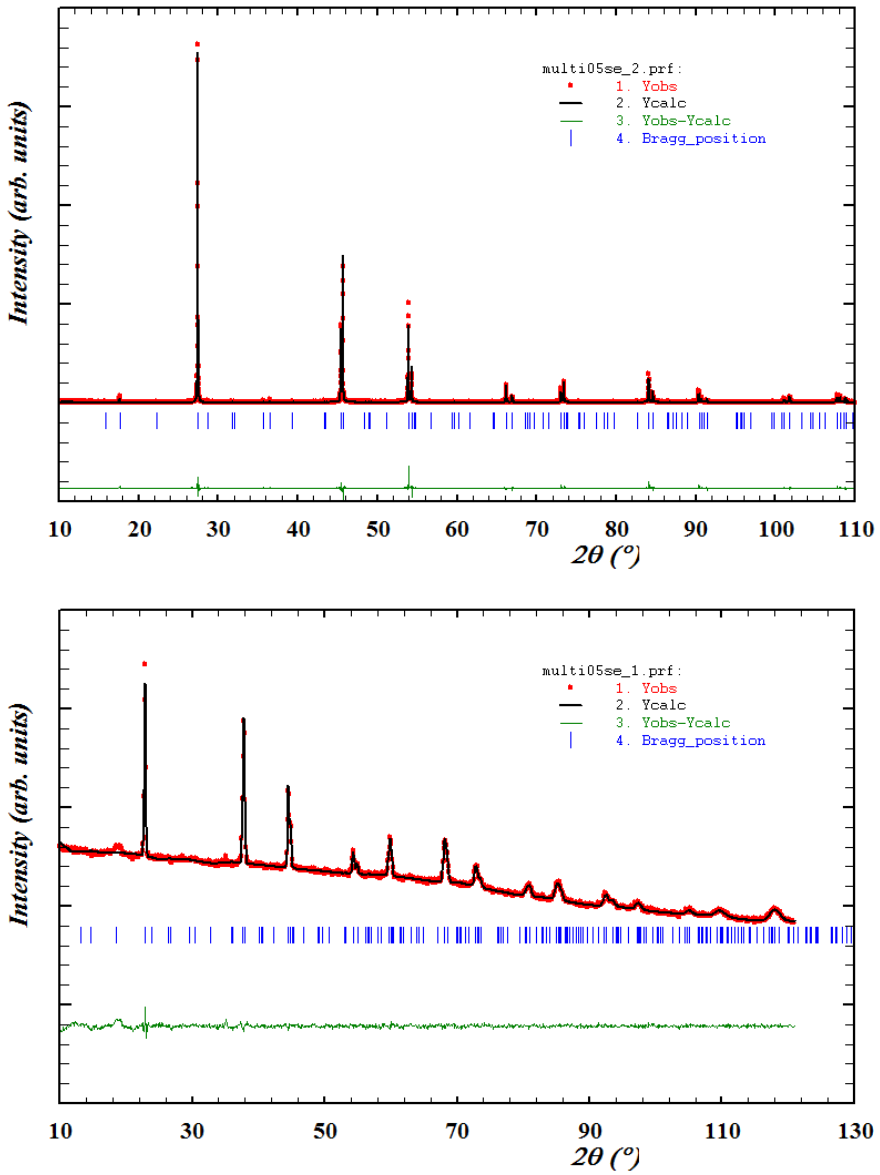

Figure I.8. Simultaneous Rietveld refinement of the X-Ray pattern, above, and Neutron pattern, below, of the $Cu_2ZnSn_{0.5}Ge_{0.5}Se_4$ single crystal.

```
!  Zero    Code    SyCos    Code   SySin    Code  Lambda     Code MORE ->Patt# 1
 -0.24852   11.0  0.00000    0.0  0.00000    0.0 0.000000    0.00   0
!
!  Zero    Code    SyCos    Code   SySin    Code  Lambda     Code MORE ->Patt# 2
 -0.02312   21.0  0.00000    0.0  0.00000    0.0 0.000000    0.00   0
!-------------------------------------------------------------------------------
!  Data for PHASE number:   1  ==> Current R_Bragg for Pattern#  1:     7.80
!  Data for PHASE number:   1  ==> Current R_Bragg for Pattern#  2:     4.52
!-------------------------------------------------------------------------------
SnGe05SeCVT
!
!Nat Dis Ang Jbt Isy Str Furth        ATZ     Nvk More
   7   0   0   0   0   0   0      18782.9922   0   0
!Contributions (0/1) of this phase to the  2 patterns
 1 1
!Irf Npr Jtyp  Nsp_Ref Ph_Shift for Pattern#  1
   0   7    1      0        0
! Pr1    Pr2    Pr3   Brind.   Rmua   Rmub   Rmuc     for Pattern#  1
  1.000  1.000  2.000  1.000  0.000  0.000  0.000
!Irf Npr Jtyp  Nsp_Ref Ph_Shift for Pattern#  2
   0   5    0      0        0
! Pr1    Pr2    Pr3   Brind.   Rmua   Rmub   Rmuc     for Pattern#  2
  2.000  0.000  4.000  1.000  0.000  0.000  0.000
!
82                        <--Space group symbol
!Atom   Typ       X        Y        Z      Biso       Occ     In Fin N_t Spc /Codes
Se8i   Se      0.25780  0.24271  0.12677  0.00000   4.00000   0   0   0     0
                151.00   161.00   171.00     0.00      0.00
Cu2a   Cu      0.00000  0.00000  0.00000  0.00000   1.00000   0   0   0     0
                  0.00     0.00     0.00     0.00      0.00
Cu2d   Cu      0.00000  0.50000  0.75000  0.00000   0.97189   0   0   0     0
                  0.00     0.00     0.00     0.00      0.00
Sn2b   Sn      0.00000  0.00000  0.50000  0.00000   0.43000   0   0   0     0
                  0.00     0.00     0.00     0.00      0.00
Ge2b   Ge      0.00000  0.00000  0.50000  0.00000   0.48000   0   0   0     0
                  0.00     0.00     0.00     0.00      0.00
Zn2c   Zn      0.00000  0.50000  0.25000  0.00000   0.90606   0   0   0     0
                  0.00     0.00     0.00     0.00      0.00
Cu2c   Cu      0.00000  0.50000  0.25000  0.00000   0.01110   0   0   0     0
                  0.00     0.00     0.00     0.00      0.00
!-------> Profile Parameters for Pattern #  1
!  Scale        Shape1       Bov       Str1      Str2      Str3   Strain-Model
 0.54138E-01   0.00000   1.24450   0.00000   0.00000   0.00000        0
    31.00000     0.000   191.000     0.000     0.000     0.000
!       U         V         W         X         Y        GauSiz   LorSiz Size-Model
   1.107394  -0.645100   0.166904   0.000000   0.000000   0.000000   0.000000    0
    111.000     0.000     0.000     0.000     0.000     0.000     0.000
!     a         b         c        alpha      beta       gamma      #Cell Info
   5.642214  5.642214  11.173334  90.000000  90.000000  90.000000
   51.00000  51.00000  61.00000   0.00000    0.00000    0.00000
!  Pref1    Pref2      Asy1      Asy2      Asy3      Asy4       S_L       D_L
  1.00000  0.00000  0.00000  0.00000  0.00000  0.00000  0.00000  0.00000
     0.00     0.00     0.00     0.00     0.00     0.00     0.00     0.00
!-------> Profile Parameters for Pattern #  2
!  Scale        Shape1       Bov       Str1      Str2      Str3   Strain-Model
 0.18625E-04   0.78578   1.00064   0.00000   0.00000   0.00000        0
    41.00000    81.000   181.000     0.000     0.000     0.000
!       U         V         W         X         Y        GauSiz   LorSiz Size-Model
   0.010383  0.000002  0.002622   0.000000   0.000000   0.000000   0.000000    0
    121.000   131.000   141.000     0.000     0.000     0.000     0.000
!     a         b         c        alpha      beta       gamma      #Cell Info
   5.642214  5.642214  11.173334  90.000000  90.000000  90.000000
   51.00000  51.00000  61.00000   0.00000    0.00000    0.00000
!  Pref1    Pref2      Asy1      Asy2      Asy3      Asy4
  0.03438  0.00000  0.05740  0.03298  0.00000  0.00000
    71.00     0.00    91.00   101.00     0.00     0.00
!  2Th1/TOF1    2Th2/TOF2  Pattern to plot
     10.091     110.000       1
```

$Cu_2ZnSn_{0.7}Ge_{0.3}Se_4$

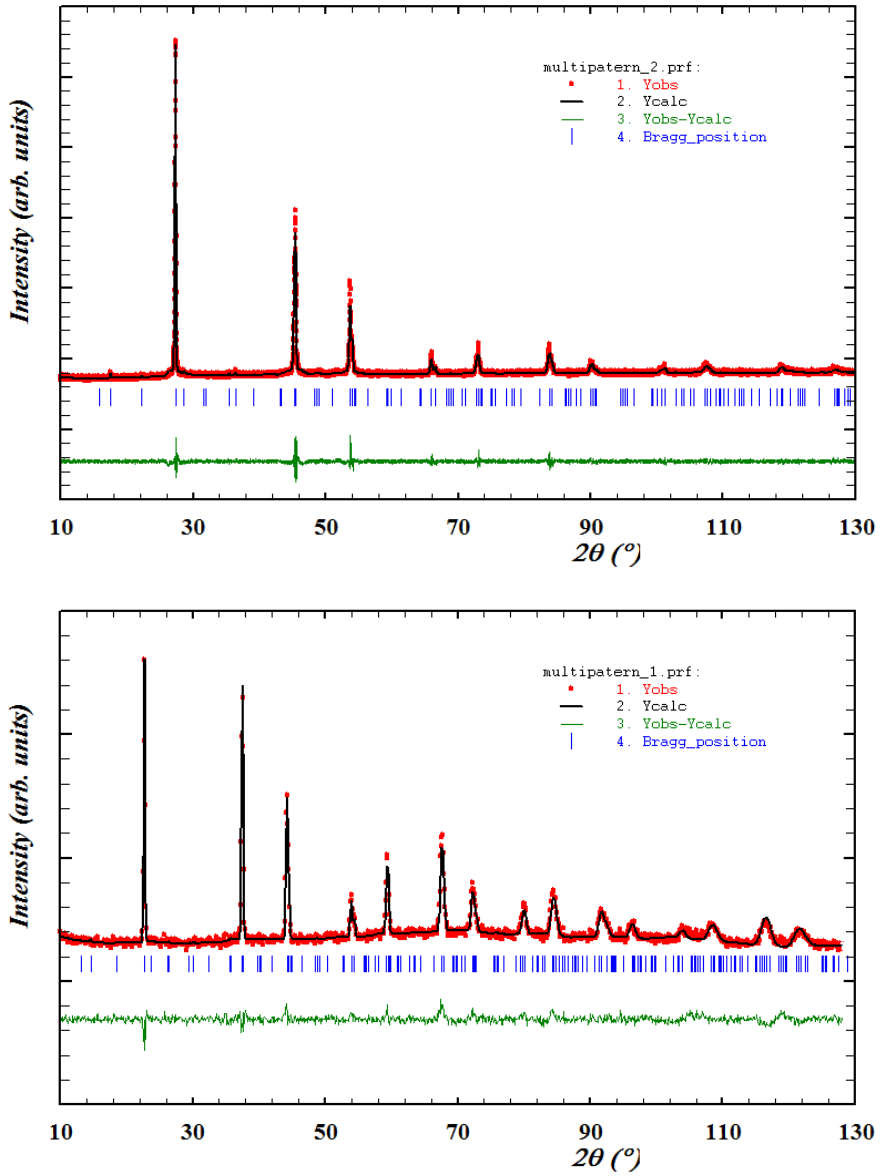

Figure I.9. Simultaneous Rietveld refinement of the X-Ray pattern, above, and Neutron pattern, below, of the $Cu_2ZnSn_{0.7}Ge_{0.3}Se_4$ single crystal.

```
!
!  Zero    Code    SyCos    Code   SySin    Code  Lambda     Code MORE ->Patt# 1
 -0.07311   41.0  0.00000    0.0  0.00000    0.0 0.000000    0.00   0
!
!  Zero    Code    SyCos    Code   SySin    Code  Lambda     Code MORE ->Patt# 2
  0.14777   31.0  0.00000    0.0  0.00000    0.0 0.000000    0.00   0
!-------------------------------------------------------------------------------
!  Data for PHASE number:   1  ==> Current R_Bragg for Pattern#  1:    13.29
!  Data for PHASE number:   1  ==> Current R_Bragg for Pattern#  2:     5.03
!-------------------------------------------------------------------------------
CuZnSn7Ge3SeCVT
!
!Nat Dis Ang Jbt Isy Str Furth        ATZ     Nvk More
   8   0   0   0   0   0   0      19235.7070   0   0
!Contributions (0/1) of this phase to the  2 patterns
 1 1
!Irf Npr Jtyp  Nsp_Ref Ph_Shift for Pattern#  1
   0   7    1      0        0
! Pr1    Pr2    Pr3    Brind.   Rmua   Rmub   Rmuc     for Pattern#  1
  1.000  1.000  2.000  1.000  0.000  0.000  0.000
!Irf Npr Jtyp  Nsp_Ref Ph_Shift for Pattern#  2
   0   5    0      0        0
! Pr1    Pr2    Pr3    Brind.   Rmua   Rmub   Rmuc     for Pattern#  2
  1.000  1.000  2.000  1.000  0.000  0.000  0.000
!
82                      <--Space group symbol
!Atom   Typ       X         Y         Z      Biso       Occ     In Fin N_t Spc /Codes
Se8g   Se      0.25172   0.25730   0.12917  0.00000   4.00000   0   0   0     0
                151.00    161.00    171.00     0.00      0.00
Cu2a   Cu      0.00000   0.00000   0.00000  0.00000   1.00000   0   0   0     0
                  0.00      0.00      0.00     0.00      0.00
Cu2d   Cu      0.00000   0.50000   0.75000  0.00000   0.97265   0   0   0     0
                  0.00      0.00      0.00     0.00      0.00
Zn2d   Zn      0.00000   0.50000   0.75000  0.00000   0.00265   0   0   0     0
                  0.00      0.00      0.00     0.00      0.00
Sn2b   Sn      0.00000   0.00000   0.50000  0.00000   0.60983   0   0   0     0
                  0.00      0.00      0.00     0.00      0.00
Ge2b   Ge      0.00000   0.00000   0.50000  0.00000   0.28983   0   0   0     0
                  0.00      0.00      0.00     0.00      0.00
Zn2b   Zn      0.00000   0.00000   0.50000  0.00000   0.00983   0   0   0     0
                  0.00      0.00      0.00     0.00      0.00
Zn2C   Zn      0.00000   0.50000   0.25000  0.00000   1.00466   0   0   0     0
                  0.00      0.00      0.00     0.00      0.00
!-------> Profile Parameters for Pattern #  1
!  Scale        Shape1      Bov       Str1      Str2      Str3   Strain-Model
 0.64197E-02   0.00000   0.67794   0.00000   0.00000   0.00000        0
    11.00000     0.000   121.000     0.000     0.000     0.000
!       U         V         W         X         Y        GauSiz   LorSiz Size-Model
   1.158207  -0.579693   0.139368   0.000000   0.000000   0.000000   0.000000    0
    111.000     0.000     0.000     0.000     0.000     0.000      0.000
!      a         b         c        alpha      beta       gamma      #Cell Info
   5.659208  5.659208  11.229566  90.000000  90.000000  90.000000
   51.00000  51.00000  61.00000   0.00000    0.00000    0.00000
!  Pref1    Pref2     Asy1      Asy2      Asy3      Asy4      S_L       D_L
  1.00000  0.00000  0.00000  0.00000  0.00000  0.00000  0.00000  0.00000
     0.00     0.00     0.00     0.00     0.00     0.00     0.00     0.00
!-------> Profile Parameters for Pattern #  2
!  Scale        Shape1      Bov       Str1      Str2      Str3   Strain-Model
 0.11564E-04   0.00000   0.40151   0.00000   0.00000   0.00000        0
    21.00000     0.000   101.000     0.000     0.000     0.000
!       U         V         W         X         Y        GauSiz   LorSiz Size-Model
   0.381705  -0.112806   0.050496   0.000000   0.000000   0.000000   0.000000    0
    71.000     81.000     91.000     0.000     0.000     0.000      0.000
!      a         b         c        alpha      beta       gamma      #Cell Info
   5.659208  5.659208  11.229566  90.000000  90.000000  90.000000
   51.00000  51.00000  61.00000   0.00000    0.00000    0.00000
!  Pref1    Pref2      Asy1      Asy2      Asy3      Asy4
  0.15548  0.00000 -0.06227  0.03138  0.00000  0.00000
   131.00     0.00    141.00    151.00     0.00      0.00
!  2Th1/TOF1    2Th2/TOF2  Pattern to plot
     10.099      110.000       1
```

$Cu_2ZnSnSe_4$

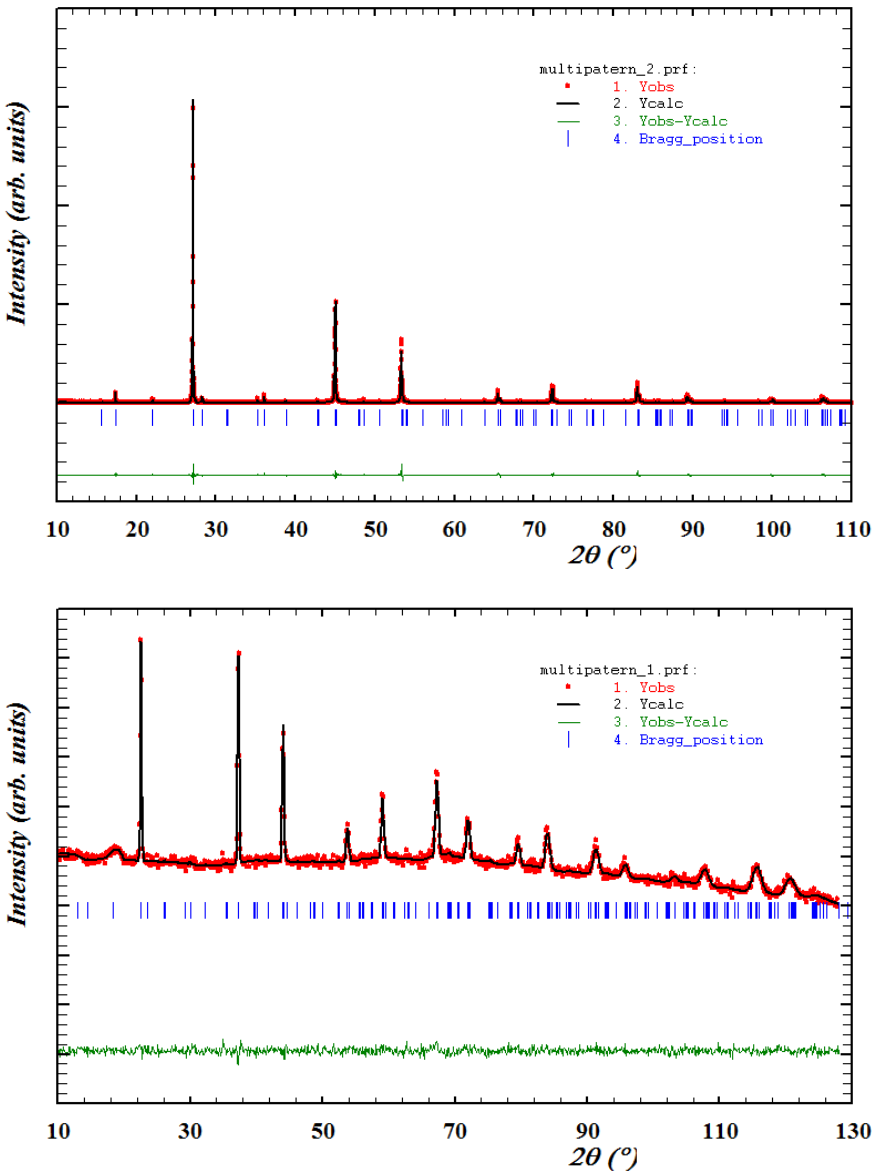

Figure I.10. Simultaneous Rietveld refinement of the X-Ray pattern, above, and Neutron pattern, below, of the $Cu_2ZnSnSe_4$ single crystal.

```
!  Zero    Code    SyCos    Code   SySin    Code  Lambda     Code MORE ->Patt# 1
 -0.10744   51.0  0.00000    0.0  0.00000    0.0 0.000000    0.00   0
!
!  Zero    Code    SyCos    Code   SySin    Code  Lambda     Code MORE ->Patt# 2
 -0.04902   11.0  0.00000    0.0  0.00000    0.0 0.000000    0.00   0
!-------------------------------------------------------------------------------
!  Data for PHASE number:   1  ==> Current R_Bragg for Pattern#  1:    10.59
!  Data for PHASE number:   1  ==> Current R_Bragg for Pattern#  2:     5.19
!-------------------------------------------------------------------------------
SnSeCVT
!
!Nat Dis Ang Jbt Isy Str Furth        ATZ     Nvk More
   6   0   0   0   0   0   0      19526.0000   0   0
!Contributions (0/1) of this phase to the  2 patterns
 1 1
!Irf Npr Jtyp  Nsp_Ref Ph_Shift for Pattern#  1
   0   7    1      0        0
! Pr1    Pr2    Pr3    Brind.    Rmua    Rmub    Rmuc     for Pattern#  1
  1.000  1.000  2.000  1.000  0.000  0.000  0.000
!Irf Npr Jtyp  Nsp_Ref Ph_Shift for Pattern#  2
   0   5    0      0        0
! Pr1    Pr2    Pr3    Brind.    Rmua    Rmub    Rmuc     for Pattern#  2
  1.000  1.000  2.000  1.000  0.000  0.000  0.000
!
82                      <--Space group symbol
!Atom   Typ       X         Y         Z      Biso       Occ     In Fin N_t Spc /Codes
Se8    Se      0.26615   0.24763   0.13032  0.00000   4.00000   0   0   0     0
                171.00    181.00    191.00     0.00      0.00
Cu2a   Cu      0.00000   0.00000   0.00000  0.00000   0.94717   0   0   0     0
                  0.00      0.00      0.00     0.00      0.00
Cu2c   Cu      0.00000   0.50000   0.25000  0.00000   0.92863   0   0   0     0
                  0.00      0.00      0.00     0.00      0.00
Zn2c   Zn      0.00000   0.50000   0.25000  0.00000   0.00675   0   0   0     0
                  0.00      0.00      0.00     0.00      0.00
Sn2b   Sn      0.00000   0.00000   0.50000  0.00000   0.94000   0   0   0     0
                  0.00      0.00      0.00     0.00      0.00
Zn2d   Zn      0.00000   0.50000   0.75000  0.00000   0.96571   0   0   0     0
                  0.00      0.00      0.00     0.00      0.00
!-------> Profile Parameters for Pattern #  1
!  Scale        Shape1       Bov       Str1       Str2       Str3   Strain-Model
 0.12329E-01   0.00000   0.47338   0.00000   0.00000   0.00000        0
    41.00000     0.000   151.000     0.000     0.000     0.000
!       U         V         W         X         Y        GauSiz   LorSiz Size-Model
   1.158136  -0.579693   0.139368  0.000000  0.000000  0.000000  0.000000     0
     61.000     0.000     0.000     0.000     0.000     0.000     0.000
!     a         b         c        alpha      beta       gamma      #Cell Info
   5.695577  5.695577  11.345606  90.000000  90.000000  90.000000
   21.00000  21.00000  31.00000   0.00000    0.00000    0.00000
!  Pref1    Pref2      Asy1      Asy2      Asy3      Asy4       S_L       D_L
  1.00000  0.00000  0.00000  0.00000  0.00000  0.00000  0.00000  0.00000
     0.00     0.00     0.00     0.00     0.00     0.00     0.00     0.00
!-------> Profile Parameters for Pattern #  2
!  Scale        Shape1       Bov       Str1       Str2       Str3   Strain-Model
 0.15433E-04   0.97847   0.93793   0.00000   0.00000   0.00000        0
    81.00000   131.000   161.000     0.000     0.000     0.000
!       U         V         W         X         Y        GauSiz   LorSiz Size-Model
   0.009833  0.010507  0.000390  0.000000  0.000000  0.000000  0.000000     0
     71.000    101.000    111.000     0.000     0.000     0.000     0.000
!     a         b         c        alpha      beta       gamma      #Cell Info
   5.695577  5.695577  11.345606  90.000000  90.000000  90.000000
   21.00000  21.00000  31.00000   0.00000    0.00000    0.00000
!  Pref1    Pref2      Asy1      Asy2      Asy3      Asy4
 -0.11154  0.00000  0.03631  0.02741  0.00000  0.00000
   141.00     0.00   121.00    91.00     0.00     0.00
!  2Th1/TOF1    2Th2/TOF2  Pattern to plot
     10.091     110.000       1
```

I.3. Polycrystalline refinements by neutron diffraction data

I.3.1. Sulfur polycrystallines

$Cu_2ZnSn_{0.7}Ge_{0.3}S_4$

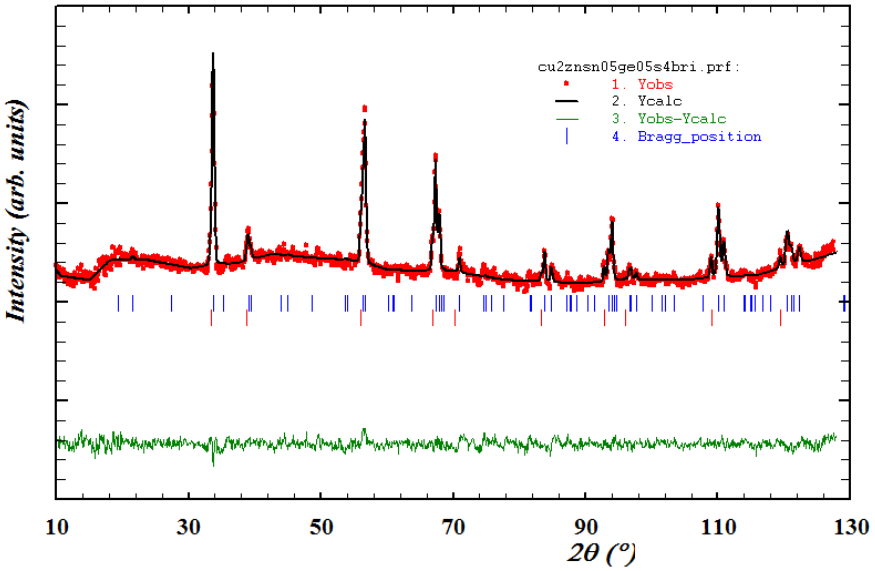

Figure I.11. Rietveld refinement of the neutron pattern of the $Cu_2ZnSn_{0.5}Ge_{0.5}S_4$ polycrystalline.

```
!  Zero    Code    SyCos    Code   SySin    Code  Lambda     Code MORE ->Patt# 1
 -0.01600   11.0  0.00000     0.0  0.00000     0.0 0.000000    0.00   0
!-------------------------------------------------------------------------------
!  Data for PHASE number:   1  ==> Current R_Bragg for Pattern#  1:    13.55
!-------------------------------------------------------------------------------
CZTSBRI
!
!Nat Dis Ang Pr1 Pr2 Pr3 Jbt Irf Isy Str Furth       ATZ    Nvk Npr More
   6   0   0 1.0 1.0 2.0   0   0   0   0   0      13371.021   0   7   0
!
82                     <--Space group symbol
!Atom   Typ       X         Y         Z      Biso       Occ     In Fin N_t Spc /Codes
S8g    S       0.24098   0.23988   0.12142  0.00000   4.00000   0   0   0    0
                61.00     121.00    131.00     0.00      0.00
Cu2a   Cu      0.00000   0.00000   0.00000  0.00000   1.00000   0   0   0    0
                 0.00      0.00      0.00     0.00      0.00
Cu2c   Cu      0.00000   0.50000   0.25000  0.00000   1.00000   0   0   0    0
                 0.00      0.00      0.00     0.00      0.00
Sn2b   Sn      0.00000   0.00000   0.50000  0.00000   0.60901   0   0   0    0
                 0.00      0.00      0.00     0.00      0.00
Ge2b   Ge      0.00000   0.00000   0.50000  0.00000   0.34232   0   0   0    0
                 0.00      0.00      0.00     0.00      0.00
Zn2d   Zn      0.00000   0.50000   0.75000  0.00000   1.00000   0   0   0    0
                 0.00      0.00      0.00     0.00      0.00
!-------> Profile Parameters for Pattern #  1
!  Scale        Shape1       Bov       Str1      Str2      Str3   Strain-Model
 0.38933E-01   0.00000   1.42329   0.00000   0.00000   0.00000        0
    21.00000     0.000     0.000     0.000     0.000     0.000
!       U         V         W         X         Y        GauSiz   LorSiz Size-Model
   0.103378  -0.165300   0.165400   0.000000   0.093548   0.000000   0.000000    0
     51.000     0.000     0.000     0.000     71.000     0.000      0.000
!      a         b         c        alpha      beta       gamma      #Cell Info
   5.382443  5.382443  10.658083  90.000000  90.000000  90.000000
   31.00000  31.00000  41.00000   0.00000    0.00000    0.00000
!  Pref1    Pref2      Asy1      Asy2      Asy3      Asy4      S_L       D_L
  0.00000  0.00000   0.00000   0.00000   0.00000   0.00000   0.04000   0.04000
     0.00     0.00      0.00      0.00      0.00      0.00      0.00      0.00
!-------------------------------------------------------------------------------
!  Data for PHASE number:   2  ==> Current R_Bragg for Pattern#  1:     9.62
!-------------------------------------------------------------------------------
 ####   ZnS  ####
!
!Nat Dis Ang Pr1 Pr2 Pr3 Jbt Irf Isy Str Furth       ATZ    Nvk Npr More
   2   0   0 0.0 0.0 1.0   0   0   0   0   0     224501.766   0   7   1
!
!Jvi Jdi Hel Sol Mom Ter  Brind   RMua    RMub    RMuc   Jtyp  Nsp_Ref Ph_Shift N_Domains
   0   3   0   0   0   0  1.0000  0.0000  0.0000  0.0000    1       0       0       0
!
! Max_dst(dist) (angles)  Bond-Valence Calc.
       3.0000      3.0000
F -4 3 m               <--Space group symbol
!Atom   Typ       X         Y         Z      Biso       Occ     In Fin N_t Spc /Codes
Zn     Zn      0.00000   0.00000   0.00000  0.00000   1.00000   0   0   0    0
                 0.00      0.00      0.00     0.00      0.00
S      S       0.25000   0.25000   0.25000  0.00000   1.00000   0   0   0    0
                 0.00      0.00      0.00     0.00      0.00
!-------> Profile Parameters for Pattern #  1
!  Scale        Shape1       Bov       Str1      Str2      Str3   Strain-Model
 0.93049E-03   0.00000   1.81311   0.00000   0.00000   0.00000        0
   101.00000     0.000    81.000     0.000     0.000     0.000
!       U         V         W         X         Y        GauSiz   LorSiz Size-Model
   0.083585  -0.165300   0.165400   0.000000   0.058900   0.000000   0.000000    0
     91.000     0.000     0.000     0.000     0.000      0.000      0.000
!      a         b         c        alpha      beta       gamma      #Cell Info
   5.409752  5.409752  5.409752  90.000000  90.000000  90.000000
  111.00000  111.00000  111.00000   0.00000    0.00000    0.00000
!  Pref1    Pref2      Asy1      Asy2      Asy3      Asy4      S_L       D_L
  0.00000  0.00000   0.00000   0.00000   0.00000   0.00000   0.04000   0.04000
     0.00     0.00      0.00      0.00      0.00      0.00      0.00      0.00
!  2Th1/TOF1    2Th2/TOF2  Pattern to plot
       1.000     128.000       1
```

$Cu_2ZnSn_{0.7}Ge_{0.3}S_4$

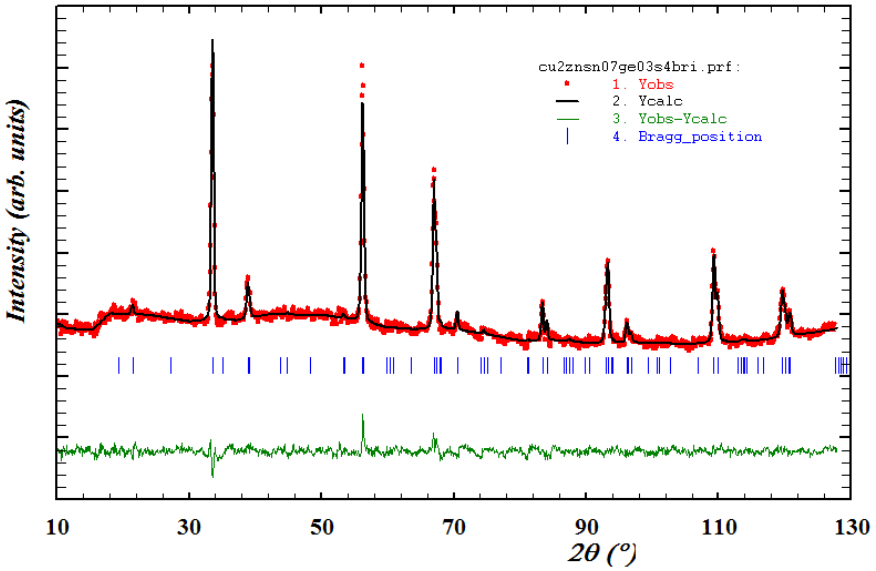

Figure I.12. Rietveld refinement of the neutron pattern of the $Cu_2ZnSn_{0.7}Ge_{0.3}S_4$ polycrystalline.

```
!  Zero    Code    SyCos    Code   SySin    Code  Lambda     Code MORE ->Patt# 1
  0.02361   11.0  0.00000     0.0  0.00000     0.0 0.000000    0.00   0
!-------------------------------------------------------------------------------
!  Data for PHASE number:   1  ==> Current R_Bragg for Pattern#  1:     9.17
!-------------------------------------------------------------------------------
CZTSBRI
!
!Nat Dis Ang Pr1 Pr2 Pr3 Jbt Irf Isy Str Furth       ATZ    Nvk Npr More
   6   0   0 1.0 1.0 2.0   0   0   0   0   0      13240.653   0   7   0
!
82                     <--Space group symbol
!Atom   Typ       X         Y         Z       Biso       Occ     In Fin N_t Spc /Codes
S8g    S       0.24481   0.27450   0.11397   0.00000   4.00000   0   0   0    0
                301.00    311.00     51.00      0.00      0.00
Cu2a   Cu      0.00000   0.00000   0.00000   0.00000   1.00000   0   0   0    0
                  0.00      0.00      0.00      0.00      0.00
Cu2c   Cu      0.00000   0.50000   0.25000   0.00000   1.00000   0   0   0    0
                  0.00      0.00      0.00      0.00      0.00
Sn2b   Sn      0.00000   0.00000   0.50000   0.00000   0.65681   0   0   0    0
                  0.00      0.00      0.00      0.00      0.00
Ge2b   Ge      0.00000   0.00000   0.50000   0.00000   0.20804   0   0   0    0
                  0.00      0.00      0.00      0.00      0.00
Zn2d   Zn      0.00000   0.50000   0.75000   0.00000   1.00000   0   0   0    0
                  0.00      0.00      0.00      0.00      0.00
!-------> Profile Parameters for Pattern #  1
!  Scale        Shape1       Bov       Str1       Str2       Str3    Strain-Model
 0.98243E-01   0.00000   1.90695   0.00000   0.00000   0.00000        0
    21.00000     0.000     0.000     0.000     0.000     0.000
!      U         V         W         X         Y       GauSiz   LorSiz Size-Model
   0.078930  -0.165300   0.165400   0.000000   0.129662   0.000000   0.000000    0
     61.000     0.000     0.000     0.000    291.000     0.000      0.000
!     a         b         c       alpha      beta       gamma      #Cell Info
   5.404935  5.404935  10.737881  90.000000  90.000000  90.000000
   31.00000  31.00000  41.00000   0.00000    0.00000    0.00000
!  Pref1    Pref2      Asy1      Asy2      Asy3      Asy4       S_L       D_L
  0.00000  0.00000   0.00000   0.00000   0.00000   0.00000   0.04000   0.04000
     0.00     0.00      0.00      0.00      0.00      0.00      0.00      0.00
!  2Th1/TOF1    2Th2/TOF2   Pattern to plot
      1.000      128.000         1
```

Cu_2ZnSnS_4

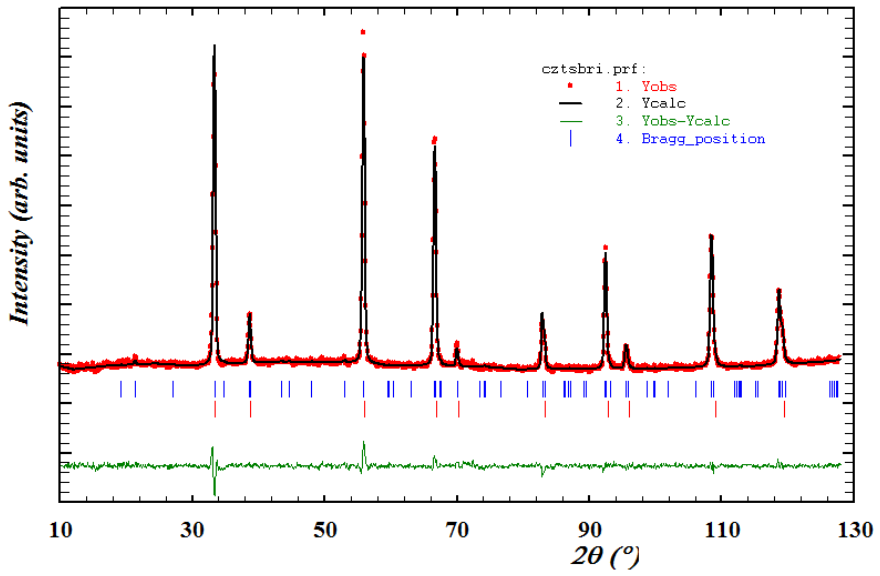

Figure I.13. Rietveld refinement of the neutron pattern of the Cu_2ZnSnS_4 polycrystalline.

```
!  Zero    Code    SyCos    Code   SySin    Code  Lambda     Code MORE ->Patt# 1
 -0.03648   11.0  0.00000     0.0  0.00000     0.0 0.000000    0.00   0
!-------------------------------------------------------------------------------
!  Data for PHASE number:   1  ==> Current R_Bragg for Pattern#  1:     4.74
!-------------------------------------------------------------------------------
CZTSBRI
!
!Nat Dis Ang Pr1 Pr2 Pr3 Jbt Irf Isy Str Furth       ATZ    Nvk Npr More
   5   0   0 1.0 1.0 2.0   0   0   0   0   0      13479.192   0   7   0
!
82                     <--Space group symbol
!Atom   Typ       X         Y         Z       Biso       Occ     In Fin N_t Spc /Codes
S8g    S       0.24252   0.24562   0.12803   0.00000    4.00000   0   0   0    0
                121.00    121.00    131.00      0.00       0.00
Cu2a   Cu      0.00000   0.00000   0.00000   0.00000    0.95852   0   0   0    0
                  0.00      0.00      0.00      0.00       0.00
Cu2c   Cu      0.00000   0.50000   0.25000   0.00000    0.85478   0   0   0    0
                  0.00      0.00      0.00      0.00       0.00
Sn2b   Sn      0.00000   0.00000   0.50000   0.00000    0.98560   0   0   0    0
                  0.00      0.00      0.00      0.00       0.00
Zn2d   Zn      0.00000   0.50000   0.75000   0.00000    0.92957   0   0   0    0
                  0.00      0.00      0.00      0.00       0.00
!-------> Profile Parameters for Pattern #  1
!  Scale        Shape1       Bov       Str1      Str2      Str3   Strain-Model
 0.14371       0.00000   1.95299   0.00000   0.00000   0.00000        0
    21.00000      0.000    71.000      0.000     0.000     0.000
!       U         V         W         X         Y        GauSiz   LorSiz Size-Model
   0.064331  -0.165300   0.165400   0.000000   0.124318   0.000000   0.000000    0
     51.000      0.000     0.000      0.000     60.500      0.000      0.000
!     a         b         c        alpha      beta       gamma      #Cell Info
   5.432393  5.432393  10.830482  90.000000  90.000000  90.000000
   31.00000  31.00000  41.00000    0.00000    0.00000    0.00000
!  Pref1    Pref2      Asy1      Asy2      Asy3      Asy4      S_L       D_L
  0.15977  0.00000   0.00000   0.00000   0.00000   0.00000   0.04000   0.04000
     0.00      0.00      0.00      0.00      0.00      0.00      0.00      0.00
!-------------------------------------------------------------------------------
!  Data for PHASE number:   2  ==> Current R_Bragg for Pattern#  1:     4.04
!-------------------------------------------------------------------------------
 ####   ZnS  ####
!
!Nat Dis Ang Pr1 Pr2 Pr3 Jbt Irf Isy Str Furth       ATZ    Nvk Npr More
   2   0   0 0.0 0.0 1.0   0   0   0   0   0     224501.766   0   7   1
!
!Jvi Jdi Hel Sol Mom Ter  Brind   RMua    RMub    RMuc    Jtyp  Nsp_Ref Ph_Shift N_Domains
   0   3   0   0   0   0  1.0000  0.0000  0.0000  0.0000    1       0       0       0
!
! Max_dst(dist) (angles)  Bond-Valence Calc.
        3.0000       3.0000
F -4 3 m               <--Space group symbol
!Atom   Typ       X         Y         Z       Biso       Occ     In Fin N_t Spc /Codes
Zn     Zn      0.00000   0.00000   0.00000   0.00000    1.00000   0   0   0    0
                  0.00      0.00      0.00      0.00       0.00
S      S       0.25000   0.25000   0.25000   0.00000    1.00000   0   0   0    0
                  0.00      0.00      0.00      0.00       0.00
!-------> Profile Parameters for Pattern #  1
!  Scale        Shape1       Bov       Str1      Str2      Str3   Strain-Model
 0.10429E-02   0.00000   2.14715   0.00000   0.00000   0.00000        0
   101.00000      0.000    81.000      0.000     0.000     0.000
!       U         V         W         X         Y        GauSiz   LorSiz Size-Model
   0.200361  -0.165300   0.165400   0.000000   0.058900   0.000000   0.000000    0
     91.000      0.000     0.000      0.000     0.000      0.000      0.000
!     a         b         c        alpha      beta       gamma      #Cell Info
   5.408276  5.408276  5.408276  90.000000  90.000000  90.000000
  111.00000  111.00000  111.00000    0.00000    0.00000    0.00000
!  Pref1    Pref2      Asy1      Asy2      Asy3      Asy4      S_L       D_L
  0.00000  0.00000   0.00000   0.00000   0.00000   0.00000   0.04000   0.04000
     0.00      0.00      0.00      0.00      0.00      0.00      0.00      0.00
!  2Th1/TOF1    2Th2/TOF2  Pattern to plot
       1.000      128.000       1
```

I.3.2. Selenium polycrystalline

$Cu_2ZnGeSe_4$

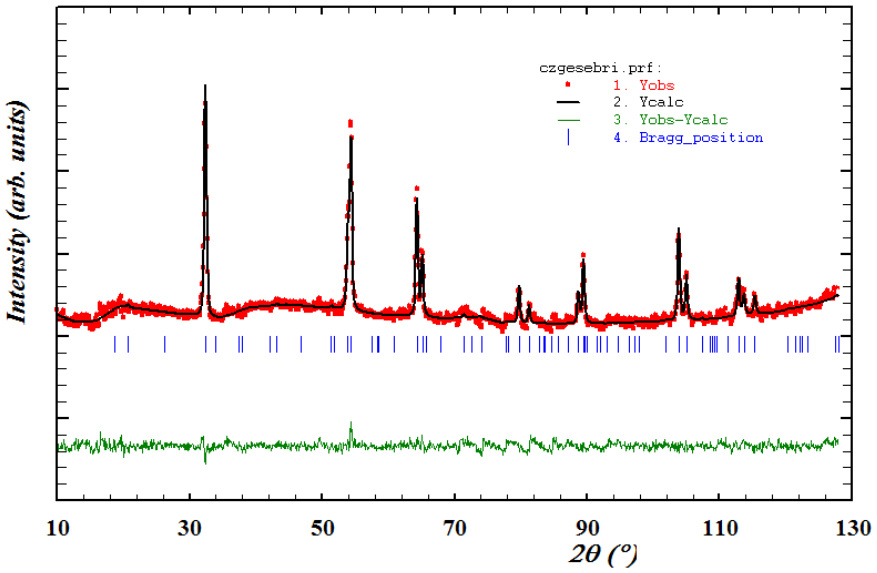

Figure I.14. Rietveld refinement of the neutron pattern of the $Cu_2ZnGeSe_4$ polycrystalline.

```
!  Zero    Code    SyCos    Code   SySin    Code  Lambda     Code MORE ->Patt# 1
  0.04391   11.0  0.00000     0.0  0.00000     0.0 0.000000     0.00   0
!-------------------------------------------------------------------------------
!  Data for PHASE number:   1  ==> Current R_Bragg for Pattern#  1:    10.29
!-------------------------------------------------------------------------------
CZTSBRI
!
!Nat Dis Ang Pr1 Pr2 Pr3 Jbt Irf Isy Str Furth       ATZ    Nvk Npr More
   5   0   0 1.0 1.0 2.0   0   0   0   0   0      18293.680   0   7   0
!
82                     <--Space group symbol
!Atom   Typ       X         Y         Z      Biso       Occ     In Fin N_t Spc /Codes
Se8    Se      0.25199   0.23330   0.12219  0.00000   4.00000   0   0   0     0
                281.00    281.00    291.00     0.00      0.00
Cu2a   Cu      0.00000   0.00000   0.00000  0.00000   1.00000   0   0   0     0
                  0.00      0.00      0.00     0.00      0.00
Cu2d   Cu      0.00000   0.50000   0.75000  0.00000   1.00000   0   0   0     0
                  0.00      0.00      0.00     0.00      0.00
Ge2b   Ge      0.00000   0.00000   0.50000  0.00000   0.88130   0   0   0     0
                  0.00      0.00      0.00     0.00      0.00
Zn2c   Zn      0.00000   0.50000   0.25000  0.00000   0.99070   0   0   0     0
                  0.00      0.00      0.00     0.00      0.00
!-------> Profile Parameters for Pattern #  1
!  Scale      Shape1      Bov       Str1      Str2      Str3   Strain-Model
 0.28483E-01   0.00000   1.86794   0.00000   0.00000   0.00000       0
    21.00000     0.000   301.000     0.000     0.000     0.000
!     U          V         W         X         Y       GauSiz    LorSiz Size-Model
   0.060181  -0.165300   0.165400  0.000000  0.160128  0.000000  0.000000     0
    261.000      0.000      0.000     0.000   271.000     0.000     0.000
!     a          b         c       alpha      beta       gamma     #Cell Info
   5.608989   5.608989  11.043691  90.000000  90.000000  90.000000
   31.00000   31.00000   41.00000   0.00000    0.00000    0.00000
!  Pref1    Pref2      Asy1      Asy2      Asy3      Asy4       S_L       D_L
  0.00000  0.00000   0.00000   0.00000   0.00000   0.00000   0.04000   0.04000
     0.00     0.00      0.00      0.00      0.00      0.00      0.00      0.00
!  2Th1/TOF1    2Th2/TOF2  Pattern to plot
       1.000      128.000       1
```

$Cu_2ZnSn_{0.3}Ge_{0.7}Se_4$

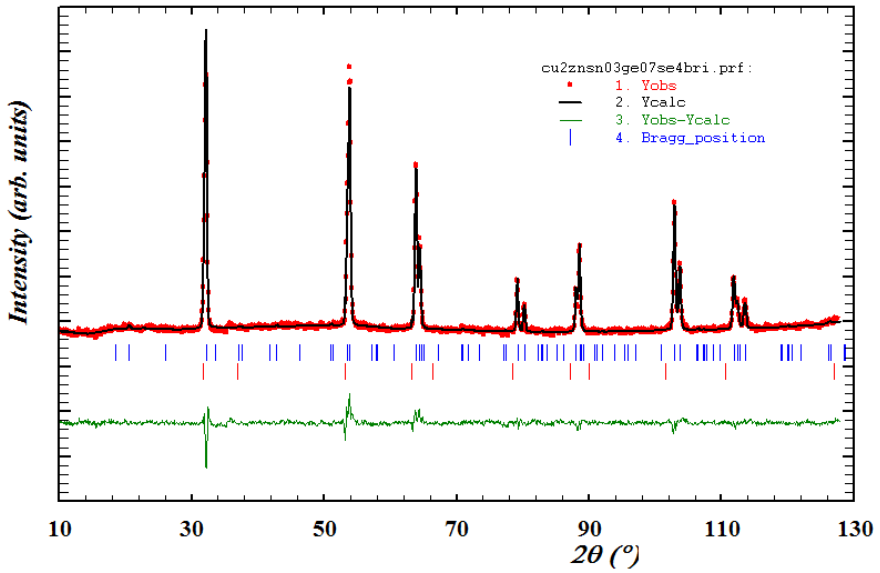

Figure I.15. Rietveld refinement of the neutron pattern of the $Cu_2ZnSn_{0.3}Ge_{0.7}Se_4$ polycrystalline.

```
!  Zero    Code    SyCos    Code   SySin    Code  Lambda     Code MORE ->Patt# 1
  0.02723   11.0  0.00000     0.0  0.00000     0.0 0.000000    0.00   0
!-------------------------------------------------------------------------------
!  Data for PHASE number:   1  ==> Current R_Bragg for Pattern#  1:     9.27
!-------------------------------------------------------------------------------
CZTSBRI
!
!Nat Dis Ang Pr1 Pr2 Pr3 Jbt Irf Isy Str Furth       ATZ    Nvk Npr More
   6   0   0 1.0 1.0 2.0   0   0   0   0   0      18896.539   0   7   0
!
82                     <--Space group symbol
!Atom   Typ       X         Y         Z      Biso       Occ     In Fin N_t Spc /Codes
Se8g   Se      0.25744   0.25857   0.12564  0.00000   4.00000   0   0   0    0
                261.00    261.00    261.00     0.00      0.00
Cu2a   Cu      0.00000   0.00000   0.00000  0.00000   1.00000   0   0   0    0
                  0.00      0.00      0.00     0.00      0.00
Cu2c   Cu      0.00000   0.50000   0.25000  0.00000   1.00000   0   0   0    0
                  0.00      0.00      0.00     0.00      0.00
Sn2b   Sn      0.00000   0.00000   0.50000  0.00000   0.36620   0   0   0    0
                  0.00      0.00      0.00     0.00      0.00
Ge2b   Ge      0.00000   0.00000   0.50000  0.00000   0.54693   0   0   0    0
                  0.00      0.00      0.00     0.00      0.00
Zn2d   Zn      0.00000   0.50000   0.75000  0.00000   0.98530   0   0   0    0
                  0.00      0.00      0.00     0.00      0.00
!-------> Profile Parameters for Pattern #  1
!  Scale        Shape1       Bov       Str1      Str2      Str3   Strain-Model
 0.57103E-01   0.00000   1.55586   0.00000   0.00000   0.00000        0
    21.00000     0.000   251.000     0.000     0.000     0.000
!       U         V         W         X         Y       GauSiz   LorSiz Size-Model
   0.106101  -0.165300   0.165400   0.000000   0.058900   0.000000   0.000000    0
    241.000     0.000     0.000     0.000     0.000     0.000      0.000
!      a         b         c       alpha      beta      gamma      #Cell Info
   5.641222  5.641222  11.158713  90.000000  90.000000  90.000000
   31.00000  31.00000  41.00000   0.00000    0.00000    0.00000
!  Pref1    Pref2      Asy1      Asy2      Asy3      Asy4      S_L       D_L
  0.00000  0.00000   0.00000   0.00000   0.00000   0.00000   0.04000   0.04000
     0.00     0.00      0.00      0.00      0.00      0.00      0.00      0.00
!-------------------------------------------------------------------------------
!  Data for PHASE number:   2  ==> Current R_Bragg for Pattern#  1:    21.32
!-------------------------------------------------------------------------------
 ####   ZnSe  ####
!
!Nat Dis Ang Pr1 Pr2 Pr3 Jbt Irf Isy Str Furth       ATZ    Nvk Npr More
   2   0   0 0.0 0.0 1.0   0   0   0   0   0     332559.344   0   7   1
!
!Jvi Jdi Hel Sol Mom Ter  Brind   RMua    RMub    RMuc   Jtyp  Nsp_Ref Ph_Shift N_Domains
   0   3   0   0   0   0  1.0000  0.0000  0.0000  0.0000    1       0       0       0
!
! Max_dst(dist) (angles)  Bond-Valence Calc.
       3.0000      3.0000
F -4 3 m               <--Space group symbol
!Atom   Typ       X         Y         Z      Biso       Occ     In Fin N_t Spc /Codes
Zn4a   Zn      0.00000   0.00000   0.00000  0.00000   1.00000   0   0   0    0
                  0.00      0.00      0.00     0.00      0.00
Se4c   Se      0.25000   0.25000   0.25000  0.00000   1.00000   0   0   0    0
                  0.00      0.00      0.00     0.00      0.00
!-------> Profile Parameters for Pattern #  1
!  Scale        Shape1       Bov       Str1      Str2      Str3   Strain-Model
 0.10495E-02   0.00000  13.59444   0.00000   0.00000   0.00000        0
   101.00000     0.000   111.000     0.000     0.000     0.000
!       U         V         W         X         Y       GauSiz   LorSiz Size-Model
  -0.332689  -0.165300   0.165400   0.000000   0.058900   0.000000   0.000000    0
    91.000      0.000     0.000     0.000     0.000     0.000      0.000
!      a         b         c       alpha      beta      gamma      #Cell Info
   5.683625  5.683625  5.683625  90.000000  90.000000  90.000000
   81.00000  81.00000  81.00000   0.00000    0.00000    0.00000
!  Pref1    Pref2      Asy1      Asy2      Asy3      Asy4      S_L       D_L
  0.00000  0.00000   0.00000   0.00000   0.00000   0.00000   0.04000   0.04000
     0.00     0.00      0.00      0.00      0.00      0.00      0.00      0.00
!  2Th1/TOF1   2Th2/TOF2  Pattern to plot
      1.000     128.000       1
```

$Cu_2ZnSn_{0.5}Ge_{0.5}Se_4$

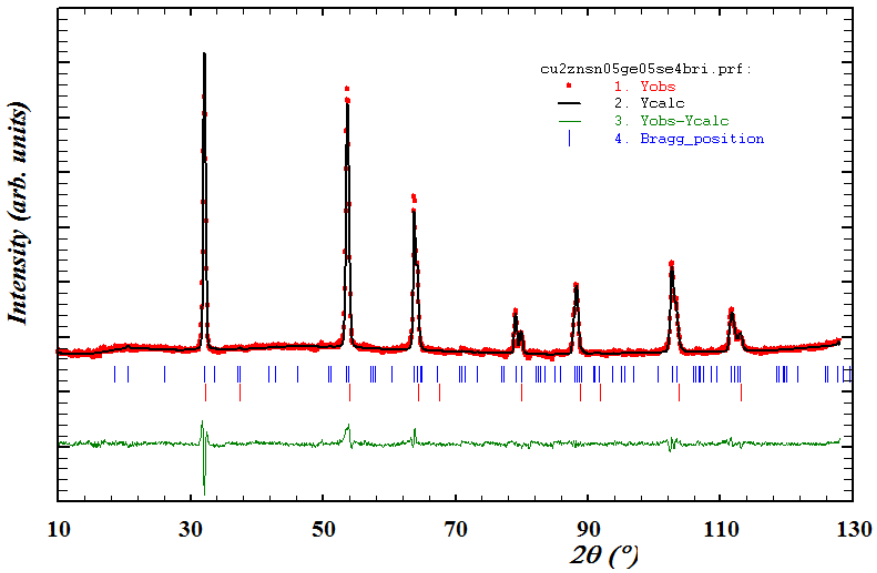

Figure I.16. Rietveld refinement of the neutron pattern of the $Cu_2ZnSn_{0.5}Ge_{0.5}$ Se_4 polycrystalline.

```
!  Zero    Code    SyCos    Code   SySin    Code  Lambda     Code MORE ->Patt# 1
  0.00441   11.0  0.00000     0.0  0.00000     0.0 0.000000    0.00   0
!-------------------------------------------------------------------------------
!  Data for PHASE number:   1  ==> Current R_Bragg for Pattern#  1:     7.91
!-------------------------------------------------------------------------------
CZTSBRI
!
!Nat Dis Ang Pr1 Pr2 Pr3 Jbt Irf Isy Str Furth       ATZ    Nvk Npr More
   6   0   0 1.0 1.0 2.0   0   0   0   0   0      19120.664   0   7   0
!
82                     <--Space group symbol
!Atom   Typ       X         Y         Z      Biso       Occ     In Fin N_t Spc /Codes
Se8g   Se      0.26967   0.26137   0.12629  0.00000   4.00000    0   0   0    0
                 51.00     261.00    271.00     0.00      0.00
Cu2a   Cu      0.00000   0.00000   0.00000  0.00000   1.00000    0   0   0    0
                  0.00      0.00      0.00     0.00      0.00
Cu2c   Cu      0.00000   0.50000   0.25000  0.00000   1.00000    0   0   0    0
                  0.00      0.00      0.00     0.00      0.00
Sn2b   Sn      0.00000   0.00000   0.50000  0.00000   0.49000    0   0   0    0
                  0.00      0.00      0.00     0.00      0.00
Ge2b   Ge      0.00000   0.00000   0.50000  0.00000   0.45000    0   0   0    0
                  0.00      0.00      0.00     0.00      0.00
Zn2d   Zn      0.00000   0.50000   0.75000  0.00000   0.97530    0   0   0    0
                  0.00      0.00      0.00     0.00      0.00
!-------> Profile Parameters for Pattern #  1
!  Scale        Shape1       Bov        Str1       Str2       Str3   Strain-Model
 0.90672E-01   0.00000    1.73564    0.00000    0.00000    0.00000        0
    21.00000     0.000      0.000      0.000      0.000      0.000
!      U          V          W          X          Y        GauSiz    LorSiz Size-Model
   0.210838  -0.165300   0.165400   0.000000   0.058900   0.000000   0.000000    0
      0.000      0.000      0.000      0.000      0.000      0.000      0.000
!      a          b          c        alpha       beta       gamma      #Cell Info
   5.648028   5.648028  11.197145  90.000000  90.000000  90.000000
   31.00000   31.00000   41.00000    0.00000    0.00000    0.00000
!  Pref1    Pref2      Asy1       Asy2       Asy3       Asy4       S_L        D_L
  0.00000  0.00000   0.00000    0.00000    0.00000    0.00000   0.04000   0.04000
     0.00     0.00      0.00       0.00       0.00       0.00      0.00      0.00
!-------------------------------------------------------------------------------
!  Data for PHASE number:   2  ==> Current R_Bragg for Pattern#  1:     7.68
!-------------------------------------------------------------------------------
 ####   ZnSe  ####
!
!Nat Dis Ang Pr1 Pr2 Pr3 Jbt Irf Isy Str Furth       ATZ    Nvk Npr More
   2   0   0 0.0 0.0 1.0   0   0   0   0   0     332559.344   0   7   1
!
!Jvi Jdi Hel Sol Mom Ter  Brind    RMua     RMub     RMuc    Jtyp  Nsp_Ref Ph_Shift N_Domains
   0   3   0   0   0   0  1.0000  0.0000   0.0000   0.0000     1       0       0       0
!
! Max_dst(dist) (angles)  Bond-Valence Calc.
      3.0000       3.0000
F -4 3 m               <--Space group symbol
!Atom   Typ       X         Y         Z      Biso       Occ     In Fin N_t Spc /Codes
Zn4a   Zn      0.00000   0.00000   0.00000  0.00000   1.00000    0   0   0    0
                  0.00      0.00      0.00     0.00      0.00
Se4c   Se      0.25000   0.25000   0.25000  0.00000   1.00000    0   0   0    0
                  0.00      0.00      0.00     0.00      0.00
!-------> Profile Parameters for Pattern #  1
!  Scale        Shape1       Bov        Str1       Str2       Str3   Strain-Model
 0.15804E-02   0.00000    3.32214    0.00000    0.00000    0.00000        0
    91.00000     0.000     71.000      0.000      0.000      0.000
!      U          V          W          X          Y        GauSiz    LorSiz Size-Model
   0.755515  -0.165300   0.165400   0.000000   0.058900   0.000000   0.000000    0
     61.000      0.000      0.000      0.000      0.000      0.000      0.000
!      a          b          c        alpha       beta       gamma      #Cell Info
   5.597635   5.597635   5.597635  90.000000  90.000000  90.000000
   81.00000   81.00000   81.00000    0.00000    0.00000    0.00000
!  Pref1    Pref2      Asy1       Asy2       Asy3       Asy4       S_L        D_L
  0.00000  0.00000   0.00000    0.00000    0.00000    0.00000   0.04000   0.04000
     0.00     0.00      0.00       0.00       0.00       0.00      0.00      0.00
!  2Th1/TOF1    2Th2/TOF2  Pattern to plot
      1.000      128.000       1
```

$Cu_2ZnSn_{0.7}Ge_{0.3}Se_4$

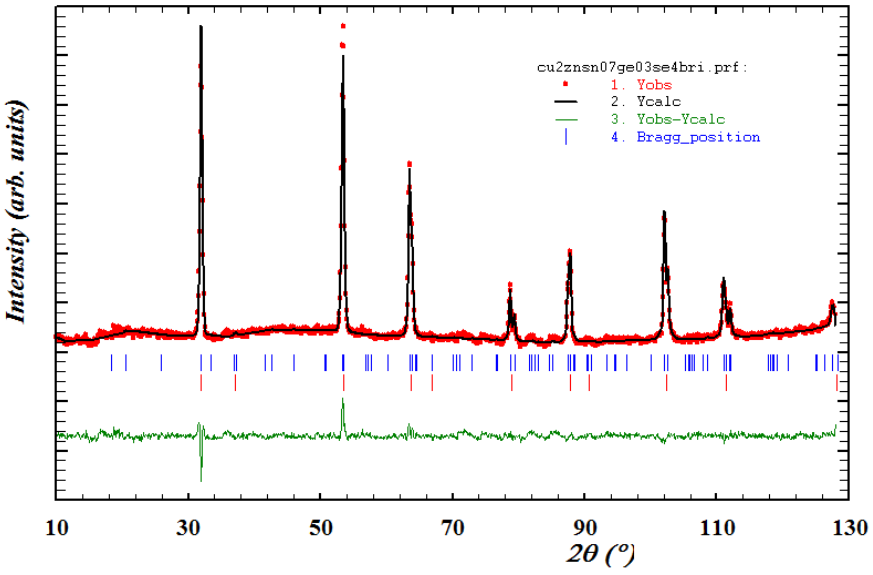

Figure I.17. Rietveld refinement of the neutron pattern of the $Cu_2ZnSn_{0.7}Ge_{0.3}$ Se_4 polycrystalline.

```
!  Zero    Code    SyCos    Code   SySin    Code  Lambda     Code MORE ->Patt# 1
  0.01243   11.0  0.00000     0.0  0.00000     0.0 0.000000    0.00   0
!-------------------------------------------------------------------------------
!  Data for PHASE number:   1  ==> Current R_Bragg for Pattern#  1:    13.29
!-------------------------------------------------------------------------------
CZTSBRI
!
!Nat Dis Ang Pr1 Pr2 Pr3 Jbt Irf Isy Str Furth       ATZ    Nvk Npr More
   6   0   0 1.0 1.0 2.0   0   0   0   0   0      19368.939   0   7   0
!
82                     <--Space group symbol
!Atom   Typ       X         Y         Z      Biso       Occ     In Fin N_t Spc /Codes
Se8g   Se      0.25398   0.25008   0.13044   0.00000    4.00000   0   0   0    0
              241.00    271.00    281.00      0.00       0.00
Cu2a   Cu      0.00000   0.00000   0.00000   0.00000    1.00000   0   0   0    0
                0.00      0.00      0.00      0.00       0.00
Cu2c   Cu      0.00000   0.50000   0.25000   0.00000    1.00000   0   0   0    0
                0.00      0.00      0.00      0.00       0.00
Sn2b   Sn      0.00000   0.00000   0.50000   0.00000    0.68000   0   0   0    0
                0.00      0.00      0.00      0.00       0.00
Ge2b   Ge      0.00000   0.00000   0.50000   0.00000    0.26000   0   0   0    0
                0.00      0.00      0.00      0.00       0.00
Zn2d   Zn      0.00000   0.50000   0.75000   0.00000    0.96000   0   0   0    0
                0.00      0.00      0.00      0.00       0.00
!-------> Profile Parameters for Pattern #  1
!  Scale      Shape1      Bov        Str1       Str2       Str3   Strain-Model
 0.40779E-01   0.00000   1.38352   0.00000    0.00000    0.00000       0
    21.00000     0.000     0.000     0.000      0.000      0.000
!      U          V         W         X          Y        GauSiz   LorSiz Size-Model
   0.089046  -0.165300   0.165400   0.000000   0.058900   0.000000   0.000000    0
      0.000      0.000     0.000      0.000      0.000      0.000      0.000
!      a          b         c        alpha      beta       gamma      #Cell Info
   5.669302   5.669303  11.259559  90.000000  90.000000  90.000000
   31.00000   31.00000   41.00000    0.00000    0.00000    0.00000
!  Pref1    Pref2      Asy1      Asy2      Asy3      Asy4      S_L       D_L
  0.00000  0.00000   0.00000   0.00000   0.00000   0.00000   0.04000   0.04000
     0.00     0.00      0.00      0.00      0.00      0.00      0.00      0.00
!-------------------------------------------------------------------------------
!  Data for PHASE number:   2  ==> Current R_Bragg for Pattern#  1:     5.03
!-------------------------------------------------------------------------------
 ####   ZnSe  ####
!
!Nat Dis Ang Pr1 Pr2 Pr3 Jbt Irf Isy Str Furth       ATZ    Nvk Npr More
   2   0   0 0.0 0.0 1.0   0   0   0   0   0     332559.344   0   7   1
!
!Jvi Jdi Hel Sol Mom Ter  Brind   RMua    RMub    RMuc   Jtyp  Nsp_Ref Ph_Shift N_Domains
   0   3   0   0   0   0  1.0000  0.0000  0.0000  0.0000    1       0       0       0
!
! Max_dst(dist) (angles)  Bond-Valence Calc.
      3.0000      3.0000
F -4 3 m               <--Space group symbol
!Atom   Typ       X         Y         Z      Biso       Occ     In Fin N_t Spc /Codes
Zn4a   Zn      0.00000   0.00000   0.00000   0.00000    1.00000   0   0   0    0
                0.00      0.00      0.00      0.00       0.00
Se4c   Se      0.25000   0.25000   0.25000   0.00000    1.00000   0   0   0    0
                0.00      0.00      0.00      0.00       0.00
!-------> Profile Parameters for Pattern #  1
!  Scale      Shape1      Bov        Str1       Str2       Str3   Strain-Model
 0.24324E-02   0.00000   2.39879   0.00000    0.00000    0.00000       0
    51.00000     0.000   251.000     0.000      0.000      0.000
!      U          V         W         X          Y        GauSiz   LorSiz Size-Model
   1.939323  -0.165300   0.165400   0.000000   0.058900   0.000000   0.000000    0
    261.000      0.000     0.000      0.000      0.000      0.000      0.000
!      a          b         c        alpha      beta       gamma      #Cell Info
   5.654593   5.654593   5.654593  90.000000  90.000000  90.000000
   81.00000   81.00000   81.00000    0.00000    0.00000    0.00000
!  Pref1    Pref2      Asy1      Asy2      Asy3      Asy4      S_L       D_L
  0.00000  0.00000   0.00000   0.00000   0.00000   0.00000   0.04000   0.04000
     0.00     0.00      0.00      0.00      0.00      0.00      0.00      0.00
!  2Th1/TOF1    2Th2/TOF2  Pattern to plot
      1.000      128.000       1
```

$Cu_2ZnSnSe_4$

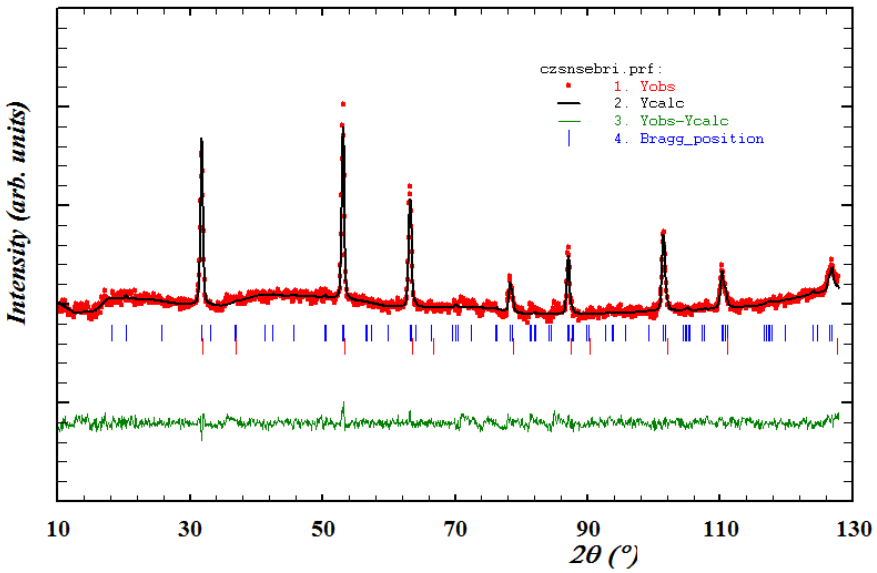

Figure I.18. Rietveld refinement of the neutron pattern of the $Cu_2ZnSnSe_4$ polycrystalline.

```
!  Zero    Code    SyCos    Code   SySin    Code  Lambda     Code MORE ->Patt# 1
  0.02465   11.0  0.00000    0.0  0.00000    0.0 0.000000    0.00   0
!-------------------------------------------------------------------------------
!  Data for PHASE number:   1  ==> Current R_Bragg for Pattern#  1:    14.27
!-------------------------------------------------------------------------------
CZTSBRI
!
!Nat Dis Ang Pr1 Pr2 Pr3 Jbt Irf Isy Str Furth       ATZ    Nvk Npr More
   5   0   0 1.0 1.0 2.0   0   0   0   0   0      20005.160   0   7   0
!
82                     <--Space group symbol
!Atom   Typ       X         Y         Z      Biso       Occ     In Fin N_t Spc /Codes
Se8    Se      0.26545   0.24557   0.12987  0.00000   4.00000    0   0   0    0
                121.00    111.00    101.00     0.00      0.00
Cu2a   Cu      0.00000   0.00000   0.00000  0.00000   1.00000    0   0   0    0
                  0.00      0.00      0.00     0.00      0.00
Cu2d   Cu      0.00000   0.50000   0.75000  0.00000   1.00000    0   0   0    0
                  0.00      0.00      0.00     0.00      0.00
Sn2b   Sn      0.00000   0.00000   0.50000  0.00000   0.99000    0   0   0    0
                  0.00      0.00      0.00     0.00      0.00
Zn2c   Zn      0.00000   0.50000   0.25000  0.00000   0.99000    0   0   0    0
                  0.00      0.00      0.00     0.00      0.00
!-------> Profile Parameters for Pattern #  1
!  Scale        Shape1      Bov       Str1      Str2      Str3   Strain-Model
 0.18008E-01   0.00000   1.72091   0.00000   0.00000   0.00000        0
    21.00000     0.000    61.000     0.000     0.000     0.000
!       U         V         W         X         Y       GauSiz   LorSiz Size-Model
   0.073986  -0.165300   0.165400   0.000000   0.158480   0.000000   0.000000    0
     71.000     0.000     0.000     0.000     51.000     0.000      0.000
!      a         b         c        alpha      beta       gamma      #Cell Info
   5.695987   5.695987  11.350216  90.000000  90.000000  90.000000
   31.00000   31.00000   41.00000   0.00000    0.00000    0.00000
!  Pref1    Pref2      Asy1      Asy2      Asy3      Asy4      S_L       D_L
  0.00000  0.00000  0.00000  0.00000  0.00000  0.00000  0.04000  0.04000
     0.00     0.00     0.00     0.00     0.00     0.00     0.00     0.00
!-------------------------------------------------------------------------------
!  Data for PHASE number:   2  ==> Current R_Bragg for Pattern#  1:    12.09
!-------------------------------------------------------------------------------
 ####   ZnSe  ####
!
!Nat Dis Ang Pr1 Pr2 Pr3 Jbt Irf Isy Str Furth       ATZ    Nvk Npr More
   2   0   0 0.0 0.0 1.0   0   0   0   0   0     332559.344   0   7   1
!
!Jvi Jdi Hel Sol Mom Ter  Brind   RMua    RMub    RMuc   Jtyp  Nsp_Ref Ph_Shift N_Domains
   0   3   0   0   0   0  1.0000  0.0000  0.0000  0.0000    1       0       0       0
!
! Max_dst(dist) (angles)  Bond-Valence Calc.
      3.0000       3.0000
F -4 3 m               <--Space group symbol
!Atom   Typ       X         Y         Z      Biso       Occ     In Fin N_t Spc /Codes
Zn4a   Zn      0.00000   0.00000   0.00000  1.00000   1.00000    0   0   0    0
                  0.00      0.00      0.00     0.00      0.00
Se4c   Se      0.25000   0.25000   0.25000  1.00000   1.00000    0   0   0    0
                  0.00      0.00      0.00     0.00      0.00
!-------> Profile Parameters for Pattern #  1
!  Scale        Shape1      Bov       Str1      Str2      Str3   Strain-Model
 0.62714E-04   0.00000   0.00000   0.00000   0.00000   0.00000        0
    51.00000     0.000     0.000     0.000     0.000     0.000
!       U         V         W         X         Y       GauSiz   LorSiz Size-Model
   0.115641  -0.165300   0.165400   0.000000   0.058900   0.000000   0.000000    0
     91.000     0.000     0.000     0.000     0.000     0.000      0.000
!      a         b         c        alpha      beta       gamma      #Cell Info
   5.666368   5.666368   5.666368  90.000000  90.000000  90.000000
   81.00000   81.00000   81.00000   0.00000    0.00000    0.00000
!  Pref1    Pref2      Asy1      Asy2      Asy3      Asy4      S_L       D_L
  0.00000  0.00000  0.00000  0.00000  0.00000  0.00000  0.04000  0.04000
     0.00     0.00     0.00     0.00     0.00     0.00     0.00     0.00
!  2Th1/TOF1    2Th2/TOF2  Pattern to plot
       1.000      128.000       1
```

Appendix II: Raman measurements

In section 3.4.1, it was discussed if the band gap measured for $Cu_2ZnGeSe_4$ single crystal was due to the mixture of stannite-kesterite structures. In this appendix, it is plotted the Raman measurements of the two CZGSe single crystals presented in this work, one with the kesterite structure studied in the Raman (section 3.5) and structure analysis section, while the other seems to be a mixture of both structures, which was the one studied in the ellipsometry section (section 3.4).

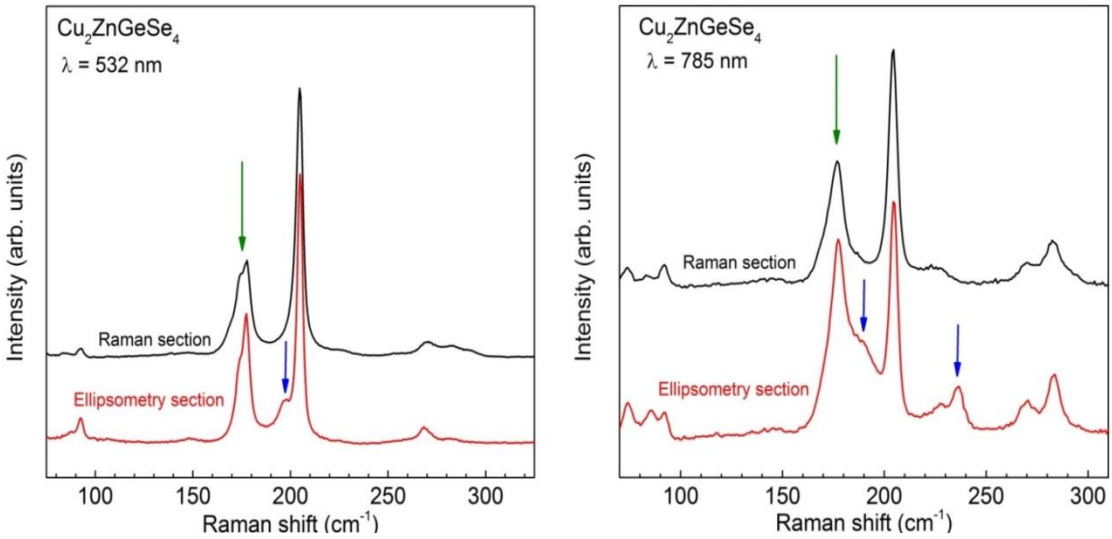

Figure II.1. Raman spectra of $Cu_2ZnGeSe_4$ single crystals measured with 532 nm, left, and 785 nm, right, excitation wavelengths marked in the plots. In black, there is the Raman spectrum of the single crystal characterized in the Raman section 3.5. The red Raman spectrum is the single crystal characterized only in the Ellipsometry section 3.4. Green arrow indicated the intensity changes between both spectra in the 170-180 cm^{-1} region. Blue arrows shown the new peaks, above appears the peak at 196 cm-1 and below appear two extra peaks at 190 cm^{-1} and 236 cm^{-1}.

Appendix III: Publications and conferences contributions

This appendix includes the publications and conferences contributions from this research.

III.1. Publications

1. "Non-stoichiometry effect and disorder in Cu_2ZnSnS_4 thin films obtained by flash evaporation: Raman scattering investigation", R. Caballero, **E. Garcia-Llamas**, J.M. Merino, M. León, I. Babichuk, V. Dzhagan, V. Strelchuk, M. Valakh, Acta Materialia 65 (2014) 412-417.
2. "Band-gap engineering of $Cu_2ZnSn_{1-x}Ge_xS_4$ single crystals and influence of the surface properties", R. Caballero, I. Victorov, R. Serna, J.M. Cano-Torres, C. Maffiotte, **E. Garcia-Llamas**, J.M. Merino, I. Bodnar, M. León, Acta Materialia 79 (2014) 181-187.
3. "Towards the growth of $Cu_2ZnSn_{1-x}Ge_xS_4$ thin films by a single-stage process: Effect of substrate temperature and composition", R. Caballero, J.M. Cano-Torres, **E. Garcia-Llamas**, X. Fontané, A. Pérez-Rodríguez, D. Greiner, C.A. Kaufmann, J.M. Merino, I. Victorov, G. Baraldi, M. Valakh, I. Bodnar, V. Izquierdo-Roca, M. León, Solar Energy Materials and Solar Cells 139 (2015) 1-9.
4. "Wide band-gap tuning $Cu_2ZnSn_{1-x}Ge_xS_4$ single crystals: optical and vibrational properties", **E. Garcia-Llamas**, J. M. Merino, R. Serna, X. Fontané, I. A. Victorov, A. Pérez-Rodríguez, M. León, I. V. Bodnar, V. Izquierdo-Roca, R. Caballero, Solar Energy Materials and Solar Cells 2015, doi:10.1016/j.solmat.2015.12.021.
5. "Multiwavelength excitation Raman scattering of $Cu_2ZnSn_{1-x}Ge_x(S,Se)_4$ solid solution in single crystals for band gap engineering and earth abundant photovoltaic application", **E. Garcia-Llamas**, M. Guc, I.V. Bodnar, X. Fontané, R. Caballero, J.M. Merino, M. León, V. Izquierdo-Roca, Journal of Alloys and Compounds 2016, doi:10.1016/j.jallcom.2016.09.035.
6. "Cu_2ZnSnS_4 thin film solar cells grown by fast thermal evaporation and thermal treatment", **E. Garcia-Llamas**, J.M. Merino, R. Gunder, K. Neldner, D. Greiner, Y. Sánchez, V. Izquierdo-Roca, E. Saucedo, A. Steigert, M. León, S. Schorr, R. Caballero, Solar Energy 2016. Under review.

III.2. Conferences contributions

Invited talk

1. "Structural and optical characterization of $Cu_2ZnSn_{1-x}Ge_x(S,Se)_4$ compounds", **E. Garcia-Llamas**, R. Caballero, I. Victorov, A. Nicorici, I. V. Bodnar, R. Serna, E. Arushanov, M. León and J. M. Merino, MSCMP-7, Chisinau, Moldavia, 2014.

Oral presentations

1. "Investigation of SnS thin films prepared by a two-stage process for photovoltaic applications", R. Caballero, V. Condé, **E. Garcia-Llamas**, J.M. Merino, M. León, Nanosmat 2014, Dublin, Ireland.

2. "Structural and optical characterizations of kesterite, possible future light absorber for solar cells", **E. Garcia-Llamas**, R. Caballero, M. León, R. Serna, I. Victorov, I. V. Bodnar, and J. M. Merino, Open Day Kestcells, Universidad Autónoma de Madrid, Madrid, Spain 2014.

3. "Wide Band-gap tuning of $Cu_2ZnSn_{1-x}Ge_x(S,Se)_4$ solid solutions for photovoltaic multi-junction devices development: a study of their optical, structural and vibrational properties", **E. Garcia-Llamas**, X. Fontané, R. Serna, I. A. Victorov, J. M. Merino, M. Guc, M. Valakh, M. León, A. Pérez-Rodríguez, I. V. Bodnar, V. Izquierdo-Roca, R. Caballero, MRS Spring Meeting 2015, San Francisco, USA.

4. "Optical and structural study of quaternary chalcogenide", **Eduard Garcia-Llamas**, José Manuel Merino, Rosalía Serna, I. V. Bodnar, I. A. Viktorov, Máximo León, Raquel Caballero, NEXTGEN NANO PV'15, Mahón, Spain, 2015.

5. "$Cu_2ZnSn(S,Se)_4$ Kesterite material for solar cells devices", **E. Garcia-Llamas**, R. Caballero, M. León, X. Fontané, R. Serna, I. A. Victorov, M. Guc, M. Valakh, A. Pérez-Rodríguez, I. V. Bodnar, V. Izquierdo-Roca, J. M. Merino, XVIII Young researchers meeting of the Nicolás Cabrera Institute, Madrid, Spain, 2015.

Poster presentations

1. "Synthesis of Cu_2ZnSnS_4 from different routes by solid state reaction", **E. Garcia-Llamas**, J.M. Merino, R. Caballero, J.M. Cano-Torres, D. Regesch, J. Sendler, S. Siebentritt, M. León, 4th European Kesterite Workshop, Berlin, Germany, 2013.
2. "Synthesis of kesterite by solid state reaction", **E. Garcia-Llamas**, J.M. Merino, R. Caballero, J.M. Cano-Torres, D. Regesch, J. Sendler, S. Siebentritt, M. León, XVI Young researchers meeting of the Nicolás Cabrera Institute, Madrid, Spain 2013.
3. "Cu_2-Zn-IV-VI_4 (IV=Ge,Sn; VI=S,Se) quaternary chalcogenide: structural and optoelectronic characterization", **E.Garcia-Llamas**, R. Caballero, I. Bodnar, I. Victorov, G. Gurieva, S. Schorr, M. León, J.M. Merino, E-MRS Spring Meeting 2014, Lille, France.
4. "Optoelectronic and structural study of quaternary chalcogenide", **E. Garcia-Llamas**, R. Caballero, I. Bodnar, I. Victorov, M. León, J.M. Merino, Congreso Nacional de Materiales, Barcelona, Spain 2014.
5. "Structural and optoelectronic characterization of pseudo-quaternary chalcogenides", **E. Garcia-Llamas**, R. Caballero, R. Serna,I. V. Bodnar, I. A. Victorov, M. León, J. M. Merino, 5th European Kesterite Workshop, Tallin, Estonia, 2014.
6. "Preliminary efficiencies of Cu_2ZnSnS_4 thin film solar cells grown by thermal evaporation and thermal treatment", **E. Garcia-Llamas**, J.M. Merino, R. Gunder, K. Neldner, Y. Sánchez, V. Izquierdo-Roca, E. Saucedo, M. León, S. Schorr, R. Caballero, 6th European Kesterite Workshop, Newcastle, England, 2015.